COLLEGE DOCTORAL PAYS DE LA LOIRE
SCIENCES DE L'INGENIERIE ET DES SYSTEMES

Oniris VetAgroBio Nantes
ÉCOLE NATIONALE

# THESE DE DOCTORAT

## ONIRIS VETAGROBIO NANTES

**ECOLE DOCTORALE N° 602**
***Sciences de l'Ingénierie et des Systèmes***
**Spécialité : « *Génie des procédés et des bioprocédés* »**

Par
**Sadhan Jyoti DUTTA**

**Development of a microwave heating treatment as a substitute for the classical retort sterilization process**

*Développement d'un traitement de chauffage par micro-ondes comme substitut au procédé classique de stérilisation en autoclave*

**Thèse présentée et soutenue à Oniris VetAgroBio Nantes, le 10 décembre 2025**

**Unité de recherche : GEPEA UMR CNRS 6144**

**Rapporteurs avant soutenance** :

| | |
|---|---|
| Catherine Renard | Directrice de recherche, INRAE, Nantes |
| Philippe Bohuon | Professeur, Institut Agro, Montpellier |

**Composition du Jury :**

| | | |
|---|---|---|
| Président : | Francis Courtois | Professeur, Université de Montpellier, Montpellier |
| Examinateurs : | Nadine Allanic | Professeure, IUT Nantes |
| | Francis Courtois | Professeur, Université de Montpellier, Montpellier |
| Dir. de thèse : | Sébastien Curet-Ploquin | Professeur, Oniris VetAgroBio, Nantes |
| Co-dir. de thèse : | Olivier Rouaud | Professeur, Oniris VetAgroBio, Nantes |

**Invité(s)**

| | |
|---|---|
| Nicolas Bélaubre | Chef de Project (R&D), CTCPA |

*Le monde est beau, et la vie est pleine,*
*Quand le cœur reste clair et l'esprit libre.*

*— Anonyme*

*The world is beautiful, and life is full,*
*When the heart remains clear and the mind free.*

*— Anonymous*

# Acknowledgement

This thesis was carried out as a CIFRE industrial doctorate, funded by the Association Nationale de la Recherche et de la Technologie (ANRT) through the CIFRE convention N° 2022/1042. It was conducted within the framework of a close collaboration between CTCPA, Oniris VetAgroBio, the GEPEA research laboratory of CNRS, and Sairem.

My first and foremost gratitude goes to my director, Professor Sébastien Curet, for being my compass and guide as I embarked on this journey of doing meaningful research at the GEPEA research lab of Oniris VetAgroBio. You have always encouraged me with new ideas and supported me throughout. I am also deeply grateful to my co-director, Professor Olivier Rouaud, for constantly motivating me during this thesis. Without both of you, I could not have imagined completing this work.

I am very thankful to Dr. Nicolas Bélaubre, who was always there for me whenever I needed help during my thesis. I also warmly thank Dr. Patrice Dole, who always highlighted new ideas and encouraged me to think in new ways and push my boundaries. I would like to thank Mr. Alexandre Thillier for sharing with me his knowledge of industrial microwaves and for always providing me with the resources I needed. My gratitude also goes to Mr. Anthony Ogé, without whom many of the technical designs would not have been possible. I am thankful to Sylvie, Delphine, and Luc, who provided me with important technical help in different circumstances during the project. Heartful thanks to Prof. Lionel Boillereaux for encouraging and recommending me to pursue this PhD. I also thank Isabelle, who was always so kind and helpful in all the administrative and non-administrative work and never let me worry about those matters. As a whole, I would like to thank the entire GEPEA lab of Oniris VetAgro Bio for welcoming me warmly into the laboratory.

I would also like to thank all my colleagues at CTCPA, who have been so wonderful in showing me the beauty of French culture, food, and tradition. Thank you, Yann and Nicolas Lehebel, for introducing me to this beautiful culture and cuisine. My gratitude also goes to my dear colleagues Sophie, Morgane, Michel, Willy, Marie-Luce, Catherine, Fabrice, and Clémence, for being such kind and wonderful colleagues. I have learned a lot from you. I sincerely thank the entire CTCPA team for wholeheartedly welcoming me and allowing me to carry out my research.

I would like to thank my CSI members, Professor Nadine Allanic and Professor Alain Ledoux, for their valuable advice and guidance during our meetings throughout my thesis.

I am also grateful to the Association Nationale Recherche Technologie (ANRT) for financially supporting this industrial thesis through the CIFRE convention N° 2022/1042.

I am very thankful to all my PhD colleagues for always being there for me. Thank you Alan for being my best partner in every possible way and all the moments we have shared in this Phd journey. Thank you Samuel for the brilliant discussions we shared, which gave me new ideas for my work. Special thank you to Anna for always being my active partner in various projects. Thank you Claire for always proposing various refreshing activities ranging from social to sports. Thank you Joudy for all your support and activities together. Thank you Maryam, Faidat, Victoire, Debora & David, Gauri, Minh, Piyush, Xin Yan, Etienne, Gabriel, Michael, Christy, Xin Hu, Saylor, Solène, Salma, Ana, Jean, Corentin, Benjamin & Benjamin, and all the others, for being such wonderful company throughout this journey. You have made a hard journey

much easier. My gratitude also goes to the entire ATD Oniris association for creating such a friendly ecosystem.

I also thank Nathalie and Soline from the Association of Foreign Researchers in Nantes for helping me with administrative tasks, which greatly facilitated my stay and allowed me to focus on my research. Also thank you for organizing the various social and cultural activities for researchers in Nantes. Thank you Anne for introducing me to the various cultural and social activities at Singa which have definitely helped refreshing the mind for research.

I am deeply grateful to my parents, Mr. Atul Dutta and Mrs. Madhubala Dutta, for always supporting me and providing me with the best education that led me to where I am today. They brought me into this world, nourished me, and helped me become who I am. Thank you to my brother Saurav for the wonderful times we have shared so far. I also warmly and wholeheartedly thank Claire for always being the most supportive and caring person to me. Thank you, Frederic, Françoise and Jean, for being so kind and wonderful. Thank you, Gaëlle, François, and Nicole, for all your kindness and also for letting me discover the beauty of French history, culture, traditions, and gastronomy.

Finally, I would like to express my sincere gratitude to all my family members, friends, colleagues, and every honest man and woman I had the chance to meet during my PhD journey. Each of you has contributed in your own way, and I will always remain grateful. I am also thankful to all the people I have met along this journey who made my stay in France so wonderful and filled with only good memories.

Sadhan Jyoti DUTTA

# Table of content

Acknowledgement ..... III
Table of content ..... V
List of Figures ..... IX
List of Tables ..... XIII
Nomenclature & Abbreviations ..... XV
Resume etendu en francais ..... XX
Chapter 1 ..... 1
Introduction ..... 1
1.1 Food sterilization ..... 1
1.2 Food packaging and counterpressure during sterilisation ..... 1
1.3 Knowledge gap and motivation ..... 2
1.4 Central hypothesis and objectives ..... 2
1.5 Thesis outline ..... 3
Chapter 2 ..... 5
Literature Review On Microwave Sterilization And Its Evolution On Food Packaging, Numerical Modelling and Engineering Developments. ..... 5
2.1 Introduction ..... 5
2.2 Sterilization approaches in food processing ..... 5
2.2.1 Conventional sterilization process ..... 8
2.2.1.1 Saturated steam sterilization ..... 9
2.2.1.2 Water based heating methods ..... 9
2.2.1.3 Steam-air sterilization ..... 9
2.2.2 Non-conventional sterilization processes ..... 10
2.2.2.1 High Pressure processing (HPP) ..... 10
2.2.2.2 Pulsed Electric Fields (PEF) Sterilization ..... 10
2.2.2.3 Ultraviolet (UV) Irradiation ..... 11
2.2.2.4 Microwave Sterilization ..... 11
2.2.2.5 Ohmic Heating ..... 11
2.3 Microwave Sterilization and Its Evolution ..... 11
2.3.1 Microwave heating in the electromagnetic spectrum ..... 11
2.3.2 Microwave heating and dielectric properties ..... 12
2.3.3 Evolution of microwave sterilization technology in food processing ..... 13
2.3.4 Microwave-Assisted Thermal Sterilization (MATS) System ..... 18
2.3.5 Role of microwave generators in sterilization process ..... 20

2.3.5.1 Magnetron-based generators: conventional power source for microwaves ..... 21
2.3.3.2 Solid-state microwave generators: precision heating for food sterilization ..... 21
2.4 Microwave Food Packaging ..... 23
2.4.1 Evolution of Microwave Packaging ..... 24
2.4.2 Properties of Microwave Packaging ..... 25
2.4.3 Internal pressure generation in microwave packaging ..... 29
2.4.4 Techniques to hold inner pressure in microwave packaging ..... 29
2.5 Structural Integrity of Flexible and Semi-Rigid Packaging ..... 31
2.5.1 Flexible and Semi-Rigid Packaging in the Food Industry ..... 31
2.5.2 Polypropylene as a Material in Food Packaging ..... 32
2.5.3 Seal Integrity and Weakness of Heat Seals ..... 32
2.5.4 Air Flow, Deformation, and Pressure in Food Trays During Heat Treatment ..... 33
2.6 Numerical Modelling and Food Sterilization ..... 33
2.6.1 Numerical modelling approaches and Computational Fluid Dynamics (CFD) ..... 36
2.6.2 Computational Fluid Dynamics–Fluid–Structure Interaction (CFD–FSI) and Structural Mechanics for Packaging Deformation ..... 36
2.6.2.1 Structural Mechanics and Fluid-Structure Interactions ..... 37
2.6.3 Failure Theory: von Mises Criterion ..... 39
2.6.4 Commercial software for numerical modelling ..... 41
2.7 Knowledge Gap and Final Remarks ..... 47
Chapter 3 ..... 49
Numerical and Experimental Study of Temperature and Headspace Pressure During Conventional Thermal Sterilization in Rigid Food Packaging Using CFD ..... 49
3.1 Introduction ..... 49
3.2 Materials and Methods ..... 50
3.2.1 Experimental study ..... 50
3.2.1.1 Model Food Preparation ..... 50
3.2.1.2 Properties of mashed potato ..... 50
3.2.1.3 Thermal sterilization ..... 52
3.2.2 Numerical modelling ..... 55
3.2.2.1 Model description ..... 58
3.3 Results and discussions ..... 63
3.3.1 Temperature distribution and model validation ..... 63
3.3.1.1 Experimental and simulated temperature distribution ..... 63
3.3.1.2 Comparison of heat transfer coefficients ..... 67
3.3.2 Pressure evolution ..... 70

3.3.2.1 Experimental and simulated pressure ..... 70
3.3.3 Model limitations and improvement opportunities ..... 73
3.4 Conclusions ..... 74
Chapter 4 ..... 76
Coupled CFD–FSI–Thermal and Structural Mechanics Analysis of Deformation in Food Packaging under Air Injection and Heat Treatment ..... 76
4.1 Introduction ..... 76
4.2 Objectives and Research Questions ..... 76
4.3 Materials and Methods ..... 77
4.3.1Experimental Study ..... 77
4.3.1.1 Tray Materials and Food Matrix ..... 77
4.3.1.2 Pressure and Temperature Measurement Devices ..... 78
4.3.1.3 Mechanical Constraint Device ..... 78
4.3.1.4 Air injection system equipped with mechanical constraint ..... 79
4.3.1.5 Imaging System for Deformation Monitoring ..... 80
4.3.1.6 Thermal treatment equipped with mechanical constraint ..... 80
4.3.2 Experimental Protocols and Designs ..... 81
4.3.3 Numerical Modelling ..... 84
4.3.3.1 Model Description ..... 84
4.3.3.2 Initial and Boundary Conditions ..... 87
4.3.3.3 Mesh independence validation ..... 89
4.4 Results and discussions ..... 90
4.4.1 Deformation–pressure coupling and model validation during air injection ..... 90
4.4.2 Rupture of packaging deformation during heat treatments ..... 95
4.4.3 Air Flow Patterns inside PP tray during Air Injection and Heat Treatment ..... 97
4.4.4 Reaction force and von Mises stress analysis of PP film ..... 104
4.4.5 Effect of Mechanical Constraint on Pressure Evolution and Rupture ..... 109
4.5 Conclusion ..... 113
Chapter 5 ..... 115
Influence of Mechanical Constraints on Thermal and Pressure Behaviour During Microwave Heating of Rigid and Flexible Food Packaging Systems ..... 115
5.1 Introduction ..... 115
5.2 Materials and Methods ..... 115
5.2.1 Materials ..... 115
5.2.1.1 Model Food ..... 115
5.2.1.2 Packaging materials ..... 116

5.2.1.3 Pressure and Temperature measurements ..... 116
5.2.2 Experimental Setup ..... 117
5.2.2.1 915 MHz microwave system with pressure regulation system ..... 117
5.2.3 Experimental Design ..... 119
5.2.3.1 Part A – Flexible Polypropylene Packaging ..... 119
5.2.3.2 Part B – Rigid Pressurized Constraint (RPC) ..... 120
5.2.4 Experimental Protocols ..... 120
5.2.4.1 Part A – Experiments with Flexible Packaging ..... 120
5.2.4.2 Part B – Experiments with Rigid Pressurized Constraint (RPC) ..... 123
5.3 Results and Discussions ..... 125
5.3.1 Temperature and Pressure Evolution in Flexible Packaging (PP Tray) ..... 125
5.3.1.1 No Mechanical Constraint (NC) ..... 125
5.3.1.2 Free deformation with Fixed Preloaded Constraint (FPC) ..... 126
5.3.1.3 Fixed Mechanical Constraint (FMC) ..... 128
5.3.2 Comparative Analysis of Mechanical Constraints in Flexible Packaging (PP trays) 129
5.3.3 Temperature and Pressure Evolution of Rigid Pressurized Constraint (RPC) ..... 131
5.4 Conclusions ..... 134
Chapter 6 ..... 136
Conclusions and prospects ..... 136
6.1 General conclusion ..... 136
6.2 Contributions to knowledge ..... 137
6.3 Recommendations for future work ..... 138
References ..... 140
Publications and Communications ..... 151

## List of Figures

Fig. 2. 1: A scheduled process in sterilization. 8
Fig. 2. 2: Non-exhaustive lists of patented devices for historical overview on microwave sterilization. 16
Fig. 2. 3: A flowchart of a microwave sterilization system with individual components 17
Fig. 2. 4: Schematic of the Microwave assisted thermal sterilization (MATS) system. 20
Fig. 2. 5: Important characteristics for microwave packaging. 24
Fig. 2. 6: Schematic of a plastic pouch holder to prevent distortion of the pouch during steam emanation. 30
Fig. 2. 7: Schematic of glass container with cylindrical potato sample and temperature sensor for microwave sterilization. 30
Fig. 2. 8: Polymeric packaging in a pressurized vessel of water to provide overpressure. 31
Fig. 2. 9: A simplistic diagram of heat transfer phenomenon during a classical thermal sterilization process. 35
Fig. 2. 10: Schematic representation of the stress components acting on an infinitesimal element of a polymer film. 41
Fig. 2. 11: Schematic of a numerical simulation process. 42
Fig. 3. 1: Formulation of Mashed Potato 50
Fig. 3. 2: Schematic of experimental setup to measure thermal conductivity of mashed potato. 51
Fig. 3. 3: Experimental system to measure thermal conductivity of mashed potato. 52
Fig. 3. 4: STERITECH® retort system at Oniris VetAgroBio, Nantes, France. 53
Fig. 3. 5: Schematic of STERITECH® retort system. 53
Fig. 3. 6: Experimental setup for conventional sterilization in retort. 54
Fig. 3. 7: Temperature probes location in metal cans: (a) top (b) center (c) headspace (d) bottom 54
Fig. 3. 8: (a) Temperature probes (b) Pressure sensor in cans 55
Fig. 3. 9: Mashed potato in cans (a) Location of temperature probes in the cans (H: headspace; T: Top; C: Center; B: Bottom) (b) Reduction in headspace after sterilization 55
Fig. 3. 10: Specific heat of mashed potato in relation with temperature 57
Fig. 3. 11: Thermal conductivity of mashed potato in relation with temperature. 58
Fig. 3. 12: 2D geometry of metal can with model food with various locations of temperature measurement. 58
Fig. 3. 13: Metal can geometry and meshing in COMSOL® Multiphysics. 59
Fig. 3. 14: Experimental temperature distribution at different locations and experimental total absolute pressure evolution inside the metal can. 64
Fig. 3. 15: Comparison between experimental and simulated temperature distribution in the mashed potato domain at top location. 65
Fig. 3. 16: Comparison between experimental and simulated temperature distribution in the mashed potato domain at center location. 65
Fig. 3. 17: Comparison between experimental and simulated temperature distribution in the mashed potato domain at bottom location. 66
Fig. 3. 18: Comparison between experimental and simulated temperature distribution in the headspace domain at headspace location 66

Fig. 3. 19: Comparison between simulated temperature distribution in the headspace domain at headspace location with and without cfd. ..... 67
Fig. 3. 20: Simulated temperature distribution using different heat transfer coefficients ..... 69
Fig. 3. 21: Comparison between experimental and simulated total headspace pressure in the container ..... 72
Fig. 3. 22: Zoomed pressure profiles for early stages (t ≤ 1000 s) of heating during the sterilization cycle ..... 72
Fig. 3. 23: Ratio of simulated pressure for dry air to simulated pressure for water vapour during the early stages (t ≤ 1000 s) of heating in sterilization cycle. ..... 73
Fig. 3. 24: Mass of water vapour generated during sterilization process predicted by model. 73
Fig. 4. 1: PP ready-to-eat food tray dimensions. ..... 78
Fig. 4. 2: Schematic of Fixed Preloaded Constraint (FPC). ..... 78
Fig. 4. 3: Schematic representation of the various components in the air injection system with mechanical constraint. ..... 79
Fig. 4. 4: Experimental setup of the air injection system equipped with mechanical constraint. ..... 79
Fig. 4. 5: Schematic representation of the various components in the thermal treatment of PP trays equipped with mechanical constraint. ..... 80
Fig. 4. 6: Experimental setup of the thermal treatment of PP trays equipped with mechanical constraint. ..... 81
Fig. 4. 7: Experimental measurement of temperature evolution of oven air. ..... 82
Fig. 4. 8: Different model construction with same tray geometry for three different models. 85
Fig. 4. 9: Schematic representation of the deformation sequence of the PP film during air injection. ..... 91
Fig. 4. 10: Experimental and simulated displacement of PP film during air injection with no constraints (NC) at different air flowrates ..... 91
Fig. 4. 11: Experimental and simulated relative pressure (P) inside PP tray during air injection with no constraints (NC) at different air flowrates ..... 92
Fig. 4. 12: Experimental displacement images and 3D simulated displacement images of PP film along with relative pressure (P) values inside the PP tray with different air flow rates at respective time of rupture ..... 94
Fig. 4. 13: Experimental and simulated relative pressure (P) during heat treatment with A2 and A3 configuration ..... 96
Fig. 4. 14: Experimental and simulated headspace temperature during heat treatment with A2 and A3 configuration ..... 97
Fig. 4. 15: Cut Plane 2D at three different locations (a) center (b) side and (c) lateral to study the air flow inside PP tray during air injection and heat treatment. ..... 98
Fig. 4. 16: Simulated air flow and velocity at Q1 = 0.1 L/min inside the tray at the time of rupture (t = 94s) along (a) Cut Plane Center (b) Cut Plane Lateral. ..... 99
Fig. 4. 17: Simulated air flow and velocity at Q2 = 0.15 L/min inside the tray at the time of rupture (t = 83s) along a) Cut Plane Center (b) Cut Plane Lateral. ..... 100
Fig. 4. 18: Simulated air flow and velocity at Q3 = 0.6 L/min inside the tray at the time of rupture (t = 25s) along (a) Cut Plane Center (b) Cut Plane Lateral ..... 101
Fig. 4. 19: Simulated air flow and temperature distribution during heat treatment inside empty PP tray at the time of rupture (t = 540s) along (a) Cut Plane Center (b) Cut Plane Side (c) Cut Plane Lateral ..... 102

Fig. 4. 20: Simulated air flow and temperature distribution during heat treatment inside PP tray containing mashed potato with a headspace at the time of rupture (t = 769s) along (a) Cut Plane Center (b) Cut Plane Side (c) Cut Plane Lateral. ..... 104
Fig. 4. 21: Simulated reaction force ($FRFz$) acting on the PP film as predicted by the model during no constraint..... 105
Fig. 4. 22: Estimation of von-Mises stress on PP film in at the experimental time of rupture ..... 108
Fig. 4. 23: Estimation of von-Mises stress on PP film in different simulated configuration at the experimental time of rupture during heat treatment on empty PP tray (A2) (t = 540 s) ..... 108
Fig. 4. 24: Estimation of von-Mises stress on PP film at the experimental time of rupture during heat treatment on PP tray with mashed potato (A3) (t = 769 s). ..... 109
Fig. 4. 25: Estimation of von-Mises stress on PP film at the experimental time of rupture during heat treatment on empty PP tray (A2) (t = 540 s) without the use of CFD ..... 109
Fig. 4. 26: Experimental relative pressure (P) inside PP tray during air injection with fixed preloaded constraint (FPC) of F1 = 5N, F2 = 20 N, and F3 = 40 N at different air flowrates ..... 111
Fig. 4. 27: Experimental reaction force on PP film during air injection with fixed preloaded constraint (FPC) at different air flowrates..... 111
Fig. 5. 1: Images of (a) Polypropylene (PP) trays (b) custom-made Polyether ether ketone (PEEK) rigid container. ..... 116
Fig. 5. 2: Experimental setup of 915 MHz microwave system combined with custom-made pressure regulation system. ..... 118
Fig. 5. 3: Detailed schematic diagram of 915 MHz microwave system with the integration of pressure regulation system. ..... 118
Fig. 5. 4: Images of pressure and temperature sensors in PP trays. ..... 121
Fig. 5. 5: Schematic of the placement of pressure and temperature sensors (center and headspace) from top, front, and side views. ..... 121
Fig. 5. 6: Schematic of a vertical compression system exerting a force of 80 N on the upper surface of the PP film. ..... 122
Fig. 5. 7: Fixed Preloaded Constraint (FPC) placed inside the 915 MHz microwave cavity. 122
Fig. 5. 8: Schematic of Fixed Mechanical Constraint (FMC) made of Polyoxymethylene (POM) containg heat sealed PP trays with pressure and temperature sensors. ..... 123
Fig. 5. 9: Images of Fixed Mechanical Constraint (FMC) placed inside 915 MHz microwave cavity. ..... 123
Fig. 5. 10: (a) Rigid Pressurized Constraint (RPC) with a cylindrical PEEK container equipped with optical fibers and pressure measurements. (b) Locations of temperature and pressure measurements from top and lateral views. ..... 124
Fig. 5. 11: Different components in Rigid Pressurized Constraint (RPC) system. ..... 125
Fig. 5. 12: Temperature (T) evolution at the center and headspace location of mashed potato and also relative pressure (P) evolution during microwave heating (915 MHz) with no constraint (NC) on PP tray. ..... 126
Fig. 5. 13: Temperature (T) evolution at the center and headspace location of mashed potato and also relative pressure (P) evolution during microwave heating (915 MHz) with fixed preloaded constraint (FPC) on PP tray. Initial force on PP film was 80 N ..... 127
Fig. 5. 14: Evolution of experimental reaction force exerted on the upper PP film surface due to pressure build-up inside PP tray in different trials with fixed preloaded constraint (FPC). ..... 128

Fig. 5. 15: Temperature (T) evolution at the center and headspace location of mashed potato and also relative pressure (P) evolution during microwave heating (915 MHz) with fixed mechanical constraint (FMC) on PP tray. ..... 129
Fig. 5. 16: Failure at heat seal zone with and without mechanical constraint. ..... 131
Fig. 5. 17: Temperature (T) evolution at the center and side location of mashed potato and also relative pressure (P) evolution during microwave sterilization process (915 MHz) with pressurized PEEK rigid container (rigid pressurized constraint). ..... 133
Fig. 5. 18: Dielectric constant ($\epsilon'$) and dielectric loss factor ($\epsilon''$) in mashed potato as a function of temperature. ..... 134

# List of Tables

Table 2. 1: Differences between the popular conventional and non-conventional sterilization techniques used in the food industry. ..... 7
Table 2. 2: Summaries of some important developments in microwave sterilization ..... 14
Table 2. 3: Differences between magnetron based generators and solid-state generators ..... 23
Table 2. 4: Thermal properties after microwave sterilization of different packaging materials ..... 26
Table 2. 5: Mechanical properties after microwave sterilization of different packaging materials. ..... 27
Table 2. 6: Barrier properties after microwave sterilization of different packaging materials . ..... 27
Table 2. 7: Different types of software used for modelling of multiphysical phenomena in process engineering. ..... 43
Table 3. 1: Thermophysical properties of mashed potato used for numerical modelling. ..... 56
Table 3. 2: Mesh independence validation. ..... 57
Table 3. 3: Global heat transfer coefficient values used in the simulation study for heating, holding, and cooling phases during retort sterilization. ..... 68
Table 3. 4: Comparison of various heat transfer coefficients for prediction of temperatures at various location using $R^2$ value. ..... 68
Table 3. 5: Moisture content (wb) evolution at different location in mashed potato before and after sterilization. ..... 71
Table 4. 1: Summary of experimental protocols and designs. ..... 83
Table 4. 2: Important parameters for numerical model. ..... 85
Table 4. 3: Parametric sweep with different combinations of Young's Modulus and Poisson Ratio of PP film. ..... 95
Table 4. 4: Experimental and simulated values of pressure and displacement of PP film at the time of rupture for air injection studies with no constraints. ..... 95
Table 4. 5: Experimental and simulated values of pressure and headspace temperature at the time of rupture for heat treatment studies with no constraints. ..... 97
Table 4. 6: Experimental values of pressure, headspace temperature and force at the time of rupture for heat treatment studies with constraints. ..... 112
Table 5. 1: Summary of Experimental Design. ..... 120
Table 5. 2: Summary of deltaP, center temperature, headspace temperature, and time of rupture for NC, FPC, and FMC configuration at the time of rupture during microwave heating. ..... 130

# Nomenclature & Abbreviations

*Latin letters*

| | |
|---|---|
| $a_w$ | water activity |
| $\boldsymbol{C}$ | stiffness tensor |
| $C_p$ | specific heat capacity of medium (J/kg/K) |
| $C_v^{surf}$ | vapour concentration at product surface (kg/m$^3$) |
| $C_v^a$ | vapour concentration at headspace air (kg/m$^3$) |
| d | displacement (m) |
| $\boldsymbol{d_s}$ | displacement vector (m) |
| E | Young's modulus (Pa) |
| F | force (N) |
| $F_{RFz}$ | simulated reaction force (N) |
| **F** | total deformation gradient tensor which describes the deformation of material element relative to its original reference configuration. |
| $\boldsymbol{F_{el}}$ | elastic part of deformation gradient, isolating the elastic (reversible) part of the total deformation |
| $\boldsymbol{F_{inel}}$ | inelastic deformation gradient, describing the irreversible part of deformation due to plasticity, viscosity, or other permanent effects. |
| $\boldsymbol{F_v}$ | body force per unit volume (N/m$^3$) |
| **g** | gravitational acceleration vector (m/s$^2$) |
| $h_c$ | convective heat-transfer coefficient (W/m$^2$/K) |
| h | heat transfer coefficient (W/m$^2$/K) |
| $h_g$ | global convection heat-transfer coefficient of retort (W/m$^2$/K) |
| $h_{oven}$ | convection heat-transfer coefficient of oven (W/m$^2$/K) |
| **I** | identity tensor |
| $I$ | phase change term (kg/s/m$^2$) |
| $J_i$ | determinant of the inelastic deformation gradient |
| **K** | Viscous stresses in the Newtonian air (Pa) |
| k | thermal conductivity of medium (W/m/K) |
| $k_m$ | mass transfer coefficient (m/s) |
| m | mass (kg) |
| n | number of moles |

P Pressure (Pa)

$P_a$ partial pressure of air (Pa)

$P_v$ partial pressure of water vapour (Pa)

$P_{tt}$ total pressure (Pa)

$\boldsymbol{q}$ heat flux vector (W/m$^2$)

$Q_{ev}$ heat loss due to evaporation (W/m$^2$)

$Q$ heat source term (W/m$^3$)

$Q_i$ air flow rate (L/min)

$Q_L$ latent heat flux associated with evaporation at the surface (W/m$^2$)

R universal gas constant (8.3145 J/mol/K)

$S$ second Piola–Kirchhoff stress tensor (N/m$^3$)

$S_{el}$ elastic stress tensor, representing the reversible, recoverable stresses due to elastic deformation (N/m$^3$)

$S_{inel}$ inelastic stress tensor, representing irreversible stresses from inelastic effects like plastic deformation, viscous effects, or thermal stress (N/m$^3$)

$S_0$ initial stresses present in film prior to loading (N/m$^3$)

$S_{ext}$ external stress, accounts for external stresses such as those induced by internal pressure (N/m$^3$)

$S_{mp}$ surface area of mashed potato surface (m$^2$).

$S_q$ stress from inelastic effects like viscous flow or temperature changes (N/m$^3$)

$S_{tt}$ total stress tensor (N/m$^3$)

T temperature (°C)

$T_m$ melting temperature (°C)

$T_r$ temperature of retort (°C)

**T** tensor expressing the relationship between normal and shear stresses acting on mutually perpendicular planes.

$T_{ext}$ temperature of the fluid away from the surface (°C)

$T_{ref}$ reference temperature (121 °C)

$T_s$ temperature at the surface of product (°C)

**u** velocity field (m/s)

t time (s)

V volume (m$^3$)

*Greek letters*

| | |
|---|---|
| $\in$ | total strain described by the Green–Lagrange strain tensor |
| $\boldsymbol{\epsilon_{el}}$ | elastic strain tensor |
| $\epsilon'$ | relative dielectric constant |
| $\epsilon''$ | relative dielectric loss factor |
| $\sigma$ | normal stress acting perpendicular to a surface (Pa) |
| $\sigma_v$ | von Mises equivalent stress (Pa) |
| $\sigma_{zj}$ | stress tensor (Pa) |
| $\tau$ | orthogonal shear stress acting tangentially to a surface (Pa) |
| $\eta_{global}$ | global energy efficiency of a microwave heating system |
| $\eta_{gen}$ | electricity-to-microwave conversion efficiency |
| $\eta_{abs}$ | microwave-to-heat conversion efficiency, which quantifies the fraction of incident microwave energy absorbed by the product and converted into thermal energy |
| $\rho$ | density (kg/m$^3$) |
| $\rho_0$ | initial density of air at ambient temperature (kg/m$^3$) |
| μ | dynamic viscosity of fluid (Pa.s) |
| $v$ | Poisson's ratio |
| $\lambda$ | latent heat of vaporization (J/kg) |

*Subscripts & Superscripts*

| | |
|---|---|
| a | air |
| avg | average |
| b | bottom location |
| c | center location |
| el | elastic |
| ev | evaporation |
| exp | experimental value |
| h | headspace location |
| inel | inelastic |
| mp | mashed potato |
| mpsurf | mashed potato surface |
| mod | model value |

| | |
|---|---|
| s | surface |
| si | side location |
| t | top location |
| tt | total |
| v | water vapour |

*Abbreviations*

| | |
|---|---|
| CFD | Computational Fluid Dynamics |
| CUT | Come up time |
| CDT | Come down time |
| DSC | Differential Scanning Calorimeter |
| FPC | Fixed Preloaded Constraint |
| FMC | Fixed Mechanical Constraint |
| FSI | Fluid–Structure Interaction |
| HPP | High Pressure Processing |
| HTST | High Temperature Short Time |
| MATS | Microwave-assisted thermal sterilization system |
| NC | No Constraint |
| PEEK | Polyether ether ketone |
| PEF | Pulsed Electric Fields |
| POM | Polyoxymethylene |
| PP | Polypropylene |
| PLA | Polylactic acid |
| OTR | Oxygen transmission rate |
| RH | Relative Humidity |
| RPC | Rigid Pressurized Constraint |
| RTE | Ready-To-Eat |
| SD | Standard Deviation |
| UV | Ultraviolet |
| WVTR | Water Vapour Transmission Rate |

# Resume etendu en francais

Ce travail de thèse porte sur l'étude d'un procédé de traitement thermique par micro-ondes comme alternative au procédé de stérilisation en autoclave. L'étude s'intéresse au comportement thermo-mécanique des emballages alimentaires sous diverses contraintes extérieures. Dans la littérature scientifique, le procédé de stérilisation classique en autoclave demeure efficace pour garantir la sécurité microbiologique des denrées alimentaires, cependant ce procédé implique l'usage d'un fluide caloporteur (vapeur d'eau principalement) utilisé pour assurer le traitement thermique d'un produit alimentaire ainsi que le maintien de la contre-pression externe. Le chauffage par micro-ondes, caractérisé par un chauffage volumique, permet de dégrader directement l'énergie électromagnétique de l'onde au sein du produit et dispose d'une faible inertie thermique comparé au chauffage conventionnel. Toutefois, la mise en œuvre de cette technologie doit intégrer en amont une compréhension détaillée des transferts de chaleur au sein des produits traités ainsi qu'une maîtrise de l'augmentation de la pression interne dans le contenant compte tenu de ses caractéristiques mécaniques. L'objectif principal de cette thèse est de caractériser ces différentes interactions, à partir d'approches expérimentales et numériques.

La première partie de la thèse s'intéresse au procédé de stérilisation conventionnelle appliqué à des cylindres métalliques rigides remplis d'un aliment modèle dont la teneur en eau est fixée, la purée de pommes de terre. Un autoclave pilote, équipé d'un système d'injection de vapeur et d'un dispositif de régulation de pression, a été instrumenté pour enregistrer les températures et pressions à plusieurs endroits au sein des contenants métalliques, notamment dans l'espace de tête et à différentes profondeurs au sein du produit alimentaire. Une modélisation numérique a été réalisée à l'aide du logiciel COMSOL Multiphysics® afin de prédire les champs de température au sein du produit et modéliser les phénomènes de convection naturelle dans l'espace de tête au cours d'un cycle complet de chauffage, maintien à température cible et refroidissement. L'analyse combinée a mis en évidence deux contributions à la pressurisation interne de l'emballage: l'expansion de l'air sec et la génération de vapeur d'eau au cours du procédé. La pression partielle d'air sec est prépondérante au début du chauffage, lorsque la température de la zone de tête augmente rapidement, tandis que la pression de vapeur contribue de manière significative à l'augmentation de la pression totale pendant la majeure partie du cycle de stérilisation. Un autre résultat important concerne la sensibilité aux conditions aux limites au niveau des parois du récipient. L'étude de sensibilité du modèle au coefficient de transfert par convection met en évidence des variations notables des vitesses de chauffage et des gradients de température au sein du produit corrélés à la variation de la pression interne dans l'emballage.

La deuxième partie du travail a consisté à évaluer les performances d'un emballage souple en polypropylène (PP) thermocollé en surface supérieure avec un film mince du même matériau. La géométrie du contenant correspond parfaitement au format utilisé pour les emballages des plats préparés cuisinés en barquette. L'étude a débuté par des expériences d'injection d'air au sein de la barquette sans produit alimentaire, afin d'analyser les effets de la pressurisation sur le déplacement géométrique du film supérieur. Une source d'air comprimé et un petit orifice d'entrée ont permis d'injecter l'air à différents débits au sein de la barquette, tandis que la forme de la barquette et la courbure du film évoluaient librement. Une caméra à haute résolution a capturé des images à fréquence fixe. L'analyse d'images, basée sur la détection de contours et

le suivi de pixels, a permis de convertir les séquences en champs de déplacement du film supérieur au cours du temps, en se concentrant sur la hauteur de la déformation centrale et sur la zone de scellage. La rupture est survenue à des pressions d'environ 45 mbar, généralement initiée près des bords ou des coins de la barquette. Des simulations numériques ont complété ces observations. Une modélisation de type CFD couplée à la mécanique des structures a été réalisée, considérant un écoulement laminaire compressible d'air dans le volume de la barquette et un film supérieur déformable. Les charges de pression exercées par le fluide sur le film supérieur ont été simulées. Les résultats numériques montrent la formation d'un dôme en surface supérieure de la barquette et ont permis de quantifier la force appliquée en dynamique sur la surface du film liée à l'expansion de l'air dans la barquette. Les simulations numériques ont montré que la réponse mécanique du film en polypropylène variait selon la configuration expérimentale. Lors de l'injection d'air, la force appliquée à la surface du film supérieur variait entre 187 N et 284 N, correspondant à des contraintes maximales de Von Mises comprises entre $2{,}1 \times 10^5$ et $3{,}4 \times 10^5$ N/m² concentrées au centre du film, tandis que des contraintes plus faibles de $1{,}6 \times 10^5$ à $2{,}6 \times 10^5$ N/m² apparaissaient aux coins. Lors du traitement thermique des barquettes vides, la contrainte maximale a diminué à environ $8{,}8 \times 10^4$ N/m² et s'est située principalement le long des grands côtés, où la plupart des ruptures de film ont été observées expérimentalement. Pour les barquettes contenant de la purée de pomme de terre, les contraintes les plus élevées, d'environ $2{,}0 \times 10^5$ N/m², se sont concentrées près des coins, en accord avec les observations expérimentales. Bien que ces contraintes soient demeurées inférieures à la limite d'élasticité du polypropylène ($25–40 \times 10^6$ N/m²), la rupture observée a été possiblement due à un ramollissement local de la zone de scellage lors du chauffage et à des effets possibles de concentration de contraintes près des coins. Il est important de préciser que le modèle développé dans cette étude ne vise pas à représenter explicitement le contact mécanique entre le film et la barquette ni les mécanismes locaux de rupture du joint de scellage. Cet ensemble d'expériences et de simulations a constitué une première étape pour mieux comprendre les pressions interne maximales admissibles jusqu'à la rupture expérimentale du film. Le modèle se concentre sur la prédiction du comportement global du système, en particulier la déformation du film, ainsi que l'évolution de la pression et de la température à l'intérieur de la barquette.

Le chauffage de la barquette a ensuite été introduit en conservant la même géométrie et le même protocole de scellage du film afin d'étudier l'influence de la température sur le comportement mécanique des barquettes. Le chauffage dans un four dont la température était programmée depuis l'ambiance pour atteindre 121 °C a conduit à une rupture plus précoce de la zone de scellage comparé aux expériences menées avec injection d'air. La rupture est survenue à des pressions internes inférieures de 10 mbar et à des températures inférieures à 60 °C au sein de la barquette. L'exposition de la barquette à la chaleur accélère le processus de rupture du film. Les expériences ont été complétées par des simulations numériques visant à analyser l'évolution couplée de la pression et du déplacement du film lors du chauffage de la barquette.

Afin d'étudier l'effet d'une contrainte mécanique externe sur la déformation et le comportement à la rupture des barquettes, un dispositif expérimental a été développé. Il se composait d'une plaque rigide en polyétheréthercétone (PEEK) placée en contact avec le film supérieur et reliée à un capteur de force permettant d'appliquer une précharge verticale et de mesurer la force résultante générée par la pressurisation interne. La présence de cette contrainte mécanique a augmenté la résistance de la barquette lors des essais d'injection d'air. Par rapport à la configuration sans contrainte, où la rupture survenait après environ 90 secondes pour une pression interne de 42 à 46 mbar, les barquettes sous contention ont présenté une rupture

légèrement retardée, survenant après environ 60 à 80 secondes mais à des pressions internes nettement plus élevées, de l'ordre de 100 à 129 mbar (forces appliquées sur le film comprises entre 110 et 130 N).

Lors des traitements thermiques des barquettes, la rupture s'est produite plus tard (540 secondes pour les barquettes vides et 770 secondes pour celles contenant de la purée de pomme de terre) et à des pressions internes plus faibles (8 à 9 mbar). Lorsque la contrainte mécanique était appliquée pendant le chauffage (5 N, 20 N, 40 N), les pressions de rupture augmentaient légèrement tandis que les temps de rupture restaient comparables.

Dans la suite de l'étude, un procédé de chauffage par micro-ondes du produit alimentaire dans la barquette a été mis en place. L'objectif était d'évaluer expérimentalement l'évolution de la température et de la pression dans l'emballage sous chauffage micro-ondes et d'évaluer expérimentalement le phénomène de rupture de la zone de scellage suivant différents modes opératoires.

Les expériences de chauffage par micro-ondes ont été réalisées à la fréquence de 915 MHz avec une cavité monomode instrumentée et reliée à un générateur micro-ondes de type « état solide » . Les barquettes contenant de la purée de pommes de terre ont été étudiées selon trois configurations : (i) sans contrainte mécanique, permettant la déformation libre du film ; (ii) avec une précharge appliquée via une plaque de PEEK en surface supérieure et reliée à un capteur de force; et (iii) avec une déformation nulle où la barquette était maintenue entre deux plaques rigides limitant totalement son mouvement vertical. Les températures ont été mesurées par des capteurs embarqués au centre de l'aliment et dans l'espace de tête de la barquette. La pression dans l'espace de tête a aussi été enregistrée au cours du temps. Pour une puissance micro-ondes incidente de 200 W, les expériences ont montré que la pression interne dans l'espace de tête augmentait progressivement pendant le chauffage par micro-ondes, atteignant environ 50 mbar juste avant la rupture. Dans la configuration sans contrainte, la rupture s'est produite après environ 280 secondes, lorsque la température dans l'espace de tête atteignait environ 50 °C et que la température au centre de l'aliment restait inférieure à 60 °C. En présence d'une contrainte mécanique de 80 N appliquée par la plaque de PEEK, la rupture est survenue à un temps similaire, entre 200 et 300 secondes, pour une température dans l'espace de tête d'environ 35 °C et une température centrale également inférieure à 60 °C. L'application de cette contrainte a augmenté la rigidité globale de la barquette et limité la déformation du film, mais la rupture s'est toujours produite au niveau de la zone de scellage. La force mesurée au moment de la rupture, excluant la précharge initiale de 80 N appliquée par la plaque de PEEK, était d'environ 30 à 40 N. Bien que la contrainte appliquée en surface supérieure ait réduit la déformation du film, le mécanisme de rupture est resté similaire à celui observé sans contrainte, avec une initiation localisée au niveau des bords de la zone de soudure. Le comportement global sous chauffage par micro-ondes est resté comparable à celui observé lors du chauffage conventionnel, bien que la rupture se soit produite plus rapidement, soit environ 250 secondes sous chauffage par micro-ondes, contre 500 à 700 secondes lors du chauffage en étuve, que la barquette contienne ou non de la purée de pommes de terre. Cette différence s'explique par la cinétique de chauffage volumique propre au procédé micro-ondes, en contraste avec le transfert de chaleur plus lent de la surface vers le cœur du produit lors du chauffage conventionnel.

Un contenant rigide a ensuite été testé afin d'évaluer l'aptitude du produit a atteindre des températures de stérilisation tout en préservant l'intégrité de l'emballage. À cette fin, un

récipient cylindrique en PEEK a été conçu et instrumenté avec des passages étanches pour les mesures de pression et de température à l'aide de fibres optiques. Le PEEK a été choisi pour sa rigidité élevée, son excellente résistance thermique, lui permettant de supporter les pressions internes et les contraintes mécaniques pendant le chauffage. De plus le PEEK peut être assimilé à un matériau transparent sous micro-ondes compte tenu de son faible facteur de dissipation (tan δ). Pour une puissance micro-ondes incidente de 400 W, le produit contenu au sein du cylindre en PEEK a atteint des températures supérieures à 118 °C (mesurées au centre du produit). La pression interne maximale au sein de l'espace de tête s'élevait à environ 0,8 bar lorsque la température se situait entre 115 °C et 121 °C, aussi bien au centre qu'au niveau des côtés du produit. Cette configuration a montré qu'un récipient en matériau polymère rigide peut être un bon candidat pour atteindre des conditions de stérilisation sous chauffage par micro-ondes.

Les systèmes de contention mécanique utilisés dans cette étude nécessitent encore des améliorations. La configuration avec plaque préchargée a permis de quantifier comment l'application d'une précharge modifie la déformation du film supérieur et la force liée à l'expansion du film sous l'effet de la pression interne dans l'emballage. Le système avec maintien de la position du film, utilisé principalement dans l'étude sous micro-ondes, n'a pas empêché les déformations latérales de la barquette, ce qui suggère qu'une contention multidirectionnelle de la barquette serait nécessaire.

Plusieurs conclusions peuvent être tirées de ce travail. La contribution de l'air sec à la pression interne totale, liée à l'expansion gazeuse et aux conditions aux limites thermiques appliquées aux parois, joue un rôle essentiel aussi bien dans le procédé en autoclave que sous chauffage par micro-ondes. Cependant, son influence sur la structure de l'emballage diffère selon le procédé : dans l'autoclave, cette augmentation de pression est compensée par la contre-pression externe exercée par l'eau ou la vapeur, tandis que sous chauffage par micro-ondes, la dilatation de l'air exerce principalement une charge mécanique sur le film supérieur. La résistance mécanique de la zone de scellage demeure le facteur déterminant contrôlant le seuil de rupture, car elle dépend directement des sollicitations thermiques et mécaniques appliquées pendant le procédé. La cinétique de rupture du film observée sous chauffage micro-ondes reste similaire à celle obtenue lors du chauffage conventionnel, la génération de pression interne constituant dans les deux cas le facteur dominant conduisant à la défaillance de la zone de scellage.

La méthodologie expérimentale et numérique développée dans ce travail constitue un cadre pour l'analyse des performances des emballages soumis à des sollicitations thermiques et mécaniques couplées. L'intégration de la dynamique des fluides numérique (CFD) couplée à la mécanique des structures permet l'analyse simultanée des champs de température, de pression et de déformation au sein des matériaux considérés. Les résultats apportent des informations quantitatives et qualitatives sur l'évolution des températures, des pressions et le développement des champs de contraintes en surface dans le film.

Dans l'ensemble, cette thèse fournit une base scientifique pour le développement de dispositifs plus performants permettant d'atteindre des températures cibles pour la stérilisation thermique sous micro-ondes. Les résultats montrent que l'intégrité structurelle des emballages alimentaires est liée à la distribution de la pressions interne dans le produit et doit prendre en considération la transmission multidirectionnelle des contraintes à l'intérieur de la structure.

# Chapter 1
# Introduction

## 1.1 Food sterilization

Conventional retort sterilisation is widely used in the food industry due to its long-standing reliability in achieving commercial sterility. However, it is also recognised for its high consumption of both energy and water. Large volumes of water are required to generate pressurised steam for the heating and cooling operations. This reliance on water contributes significantly to operating costs and environmental impact, particularly in regions where water scarcity is a critical concern. Hence, unconventional technologies such as microwave sterilisation has emerged as a promising alternative, offering internal volumetric heating, shorter process times, and potentially lower energy inputs (Atuonwu & Tassou, 2018; Tang, 2015).

One of the most notable advances in this field has been the development of Microwave-Assisted Thermal Sterilisation (MATS). MATS combines microwave heating with hot water immersion under pressure, providing faster and more uniform heating than conventional retorts. It has been validated by the U.S. FDA for commercial sterilisation of low-acid foods, which demonstrated both microbiological safety and retention of sensory and nutritional quality (Barbosa-Cánovas et al., 2014; Resurreccion et al., 2013). Industrial trials have shown that MATS can produce high-quality ready-to-eat (RTE) meals with improved texture and colour compared to retort-processed products, while reducing process times by up to 50% (Dhawan et al., 2014). Despite these benefits, MATS still depends on hydrostatic pressure from circulating water or steam to prevent packaging rupture. This reliance on water offsets some of its sustainability advantages and continues to impose high energy demands, a challenge that is particularly critical in Europe where industrial water consumption is under increasing scrutiny (Water Europe, 2023).

Again, uniform heating remains a fundamental requirement for microbial safety in all sterilisation methods (FDA, 2023). To overcome the intrinsic non-uniformity of microwave fields, microwave systems such as MATS often rely on preheating or hot water baths to reduce cold spots. However, these measures further increase water and energy use. Achieving both thermal uniformity and structural integrity of packaging in a fully water-free microwave sterilisation process remains one of the major technological barriers for industrial adoption.

## 1.2 Food packaging and counterpressure during sterilisation

Food packaging not only protects products during storage and distribution but also serves as the containment system during sterilisation, where it must withstand elevated temperatures and internal pressures without failure. Traditional rigid formats such as metal cans and glass jars offer high resistance to internal pressure but are heavy and less suited to modern single-use applications. In contrast, polymer-based trays, particularly polypropylene (PP) with heat-sealed lidding films, have become increasingly popular for ready-to-eat (RTE) meals due to their low cost, transparency, sealability, and consumer convenience (Yoon et al., 2015). During sterilisation of high-moisture foods, evaporation from the food generates vapour that accumulates in the headspace, increasing internal pressure. In conventional retort systems, this is controlled by applying external counterpressure from pressurised steam or hot water, which

balances the internal load and prevents seal rupture (P. N. Patel et al., 1991). Similarly, microwave-assisted thermal sterilisation (MATS) employs circulating pressurised water as a counterpressure medium while delivering volumetric heating by microwaves (Tang, 2015). Although effective, these methods rely on large volumes of water, increasing energy and resource demands.

### 1.3 Knowledge gap and motivation

Although advances in sterilisation technologies have improved heating efficiency and microbial safety, important knowledge gaps remain regarding the mechanical stability of flexible packaging under pressurisation. Most studies have focused on thermal distribution and microbial lethality, while comparatively little to no attention has been given to the fluid flow inside packages and its role in rupture behaviour. During heating, air and vapour circulation develops within the headspace, exerting loads on the lidding film. These flow structures may reinforce stress fields at the seal edges and corners, where ruptures consistently initiate. Yet, the dynamics of such fluid–structure interactions have not been systematically studied in the context of food packaging.

Similarly, the stress dynamics of polymer food trays under internal vapour pressure remain poorly understood. Conventional seal strength tests describe average tensile properties, but they do not capture how transient pressurisation, moisture-induced softening, or biaxial stress at seals drive real rupture events during sterilisation. Unlike rigid cans, flexible trays deform readily, leading to stress amplification and premature failure at relatively low internal pressures. Understanding these coupled effects requires more than material characterization. It demands an integrated view of heat transfer, vapour generation, airflow circulation, and structural response.

Such multiphysics interactions have been well established in other disciplines. In nuclear engineering, vessel pressurisation and thermal stresses are carefully modelled. In aerospace and fluid mechanics, vortex–jet interactions are analysed to predict structural loads. In biomedical engineering, fluid–structure interaction (FSI) is widely used to understand stresses in arteries and soft tissues. However, these approaches have never been systematically applied to food packaging, despite its similar challenges of thin-walled structures subjected to internal pressure and thermal loads.

Hence, prior to the development or optimisation of mechanical constraints for microwave sterilisation, it is essential to gain a clear understanding of the internal dynamics occurring within the packaging, such as airflow circulation, and stress localisation, which collectively govern rupture behaviour. This knowledge gap constitutes the central motivation for a multidisciplinary investigation inspired by principles from nuclear, aerospace, biomedical, and structural engineering, applied here within the domain of process engineering and food packaging.

### 1.4 Central hypothesis and objectives

The central hypothesis of this thesis is that sterilisation of high-moisture foods in non-rigid polymeric packaging, particularly polypropylene (PP) trays, significantly influences the mechanical and structural performance of the packaging. The extent of this influence depends on the food matrix, packaging material properties, and the specific processing parameters,

including temperature, and internal vapour pressure. It is further hypothesised that this effect can be mitigated, and packaging performance can be enhanced through the application of optimised mechanical constraints that redistribute stresses, and counteract deformation, without the need for hydrostatic counterpressure.

The aim of this research is to develop a scientific understanding of the coupled thermo–mechanical behaviour of non-rigid food packaging during conventional and microwave sterilisation processes, and to evaluate the potential of mechanical constraint systems as water-free alternatives to conventional counterpressure methods.

The specific objectives of the thesis are as follows:

1. The first study aims to understand the respective contributions of dry air and water vapour to the internal pressure build-up in a rigid metal container during conventional thermal sterilisation. The objective is to experimentally characterise coupled temperature–pressure evolution in sealed, food-filled containers and to develop a numerical Computational Fluid Dynamics (CFD) model that predicts the separate contributions of dry-air expansion and vapour generation to the total headspace pressurisation.
2. The second study is to investigate the rupture behaviour of flexible polypropylene (PP) trays subjected to internal pressurisation during both non-thermal (air injection) and thermal treatment. The objective is to analyse the interactions of internal pressure, airflow structures, and temperature rise to generate localised stresses, and to evaluate the influence of preloaded mechanical constraints in modification of rupture pressures, deformation patterns, and stress distributions using combined experimental tests and CFD, structural mechanics, and Fluid-Structure Interactions (FSI) simulations.
3. The third study is to evaluate the influence of mechanical constraint configurations during microwave sterilisation at 915 MHz. The objective is to assess whether flexible PP trays under fixed preloaded constraints and fixed mechanical constraints can retain internal pressure and to determine whether rigid, fully confined polymer containers can safely achieve sterilisation temperatures.

## 1.5 Thesis outline

This thesis is organised into six chapters, each addressing a specific aspect of the research. The structure progresses from a broad contextual background and critical review of the literature to detailed experimental and numerical investigations, before concluding with synthesis of findings, contributions to knowledge, and directions for future work.

**Chapter 1** introduces the research problem, outlining the industrial and environmental limitations of conventional retort sterilisation and the opportunities offered by microwave-based processing as a more sustainable alternative. It highlights the critical challenge of packaging integrity under internal pressurisation, sets out the knowledge gaps, and defines the central hypothesis and objectives of the work.

**Chapter 2** presents a critical review of the literature on food sterilisation technologies with a particular focus on microwave heating, structural mechanics of packaging and the performance of polymer-based packaging systems under high-temperature processes. Special emphasis is placed on mechanical, thermal, and barrier properties of flexible packaging, and on the current state of numerical modelling approaches for predicting pressure–temperature dynamics and

packaging deformation. Multiphysics methods are reviewed and gaps are identified in their application to food packaging. Part of this review has been published in the journal *Food Engineering Reviews* (Dutta et al., 2024b).

**Chapter 3** reports the first objective of this thesis, which investigates the role of dry air and water vapour in pressure evolution inside rigid food packaging during conventional sterilisation. Using a high-moisture model food (mashed potato), experimental measurements of temperature and pressure were obtained at multiple locations inside sealed containers. A numerical CFD model was then developed to predict local temperatures inside the container and also the separate contribution of dry air pressure and water vapour pressure to total headspace pressurisation. This study provided fundamental insight into pressure build-up mechanisms in rigid containers where packaging deformation is absent.

**Chapter 4** presents the second objective of this thesis, which examines the structural mechanics and rupture behaviour of flexible polypropylene trays under both non-thermal (air injection) and thermal treatments. Trays were tested with and without preloaded mechanical constraints, in both empty and food-filled conditions. Experimental data on displacement, rupture pressure, and reaction forces were combined with CFD–FSI simulations to analyse airflow patterns, and stress localisation.

**Chapter 5** describes the third objective of this thesis, which evaluates the influence of mechanical constraint configurations on pressure evolution, temperature distribution, and rupture behaviour during treatment with a 915 MHz solid-state microwave. Flexible PP trays were tested under three conditions: no constraint, fixed preloaded constraint, and fixed mechanical constraint. In addition, a rigid PEEK container providing full multidirectional confinement was investigated for its ability to achieve sterilisation temperatures during microwave heating.

**Chapter 6** synthesises the overall findings from the thesis and draws general conclusions on the thermo–mechanical performance of non-rigid packaging systems. It highlights the original contributions of the thesis such as the integrated CFD–FSI–thermal and structural analysis of flexible packaging, the identification of stress localisation at seal zones, and the experimental demonstration of rigid polymer container for water-free microwave sterilisation. The chapter also outlines the implications for sustainable process design, identifies remaining knowledge gaps, and provides recommendations for future research.

# Chapter 2
# Literature Review On Microwave Sterilization And Its Evolution On Food Packaging, Numerical Modelling and Engineering Developments.

## 2.1 Introduction

Sterilization is defined as the process to eliminate all microorganisms and their spores from a food product to ensure its safety and extend its shelf-life for long-term preservation. This process typically involves heating food to temperatures exceeding the boiling point of water. In food processing, sterilization is particularly essential for low-acid foods, which are conventionally treated in retort systems, either batch or continuous, under pressures ranging from 0.7 to 1 bar (relative pressure). The primary target of this process is *Clostridium botulinum*, a spore-forming bacterium known for its potential to cause botulism. To achieve a 90% reduction in bacterial population, the thermal death time of *Clostridium botulinum* at 121.1°C is approximately 2.78 minutes (Decareau, 1968).

Sterilization plays a fundamental role in food processing industry. This process ensures food preservation, food microbiological safety, and shelf life of food products (Decareau, 1968). Conventional sterilization techniques, called retort processing, are widely utilized and are well-established in the food industry. However, these conventional methods present several challenges, such as significant energy and water consumption, longer processing times, and degradation of food quality, and nutritional quality (Fu et al., 2023; Water Europe, 2023). As an alternative, microwave sterilization emerges as a promising technology to achieve faster processing. Despite its advantages, this method introduces issues such as non-uniform heating, which results in hot and cold spots (Jain, 2017). This compromises the effectiveness of sterilization. Additionally, there are also challenges related to packaging integrity, especially for non-rigid materials, and counter-pressure techniques in sealed containers that must be addressed for successful implementation. Numerical modelling and simulation serves as a valuable tool for analyzing these complexities by simulating heat and mass transfer along with the structural behaviour of food packaging materials (W. Lau, 2015). This chapter provides a comprehensive review of conventional and microwave sterilization, food packaging, and numerical modeling approaches.

## 2.2 Sterilization approaches in food processing

Sterilization of foods in the food industry involves various methods with the primary aim to eliminate harmful microorganisms and improve the shelf life of the food products. These methods are broadly categorized into conventional and non-conventional approaches. Conventional sterilization approaches rely on the application of heat for destroying the microorganisms, which includes bacteria and heat resistant spores. To achieve these microbial inactivation, closed systems such as retorts are often used. Retorts are specialized vessels, that have evolved to incorporate various heating approaches and techniques, which helps to

maintain precise control over pressure, temperature, and time. On the contrary, non-conventional sterilization methods includes the use of new techniques such as high pressure processing (HPP), ultraviolet (UV) irradiation, and microwave heating to address the gap of thermal conventional sterilization. Table 2.1 briefly summarizes the main differences between the popular conventional and non-conventional sterilization techniques used in the food industry in terms of primary mechanism, processing medium, and industrial applications. The potential for the usage of non-conventional sterilization methods have been influenced by the increasing demand for less energy and water consumption by the food industry. This section explores the major conventional and non-conventional sterilization methods used in the food industry.

*Table 2. 1: Differences between the popular conventional and non-conventional sterilization techniques used in the food industry.*

| **Criteria** | **Saturated steam** | **Water immersion** | **Water cascade** | **Steam-air** | **HPP** | **PEF** | **UV-Irradiation** | **Microwave** | **Ohmic heating** |
|---|---|---|---|---|---|---|---|---|---|
| Primary Mechanism | Thermal | Thermal | Thermal | Thermal | Non-thermal | Non-thermal | Non-thermal | Electromagnetic | Electrical |
| Processing medium | Steam | Water | Water Spray | Steam & Air | Pressure | Electric Pulses | UV Light | Microwave Energy | Electric Current |
| Industrial applications | Cans, Glass Jars | Pouches, Trays | High-Volume Processing | Pouches, Ready Meals | Juices, Dairy, Meats | Juices, Milk, Soups | Clear Liquids, Packaging | Ready-to-eat Meals, Soups | Soups, Purees, Dairy |

### 2.2.1 Conventional sterilization process

The conventional sterilization process or the thermal treatment process is the most popular method for food sterilization in the food industry. This method is widely used because of its ability to ensure uniform heat distribution across the food product. The heating mechanisms are mainly based on forced convection and conduction heating in a container for this type of treatments. In general, the conventional sterilization procedure involves a three-stage cycle (Fig. 2.1). The first stage, heating stage or CUT (come up time), is the time required for a high-flow heating medium to reach the retort temperature of 121°C and the pressure required is usually 1.5 bar above atmospheric pressure. In the second stage, holding or cooking stage, the retort maintains temperature (121°C) for a certain period of time to guarantee lethality. This varies depending on the target microorganism or anticipated microbial contamination. The pressure at this stage is maintained for example at 1.8 bar above atmospheric pressure. In the third phase, CDT (come-down time), cooling water is added for a continued temperature decline until the temperature reaches 25 °C and the pressure is decreased to 1 bar. Excessive heat processing of food can be avoided by cooling it, which also prevents the development of thermophilic microorganisms. However, the cooling process can cause retort pouches to burst. This can be avoided by applying overpressure air during the cooling procedure, which helps to maintain package integrity and avoid container deformation.

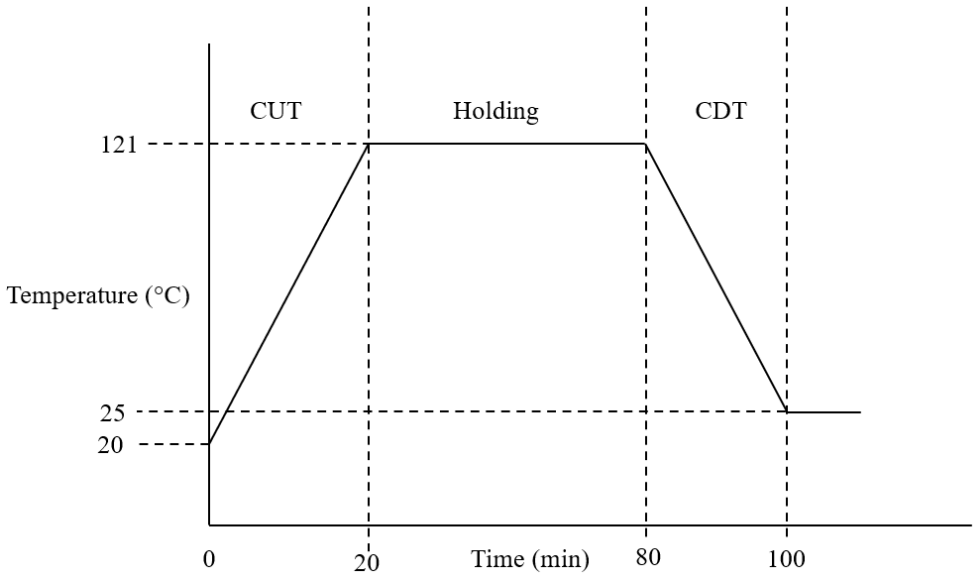



*Fig. 2. 1: A scheduled process in sterilization.*

Various heating approaches and process designs have been developed over the years to meet the specific requirements of different types of foods and packaging materials during the conventional sterilization process. Different developments have also been made in order to optimize the sterilization process in terms of energy consumptions. Following are the main approaches for conventional sterilization in brief.

#### 2.2.1.1 Saturated steam sterilization

Saturated steam sterilization is one of the most common methods during conventional food sterilization. This method works by injecting steam into a closed chamber where the food is sealed inside its packaging. The steam in contact with the packaging allows heat to transfer through conduction and convection. One important stage in this process is venting, where air is removed from the chamber. During venting, air is not evacuated abruptly but gradually displaced and replaced by pressurised steam. This controlled replacement prevents a sudden drop in internal pressure and ensures that the counter-pressure inside the retort remains balanced to avoid deformation of the packaging. Removing air is necessary to stop cold spots from forming, which can prevent proper sterilization. This method is very effective for foods stored in rigid containers like cans and glass jars. These containers can handle high temperatures and pressure without deformation or rupture. However, non-rigid packaging like flexible or semi-rigid containers can be damaged by the high pressure used in this method. Overpressure is required to protect non-rigid packaging from rupturing, but it can still cause problems with packaging integrity (Jimenez et al., 2024).

#### 2.2.1.2 Water based heating methods

Water based heating methods are widely used in the food sterilization processes, especially for food products with flexible or semi-rigid packaging. In this case, water is used as a heating medium instead of steam to achieve uniform heat distribution while maintaining the structural integrity of the food packaging (Jimenez et al., 2024).

##### *2.2.1.2.1 Water immersion systems*

In water immersion sterilization, food packaging is placed in a retort filled with hot water. The packaging can be either fully or partially submerged depending on the process. This method is used to ensure uniform heat distribution for effective sterilization. Flexible and semi-rigid packaging can deform when exposed to high temperatures during this sterilization method. To prevent this, overpressure air or steam is applied during the process. The added pressure helps maintain the shape and integrity of the food packaging. (Jimenez et al., 2024).

##### *2.2.1.2.2 Water cascade and spray systems*

In water cascade and spray sterilization, hot water is applied to food packaging inside a sealed chamber. The water is sprayed over the packaging to ensure uniform heat exposure. Pressurized water helps distribute heat uniformly across all packaging surfaces. This process improves sterilization by reducing temperature variations within the chamber. It is commonly used for processing large batches of food products efficiently (Jimenez et al., 2024).

#### 2.2.1.3 Steam-air sterilization

Steam-air sterilization is a method that combines steam with a controlled amount of air to improve heat transfer. This process is especially useful for food sterilization in flexible and semi-rigid packaging like pouches and trays. The addition of compressed air helps regulate

pressure inside the chamber during sterilization. Steam is injected into the chamber and fans are used to circulate the air and ensure uniform heat distribution across all food packagings. (Jimenez et al., 2024).

### 2.2.2 Non-conventional sterilization processes

Non-conventional sterilization processes uses alternative physical, chemical, or combined physico-chemical mechanisms to achieve microbial inactivations. In comparison to conventional sterilization processes, they are better in preserving the nutritional and sensory quality of food products. The primary difference between the conventional and non-conventional sterilization processes is that conventional sterilization processes rely on external heat transfer modes via conduction, convection, or radiation, while non-conventional sterilization processes utilizes modes like high pressure, electromagnetic, or electric-field based technologies for microbial inactivation with minimal thermal degradation of food. These methods of non-conventional sterilization processes are gaining popularity because of its ability to reduce energy and water consumption, shorten processing times, and retain nutritional and bioactive compounds which are lost during the conventional sterilization processes due to long exposure of heat (Ağagündüz et al., 2025).

Factors such as microbial resistance, food composition, process parameters and packaging compatibility determines the effectiveness of non-conventional sterilization processes. Processes such as High Pressure processing (HPP) and Pulsed Electric Fields (PEF) depends on cellular disruption without significant rise in temperature. On the other hand, processes such as microwave and ohmic heating rely on volumetric heating. Even though there are advantages of using the non-conventional processes, many challenges such as non-uniform energy distribution, process scalability, and incomplete microbial inactivation must be addressed for widespread usages and industrial adoptions (Vadivambal & Jayas, 2010).

#### 2.2.2.1 High Pressure processing (HPP)

HPP applies hydrostatic pressure, typically ranging above 600 MPa for inactivation of microorganisms. The HPP process disrupts the cellular structures and metabolic functions of microorganisms. HPP is effective particularly against vegetative bacteria but is less effective in inactivating bacterial spores. Hence, due to this limitation, HPP requires a combination of high pressure and mild heat which is called HPP-assisted thermal sterilization process for complete sterilization. HPP is commonly used for dairy products, juices, ready-to-eat meals, and meat products, where the nutritional and sensory properties are very crucial. The biggest limitation of HPP is that it is not suitable for dry or low moisture foods (X. Li & Farid, 2016).

#### 2.2.2.2 Pulsed Electric Fields (PEF) Sterilization

PEF utilizes short pulses of high voltage electricity such as 20-80 kV/cm for a very short duration (1 – 100 μs) for the inactivation of microorganisms which leads to the disruption of cell membranes. The application of electric pulses leads to the formation of pores in the microbial cell walls. This causes cellular contents to leak and eventually this leads to the death of the cell. This phenomenon is known as electroporation. PEF is effective particularly for

liquid and semi-liquid foods, such as fruit juices, milk, soups, etc. PEF is however ineffective against bacteria spores, hence its has to be combined with mild heat treatment or addition of preservatives (X. Li & Farid, 2016).

#### 2.2.2.3 Ultraviolet (UV) Irradiation

UV irradiation process utilizes short wavelength UV-C light in the range of 200 - 280 nm to destroy microorganisms by destroying their DNA and RNA and hence, prevents replication. This process is effective particularly for fruit juices and dairy products that have low turbidity. This is because particles or suspended solids can shield microorganisms from UV exposure. The primary limitation of UV Irradiation process is it has limited penetration depth and UV light has little effect on spore. Hence, it is ineffective for opaque or solid foods. Moreover, through photoreactivation, certain microorganisms can repair UV-induced DNA damage which reduces its long term effectiveness.

#### 2.2.2.4 Microwave Sterilization

Microwave sterilization relies on electromagnetic waves, typically at 915 MHz and 2450 MHz frequencies to generate heat within the food. Microwave penetrates into the food and interacts with polar molecules and ions present in the food matrices which causes volumetric heating. Microwave sterilization process is effective particularly for ready-to-eat meals where rapid heating is desirable. This process however requires specialized packaging materials which allows penetration of microwave and also ensures product safety. This process is advantageous for faster heating and reduced processing times, but it also has challenges such as non-uniform heating, and risk of cold spots. To tackle this issues, microwave has been combined with heat such as in the microwave-assisted thermal sterilization (MATS) system which uses hot water immersions to improve heating uniformity (Tang et al., 2002, 2018; Tang & Liu, 2020).

#### 2.2.2.5 Ohmic Heating

Ohmic heating relies on passing an electric current through food for internal heat generation. This process which is also called as electrical heating resistance provides rapid and uniform heating. This process is ideal for liquid and particulate foods. The biggest benefit of ohmic heating is that it is able to heat food uniformly and hence this reduces the risk of thermal gradients and overcooking. However, this process is effective only on foods with good electrical conductivity and not suitable for dry products or low moisture content products (Mesías et al., 2016).

## 2.3 Microwave Sterilization and Its Evolution

### 2.3.1 Microwave heating in the electromagnetic spectrum

Microwaves are part of the electromagnetic spectrum and operate at frequencies between 300 MHz and 300 GHz in food processing applications (Decareau, 1985). These waves are classified as non-ionizing radiation, meaning they do not cause ionization or alter the chemical

composition of food. When microwaves interact with polar molecules and charged ions in food, they generate heat through a process known as dielectric heating. This property makes microwaves highly effective for rapid and uniform heating, making them suitable for applications such as sterilization, pasteurization, and drying.

For both industrial and household use, the most commonly used microwave frequencies are 915 MHz and 2450 MHz. These frequencies are regulated by international organizations, including the Federal Communications Commission (FCC) and the International Telecommunication Union (ITU), and are designated for Industrial, Scientific, and Medical (ISM) applications. The selection of these frequencies ensures they do not interfere with telecommunication systems (Tang, 2015). The primary difference between 915 MHz and 2450 MHz frequencies lies in their penetration depth and heating efficiency. Microwaves at 915 MHz have a longer wavelength, allowing deeper penetration into food and resulting in more uniform heating. This reduces the likelihood of cold spots during processing. In contrast, microwaves at 2450 MHz have a shorter wavelength, leading to shallower penetration but faster surface heating. Due to its rapid heating capability, the 2450 MHz frequency is commonly used in household microwave ovens (Tang, 2015).

### 2.3.2 Microwave heating and dielectric properties

Microwave heating occurs when electromagnetic waves interact with food components such as water, salts, and other polar molecules. As microwaves pass through food, they cause these molecules to move, generating heat in the process. Unlike conventional heating, which relies on conduction and convection to transfer heat from the surface to the core, microwaves penetrate food and heat it from the inside by directly exciting molecules. Microwave heating is primarily governed by two mechanisms: dipolar rotation and ionic conduction (Tang, 2015). In dipolar rotation, polar molecules such as water realign with the alternating electric field of the microwaves. Since this field oscillates rapidly, the molecules continuously move, generating heat based on dielectric hysteresis. This effect is particularly strong in foods with high moisture content, as water efficiently absorbs microwave energy. Ionic conduction, on the other hand, occurs in foods that contain dissolved salts or charged particles. When exposed to microwaves, these ions move back and forth, generating heat throughout the volume of the material. Foods with higher salt content tend to heat faster due to increased ionic movement (Pandit et al., 2006).

One key advantage of microwave heating is its volumetric nature, where heat is generated throughout the food rather than being transferred from the surface inward. This results in shorter heating and sterilization times compared to conventional methods. However, a major challenge in microwave heating is its non-uniform heating pattern, where different food components heat at different rates. This issue arises because water, fats, and carbohydrates absorb microwave energy differently. To improve heating uniformity, various techniques but not only limited to such as rotating platforms, mode stirrers, and multimode microwave systems are used to distribute microwave energy more evenly.

The critical role for microwave heating is played by dielectric properties. Microwave field distribution and power absorption are strongly influenced by the dielectric properties of different materials. Materials with higher dielectric properties generally experience shallower

microwave penetration depths and higher energy dissipation, particularly at the industrial microwave frequencies of 915 MHz and 2450 MHz. A study by Gezahegn et al., (2021) demonstrated that microwave penetration depth is greater in purified deionized water than in tap water due to differences in their dielectric properties. The absence of ions in purified deionized water allows microwaves to penetrate more easily, while the presence of ions in tap water reduces penetration depth. For example, at 120°C, the microwave penetration depth in tap water was only one-third of that in purified deionized water. Overall the deionized water has lower dielectric loss factor comparing to tap water at microwave frequencies. In a microwave system using 915 MHz frequency, up to 93% of the incident microwave power reached the food product when purified water was used, compared to 85% with tap water. However, microwave power losses were found to be lower with purified water (4-7%) than with tap water (11-20%) due to ionic conductivity in tap water.

Oil, despite having a low dielectric loss factor, has also been studied for its microwave absorption properties. A recent study by (Zhou, Gezahegn, et al., 2023) found that microwave energy absorption in oil was similar to that in water. Although oil's dielectric loss factor is much lower than water's, the electric field intensity ratio between oil and water was reported to be 10:1 in a 1200 W, 2450 MHz domestic microwave oven. This finding suggests that oil can absorb microwave energy effectively. This is also mainly due to the lower heat capacity of oil comparing to water. The study also showed that soybean oil heated faster than water due to its lower specific heat, which was 50% that of water.

### 2.3.3 Evolution of microwave sterilization technology in food processing

The first microwave oven was developed by (Spencer, 1950), leading to extensive research on its applications in various fields. One of the early areas of interest for this technology was food processing. Over time, researchers began exploring its potential use in food sterilization. Within a decade, studies on microwave sterilization started gaining attention in the scientific community. Table 2.2 provides a summary of key developments in microwave sterilization, including several patented devices and their operating procedures. Fig. 2.2 presents a visual summary of major patented devices in microwave sterilization technology.

*Table 2. 2: Summaries of some important developments in microwave sterilization*

| References | Patented or developed by | Operating procedure (Power/Frequency/Application time) | Pressure utilized | Packaging | Additional Comments |
|---|---|---|---|---|---|
| Spencer, 1950 | Raytheon Co. (Mass., U.S.A.) | - | - | - | First microwave oven.<br><br>Revolutionary method to heat food with electromagnetic energy of wavelength 10 cm with air as medium. |
| Jeppson, 1964 | Applications Research Center, San Ramon, California,U.S.A. | -/900 MHz/- | 1 bar | Glass container | The glass jar acted like pressure cooker to heat milk to 121°C in 4 min |
| Landy, 1965 | Jerome J. Landy | 400W/2450MHz/20 and 15 minutes | 1.98 bar | Vapor-tight Glass tube, Mylar® (polyester film made of Biaxially-oriented polyethylene terephthalate) | Package dimensions and material quantity are controlled to manage uniform heating.<br><br>A 0.05 mm thick Mylar® gave enough rigidity and strength to maintain constant volume at rising pressures and temperatures |
| Long et al., 1966 | Continental Can Company, Inc., New York, N.Y | 900W and 800 W/915 MHz and 2450 MHz/1.5 to 3 minutes | - | Open top pouch holders.<br><br>Polymeric films such as polyethylene, both high and low density, polypropylene and polyethylene terephthalate | Dielectric constant of the product is higher than the dielectric constant of the pouch forming material. |
| Jeppson & Harper, 1967 | Cryodry Corporation, San Ramon, Calif., a corporation of California | -/200-10000 MHz/- | - | - | Temperature rise of the natural moisture content of the product is utilized to build up the internal pressure within the container.<br><br>Mechanical pressure locks is avoided by using hydrostatic pressure of mineral oil. |

| | | | | | |
|---|---|---|---|---|---|
| Kenyon et al., 1971 | U.S. Army Natick Laboratories, Natick, Massachusetts. | 10 kW/ 2,450 MHz/9-14 minutes | > 1 bar | A flexible Mylar® 0.076 mm polyolefin-0.008 mm aluminum foil-0.01 mm polyester | Air pressure was used to prevent pouch rupture.<br><br>Conveyor speed and power were regulated to provide the process time and temperature. |
| Tang et al., 2006 | Washington State University Research Foundation, Pullman, WA (US) | 6 kW/915MHz/ 30 seconds to 2 minutes | - | - | Horn-Shaped Applicator and Rectangular Cavity<br><br>Single-mode cavity<br><br>Fundamental TE-mode propagation through the system |
| Hirschey et al., 2017 | 915 Labs, LLC | 5 to 40 kW/915 MHz/ 45 seconds to about 1 minute per pass | 3 bar. | Dimension: 152.4 mm x 184.15 mm (height) x 38.1 mm Gusset<br><br>Front/Back:<br>- Barrier coated PET film /lnk/White Retort PET/Retort Grade<br><br>Gusset: Non-foil retort pouch<br>-Barrier coated PET Film/Ink/Adhesive/Retort Grade | No packaging failures in trials |

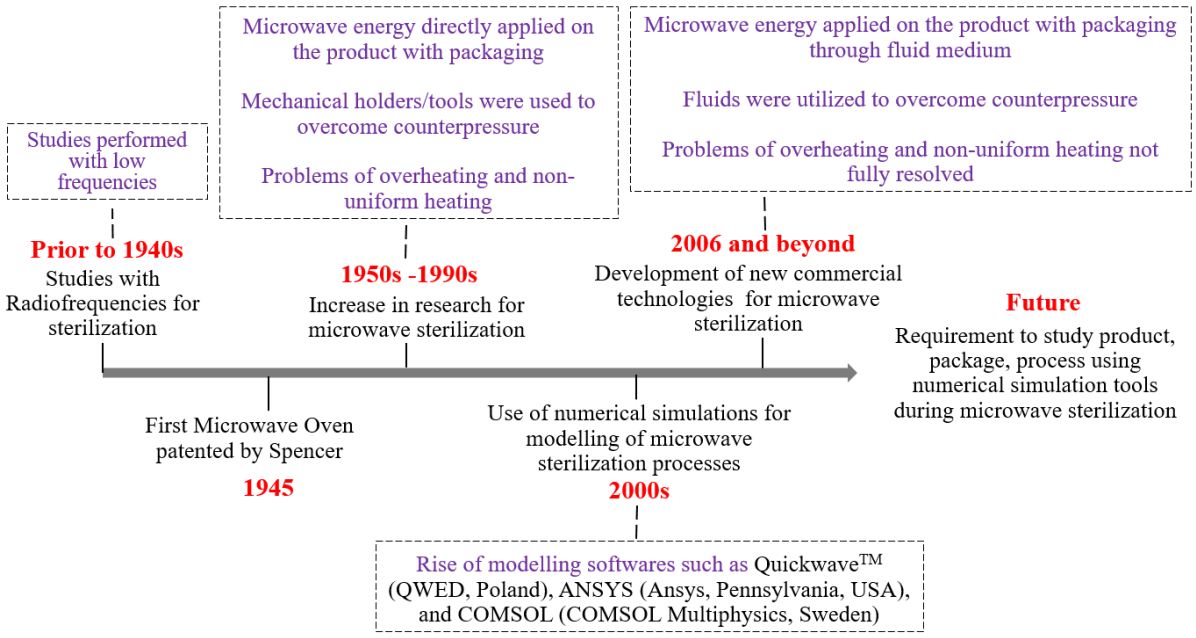



*Fig. 2. 2: Non-exhaustive lists of patented devices for historical overview on microwave sterilization.*

Microwave sterilization has evolved significantly over the decades, driven by advancements in packaging, numerical modelling, and process optimization. The driving factor for exploring microwave sterilization was the need for faster and energy-efficient thermal processing methods that could ensure food safety while maintaining product quality and nutritional value. One of the earliest studies on microwave sterilization took place at the Applications Research Center in San Ramon, California, USA. In this study, skim milk in a glass container was exposed to microwaves at a frequency of 900 MHz. The milk was heated to 121.1°C within four minutes at atmospheric pressure (Jeppson, 1964). This successful experiment encouraged further research in microwave sterilization. Another study tested the sterilization of oranges in syrup inside a metal-capped glass jar. A Litton Model 500 microwave oven, operating at a maximum power of 1 kW and a frequency of 2450 MHz, was used for this purpose. The results showed that enzymes were inactivated when the temperature reached 85°C (Lin & Li, 1971). However, the study did not specify the method used to measure temperature during the process. Researchers also began testing pouches instead of glass containers for microwave sterilization (Landy, 1965). Mylar®, a polyester film made of biaxially-oriented polyethylene terephthalate, was identified as a suitable pouch material. Packaging materials like Mylar® and polyethylene were effective because their dielectric constant was lower than that of the food inside (Long et al., 1966). Despite this, heating remained non-uniform. To improve heat distribution, a new technique used intermittent microwave energy, applying 400 W for five-second intervals at a pressure of 1.98 bar (Landy, 1965). The results improved, but uniform heating was still not achieved. The U.S. military became interested in microwave sterilization for producing high-quality, shelf-stable military food. The U.S. Army Natick Laboratories developed a specialized microwave sterilization system. This system generated 10 kW of power at 2450 MHz and

operated at pressures greater than 1 bar (Kenyon et al., 1971). The process was controlled by adjusting the conveyor speed and power settings. A more advanced system was later designed with a pressurized environment of up to 3.45 bar. This system included a Model 8000 M dual set-point on/off relay safety device. The safety device automatically turned the microwave system on or off based on a pre-set temperature. This feature prevented overheating, burning, or container explosions. The system consisted of three main parts: a microwave generation and transmission section, a microwave cavity section, and a sterilization system (Fig. 2.3). Successful sterilization was demonstrated using potatoes, where the process maintained an $F_o$ value of 3 minutes at 121.1°C. The sample was heated for 10 minutes until it reached 130°C, then cooled for 50 minutes until it stabilized at 20°C (Loh & Breene, 1983).

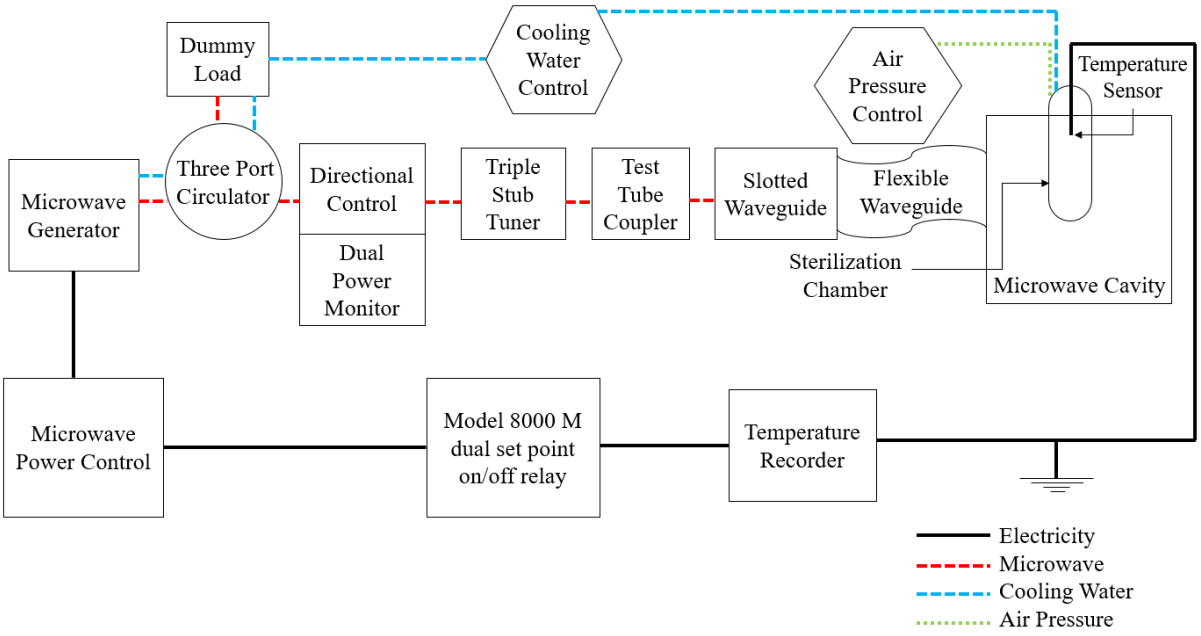



*Fig. 2. 3: A flowchart of a microwave sterilization system with individual components developed by Loh & Breene, (1983). It consists of 3 main sections, namely 1 microwave generation and transmission section, 1 microwave cavity section, and 1 sterilization system.*

According to Williams, (1993), P & T Foods, NV, Belgium was one of the first companies to commercially produce microwave-sterilized foods in sealed containers. The company manufactured various pasta products using microwaveable barrier-plastic containers with a shelf life of 9 to 12 months. Their microwave sterilization system included 50 microwave generators operating at a frequency of 2450 MHz. The system also featured a pressurized heating process, where products were preheated to 92°C at 2.3 bar before being transferred to a high-temperature compartment for further heating up to 126°C. However, detailed technical information about this system is limited due to a lack of publicly available documents.

In another study, Prakash et al., (1997) examined microwave sterilization using a system known as the Microwave Digestion System (MDS 2000), developed by CEM Corp. in Matthews, North Carolina. This system included a turntable that could hold 12 cylindrical sample vessels containing food products. The vessels were made of Teflon® to withstand high pressure and to achieve a sterilization temperature of 121°C. Fiber optic temperature sensors were inserted through the vessel walls to monitor food temperatures during processing. Pressure probes were

also attached to the vessel caps to track internal pressure changes throughout the sterilization cycle. The system was designed to rapidly reach the target temperature with minimal fluctuation, maintaining a variation of ±2°C. After the microwave treatment, locking nuts on the vessels were manually unscrewed to release internal pressure and lower the temperature immediately (Prakash et al., 1997). These systems have not been adopted for commercial food production due to challenges in scaling up for large-scale industrial applications and the need for further improvements.

### 2.3.4 Microwave-Assisted Thermal Sterilization (MATS) System

Microwave-Assisted Thermal Sterilization (MATS) is one of the most advanced and commercially viable microwave sterilization technologies developed to overcome the challenges of non-uniform heating associated with traditional microwave processing (Barbosa-Cánovas et al., 2014). MATS integrates microwave energy with hot water immersion, significantly improving heating uniformity, microbial inactivation, and product quality while reducing processing time and energy consumption.

After the 2000s, research focused on using a fluid to distribute the heat uniformly and thus avoiding overheating at the surface and edges of the product. The MATS system was developed at Washington State University Research Foundation, Pullman, WA (U.S.A.) (Fig. 2.4) as an alternative to conventional thermal sterilization methods. It was designed to address the limitations of microwave-only sterilization, which often led to overheating at the food surface while the core remained underprocessed due to uneven energy distribution.

The core principle of the MATS system is to combine microwave heating with a pressurized hot water bath, ensuring that food is sterilized uniformly while maintaining its texture, color, and nutrient composition. The process involves the following key stages (Resurreccion et al., 2013) :

1. Preheating – The packaged food enters a preheating section where it is immersed in hot water, gradually increasing the temperature before microwave exposure. This step helps minimize thermal shock and reduces excessive temperature gradients within the product.
2. Microwave Heating – Food packages pass through a series of microwave cavities, where 915 MHz microwaves are applied while submerged in pressurized hot water. The presence of water around the food acts as a thermal buffer, reducing localized overheating and enhancing heat distribution. The heating section includes four rectangular microwave cavities, each equipped with a pair of horn-shaped applicators. Each cavity has its own dedicated microwave generator. Stub tuners are placed inside the cavities to minimize power reflection and improve efficiency.
3. Holding Phase – After microwave heating, food is kept in a holding section, ensuring that the internal temperature remains at the required sterilization level for a sufficient time to inactivate Clostridium botulinum spores and other pathogens.
4. Cooling – The sterilized packages enter a cooling section, where they are rapidly cooled to prevent overcooking and preserve sensory attributes such as flavor, texture, and color

Each section has an independent water circulation system, a pressurized tank, and a plate heat exchanger for precise temperature control. A non-metallic, pocketed mesh conveyor belt moves food trays or pouches through all four sections.

In the early stages of microwave sterilization development, Pathak et al., (2003) designed a 3D computer simulation model to improve the cavity structure. Later, Washington State University developed the first pilot-scale system with finalized cavity dimensions (H. Chen et al., 2006). This system included two identical horn-shaped applicators placed at the top and bottom of a rectangular cavity. The system operated at 915 MHz using a power source of 5 kW through a waveguide measuring 128 mm × 124 mm in TE10 mode. The length of the waveguides' legs after the T-junction could be adjusted to control the phase difference between the microwaves at the entry points of the applicators. This phase adjustment allowed better control of wave interactions inside the cavity to achieve uniform heating. The system combined circulating hot water and microwave energy to maintain a temperature of 125°C within water. Compressed air pressurized the water at 2.8 bar to prevent boiling inside the cavity. The horn-shaped waveguides were covered with microwave-transparent windows to prevent steam from escaping (H. Chen et al., 2006, 2008).

Initially, the system operated in batch mode but was later modified into a continuous mode system (Resurreccion et al., 2013). This second-generation pilot-scale system used one or more magnetrons, klystrons, electronic oscillators, or solid-state sources at a 915 MHz ISM band. It included a horn-shaped applicator and a rectangular single-mode cavity with TE-mode propagation. The system reached a sterilization temperature of 121°C by combining 2.7 kW microwave power and hot water heating. Water was used in two stages: first, in the pre-heating section, a hot water bath warmed the food to around 50°C without cooking it. Second, in the sterilization section, the water surrounding the food was heated along with the food itself (H. Chen et al., 2008; Resurreccion et al., 2013; Tang et al., 2006).

A more recent MATS system was developed by 915 Labs, LLC, in the U.S. This system processes food in multiple microwave passes to reach a sterilization temperature of 135°C. Cold spot temperature probes are used to measure temperature changes during the process. The system applies microwave power ranging from 5 kW to 40 kW per pass, with most passes using between 10 kW and 20 kW. Each pass lasts between 45 seconds and one minute at a pressure of 3 bar (Hirschey et al., 2017).

One of the main challenges in these microwave sterilization systems is achieving uniform temperature distribution throughout the food product. This issue has been a major barrier to the widespread commercial adoption of microwave sterilization. Another challenge in these systems is accurately measuring temperature and pressure inside food packaging. Early studies, such as by Lin & Li, (1971), used thermocouple sensors to measure temperature at the coldest point of the product. However, due to the uneven heating caused by microwaves, it is necessary to measure temperatures at multiple locations within the package. Measuring internal pressure within food packaging has also been difficult in these systems. (Kenyon et al., 1971) attempted to control pressure inside the packaging using a valve system but could not achieve precise pressure measurements. Despite these challenges, microwave sterilization has been reported as a successful method in various studies. The success of microwave sterilization is largely due to

the accumulated lethality achieved throughout the sterilization process. Accumulated lethality refers to the total microbial inactivation based on the equivalent processing time at a reference temperature if heating and cooling occurred instantly. High temperatures result in higher lethality, making the High Temperature Short Time (HTST) method highly effective. The total lethality of the process is calculated by considering the time taken to reach the processing temperature, the holding time, and the cooling period (Decareau, 1968; Goldblith, 1966).

MATS has several advantages but also faces challenges due to its high water consumption during heating and cooling. Water is used in multiple stages, including preheating, sterilization, and cooling, which raises concerns about efficiency, cost, and environmental impact. Even though MATS recirculates water, it still requires a constant supply of high-temperature pressurized water. This increases water demand in food processing facilities, which can be problematic in areas with limited water resources. Industries focused on sustainability may also find it difficult to reduce water usage while maintaining process efficiency. Although MATS offers efficient heat transfer, its reliance on continuous pressurized hot water circulation increases energy demand, maintenance complexity, and water management challenges, often reducing the overall sustainability and cost-effectiveness compared to conventional retort systems. Another concern is the impact of hot pressurized water on equipment durability. Continuous exposure to high temperatures and pressure can cause corrosion, scaling, and mechanical wear in MATS components. Regular maintenance and cleaning are required to prevent equipment failure, which can lead to production downtime and higher operational costs.

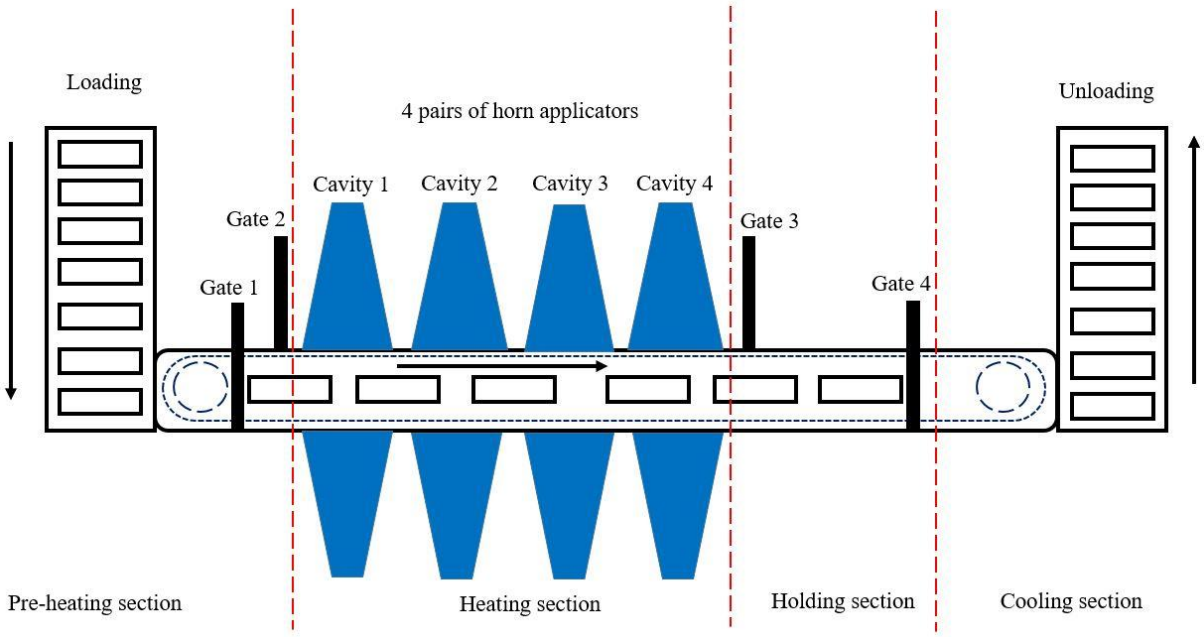



*Fig. 2. 4: Schematic of the Microwave assisted thermal sterilization (MATS) system. It comprises of four sections, namely, pre-heating, heating, holding, and cooling section.*

### 2.3.5 Role of microwave generators in sterilization process

Microwave generators play a key role in microwave sterilization by controlling power, frequency, and energy transfer to food products. These generators convert electrical energy into microwave radiation, which heats food quickly by interacting with its components. The effectiveness of microwave sterilization depends on the type of microwave generator used in the system. Different generator technologies vary in their ability to control power levels, maintain uniform heating, and improve energy efficiency. There are two main types of microwave generators used in food sterilization. Magnetron-based generators have been the standard choice for microwave heating for many years. Solid-state microwave generators are more recent technology that provides precise control over heating and energy distribution. Table 2.3 lists briefly the differences between magnetron based generators and solid-state generators.

#### 2.3.5.1 Magnetron-based generators: conventional power source for microwaves

Magnetron-based microwave generators have been the dominant technology for microwave heating and sterilization since their introduction in the 20th century. These devices generate microwaves by accelerating electrons in a vacuum tube, which interact with a magnetic field to produce high-frequency oscillations. Magnetrons are widely used in domestic microwave ovens, as well as in industrial sterilization processes that require high power outputs. One of the main advantages of magnetron-based generators is their cost-effectiveness. They are relatively inexpensive to manufacture and can generate large amounts of microwave power, making them suitable for high-volume food sterilization. In addition, they can operate at both 915 MHz and 2450 MHz. However, magnetron-based generators have several limitations that affect the efficiency of microwave sterilization. One major issue is frequency drift, which occurs because magnetrons do not produce a fixed, stable frequency. Instead, the frequency can vary during operation, leading to inconsistent energy absorption and heating patterns within the food. This variation can cause non-uniform heating, increasing the risk of cold spots where microbial survival is possible. Another limitation is limited power control. While magnetrons can operate with on-off switching or continuous-wave (CW) modes, they cannot dynamically modulate power output with high precision according to the heating requirements of the food product. This inefficiency makes it challenging to achieve uniform sterilization, especially for complex food structures with varying moisture content and density. Additionally, magnetrons have a shorter operational lifespan compared to newer technologies. Over time, their efficiency decreases due to electrode degradation, reducing microwave power output and requiring frequent replacement. This decline in performance further contributes to energy loss and process inefficiency, making magnetron-based systems less ideal for precision-driven sterilization applications (Taghian Dinani, Kubbutat, et al., 2020).

#### 2.3.3.2 Solid-state microwave generators: precision heating for food sterilization

Solid-state microwave generators represent a significant advancement in microwave heating technology. Unlike magnetrons, which generate microwaves through electron acceleration in a vacuum tube, solid-state generators use semiconductor technology to produce microwaves at a stable and controllable frequency. These generators offer greater precision, energy efficiency, and uniform heating, making them highly suitable for food sterilization applications. One of the

key advantages of solid-state generators is frequency stability. Unlike magnetrons, which experience frequency drift, solid-state generators maintain a fixed, tunable frequency throughout the sterilization process. This allows for more consistent energy absorption, allowing a better control on the hot and cold spots in food products. By optimizing the electromagnetic field distribution, solid-state systems improve heating uniformity and microbial inactivation, enhancing food safety.

Solid-state microwave generators were first proposed as a replacement for magnetrons in the early 1970s. The first patent for this technology was granted to Bruce McAvoy in 1971 (Mcavoy, 1971). At that time, solid-state generators were not practical because they could not produce high power levels above 100 watts. Recent advancements in the power semiconductor industry have renewed interest in using solid-state generators for microwave heating (Atuonwu & Tassou, 2018). These generators offer several advantages over traditional magnetrons. They provide better control of input power (Zhou, Tang, et al., 2023), improved frequency stability (Atuonwu & Tassou, 2018), higher energy efficiency (Taghian Dinani, Hasić, et al., 2020), and the ability to predict heating patterns using numerical modeling (Nget et al., 2023).

A recent study by Zhou, Tang, et al., (2023) compared the spectral stability of magnetrons and solid-state generators. In this study, commercial microwave ovens were modified to operate with two different microwave sources: a 5800 MHz solid-state generator and a 2450 MHz magnetron. The spectral characteristics of each system were analyzed using a spectrum analyzer with a dual-band dipole antenna. Three food samples were tested: tap water, distilled water, vegetable oil, and whey protein gel. The results showed that magnetron-based microwaves fluctuated around the set frequency of 2450 MHz. These variations depended on the type of food and its position inside the microwave cavity. In contrast, the solid-state generator produced a much more stable spectrum centered around 5800 MHz. The frequency band was very narrow, remaining within a 2 MHz range despite changes in food type or position (Zhou, Tang, et al., 2023).

Building on these findings, another study by Zhou, Pedrow, et al., (2023) investigated the potential for achieving more uniform heating in a multi-mode microwave cavity using a GaN-based solid-state generator. This study used a solid-state generator inside a microwave oven with a WR-159 waveguide (250 mm × 40 mm × 20 mm). The generator operated at 5800 ± 75 MHz. The heating performance was evaluated by measuring power reflections in a whey protein gel sample. Three frequency settings were tested: 5770 MHz, 5840 MHz, and a combination of 5770 MHz for 30 seconds followed by 5840 MHz for another 30 seconds. The results showed that using multiple frequencies with a solid-state generator improved heating uniformity compared to using a single frequency. This was the first study to demonstrate that solid-state generators could be used to develop multi-mode industrial microwave systems for heating single-meal-size food packages. This is an important finding because small cavity sizes have historically limited the use of single-meal packaging in microwave systems operating at 2450 MHz or 5800 MHz (Zhou, Pedrow, et al., 2023).

Another key advantage of solid-state microwave generators is their energy efficiency. The overall energy efficiency of a microwave heating system is calculated using the formula:

$$\eta_{global} = \eta_{gen}\eta_{abs} \quad 2.1$$

where, $\eta_{global}$ is global energy efficiency of a microwave heating system, $\eta_{gen}$ is the electricity-to-microwave conversion efficiency, and $\eta_{abs}$ is microwave-to-heat conversion efficiency, which quantifies the fraction of incident microwave energy absorbed by the product and converted into thermal energy. This efficiency depends primarily on the dielectric properties of the material (dielectric constant and loss factor) and the local electric field strength within the cavity.

Atuonwu & Tassou, (2018) reported that solid-state generators have slightly lower $\eta_{gen}$ values compared to magnetrons. For a 2450 MHz microwave oven operating at 200 W, $\eta_{gen}$ was 61%–69% with a solid-state generator, while a magnetron achieved 70%. At 915 MHz, the efficiency was 69% for a solid-state generator compared to 88% for a magnetron. However, solid-state generators compensate for this with significantly higher $\eta_{abs}$, which can reach 100% under optimized conditions. Magnetrons, in contrast, have much lower $\eta_{abs}$, reducing their overall efficiency. Additionally, magnetron efficiency declines to around 50% as the device ages, while solid-state generators are expected to improve in efficiency over time. Other studies have also confirmed that solid-state generator microwave ovens are more energy-efficient than magnetron-based systems (Taghian Dinani, Hasić, et al., 2020; Taghian Dinani, Kubbutat, et al., 2020).

*Table 2. 3: Differences between magnetron based generators and solid-state generators.*

| Feature | Magnetron-Based Generators | Solid-State Generators |
|---|---|---|
| **Frequency Stability** | Variable frequency | Stable frequency |
| **Energy Efficiency** | Lower efficiency | Higher efficiency |
| **Lifespan** | Shorter lifespan | Longer lifespan |
| **Cost** | Lower cost | Higher cost |
| **Real-Time Adjustment** | Not adjustable | Real-time tuning |
| **Multi-Frequency Capability** | Single frequency | Multi-frequency |

## 2.4 Microwave Food Packaging

Food packaging plays an essential role in the effectiveness of microwave sterilization by keeping food safe and protected. Since microwave heating works by volumetric heating, packaging materials must allow microwaves to pass through while remaining stable under heat. The packaging must also withstand internal pressure changes that occur during the heating process. In addition to containing food, packaging materials influence pressure control, and food quality preservation. Early microwave packaging was primarily made of glass because it is thermally stable and does not react with food. However, glass is heavy and fragile, making it unsuitable for large-scale food production. Plastic-based flexible packaging were later used to address these challenges. Advances in packaging technology led to the creation of monolayer polymer films, multilayer composites, and metal oxide-coated materials. These new materials offer improved barrier properties, greater mechanical strength, and better resistance to pressure changes. Fig. 2.5 highlights the important characteristics of microwave packaging.

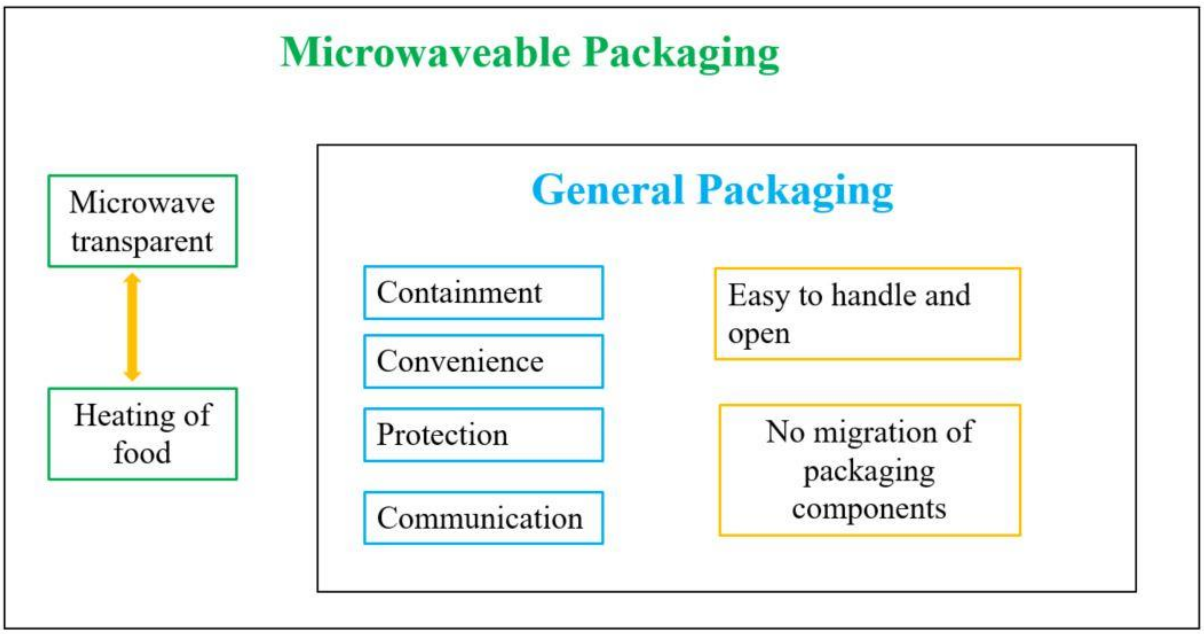



*Fig. 2. 5: Important characteristics for microwave packaging.*

### 2.4.1 Evolution of Microwave Packaging

Early developments in microwave sterilization primarily used glass containers due to their stability under high temperatures (Jeppson, 1964; Lin & Li, 1971; Loh & Breene, 1983). Over time, polymer-based packaging began to be used, starting with monolayer films (Ayoub et al., 1974; Kenyon et al., 1971) and later progressing to multilayer structures (Hirschey et al., 2017). A key factor in selecting packaging materials was their ability to withstand high temperatures within short processing times. Another important consideration was the packaging's ability to resist internal pressure changes during heating (Kenyon et al., 1971).

Monolayer pouches have limitations in handling high temperatures and pressure during microwave sterilization (Al-Ghamdi, 2020). To improve their performance, metal oxide coatings were introduced to enhance oxygen barrier properties. Thin layers of metal oxides, such as SiOx and AlOx, were applied using a plasma coating process. However, single metal oxide layers often developed cracks or pinholes under high-temperature conditions (Ayvaz et al., 2012; Parhi et al., 2019). To address this issue, multilayer structures with two metal oxide layers were developed for high-temperature food processing. In one study, polyethylene terephthalate (PET) pouches coated with double layers of aluminum oxide ($Al_2O_3$) provided better protection than ethylene vinyl alcohol (EVOH)-based pouches. These pouches offered superior resistance to water vapor and oxygen permeability during microwave-assisted thermal sterilization (MATS) processing. The pouches were tested at a sterilization lethality of $F_0 = 12.7$ mins at 121°C and an operating pressure of 2.3 bar ($F_0$ represents the equivalent time in minutes at 121 °C required to achieve a specific level of microbial inactivation, typically corresponding to a 12-log reduction of *Clostridium botulinum* spores). Results showed that the double metal oxide-coated pouches maintained their integrity throughout the MATS process. These pouches were also capable of storing food at room temperature for 3 to 5 years. Additionally, such

packaging is being explored for extended space missions by NASA, ESA, and other space agencies (J. Patel et al., 2021). However, further studies are needed to evaluate the interaction of these packaging materials with microwaves in systems other than MATS, especially when using alternative heating mediums.

### 2.4.2 Properties of Microwave Packaging

Microwave packaging must meet specific requirements to ensure safe and uniform heating during sterilization. One important requirement is microwave transparency, meaning the packaging material must allow microwaves to pass through without significant absorption or reflection. If the packaging absorbs too much microwave energy, it can cause uneven heating or localized overheating. Another key factor is heat resistance, as microwave sterilization requires food to be heated above 121°C. The packaging must remain stable at high temperatures without softening, melting, or breaking down. If the material loses its structure under heat, it can affect food safety and packaging performance.

Many studies have examined the use of multilayer pouches for high-temperature microwave sterilization. Tables 2.4, 2.5, and 2.6 summarize findings related to their thermal, mechanical, and barrier properties under different processing conditions. Thermal properties are crucial because changes in these properties during or after processing can impact the mechanical strength and barrier effectiveness of packaging materials. Among these properties, melting temperature ($T_m$) is a critical factor, as it determines the temperature at which the material transitions from a solid to a liquid under a specific pressure. This melting temperature establishes the upper temperature limit for sterilization. The packaging material must also have strong mechanical properties to endure high-temperature sterilization. Two key mechanical properties are tensile strength and tear resistance. Tensile strength measures the maximum stress a material can withstand before breaking when stretched. Tear resistance indicates the material's ability to resist tearing forces. Small variations in mechanical properties do not significantly impact overall packaging performance. However, when processing conditions involve higher temperatures and longer exposure times, packaging durability can be compromised.

Barrier properties are the most affected by high-temperature sterilization. The effectiveness of a packaging material as a barrier depends on the number of layers and the composition of those layers. Extended exposure to high temperatures further reduces barrier performance. Two important parameters used to evaluate barrier properties are oxygen transmission rate (OTR) and water vapor transmission rate (WVTR). OTR measures the steady-state rate at which oxygen permeates through a film under specific temperature and humidity conditions. WVTR similarly quantifies the rate at which water vapor passes through the packaging material. Studies have shown that both OTR and WVTR increase when microwave processing time is extended from 9 minutes to 28 minutes at 121.1°C (Al-Ghamdi, 2020).

Beyond these factors, dielectric properties of packaging materials also play a role in microwave sterilization. However, research on the dielectric behavior of food packaging materials remains limited. Some available data on dielectric properties of specific polymers can be found in (M. Chen et al., 1993).

*Table 2. 4: Thermal properties after microwave sterilization of different packaging materials*

| Packaging | Process Conditions (Temperature/ Pressure/ Time) | Packaging material layer/ Melting temperature ($T_m$(°C)) | References |
|---|---|---|---|
| Polypropylene (PP) | - | PP/160 – 166°C | Maddah, 2016 |
| Polylactic acid (PLA) | - | PLA/165°C | Farah et al., 2016 |
| Coated PET/PA 6/PP | 124 °C/241 kPa/15 min | PP/161.5 ± 0.1<br>PA/218.9 ± 0.1<br>PET/254.6 ± 0.2 | Dhawan et al., 2014 |
| | 124 °C/241 kPa/39 min | PP/161.6 ± 0.3<br>PA/219.2 ± 0.2<br>PET/254.6 ± 0.1 | |
| | 117 °C/-/30 min | PP/167.4<br>PA/223.1 | |
| SiOx PET/PA6/cPP | 75 °C/101.1 kPa/30 min | PET/258.2<br>PA/225.0<br>PP/166.4 | Ramalingam et al., 2015 |
| | 117 °C/-/30 min | PET/258.3<br>PA/224.5<br>PP/166.6 | |
| PE/PA6/PE | 75 °C/101.1 kPa/30 min | PE/112.3 ± 0.6<br>PA6/222.2 ± 0.2 | Halim et al., 2009 |
| PP/PA6/PP | 75 °C/101.1 kPa/30 min | PP/164.1 ± 0.2<br>PA/221.6 ± 0.2 | |
| PE/NanoPA6/PE* | 75 °C/101.1 kPa/30 min | PE/112.5 ± 0.8<br>PA6/221.7± 0.1 | |
| PP/NanoPA6/PP | 75 °C/101.1 kPa/30 min | PP/164.3 ± 0.3<br>PA/221.3 ± 0.1 | |
| PET-BO/PE* | 90 °C/101.1 kPa/20 min | PET/252.4 ± 0.2<br>PE/116.7 ± 0.2 | Fleckenstein et al., 2016 |
| PP-BO/PE | 90 °C/101.1 kPa/20 min | PP/162.6 ± 0.5<br>PE/124.9 ± 0.4 | |
| PET/PET/LLDPE | 93 °C/101.1 kPa/36 min | PET/256.1 ± 0.7<br>PET/167.3 ± 0.5<br>LLDPE/124.0 ± 0.9 | Bhunia et al., 2016 |
| | 93 °C/-/52 min | PET/257.2 ± 0.7<br>PET/167.7 ± 0.1<br>LLDPE/123.1 ± 0.1 | |

*Table 2. 5: Mechanical properties after microwave sterilization of different packaging materials.*

*Not all the data are at sterilization temperature

| Packaging | Process Conditions (Temperature/Pressure/Time) | Tensile Strength (MPa) | References |
|---|---|---|---|
| Polypropylene (PP) | - | 22-34 | Maddah, 2016 |
| Polylactic acid (PLA) | - | 59 | Farah et al., 2016 |
| SiOx PET/PA6/PP (Machine direction) | 117 °C/-/30 min | 46.0 ± 5.11 | Ramalingam et al., 2015 |
| SiOx PET/PA6/PP (Cross-machine direction) | 117 °C/-/30 min | 48.3 ± 2.39 | |
| PP/PE | 90°C/-/20 min | 98.1 ± 3.9 | Fleckenstein et al., 2016 |
| PET/PE | 90 °C/-/20 min | 47.7 ± 2.8 | |

*Table 2. 6: Barrier properties after microwave sterilization of different packaging materials.*

| Packaging | Process Conditions (Temperature/Pressure/Time) | Oxygen transmission rate(OTR)($cm^3.m^{-2}.day^{-1}$) | Water vapor transmission rate(WVTR)($g.m^{-2}.day^{-1}$) | References |
|---|---|---|---|---|
| PET//EVOH//PP | 121.1 °C/-/9 min | 0.79 ± 0.01 | - | Mokwena et al., 2009 |
| | 121.1 °C/-/15 min | 1.58 ± 0.38 | - | |
| | 121.1 °C/179.3 kPa/28 min | 1.75 ± 0.04 | - | |
| PET//PP//PA/EVOH/PA//PP | 121.1 °C/-/9 min | 1.58 ± 0.22 | - | |
| | 121.1 °C/-/15 min | 2.30 ± 0.32 | - | |
| | 121.1 °C/179.3 kPa/28 min | 4.57 ± 0.59 | - | |
| PET//PA//PP | 121.1 °C/241.3 kPa/9 min | 0.25–0.27 | 1.48–1.50 | Dhawan et al., 2014 |
| Coated PET//PA6//PP | 121.1 °C/241.3 kPa/28 min | 0.60 | 3.60–3.80 | |
| | 121.1 °C/241.3 kPa/28 min | 1.25–1.29 | 3.60–3.80 | |

| | | | | |
|---|---|---|---|---|
| SiOx PET/PA6/PP | 117 °C/-/30 min | 4.50–5.50 | 1.30–1.45 | Ramalingam et al., 2015 |
| PP/NanoPA6/EVOH/PP | 121 °C/-/30 min | - | - | Halim et al., 2009 |
| PP/NanoPA6/PP | 121 °C/-/30 min | 15.00–19.00 | 5.50–6.00 | |
| PP/EVOH/PP | 124°C/234 kPa/40.14 min | 1.27±0.10 | 1.65±0.33 | Al-Ghamdi, 2020 |

### 2.4.3 Internal pressure generation in microwave packaging

Internal pressure builds up in microwave packaging due to the conversion of water into steam during heating. When microwaves interact with water molecules, dipolar rotation and ionic conduction generate frictional heat. This heat causes water to evaporate, forming steam that occupies a larger volume than liquid water. As steam accumulates inside the sealed package, internal pressure increases (Tang et al., 2002). Several factors influence pressure buildup, including food composition, moisture content, and the dielectric properties of the packaging material. Foods with higher water content produce more steam, leading to greater internal pressure. The rate at which microwave energy is absorbed also affects pressure buildup, as higher absorption leads to faster steam generation and larger pressure fluctuations (Chandrasekaran et al., 2013). If internal pressure is not properly managed, it can exceed the structural capacity of the packaging, causing swelling, deformation, or rupture. This issue is especially concerning for flexible packaging, where excessive steam accumulation can result in the deformation and rupture of the packaging. To prevent these failures, effective pressure control strategies are required to maintain package integrity and ensure efficient sterilization.

### 2.4.4 Techniques to hold inner pressure in microwave packaging

The management of internal pressure in microwave food packaging is a crucial aspect of ensuring package stability, preventing rupture, and maintaining food quality. Overpressure occurs when the internal pressure inside food packaging rises due to an increase in temperature during heating. As food heats up, water inside the package turns into steam, causing internal pressure to exceed atmospheric pressure (Jeppson & Harper, 1967). In early microwave sterilization systems, mechanical holders were used to provide counter pressure for glass containers (Jeppson, 1964). A similar approach was applied to polymeric packaging, where open pouches allowed excess steam to escape (Long et al., 1966). Some studies explored using stronger materials, such as Mylar®, along with air pressure to prevent pouch rupture (Kenyon et al., 1971). Researchers also developed a pressurized system operating at 3.45 bar to control steam pressure in glass containers during microwave sterilization. This system was equipped with a Model 8000 M dual set-point on/off relay safety device to regulate pressure (Loh & Breene, 1983).

Other studies have investigated the use of liquids, such as water by Wang et al., (2003a) and mineral oil, instead of mechanical holders to provide counter pressure. Mineral oil was chosen because it is heavier than water and does not absorb microwave energy (Jeppson & Harper, 1967). More recently, the MATS system has adopted water to manage counter pressure. In addition to pressure control, water also improves heating uniformity in solid food products by enhancing heat transfer through convection (H. Chen et al., 2008; Hirschey et al., 2017; Tang et al., 2006). However, limited data is available on how water absorbs microwaves and its overall efficiency in microwave energy utilization. Fig. 2.6, 2.7, and 2.8 illustrate different methods used to control overpressure in food packaging during microwave sterilization. Recent advancements in numerical simulation and modeling tools have made it easier to analyze overpressure and other microwave-related phenomena in food packaging.

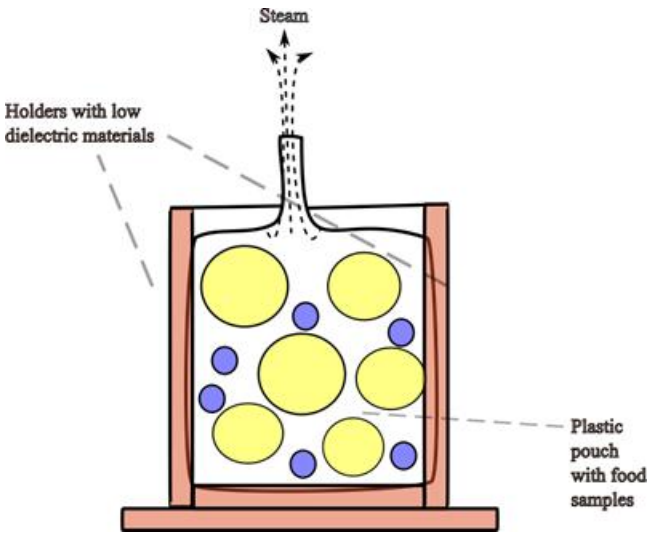



*Fig. 2. 6: Schematic of a plastic pouch holder to prevent distortion of the pouch during steam emanation. Adapted from Long et al., (1966). This packaging was developed so that the pressure generated inside the package during microwave sterilization is released through a partial opening at the top.*

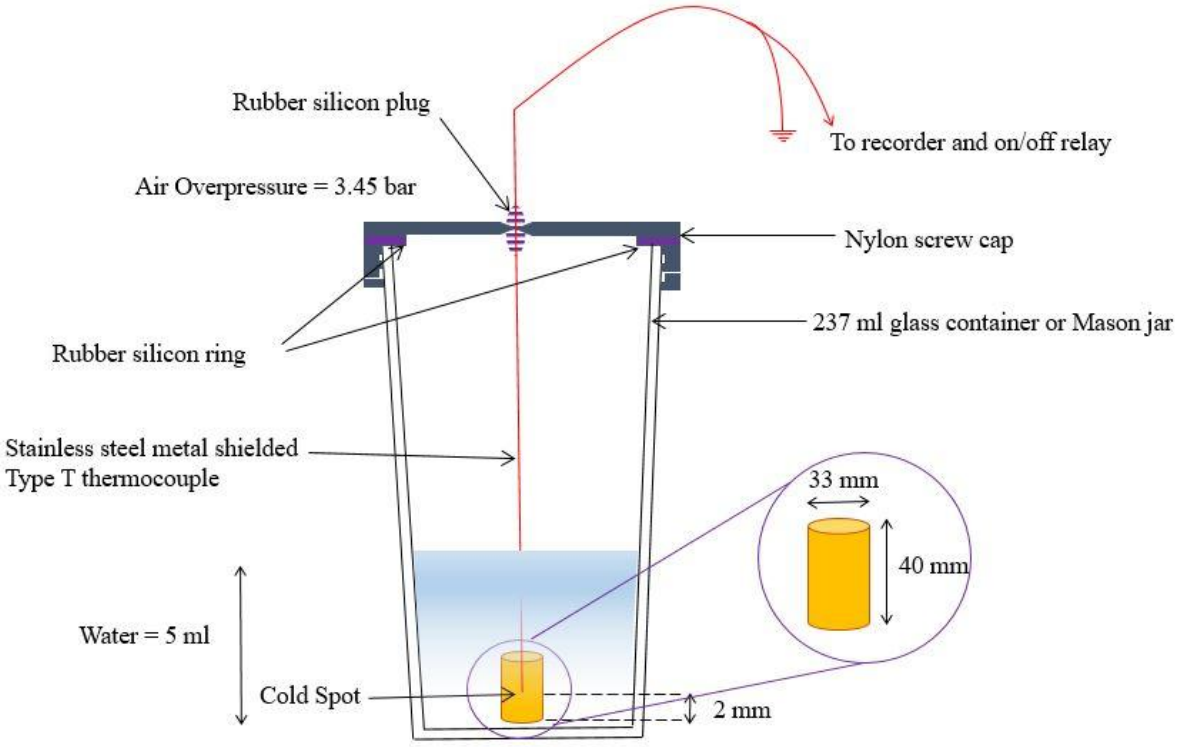



*Fig. 2. 7: Schematic of glass container with cylindrical potato sample and temperature sensor for microwave sterilization. Adapted from Loh & Breene, (1983). This packaging container was made of glass for the maximum transmission of microwaves to reach the product.*

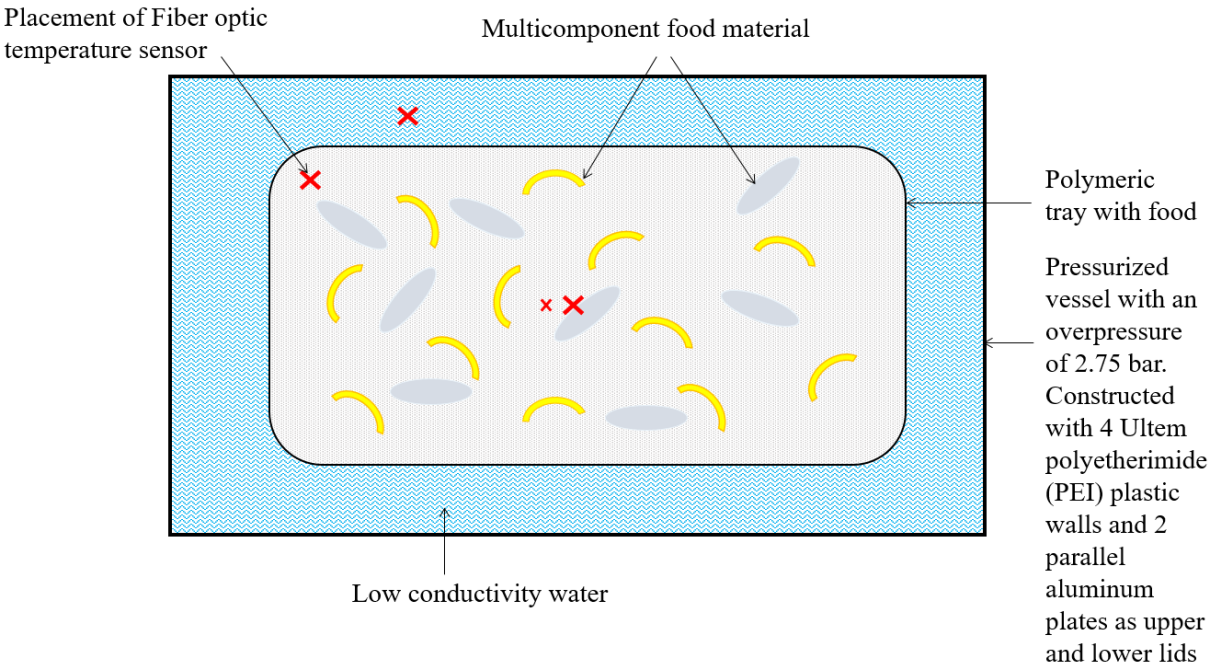



*Fig. 2. 8: Polymeric packaging in a pressurized vessel of water to provide overpressure. Adapted from Wang et al., (2003b). This packaging container utilized polymers due to its lightweight nature and also microwave transparency.*

## 2.5 Structural Integrity of Flexible and Semi-Rigid Packaging

The methods described above focused on the usages of external counter-pressure systems and holders that can stabilize food packages during microwave sterilization. However, even with these techniques, the packaging itself must be strong enough to resist internal forces created during heating. In practice, the safety of food packaging depends not only on external support but also on the intrinsic properties of the packaging material, the quality of the seals, and pressure and deformation development inside the sealed tray. The following section reviews the structural integrity of flexible and semi-rigid packaging, with emphasis on polypropylene trays, seal performance, and rupture mechanisms during heat treatment.

### 2.5.1 Flexible and Semi-Rigid Packaging in the Food Industry

Flexible and semi-rigid packaging has become a dominant choice in the food industry because it combines low weight, low cost, and effective product protection (Al-Ghamdi, 2020). It acts as a barrier to oxygen, moisture, and light, which are the main factors responsible for food degradation and loss of quality. Flexible and semi-rigid packaging formats include pouches, lidding films, and ready-to-eat food trays. These formats can be easily shaped and sealed, which facilitates portioning and improves consumer convenience. Their low bulk density and formability reduce transportation costs and allow efficient use of storage space. To ensure product safety, such packages must be sealed to provide a closed system that prevents contamination and leakage. Heat sealing is the most widely applied method, in which thermoplastic seal layers are heated until molecular chains gain mobility, diffuse across the interface, and entangle. On cooling, this interface solidifies to form a continuous joint with mechanical strength (Ilhan et al., 2021).

Flexible and semi-rigid packagings are also widely used in thermal sterilization processes. In such treatments, sealed packages are exposed to temperatures up to 121 °C to achieve microbial inactivation and long shelf life. The light nature of such packagings allows efficient heat transfer from the heating medium to the food, which ensures process uniformity and safety (Al-Ghamdi, 2020; Bamps et al., 2023). However, sterilization and pasteurization also creates challenging conditions because the headspace inside the package undergoes expansion and increased pressure. To avoid rupture, an external counter pressure is applied in retorts using steam or water. This external pressure balances the internal expansion, thereby preventing excessive deformation of the packaging. As a result, flexible and semi-rigid packaging serves not only as a food container but also as a structural component that must remain stable under the combined effects of heat, internal pressure, and counter pressure during thermal treatments such as sterilization.

### 2.5.2 Polypropylene as a Material in Food Packaging

Polypropylene (PP) is one of the most widely used polymers in the food packaging industry. It is a semicrystalline thermoplastic produced from the polymerization of propylene monomers. PP is valued for its low density, and rigidity. It also provides good barrier properties against moisture and fats, which are essential in food preservation (Bamps et al., 2023). In ready-to-eat food applications, PP is commonly used to manufacture rigid trays. These trays are lightweight yet strong and are capable of withstanding the conditions of pasteurization and sterilization (Al-Ghamdi, 2020). The melting temperature of PP ranges between 145 and 175 °C depending on the homopolymer or copolymer grade (Bamps et al., 2023). This range makes it suitable for high-temperature processing up to 121 °C, which is the standard condition for sterilization.

The mechanical strength of PP is a key factor in its use for food trays. The yield strength of PP films and sheets typically lies between $25 \times 10^6$ and $40 \times 10^6$ N/m² (Al-Ghamdi, 2020). Yield strength marks the stress limit beyond which the material undergoes permanent deformation. Exceeding this threshold during processing can result in the breakage of the PP material. PP trays are also favored because of their versatility in thermoforming. The material can be molded into various shapes and sizes, allowing manufacturers to produce single-portion or multi-compartment meal trays. In addition, the recyclability of PP further supports its selection as a packaging material in line with sustainability goals.

### 2.5.3 Seal Integrity and Weakness of Heat Seals

In flexible and semi-rigid food packaging, the seal is the most critical element because it provides hermetic closure and ensures product safety throughout processing and storage (Ilhan et al., 2021). In ready-to-eat food trays, the lidding film is bonded to the tray flange by a heat-sealing process. The reliability of this joint determines whether the packaging can withstand the stresses imposed during processes such as sterilization. The resulting seal strength from the joint depends on sealing temperature, dwell time, pressure, and the material properties of the sealant layer (Ilhan et al., 2021).

The weakest region of a food tray system is typically the seal interface at the flange. During sterilization, headspace gases expand and water vapor is generated from the food. These effects increase the pressure acting on the lidding film. Although counter pressure is applied in systems like retort during sterilization to balance internal expansion, local stresses remain concentrated

in the seal area. If the stresses exceed the effective seal strength, rupture or leakage can occur (Al-Ghamdi, 2020). Seal failures in food trays can be classified into two main categories. The first category, seal failure modes, includes adhesive failure at the interface between the lidding film and the tray flange, and cohesive failure within the sealant layer itself. The second category is film tear, which occurs when the seal is stronger than the film, and the stress causes rupture of the bulk packaging material. Contaminants such as oil, fat, or food particles trapped in the flange area can further reduce adhesion and promote localized rupture (Bamps et al., 2023).

### 2.5.4 Air Flow, Deformation, and Pressure in Food Trays During Heat Treatment

The evolution of internal pressure during heat treatment in sealed food trays arises from two main sources: expansion of air present in the headspace and evaporation of water vapour from the food. It is generally believed that the dominant contribution to pressure comes from vapour release especially in high heat treatment processes like sterilization, while the expansion of dry air has only a minor effect. This is especially relevant in high-moisture foods such as mashed potato, where continuous evaporation occurs as the temperature increases during longer duration of processing times (Al-Ghamdi, 2020; Dutta et al., 2024a). However, there is still the requirement to study about the role of dry air and water vapour contributions to total headspace pressure in the various stages during a sterilization process. At constant head space volume, the water vapour generation from the food increases the total headspace pressure and buoyancy forces establish convective motion of air within the confined headspace. This circulation gives rise to temperature gradients within the head space and the pressure increase leads to local forces applied on the inner surface of the lidding film (Han et al., 2015). These loads cause deformation of the flexible lid film. The extent of the deformation depend on both the magnitude of headspace pressure and the distribution of the internal air flow. This in turn induces stresses leading to stress concentrations along the flange boundaries. As per our knowledge, this has not been particularly studied so far to provide a clear explanation about the rupture in flexible and semi-rigid food packagings and hence needs investigation using both experimental and numerical modelling tools.

## 2.6 Numerical Modelling and Food Sterilization

Numerical modeling is an important tool for improving the sterilization process by analyzing heat distribution and flow dynamics. Food processing technologies involve multiple physical processes, including heat transfer, mass transfer, and electromagnetism when microwaves are used. Understanding these processes helps improve equipment design, optimize processing conditions, and enhance food quality and consumer acceptance. Modelling and simulation allows to study temperature distribution, heating patterns, electric field behaviour, and variations in heating efficiency. These tools help identify hot and cold spots in microwave sterilization and improve process control.

Mathematical modelling provides a way to represent real-world food processing systems using computer simulations. This approach helps apply theoretical knowledge to practical applications. In sterilization modelling, heat transfer is one of the most important factors to consider. Conventional sterilization systems use autoclaves with metallic walls to heat food products. The food is placed in containers made of metal cans, glass jars, or polymer packaging.

These containers are arranged in metal trays inside the autoclave. Steam and compressed air are introduced into the chamber to regulate temperature and pressure. The sterilization process follows a set schedule to ensure food safety.

During sterilization, the heat transfer is calculated using the general heat transfer equation for both the solids and fluid domain (Chen et al., 2014):

$$\rho C_p \frac{\partial T}{\partial t} + \rho C_p \boldsymbol{u}.\nabla T + \nabla.\boldsymbol{q} = Q \qquad 2.2$$

where the heat flux vector $\boldsymbol{q}$ is defined using Fourier's law:

$$\boldsymbol{q} = -k\nabla T \qquad 2.3$$

where, $Q$ is the heat source term (W.m$^{-3}$), $\rho$ is the density of medium (kg.m$^{-3}$), $C_p$ is the specific heat capacity of medium (J.kg$^{-1}$.K$^{-1}$), k is the thermal conductivity of medium (W.m$^{-1}$.K$^{-1}$), **u** is the velocity field (m.s$^{-1}$) of the surrounding air domain.

The boundary condition involved for the top surface of a product placed in a container involves both evaporation and natural convection phenomena (Nget et al., 2023).

$$k\frac{dT}{dn} = h_c(T_{ext} - T_s) + Q_{ev} \qquad \forall t > 0 \qquad 2.4$$

where, $Q_{ev}$ is the heat loss due to evaporation, $h_c$ is the convective heat-transfer coefficient, $T_{ext}$ is temperature of the fluid away from the surface, $T_s$ is the temperature at the surface of the product.

A simple diagram illustrating heat transfer in conventional thermal sterilization is shown in Fig. 2.9. Steam, compressed air, and water sprays enter the vessel to transfer heat to the container, product and tray, while the mixture of air and steam exits through vents; the compressed air also provides the counter-pressure needed to protect the package.

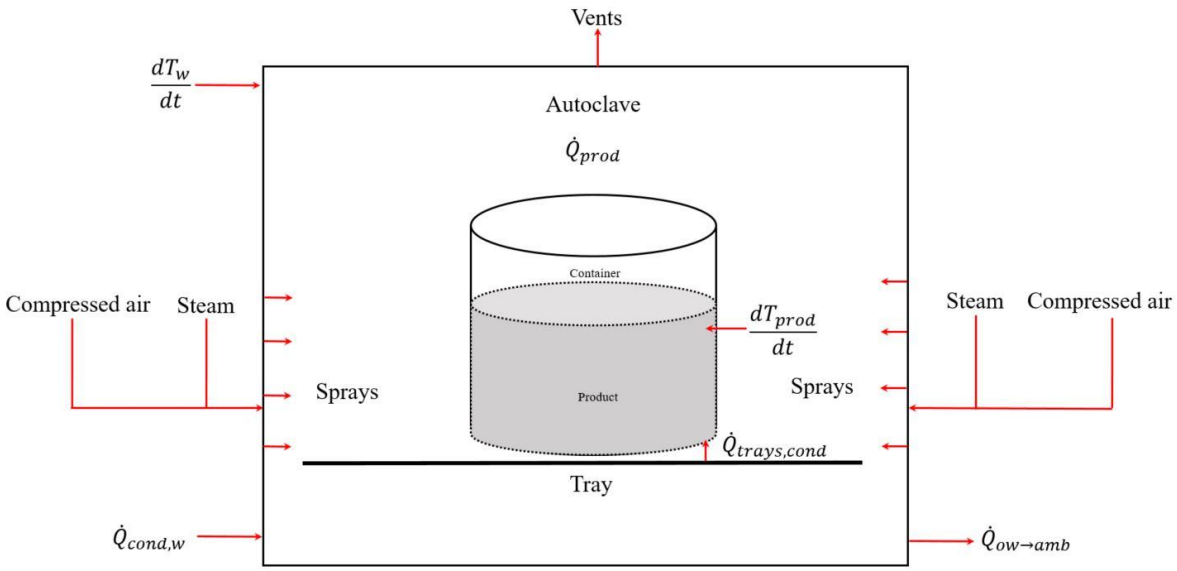


*Fig. 2. 9: A simplistic diagram of heat transfer phenomenon during a classical thermal sterilization process. Heat transfer in an autoclave consisting of the product inside a container on a tray. Compressed air, steam, and water sprays are the inlet boundary conditions and mixture of air and steam through the vents are the outlet boundary conditions for the autoclave. Heat transfer takes place on the walls of the autoclave, trays, container, and product through steam. Compressed air is used to maintain the counter-pressure.*

$\frac{dT_w}{dt} = \frac{1}{C_w}\left[\dot{Q}_{cond,w} - \dot{Q}_{ow\rightarrow amb}\right]$

$\frac{dT_{prod}}{dt} = \frac{1}{m_{prod.}C_{p,prod}}\left(\frac{k_{prod}A_{prod}}{L_{prod}}\left(T_{prod,surf} - T_{prod}\right)\right)$

$C_w = m_w . C_{p,w}$

$\dot{Q}_{prod} = \dot{Q}_{sense,prod} + \dot{Q}_{cond,prod} + \dot{Q}_{sprays,prod}$

$\dot{Q}_{cond,w} = \frac{F_{air}}{R_{vert,wavy}} . A_{cond,w} . (T_{sat} - T_w)$

$\dot{Q}_{trays,cond} = \frac{F_{air}}{R_{trays,cond}} . A_{trays} . (T_{mix} - T_{trays})$

$\dot{Q}_{ow\rightarrow amb} = \frac{1}{R_{conv}} . A_{ow} . (T_w - T_{amb})$

$\frac{dT_w}{dt}$= *Rate of change of autoclave wall temperature*

$\frac{dT_{prod}}{dt}$= *Rate of change of product temperature*

$\frac{1}{R_{conv}}$ = *convective heat transfer coefficient;*

$\frac{1}{R_{trays,cond}}$= *condensate heat transfer coefficient at the tray surface;*

$\frac{1}{R_{vert,wavy}}$= *condensate heat transfer coefficient of wavy laminar film;*

$A_{cond,w}$ = *Total wall surface area;*

$A_{trays}$ = *Total wall surface area of trays;*

$C_{p,prod}$ = *specific heat capacity of products;*

$C_{p,w}$ = *specific heat of stainless steel;*

$C_w$ = *thermal capacitance;*

$F_{air}$ = *describes reduction in condensation heat transfer rate due to presence of air within the mixture;*

$k_{prod}$ = *thermal conductivity of product;*

$L_{prod}$ = *distance between product surface and product centre;*

$m_{prod}$ = *total mass of product;*

$m_w$ = *mass of autoclave walls;*

$\dot{Q}_{cond,prod}$ = *rate of condensation heat transfer;*

$\dot{Q}_{cond,w}$ = *rate of heat transfer to autoclave walls via condensation;*

$\dot{Q}_{ow\rightarrow amb}$ = *rate of heat losses to ambient from outer walls via natural convection;*

$\dot{Q}_{sense,prod}$ = *rate of sensible heat transfer which is equivalent to power;*

$\dot{Q}_{sprays,prod}$ = *rate of heat transfer from the sprays to the product;*

$\dot{Q}_{trays,cond}$ = *rate of heat transfer from the tray to the product;*

$T_{mix}$ = *temperature of steam air mixture;*

$T_{prod}$ = *average product centre temperature;*

$T_{prod,surf}$ = *average product surface temperature;*

$T_{sat}$ = *saturated steam temperature;*

$T_{trays}$ =*average temperature of trays;*

$T_w$ = *autoclave wall temperature;*

**Description of the terms used in Fig. 2.9.*

### 2.6.1 Numerical modelling approaches and Computational Fluid Dynamics (CFD)

Computational Fluid Dynamics (CFD) is one of the most widely used numerical modeling tools for analyzing and optimizing traditional food processing technologies (W. Lau, 2015). This method solves partial differential equations related to mass, momentum, and energy conservation, including continuity, Navier–Stokes, and Fourier equations. Modelling becomes more complex when multiphysics interactions, such as microwave heating, are involved. In these cases, additional equations, such as Maxwell's equations, must be solved to account for electromagnetic field interactions. Heat transfer in food can occur through convection, conduction, or a combination of both. Due to its mathematical simplicity, most numerical models assume that heat transfer occurs primarily through conduction. However, convection cannot be ignored, as it significantly affects heat distribution. Certain food products, such as canned tuna, purees, thick syrups, and concentrates, are typically modeled as conduction-heated systems (Abdul Ghani et al., 1999). To improve model accuracy, both conduction and convection heat transfer must be considered for these food types.

In conventional thermal processing, the slowest heating zone, known as the cold point, is usually located at the geometric center of the food container. The rate at which this cold point heats up depends on the package's shape, size, and the food's thermophysical properties. Numerical models developed for microwave heating helps to study how food composition and dielectric properties influence heat distribution (Auksornsri, Bornhorst, et al., 2018; Auksornsri, Tang, et al., 2018). Some of these models focus on specific food systems, such as mashed potatoes (Bornhorst, Tang, et al., 2017), green peas (Bornhorst, Liu, et al., 2017), and whey gel systems (M. H. Lau et al., 2003). Other studies have examined how microwave energy interacts with electric fields (Jain et al., 2018) and identified hot and cold spots in food during heating (Bhuwan Pandit et al., 2007; Pandit et al., 2006; Tolve et al., 2016; W. Zhang et al., 2014).

### 2.6.2 Computational Fluid Dynamics–Fluid–Structure Interaction (CFD–FSI) and Structural Mechanics for Packaging Deformation

While CFD provides valuable insights into the fluid domain, it does not capture how packaging materials deform or fail under the influence of internal pressure and airflow. To study this behavior, CFD must be coupled with structural mechanics for achieving fluid–structure interaction (FSI). The fluid inside a food packaging applies pressure and shear stresses on the structure, and the structure deforms. This deformation alters the geometry of the fluid domain and modifies the flow field. The process is intrinsically coupled and requires simultaneous or iteratively partitioned solution of the domains (Dowell & Hall, 2001). In practice, the choice of coupling strategy also depends on the numerical method employed, such as the Finite Element Method (FEM), the Finite Volume Method (FVM), or other multiphysics approaches. In modern formulations, this coupling is enforced at the interface through kinematic and dynamic continuity and can be realized with monolithic or partitioned solvers, including isogeometric and ALE-based strategies (Bazilevs et al., 2012).

The momentum conservation equation in CFD, expressed in the form of the Navier–Stokes equation, is given by (Allué Hoyos, 2014):

$$\frac{d(\rho \boldsymbol{u})}{dt} + \rho(\boldsymbol{u}.\nabla)\boldsymbol{u} = \rho \boldsymbol{g} - \nabla \mathrm{P} + \mu \nabla^2 \boldsymbol{u} \quad (2.5)$$

where $\rho$ is density (kg/m$^3$), **u** is the velocity vector describing the local fluid motion within the domain (m/s), t is time (s), P is pressure (Pa), **g** is gravitational acceleration vector (m/s$^2$), μ is dynamic viscosity of fluid (Pa.s).

The first term on the left-hand side represents the temporal change of the fluid velocity, capturing how the velocity field evolves with respect to air flow or expands inside the packaging material. The second term on the left-hand side accounts for convective acceleration, describing the velocity changes as air circulates within the headspace. On the right-hand side, the first term represents the contribution of body forces such as gravity. The second term represents the pressure. The third term accounts for viscous diffusion of momentum, representing internal friction within the fluid arising from velocity gradients.

The continuity equation is also solved in general to ensure mass conservation (El Ouafa et al., 2024):

$$\frac{\partial \rho}{\partial t} + \nabla.(\rho \mathbf{u}) = 0 \quad (2.6)$$

#### 2.6.2.1 Structural Mechanics and Fluid-Structure Interactions

In food packaging, the structural response is modelled by applying the equations of solid mechanics to the tray–film system. The conservation of momentum for a deformable solid is expressed as (Oden & Edition, 2008):

$$\rho \frac{\partial^2 \boldsymbol{d_s}}{\partial t^2} = \nabla.S + \boldsymbol{F}_v \quad (2.7)$$

where $\rho$ is the density of the solid (kg/m$^3$), $\boldsymbol{d_s}$ is the displacement vector (m), $S$ the second Piola–Kirchhoff stress tensor, and $\boldsymbol{F}_v$ is the body force per unit volume (N/m$^3$).

The total stress tensor is written as the sum of elastic and inelastic contributions (Lubarda & Krajcinovic, 1995) :

$$S = S_{inel} + S_{el} \quad (2.8)$$

where, $S_{el}$ is the elastic stress tensor, representing the reversible, recoverable stresses due to elastic deformation and $S_{inel}$ is the inelastic stress tensor, representing irreversible stresses from inelastic effects like plastic deformation, viscous effects, or thermal stress.

The elastic strain tensor represents the change in shape and size due to elastic deformation. It is described using the Green–Lagrange formulation (Ciancio et al., 2008):

$$\boldsymbol{\epsilon_{el}} = \frac{1}{2}(\mathbf{F}_{el}^T \mathbf{F}_{el} - \mathbf{I}) \quad (2.9)$$

where, $\mathbf{F}_{el}$ is the elastic part of the deformation gradient, isolating the elastic (reversible) part of the total deformation, and **I** is the identity tensor. The term $F_{el}^T F_{el}$ describes material stretches and shape changes in a purely elastic way.

The total deformation gradient was decomposed into elastic and inelastic parts as (Lubarda & Krajcinovic, 1995):

$$\mathbf{F}_{el} = \mathbf{F}\mathbf{F}_{inel}^{-1} \tag{2.10}$$

where, **F** is the total deformation gradient tensor which describes the deformation of material element relative to its original reference configuration. $F_{inel}$ is the inelastic deformation gradient, describing the irreversible part of deformation due to plasticity, viscosity, or other permanent effects.

The elastic stress was evaluated as (Lubarda & Krajcinovic, 1995):

$$S_{el} = J_i \boldsymbol{F}_{inel}^{-1}(\boldsymbol{C}: \epsilon_{el}) F_{inel}^{-T} \tag{2.11}$$

where, $J_i$ is the determinant of the inelastic deformation gradient $\boldsymbol{F}_{inel}$, representing volume change due to inelastic deformation. $F_{inel}^{-1}$ and $F_{inel}^{-T}$ are terms that adjust for the inelastic deformation when calculating the elastic stress, $\boldsymbol{C}$ is the stiffness tensor. ( ":" is the double dot product between tensors).

The inelastic stress component, which represents the contribution of irreversible or path-dependent effects on the total stress in the material is expressed as (Thorborg et al., 2012):

$$S_{inel} = S_0 + S_{ext} + S_q \tag{2.12}$$

where, $S_0$ denotes initial stresses present in the film prior to loading, $S_{ext}$is external stress, accounts for external stresses such as those induced by internal pressure, $S_q$ is stress from inelastic effects like viscous flow or temperature changes.

The total strain is described by the Green–Lagrange strain tensor (Reddy, 2015):

$$\in = \frac{1}{2}[(\nabla \boldsymbol{d_2})^T + \nabla \boldsymbol{d_s} + (\nabla \boldsymbol{d_s})^T \nabla \boldsymbol{d_s}] \tag{2.13}$$

where, $\in$ is the Green-Lagrange strain tensor, which provides a measure of the total strain considering both linear (small) and non-linear (large) deformations, and $\boldsymbol{d_s}$ is the displacement vector.

The stiffness tensor ($\boldsymbol{C}$) which characterizes the material's elastic properties, determines the stress relation to strain in the elastic range. It is related to the material constants as (L. Zhang et al., 2014):

$$\boldsymbol{C} = \boldsymbol{C}(E, v) \tag{2.14}$$

where, E is the Young's modulus of PP, and $v$ is the Poisson's ratio of PP.

A simplified mathematical relationship can be expressed as (Quickfem, 2023):

$$\boldsymbol{C} = \frac{E}{1 - v^2} \begin{bmatrix} 1 & v & 0 \\ v & 1 & 0 \\ 0 & 0 & \dfrac{1 - v}{2} \end{bmatrix} \tag{2.15}$$

More details about the mathematical relationship of $\boldsymbol{C}$ with E and $\nu$ can be found in L. Zhang et al., (2014) and Basar et al., (2001).

Structural mechanics provides the framework for analyzing solid materials deformation under load. For PP trays and films, material parameters such as Young's modulus, Poisson's ratio, and yield strength govern the mechanical response. One approach, described by Dowell and Hall (2001), solves the solid problem to obtain displacements and stresses in the packaging, which are then used to update the fluid domain geometry in a two-way FSI loop. Solving the solid problem gives displacements and stresses in the packaging during thermal and non-thermal treatments, which, in turn, update the fluid domain shape in a two-way FSI loop (Dowell & Hall, 2001). However, this approach corresponds to a specific case described in that study and cannot be directly generalized. In COMSOL Multiphysics®, for example, the coupling between fluid flow and structural deformation is handled through predefined FSI interfaces that simultaneously solve the governing equations of both domains to ensure consistent force and displacement transfer. For food packaging trays, an integrated FSI approach is particularly relevant, since the deformation occurring during heat treatment alters the headspace volume and consequently affects air flow (Fragassa et al., 2019).

Similar methodologies are already well-established across other engineering fields such as nuclear engineering, aerodynamics engineering, and biomedical engineering fields, which have motivated their usages here in this study. In aerodynamics, coupled FSI has been used to analyze flexible canopies such as parafoils, where airflow drives large membrane deformation and the aerodynamic loads depend on the evolving shape (H. Zhu et al., 2021). In nuclear engineering, thermomechanical simulations of pressurized thermal shock events resolve transient fluid loads and structural stresses in reactor pressure vessels (Annor-Nyarko et al., 2022). In medical biomechanics, FSI has been employed to study the role of airflow for deforming compliant airways and induces spatially heterogeneous stress in soft tissues, providing a direct precedent for linking internal flow to stress localization in thin flexible boundaries (P. Li et al., 2023; X. Sun et al., 2007).

Hence, for this study, FSI provides the necessary link between internal air flow and the mechanical response of PP food trays, enabling analysis of stress development in the sealing region that is not accessible through experiments alone. To interpret whether the simulated stresses are critical for failure, a material-based criterion is required. The next section introduces the von Mises stress framework as the basis for assessing potential rupture under multiaxial loading of the lidding film–seal system.

### 2.6.3 Failure Theory: von Mises Criterion

The prediction of failure in polymer packaging requires a framework that can represent complex stress states generated during heat treatment. In food trays, stresses arise from the combined effects of internal pressure, fluid flow, and deformation of the lidding film. Because these stresses act in multiple directions, a scalar measure is needed to represent the combined loading state. The von Mises criterion, also referred to as the distortion energy theory, provides such a measure. It evaluates the energy associated with shape distortion in a material and converts a three-dimensional stress state into an equivalent uniaxial value, the von Mises equivalent stress.

At any point within a polymer film or tray wall subjected to internal loading, the internal state of stress can be described by isolating an infinitesimally small cubic element of the material

and examining the stresses acting on each of its faces. Each face of this element experiences one normal stress (σ), acting perpendicular to the surface, and two orthogonal shear stresses (τ), acting tangentially to the surface (Semeliss et al., 1990).

To quantitatively describe the state of stress within the packaging material, the nine stress components acting on the infinitesimal element can be conveniently represented in the form of a second-order stress tensor. This tensor (**T**) expresses the relationship between normal and shear stresses acting on mutually perpendicular planes and is written as (Semeliss et al., 1990):

$$\boldsymbol{T} = \begin{bmatrix} \sigma_1 & \tau_{1,2} & \tau_{1,3} \\ \tau_{2,1} & \sigma_2 & \tau_{2,3} \\ \tau_{3,1} & \tau_{2,3} & \sigma_3 \end{bmatrix} \quad 2.16$$

For a general stress state, the von Mises equivalent stress ($\sigma_v$) is expressed as (Semeliss et al., 1990):

$$\sigma_v = \sqrt{\frac{1}{2}[(\sigma_1 - \sigma_2)^2 + (\sigma_2 - \sigma_3)^2 + (\sigma_3 - \sigma_1)^2]} \quad 2.17$$

where, $\sigma_1, \sigma_2, and\ \sigma_3$ are the principal stresses, defined as the eigenvalues of the stress tensor (**T**) obtained by solving the characteristic equation (Semeliss et al., 1990):

$$\left|\sigma_{ij} - \sigma\delta_{ij}\right| = 0 \quad 2.18$$

where, $\sigma_{ij}$ represents the components of the stress tensor, $\sigma$ is the principal stress (scalar), $\delta_{ij}$ is the Kronecker delta. They represent the normal stresses acting on three mutually perpendicular planes where the shear stresses are zero. Fig. 2.10 presents a schematic representation of these stress components, illustrating the combined action of normal and shear stresses that define the general 3D stress state in the packaging material.

According to the theory, yielding or rupture is expected when (Semeliss et al., 1990):

$$\sigma_v \geq \sigma_y \quad 2.19$$

where, $\sigma_y$ is the yield strength of the material.

The von Mises stress does not provide a direct rupture prediction for PP films. Instead, it is used in this study to identify zones of stress concentrations on the film. This approach is commonly applied in polymer mechanics to assess the onset of yielding and local deformation in thermoplastic films. Previous studies such as by Garrell et al., (2003) and Sheng, (2013) have already used von Mises stress distributions to locate critical regions where rupture or plastic failure initiates under combined thermal and mechanical loading. Areas with higher von Mises stress indicate where the material is most likely to weaken and where rupture is more prone to initiate during thermal and non-thermal treatments.

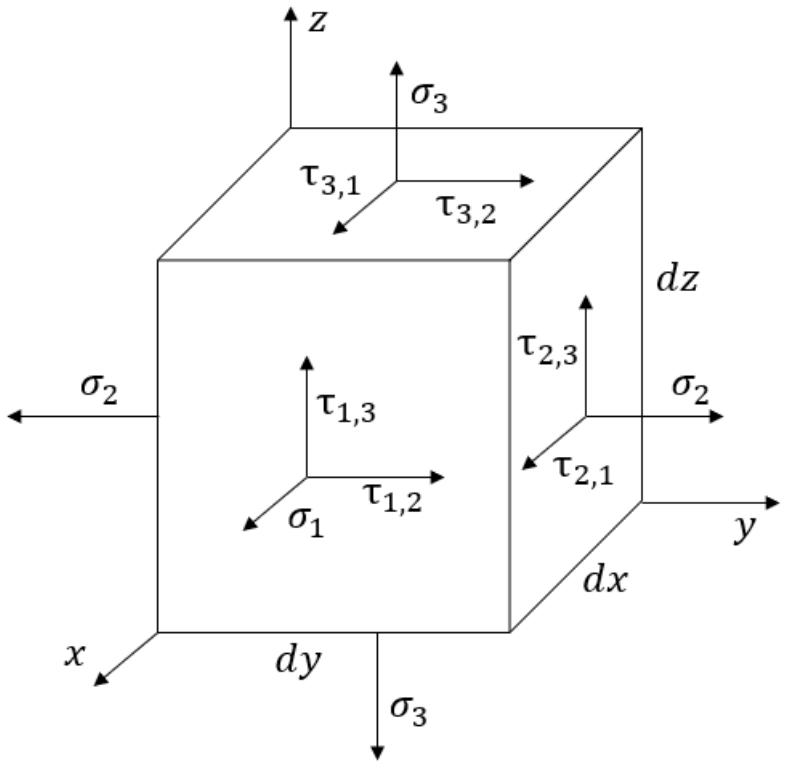



*Fig. 2. 10: Schematic representation of the stress components acting on an infinitesimal element of a polymer film.*

### 2.6.4 Commercial software for numerical modelling

Several commercial software programs are available for modeling heat and mass transfer, electromagnetics, and multiphysics phenomena. Some widely used software includes FLOW 3-D (Flow Science, USA), PHOENICS (CHAM, UK), OpenFOAM® (OpenCFD Ltd., UK), CST Studio Suite (Dassault Systèmes, France), QuickWave™ (QWED, Poland), ANSYS® (ANSYS, USA), and COMSOL® (COMSOL® Multiphysics, Sweden). Each software has unique advantages. COMSOL® provides extensive access to physics-based modeling, while CST Studio Suite is based on the resolution of electromagnetic problems. ANSYS® supports generic physics models and offers time-efficient simulations, whereas QuickWave™ has demonstrated superior performance in electromagnetic modeling compared to COMSOL® and ANSYS® (Komarov & Yakovlev, 2001; Segui, 2013). Despite these differences, all software programs rely on similar methods to solve heat transfer and Maxwell's equations. The primary distinction lies in their numerical discretization techniques. COMSOL® employs the Finite Element Method (FEM), QuickWave™ uses the Finite Difference Time Domain (FDTD) method, and FLOW 3-D, PHOENICS, and ANSYS® apply the Finite Volume Method (FVM) for CFD modeling.

Other specialized software focuses on electromagnetic simulations using alternative numerical techniques. These methods include the Transmission Line Method (TLM), Geometric Theory of Diffraction, Method of Moments (MOM), and Boundary Element Method (BEM) (Jain, 2017). Among these approaches, FEM and FDTD are the two most commonly applied numerical methods for microwave heating simulations (Celuch et al., 2020). Table 2.7

summarizes various studies for modelling of multiphysical phenomena in process engineering. A schematic representation of the numerical simulation steps is illustrated in Fig. 2.11.

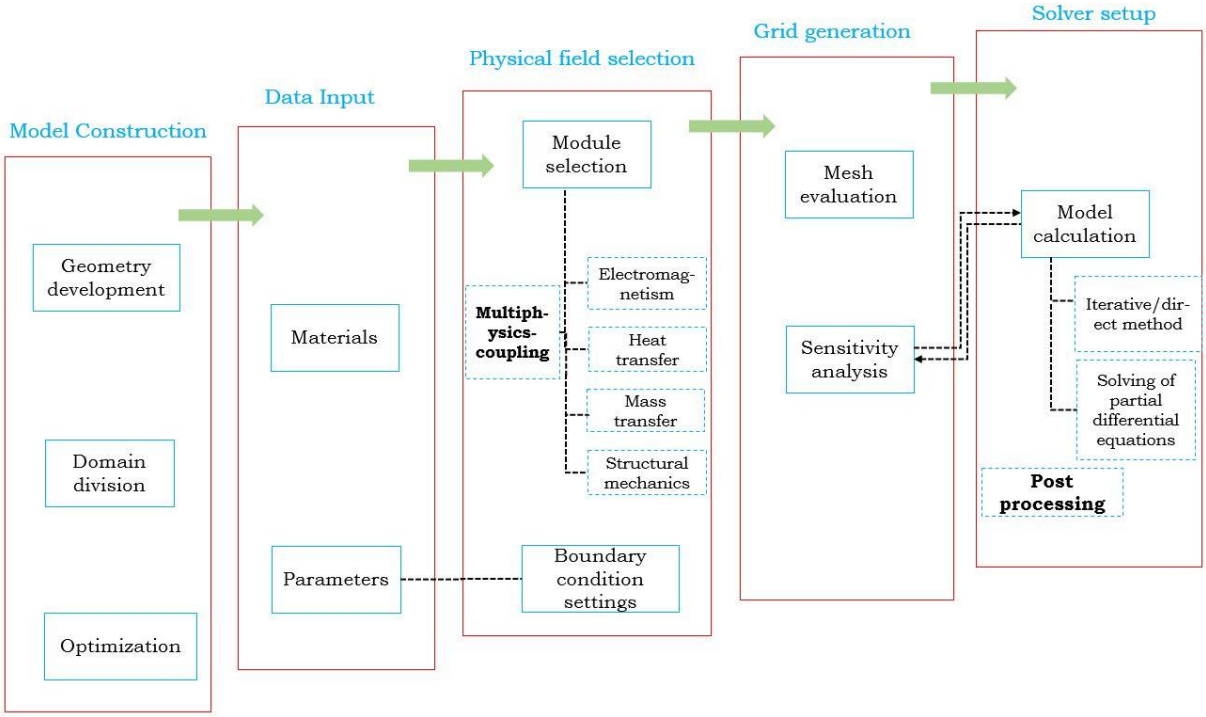



*Fig. 2. 11: Schematic of a numerical simulation process. Adapted from H. Yang et al., (2023).*

*Table 2. 7: Different types of software used for modelling of multiphysical phenomena during microwave heating.*

| References | Objective | Average final temperature in the model | Software used for modelling | Geometry /Physical phenomenon considered | Frequency used | Numerical Methods used |
|---|---|---|---|---|---|---|
| Geedipalli et al., 2007 | To model the microwave heating of food while rotating.<br><br>To solve for electric field intensity (E).<br><br>To calculate the power (P) absorbed by food from the microwaves, which is used as a source term in heat transfer equation.<br><br>To create geometry and mesh for electromagnetic computations.<br><br>To solve the transient diffusion equation for heat transfer.<br><br>To create the geometry and mesh for the heat transfer simulations. | 75°C | ANSYS v.8 (Canonsburg, PA, USA)<br>FIDAP (Fluent, Inc., Lebanon, NH)<br>GAMBIT (Fluent, Inc., Lebanon, NH) | 3D/Electromagnetics, Heat transfer | 2450 MHz | FEM<br>FEM<br>FVM |
| Yang et al., 2022 | To study experimentally and numerically about continuous microwave heating of highly viscous surimi materials.<br><br>To construct the geometry.<br><br>To select the physical field.<br><br>To define boundary conditions.<br><br>To generate mesh. | 55°C | COMSOL® Multiphysics (V. 5.6, COMSOL®, Stockholm, Sweden) | 3D/Electromagnetics, Heat transfer, Momentum transfer, Fluid dynamics | 2450 MHz | FEM |
| Su et al., 2021 | To develop a comprehensive physically based theoretical model of the intermittent microwave (IMW) thermal process while | 86.17 °C and 85.34°C | COMSOL® Multiphysics (V. 5.6, COMSOL®, | 3D/Electromagnetics, Heat transfer, | 2450 MHz | FEM |

| | | | | | | |
|---|---|---|---|---|---|---|
| | considering electromagnetic energy, multiphase transport, phase change, large deformation, and glass transition.<br><br>To solve multiphase transport and deformation in the porous dielectric materials during the thermal process. | | Stockholm, Sweden) + MUMPS direct solver | Momentum transfer, Mass transfer | | |
| Resurreccion et al., 2013 | To create a computer simulation model for the MATS system while considering coupled solution of electromagnetic field and heat transfer phenomena in food packages moving in multiple microwave cavities.<br><br>To create the MATS-computer simulation model by eliminating node transformation through the synchronization of electromagnetic nodes with temperature nodes for heat transfer. | 123°C | QuickWave™ v7.5 | 3D/Electromagnetics, Heat transfer | 915 MHz | FDTD |
| Zhang et al., 2001 | To develop numerical model by coupling electromagnetics, heat transfer, and first order, bacterial-destruction and marker-formation kinetics to predict temperatures and thermal-time distributions during microwave sterilization.<br><br>To solve for electromagnetic fields.<br><br>To solve for temperature distributions. | 121°C | EMAS (Ansoft Corporation, Pittsburgh, PA) | 3D/Electromagnetics, Heat transfer, Microbial kinetics | 2450 MHz | FEM |
| | | | NASTRAN (MacNeal-Schwendler Corporation, Los Angeles, CA) | | | FEM |
| Pitchai, 2011 | To develop a holistic coupled electromagnetic and heat transfer model for domestic microwave heating.<br><br>To develop a comprehensive coupled electromagnetic (EM) and heat transfer model. | 45-55°C | QuickWave™ v7.5 (QWED Sp.z o.o., Warsaw, Poland) | 3D/Electromagnetics, Heat transfer | 2450 MHz | FDTD |
| Chen et al., 2008 | To simulate microwave heating of moving food packages in continuous industrial microwave sterilization. | 121°C | Quick-Wave-3D (QW3D, Warsaw, Poland) | 3D/Electromagnetics, Heat transfer | 915 MHz | FDTD (Conformal algorithm) |

| | | | | | | |
|---|---|---|---|---|---|---|
| | To simulate microwave heating of moving food packages in continuous industrial microwave sterilization. | | | | | |
| Teleken et al., 2023 | To develop a mathematical model for tomato pulp in a continuous-flow microwave heating system undergoing thermal treatment.<br><br>To solve the mathematical model using the RF Module with the interface of the Frequency Domain. | 120°C | COMSOL® Multiphysics® software version 5.5 | 3D/Electromagnetics, Heat transfer, Momentum transfer, Microbial kinetics | 915 MHz | FEM |
| Lespinard et al., 2019 | To develop a comprehensive computer simulation model for pre-packaged milk during microwave heating.<br><br>To solve the numerical model with simultaneous heat and momentum transfer including electromagnetic field distribution. | 100°C | COMSOL® Multiphysics software version 4.0 | 2D/Electromagnetics, Heat transfer, Momentum transfer | 2450 MHz | FEM |
| Zhu et al., 2007 | To study the heat transfer in liquids during microwave heating in circular duct using numerical method.<br><br>To model heating patterns of a liquid product considering electromagnetics. | 120°C | - | 3D/Electromagnetics, Heat transfer, Momentum transfer | 915 MHz | FDTD |
| Curet et al., 2008 | To study the microwave heating of Tylose™.<br><br>To develop the numerical model and solve heat transfer under microwave heating | 30°C | COMSOL® Multiphysics software version 3.3 | 2D/Electromagnetics, Heat transfer | 2450 MHz | FEM |
| De Albuquerque et al., 2021 | To study the effect of heating rates during microbial inactivation by microwave heating.<br><br>To solve 3D model of microbial inactivation coupled with heat transfer during microwave heating. | 63°C | COMSOL® Multiphysics software version 5.3a | 3D/Electromagnetics, Heat transfer, Microbial Kinetics | 2450 MHz | FEM |

| | | | | | | |
|---|---|---|---|---|---|---|
| Luan et al., 2016 | To analyze microwave propagation mode and electric field distribution inside the MATS system through numerical simulation.<br><br>To develop the computer simulation model. | 121°C | QuickWave version 7.5 (QW3D, Warsaw, Poland) | 3D/Electromagnetics, Heat transfer | 915 MHz | FDTD |
| Cherbański & Rudniak, 2013 | To develop a 3D comprehensive numerical model of microwave induced natural convection in water in a resonant microwave field.<br><br>To develop coupled heat transfer and fluid dynamics model. | 37°C | Ansys Fluent | 3D/Electromagnetics, Heat transfer, Fluid dynamics | 2450 MHz | FVM (Finite Volume Method) |
| Ye et al., 2017 | To develop a new multi-material turntable structure to improve the heating uniformity of microwave processing materials.<br><br>To analyze the measured temperature data. | 35-50°C | FISO Command WorkStation (v1.10.9; FISO Technologies, Quebec, QC, Canada) | 3D/Electromagnetics, Heat transfer | 2450 MHz | - |
| Zhang et al., 2016 | To analyze quality changes in the product after sterilization with microwaves.<br><br>To model the kinetics of moisture loss, lipid oxidation, and shelf-life prediction. | 124°C | Specific to the MATS system | Electromagnetics, Heat transfer, Lipid oxidation kinetics, mass transfer, color change kinetics | 915 MHz | - |
| Nget et al., 2023 | To develop a digital-twin for microwave heating of Cambodian pâté<br><br>To develop a model for predicting moisture loss during microwave heating | 80°C | COMSOL® Multiphysics (V. 5.6, COMSOL, Stockholm, Sweden) | 3D/Electromagnetics, Heat transfer, Mass transfer | 915 MHz | FEM |

## 2.7 Knowledge Gap and Final Remarks

Microwave sterilization has advanced significantly with improvements in numerical modelling, packaging materials, and techniques such as Microwave-Assisted Thermal Sterilization (MATS). Despite these advancements, several challenges must be addressed to make microwave sterilization more efficient and widely adopted in the food industry. One major issue is the non-uniform heating of food, which creates hot and cold spots that can affect microbial inactivation and food quality. The complexity of different food components makes it difficult to achieve uniform heating throughout the product. Although numerical modelling techniques like CFD help predict heat and mass transfer, real-time validation of these models remains a challenge. A second and often overlooked limitation lies in the absence of coupled thermo-mechanical analysis of packaging systems, where internal pressurization interacts with the structural response of films and seals during heating. Most previous studies have not investigated the mechanical deformation, stress concentration, and rupture behaviour that occur under combined thermal and pressure loading. Similarly, few studies have monitored pressure and mechanical loads simultaneously, leaving the evolution of internal stresses largely unquantified. This absence of coupled thermal–mechanical data limits the validation of fluid–structure interaction (FSI) models for food packaging. Another challenge involves microwave packaging and pressure control. While MATS systems maintain external counter-pressure using water to protect flexible packages, the criteria for pressure balancing remain empirical rather than physics-based. The need for standardized methodologies that link internal pressure evolution and structural integrity is particularly critical for semi-rigid food packagings. This study is important as it investigates pressure buildup that can cause deformation, or rupture of food packaging.

While multilayer polymer films, metal oxide coatings, and self-venting packaging technologies have improved, their durability, cost, and large-scale application need further study. The use of liquid counterpressure systems and venting mechanisms also lacks standardized design criteria, leading to variations in sterilization performance across different food products. In numerical modelling, methods like FEM, FVM, and FDTD are commonly used. Current microwave sterilization models do not fully account for the multi-physics interactions that occur during heating. The literature remains limited in modelling the transition from rigid to deformable containers, where the headspace acts as a compressible fluid domain interacting with thin, flexible films. Capturing such thermo-fluid–structural coupling is essential to predict deformation and to design packages that maintain integrity under sterilization conditions.

Scalability is another challenge in microwave sterilization technology. Cost-benefit analyses comparing microwave sterilization with conventional methods such as retort processing are needed to assess long-term operational costs, energy efficiency, and food quality retention. Regulatory approval and standardized guidelines for microwave sterilization are still lacking, making it difficult for food manufacturers to integrate these systems into existing production lines.

Addressing these challenges requires interdisciplinary collaboration that bridges food engineering, materials science, computational modelling, and structural mechanics. A coupled

understanding of the interactions among heat transfer, internal pressurization, and material deformation remains limited in current literature. Previous research has mainly examined thermal performance or microbial inactivation, without adequately exploring the mechanical response of packaging under combined thermal and pressure loads. Developing such an understanding is essential to describe the physical environment inside sealed containers during sterilization and to identify the factors governing their structural stability.

The present thesis aims to fill these knowledge gaps by studying the contribution of internal pressure during sterilization and its relationship with the applied thermal treatment. This coupled analysis provides the basis to understand the structural mechanics of food packaging under realistic processing conditions. The study serves as a preliminary framework for designing mechanical constraint systems capable of maintaining packaging integrity during microwave heating, with the objective of minimizing both energy and water consumption. Establishing this physical foundation will support the development of future sterilization processes that are both sustainable and compatible with next-generation packaging technologies, enabling the optimization of packaging design, improvement of process reliability, and advancement of microwave sterilization.

# Chapter 3

# Numerical and Experimental Study of Temperature and Headspace Pressure During Conventional Thermal Sterilization in Rigid Food Packaging Using CFD

## 3.1 Introduction

In thermal processing of packaged foods, the structural integrity of the container is essential for ensuring product safety and quality. Any deformation or failure of the packaging during sterilization may compromise the seal, allow contamination, and result in product rejection. While rigid metal cans are generally considered stable under thermal and pressure stress, the internal conditions during processing, particularly the build-up of pressure in the headspace, may still pose challenges for certain food formulations and process parameters. Excessive internal pressure may originate from vapor generation, thermal expansion of entrapped gases, or food movement, and can exert mechanical forces on the container and sealing zones (Szpicer et al., 2025).

During conventional sterilization, food products are subjected to elevated temperatures (> 100°C) in a pressurized steam environment to achieve commercial sterility. The interplay between heat transfer, vapour formation, and pressure dynamics inside the sealed system is complex. The rate and uniformity of temperature increase are influenced by the thermal properties of the food, container geometry, and the convective environment in the retort (Al-Sharify et al., 2025). In parallel, moisture within the food evaporates as temperature rises, generating water vapour that accumulates in the headspace and increases the internal pressure. If the pressure exceeds the external steam pressure, the packaging may undergo stress, potentially affecting long-term seal integrity (Ilhan et al., 2021).

While previous studies have focused extensively on temperature distribution in thermal processing, limited research has addressed the simultaneous evolution of internal pressure, particularly in relation the headspace and its physical–thermal behaviour. In this context, "headspace behaviour" refers to the combined phenomena occurring in the gas region above the food, including thermal expansion of entrapped air, evaporation and condensation of water vapour, and changes in effective headspace volume during heating. Most existing models assumed simplified boundary conditions, do not incorporate vapour–liquid phase interactions, and rarely validate pressure predictions experimentally. For example Ghai et al., (2011), Awuah (2003), Patel et al. (1991), and J. Zhang et al. (1992) compared model results with experimental pressure data. These studies are among the few that investigated experimental validation of headspace pressure, a type of work that remains very rare in the literature. Comprehensive studies that link pressure data with numerical models under thermal sterilization conditions are still missing. Moreover, the behaviour of water vapor as a dynamic contributor to internal pressure and also the influence of parameters such as heat transfer coefficient on internal temperatures has not been studied in detail under realistic food processing conditions.

The objective of this chapter is to investigate the evolution of temperature and pressure during conventional thermal sterilization in rigid metal containers filled with mashed potato as a model food. The study aims to evaluate the influence of heat transfer coefficients on temperature prediction accuracy, assess the role of CFD by comparing simulations with and without fluid flow, and separate the contributions of dry air and water vapour to total headspace pressure.

This work aims to improve the understanding of internal pressure development during sterilization and to provide useful insights that can be extended to studies on flexible or semi-rigid packaging systems, where deformation caused by pressure plays a more significant role.

## 3.2 Materials and Methods

### 3.2.1 Experimental study

#### 3.2.1.1 Model Food Preparation

A model food sample is essential for replicating the properties of a real food product for validation of experiments. The specific requirements for the study was a model food that has a solid characteristic with minimum phases as possible. Hence, mashed potato was chosen as the model food product. Dry potato flakes (Mousline®, Picarde, France) with a composition of 99% potato, turmeric, antioxidant, rosemary extracts, emulsifier: mono- and diglycerides of fatty acids (vegetable origin) were bought from the supermarkets. A mixture of water and mashed potato flakes were used for the preparation of the mashed potato sample. A series of trials were performed to find a good ratio of water to potato flakes, as a homogeneous solid texture was desired. The dry flakes-water mixture was mixed in a blender for 2 minutes (Fig. 3.1). The texture of the different ratios were analyzed considering their homogeneous solid texture. It was analyzed visually and by touch. The parameters were not to have small powdered potato flakes and not to have a liquid texture. Hence, for the model food, the final desired ratio to be used in further studies during this work was found to be in the ratio of 3:1 for water to dry potato flakes (mass fractions).




*Fig. 3. 1: Formulation of Mashed Potato*

#### 3.2.1.2 Properties of mashed potato

*3.2.1.2.1 Moisture content of mashed potato before and after sterilization*

Moisture content analysis was performed for the final mashed potato sample. The protocol laid by AOAC (2000) was used for the moisture content analysis. The mashed potato sample was placed in an air convection oven for 2h 30 min at 130°C. Moisture content analysis of mashed potato was also conducted after the thermal sterilization process at various locations of mashed potato (top, center, bottom) using the same method.

*3.2.1.2.2 Specific heat of mashed potato*

Specific heat of mashed potato was measured using a Differential Scanning Calorimeter (DSC) (µDSC7 Evo, Setaram Instrumentation, Kep Technologies, Mougins, France). The samples of mashed potato were placed in the pans of the DSC equipment. A program was set which is as follows: a heating rate of 1 °C/min was applied for 8400 s. from 0°C to 140°C, hold for 600 s at 140°C, and cool at a cooling rate of 1.2 °C/min for 6000 s until the final temperature reaches 20°C. Data from both the heating and cooling phases were used to calculate the specific heat of mashed potato.

*3.2.1.2.3 Thermal conductivity of mashed potato*

Thermal conductivity (k) was measured using a thermal analyzer (TEMPOS TEM00001220) with probe KS-3 (Meter, München, Germany). A special system (Fig. 3.2, 3.3) was designed for this purpose. The system consists of a can that holds the mashed potato inside. A probe to measure the thermal conductivity was placed in the center of the sample. A temperature probe is connected to the sample to monitor the temperature. An insulated tube is attached to the lid of the container to release excess pressure during high temperature heating process, especially higher than 80°C. This is because initial pre-trials showed that the mashed potato started to expand and escape from the can at temperatures above 80 °C. Therefore, the insulated tube was necessary to avoid product loss and to maintain stable measurement conditions. The thermal conductivity measurement is based on the transient line heat source method. It involves a probe with an embedded heating element and temperature sensor. At the set particular temperature of measurement, the probes applies a constant heat flux, causing the temperature around the probe to rise. The temperature sensor monitors this increase over time. By analyzing the temperature kinetics, the thermal conductivity of the mashed potatoes is determined. Readings are conducted in intervals of 10°C from 10°C to 100°C.

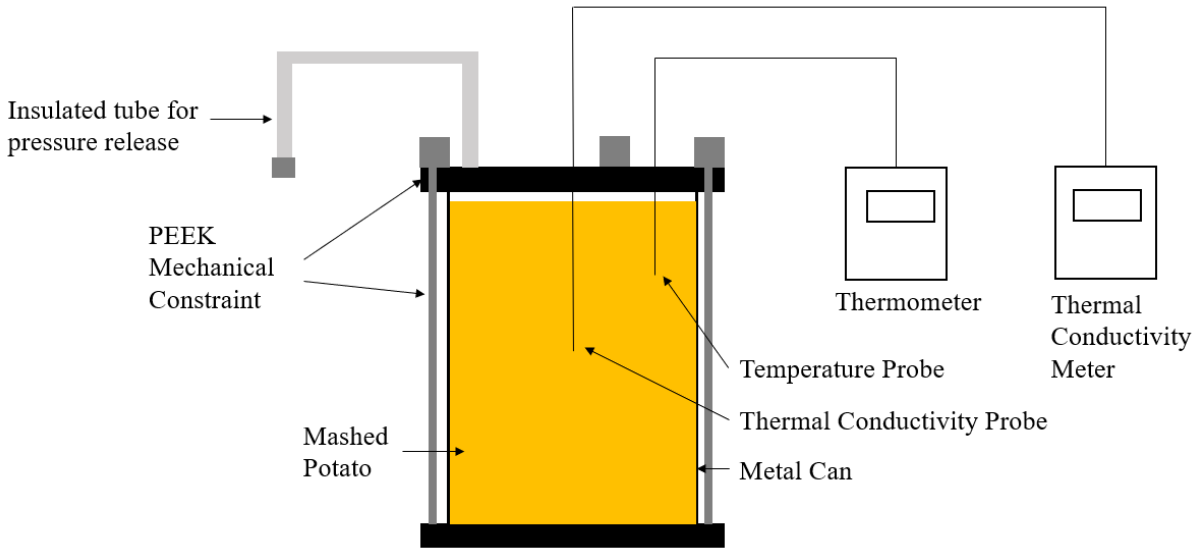



*Fig. 3. 2: Schematic of experimental setup to measure thermal conductivity of mashed potato.*



*Fig. 3. 3: Experimental system to measure thermal conductivity of mashed potato.*

*3.2.1.2.4 Density of mashed potato*

The density of the mashed potato was measured as bulk density using a controlled cylinder. The mass of the mashed potato inside the controlled cylinder was measured and density was calculated by dividing the sample mass by a mass of water filling the same volume. Density measurements were carried out only at ambient temperature and were not evaluated as a function of temperature.

**3.2.1.3 Thermal sterilization**

Thermal sterilization experiments were carried out using a pilot-scale STERITECH® retort system located at Oniris VetAgroBio, Nantes, France (Fig. 3.4). Fig. 3.5 shows a schematic of the Steritech® retort system. The retort system used saturated steam as the heating medium, which transfers heat to the food containers placed inside the retort chamber. The vapour pressure inside the retort was maintained between 2 and 4 bar, which corresponds to a saturated steam temperature of about 120–140 °C. Cold water was used during the cooling stage to lower the temperature, with occasional release of steam from the retort chamber. The sterilization cycle included three stages: heating (come-up time or CUT), holding, and cooling (come-down time or CDT). The temperature and pressure during all these stages were controlled and monitored using the system's built-in control panel. Fig. 3.6 shows a schematic of the experimental setup for conventional sterilization in the retort. For each experimental run, 14 metal cans with a height of 107 mm and a diameter of 72 mm were filled with mashed potato and sealed, keeping a fixed headspace of 25 mm. SSR Type T thermocouples (Ellab SARL, France) were inserted into the metal cans to monitor the temperature (Fig. 3.7). A total of 13 thermocouples were used: 12 inserted into the cans at different positions (top, center, bottom, and headspace) and one placed inside the retort to measure the surrounding environment (Fig. 3.8). For pressure measurements inside the cans, NanoVACQ PT sensors (TMI Orion, SA, France) were used, which were inserted into the headspace region of the cans containing the mashed potato. Fig. 3.9 shows the location of the temperature probes inside the can. All temperature data were collected in real-time using a computer interface, while the pressure data

were stored in the sensors and retrieved after the experiments. The sterilization conditions, including heating rate, holding time, and cooling procedure, were preprogrammed before each experimental run. All experiments were conducted in triplicates unless otherwise noted.




*Fig. 3. 4: STERITECH® retort system at Oniris VetAgroBio, Nantes, France.*

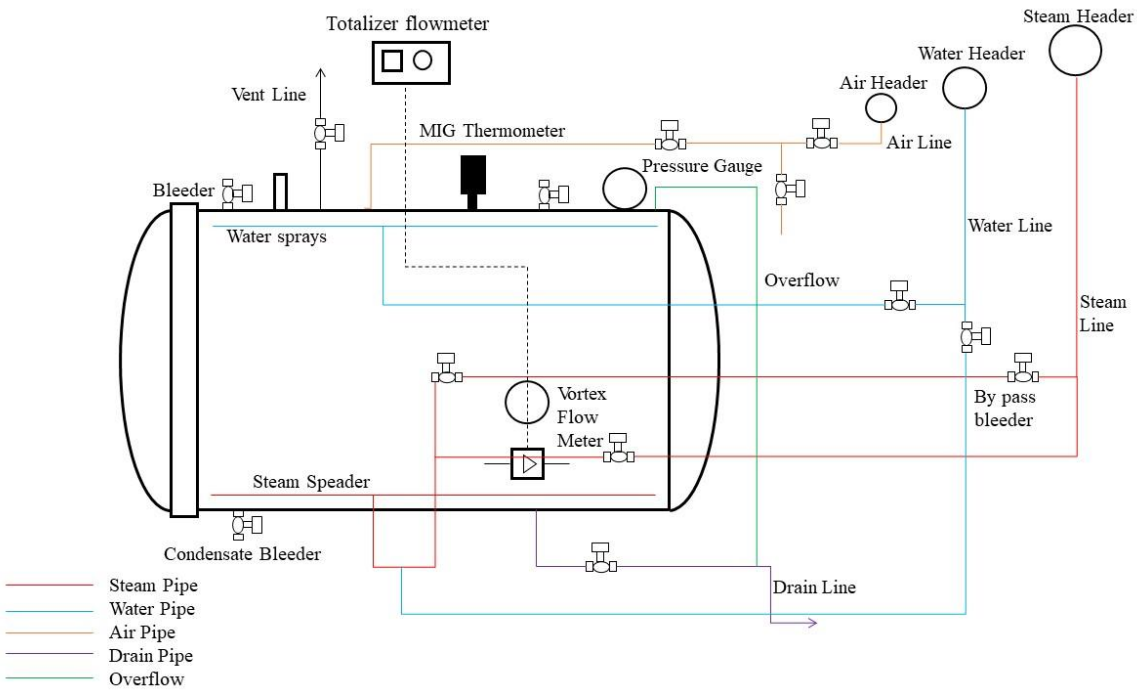



*Fig. 3. 5: Schematic of STERITECH® retort system.*

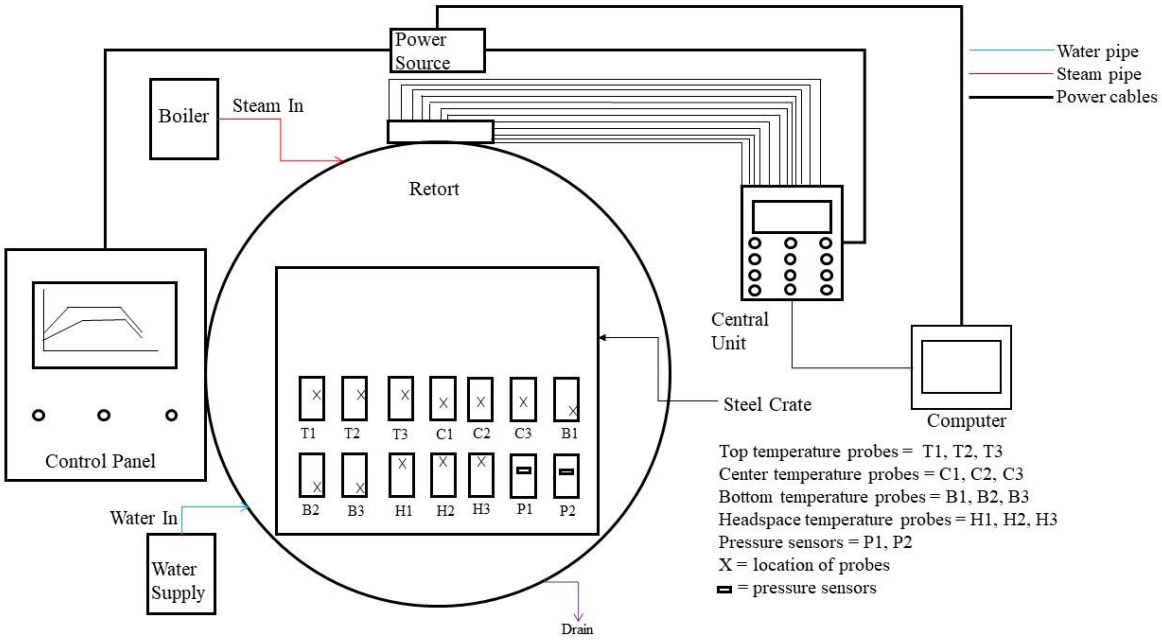
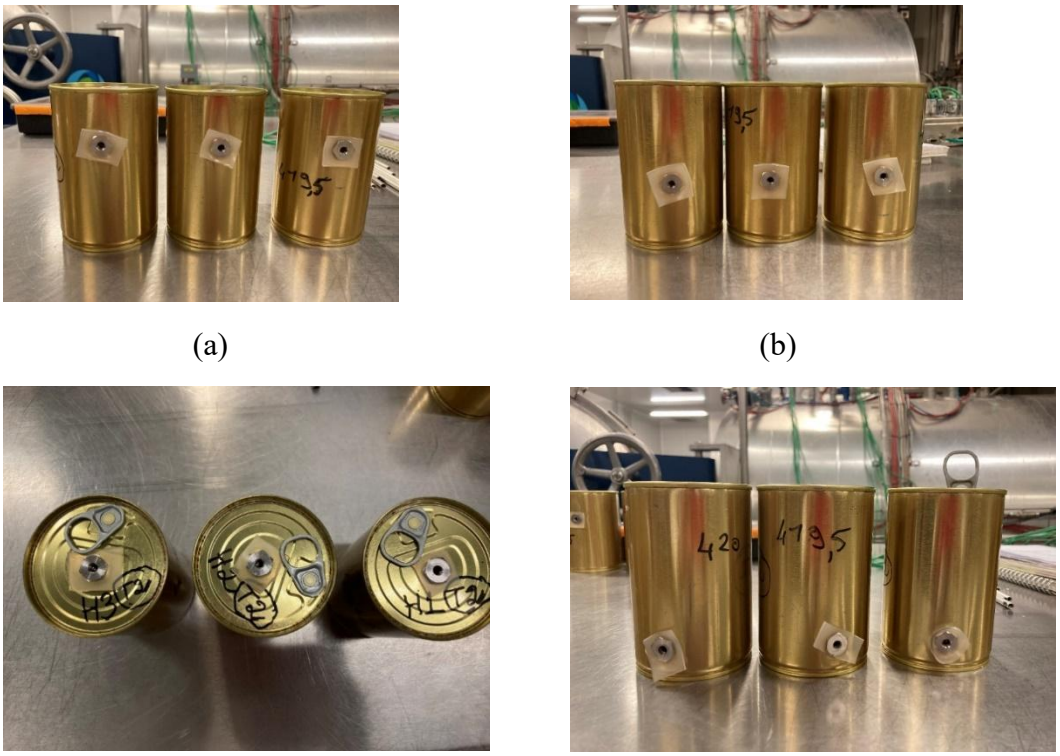



*Fig. 3. 6: Experimental setup for conventional sterilization in retort.*



(a) (b)

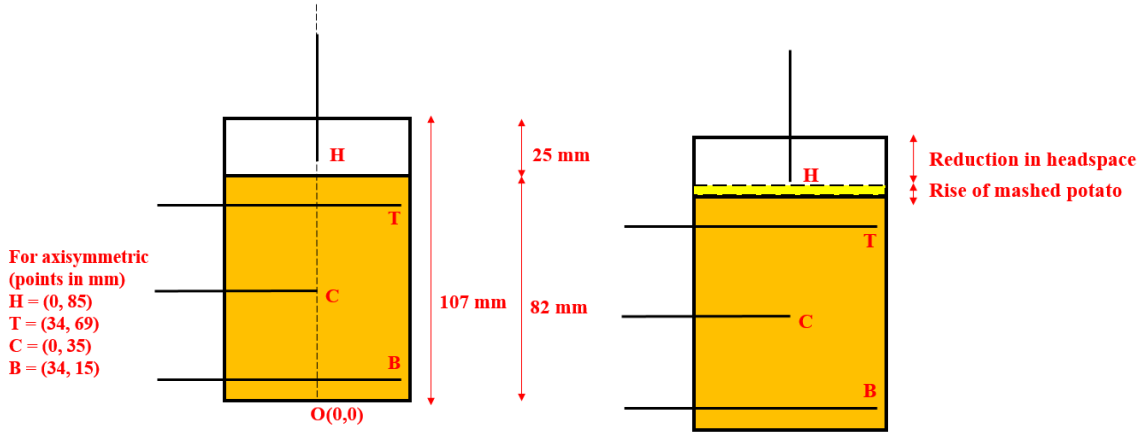
(c) (d)

*Fig. 3. 7: Temperature probes location in metal cans: (a) top (b) center (c) headspace (d) bottom*



(a) (b)

*Fig. 3. 8: (a) Temperature probes (b) Pressure sensor in cans*




(a) (b)

*Fig. 3. 9: Mashed potato in cans (a) Location of temperature probes in the cans (H: headspace; T: Top; C: Center; B: Bottom) (b) Reduction in headspace after sterilization*

### 3.2.2 Numerical modelling

Numerical modelling was carried out using COMSOL® Multiphysics 6.3 to simulate heat transfer within mashed potato and pressure within the head space during thermal sterilization. A 2D-axisymmetric geometry was created to represent the vertical cross-section of the metal can, including the mashed potato as the solid food domain and the headspace as the air domain. This approach was chosen because the can is cylindrical and has revolution symmetry following its vertical axis. Two physics interfaces were used for the simulation in COMSOL®: Heat Transfer in Solids and Fluids to model heat conduction in the food and heat transfer in the air, and Laminar Flow to model fluid flow during heat transfer. The heat flux at the walls was modelled using a convective heat flux boundary condition, with a global convective heat transfer coefficient and by taking into account the external temperature of the steam. Since the intensity of heat transfer changes during the heating, holding, and cooling stages, different coefficients were assigned for each phase, and three sets of values were tested to study the

sensitivity of temperature predictions to this parameter. The thermophysical properties of mashed potato such as specific heat capacity, thermal conductivity, and density, were included into COMSOL® based on experimental measurements (Table 3.1). The specific heat and thermal conductivity of mashed potato were defined as a function of temperature. The thermal properties of the metal can (stainless steel) were imported from COMSOL® material library. Thermophysical properties of air were also taken from the COMSOL® material library. Mesh sensitivity analysis was also conducted with 7 configurations to validate mesh independence (Table 3.2). The objective was to obtain the same numerical results whatever the size of the mesh. Along with that, the coefficient of determination ($R^2$) was calculated using simulated and experimental values of temperature evolution at the center location (cold spot) (Eq. 3.1). The time-dependent study was run over the full sterilization period to capture the evolution of temperature and pressure. Pressure in the headspace was also determined using the ideal gas law. In this configuration, the CFD model simulated only the contribution of dry air pressure, while water vapour pressure was estimated separately and compared with experimental measurements of total pressure. This approach allowed the role of dry air to be distinguished from that of water vapour in the overall pressurization of the can. All simulations were performed using COMSOL®'s built-in solver, and temperature and pressure data were extracted using post-processing tools within the software. In order to signify the role of CFD in heat transfer, simulation was also carried out with and without CFD.

$$R^2 = \frac{\sum_{i=1}^{n}(\hat{y}_i - y_i)^2}{\sum_{i=1}^{n}(y_i - \overline{y_i})^2} \qquad 3.1$$

where, $\hat{y}_i$ is the predicted value obtained from the model at data point $i$, $y_i$ is the experimental value at data point $i$, $\overline{y_i}$ is the average of all observed values, and $n$ is the number of data points.

*Table 3. 1: Thermophysical properties of mashed potato used for numerical modelling.*

| Parameters | | Values | References |
|---|---|---|---|
| **Density of mashed potato** | $\rho_{mp}$ | $1052.96\ kg/m^3$ | measured |
| **Mass transfer coefficient** | $k_m$ | $0.008\ m/s$ | Gulati et al., 2016 |
| **Specific heat of mashed potato** | $Cp_{mp}$ | Experimental data imported to model as interpolation function (Fig. 3.10) | measured |
| **Thermal conductivity of mashed potato** | $k_{mp}$ | Experimental data imported to model as interpolation function (Fig. 3.11) | measured |

*Table 3. 2: Mesh independence validation.*

| Scenario | Element size | Number of triangular elements | $R^2$ |
|---|---|---|---|
| **1** | Extremely coarse | 202 | 0.87* |
| **2** | Extra coarse | 340 | 0.87* |
| **3** | Coarser | 548 | 0.87* |
| **4** | Coarse | 1061 | 0.87* |
| **5** | Normal | 1495 | 0.87* |
| **6** | Fine | 2378 | 0.87* |
| **7** | Finer | 6191 | 0.87* |

*$R^2$ calculated using simulated and experimental values of temperature evolution at the center location (cold spot).

A 2D geometry of the metal can with model food where temperature is measured at various locations in the model is depicted in Fig. 3.12.

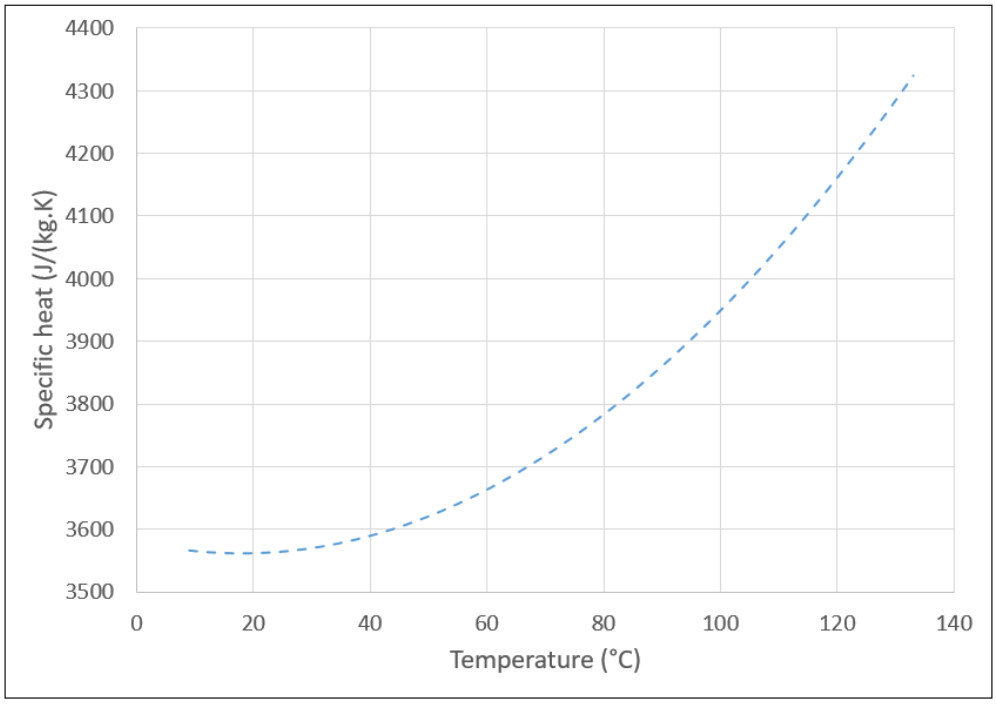



*Fig. 3. 10: Specific heat of mashed potato in relation with temperature*

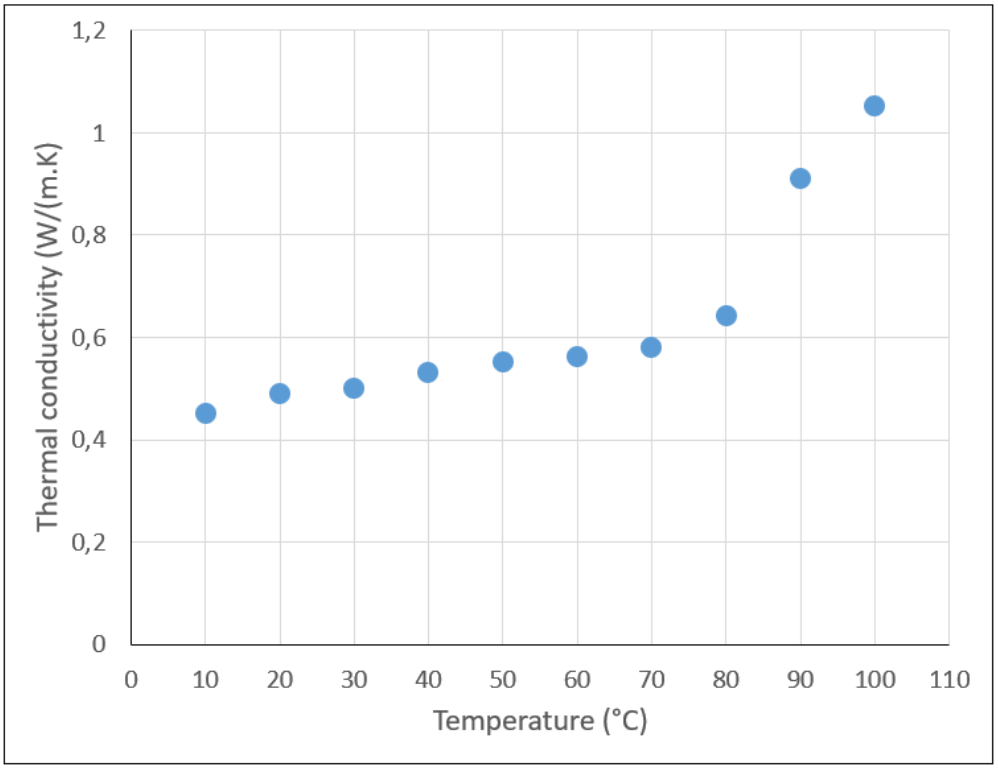



*Fig. 3. 11: Thermal conductivity of mashed potato in relation with temperature.*

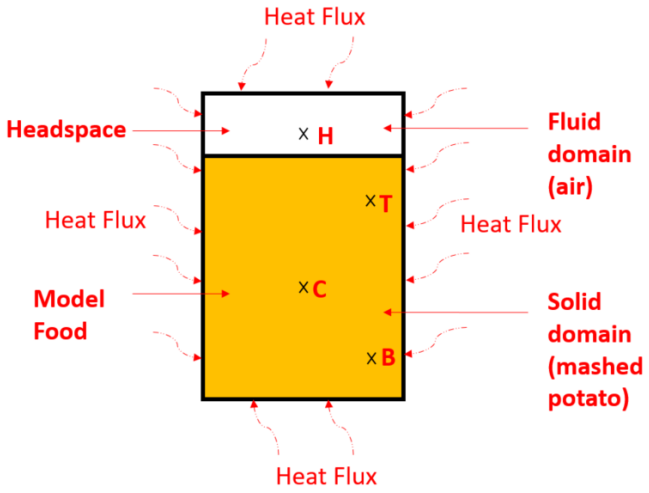



*Fig. 3. 12: 2D geometry of metal can with model food with various locations of temperature measurement.*

### 3.2.2.1 Model description

A 2D-axisymmetric geometry of a metal can with radius 36 mm and height 107 mm containing model food (mashed potato) was constructed in COMSOL® Multiphysics (Fig. 3.13). The geometry had two domains: the solid domain containing the model food, and the fluid domain containing the air. The Finite Element model was used for a thorough examination of the temperature distribution and pressure distribution within the can during thermal sterilization process. A compressible flow (Ma<0.3) was assumed as air density changes due to temperature

and pressure. The study was computed from 0 s to 7215 s with mesh size of 1061 elements (from scenario 4 in Table 3.2). Since the results were not influenced by the mesh sizes, the scenario 4 with this mesh size was chosen throughout this study. Inbuilt operators from COMSOL® were used to calculate the average of variables (pressure and temperature) in the headspace domain.

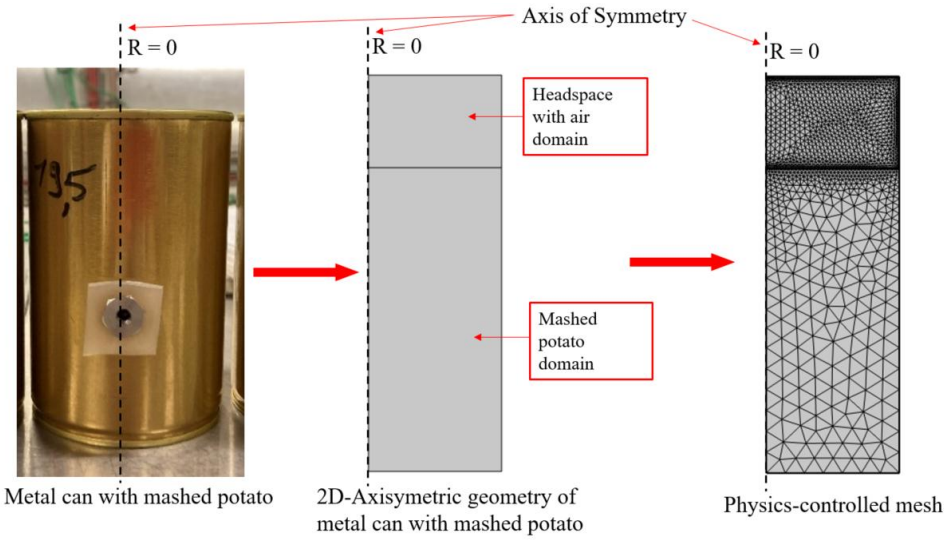



*Fig. 3. 13: Metal can geometry and meshing in COMSOL® Multiphysics.*

The heat transfer is calculated using the general heat transfer equation for both mashed potato (mp) domain and headspace (air) domain:

$$\rho_{mp} C_{p,mp} \frac{\partial T_{mp}}{\partial t} + \nabla . \boldsymbol{q} = 0 \qquad 3.2$$

$$\boldsymbol{q} = -k_{mp} \nabla T_{mp} \qquad 3.3$$

$$\rho_a C_{p,a} \frac{\partial T_a}{\partial t} + \rho_a C_{p,a} \boldsymbol{u} . \nabla T_a + \nabla . \boldsymbol{q} = 0 \qquad 3.4$$

$$\boldsymbol{q} = -k_a \nabla T_a \qquad 3.5$$

where, $\rho_{mp}$ is the density of mashed potato (kg/m$^3$), $\rho_a$ is the density of air (kg/m$^3$), $C_{p,mp}$ is the specific heat of mashed potato (J/kg/K), $C_{p,a}$ is the specific heat of air (J/kg/K), $T_a$ is temperature of air (K), $T_{mp}$ is temperature of mashed potato (K), $k_{mp}$ is thermal conductivity of mashed potato (W/m/K), $k_a$ is thermal conductivity of air (W/m/K), $\boldsymbol{q}$ is heat flux vector (W/m$^2$), and $\boldsymbol{u}$ is velocity vector of air flow (m/s).

Evaporation was assumed to occur at the food surface, representing the phase change of water from the mashed potato to the headspace. It was implemented at the surface boundary of the mashed potato, as proportional to the interfacial mass flux between the product surface and the surrounding air (H. Li et al., 2019):

$$Q_L = -\lambda I \tag{3.6}$$

where,

$$I = k_m(C_v^{surf} - C_v^a) \tag{3.7}$$

where, $Q_L$ is the latent heat flux associated with evaporation at the surface (W/m$^2$), $I$ is the interfacial mass flux of water vapour from the food surface to headspace air (kg/m$^2$/s), and $C_v^{surf}$ and $C_v^a$ are the vapour concentration at the product surface and headspace air respectively (kg/m$^3$), and $k_m$ is the mass transfer coefficient (m/s).

The latent heat of vaporization of liquid water ($\lambda$) is calculated as the function of temperature using the empirical formula (Nget et al., 2023):

$$\lambda = 1.91846 \times 10^6 \times \frac{T_{avg}^{mpsurf}}{T_{avg}^{mpsurf} - 33.91} \tag{3.8}$$

where, $\lambda$ is the latent heat of evaporation (J/kg), $T_{avg}^{mpsurf}$ is the average surface temperature of mashed potato (K).

The initial temperature for the mashed potato, headspace air and the surrounding air inside the retort was considered as 16°C.

At the can walls, heat transfer was represented by a convective boundary condition as:

$$q_0 = h_g(T_r - T) \tag{3.9}$$

where $q_0$ is the heat transfer from the retort to the can walls (W/m$^2$), $T_r$ is the temperature of the retort defined from experiments, and $h_g$ is the global heat transfer coefficient (W/m²/K). Because heat transfer varies between heating, holding, and cooling phases, three sets of global heat transfer coefficients ($h_{g1}, h_{g2}, and\ h_{g3}$) were defined (in the next section). These sets were chosen to represent low, medium, and high heat transfer conditions based on literature ranges. For example, Varga & Oliveira (2000) reported values between 150–200 W/m²/K during heating and 90–140 W/m²/K during cooling in a batch retort. Burfoot & Self (1988) observed higher values of 830–1550 W/m²/K for meat cubes during sterilization, while McGinnis (1986) showed that heat transfer coefficients could vary between 700–3000 W/m²/K during retort sterilization. Together, these studies show that $h_g$ can vary widely during retort sterilization. Based on this knowledge, the three sets of coefficients used in this work were designed to span a representative low-to-high range so that their effect on the predicted temperature evolution inside the can could be evaluated numerically.

The general time-dependent formulation of the global heat transfer coefficient was expressed as:

$$h_g = \begin{cases} h_{heating} & 0\ s\ < t_{He} \leq 1200\ s \\ h_{holding} & 1200\ s\ < t_{Ho} \leq 4821\ s \\ h_{cooling} & 4821\ s\ < t_{Co} \leq 7215\ s \end{cases} \tag{3.10}$$

where, $t_{He} = heating\ time, t_{Ho} = holding\ time, t_{Co} = cooling\ time$

The COMSOL® Laminar Flow interface solves the Navier-Stokes, and continuity equations within air domain. Convective heat transfer is governed by solving the Navier–Stokes equations coupled with heat transfer, which accounts for both fluid flow and temperature distribution. The momentum conservation equation and continuity equation are written as:

$$\frac{d(\rho_a \boldsymbol{u})}{dt} + \rho_a(\boldsymbol{u}.\nabla)\boldsymbol{u} = \rho_a \boldsymbol{g} - \nabla \mathrm{P} + \mu_a \nabla^2 \boldsymbol{u} \quad 3.11$$

$$\frac{\partial \rho_a}{\partial t} + \nabla.(\rho \boldsymbol{u}) = 0 \quad 3.12$$

where $\rho_a$ is the density of air (kg/m$^3$), **u** is the velocity vector describing the air motion within the headspace domain (m/s), t is time (s), P is pressure (Pa), **g** is gravitational acceleration vector (m/s$^2$), $\mu_a$ is dynamic viscosity of air (Pa.s).

A no-slip boundary condition was applied to the walls.

$$\boldsymbol{u} = 0 \; on \; the \; can \; wall \; surface \quad 3.13$$

The initial value of the velocity field in the headspace was set to zero, as the air was assumed to be at rest before heating began.

In addition to the CFD, the ideal gas law was used separately to calculate the dry air pressure in the headspace based on its thermodynamic state. It was used as a relation to evaluate the vapour pressure concentration:

$$P_a V_h = n_a R T_{a_avg} \quad 3.14$$

where, $P_a$ is dry air pressure (Pa), $V_h$ is headspace volume (m$^3$), $n_a$ is number of moles of air, $R$ is ideal gas constant ($8.3145\ J/mol/K$), $T_{a_avg}$ is average headspace temperature (K).

Dalton's law of partial pressure was used to account for the presence of both dry air and water vapour:

$$P_{tt} = P_a + P_v \quad 3.15$$

where $P_{tt}$ is the total pressure (Pa), $P_a$ is dry air pressure (Pa), and $P_v$ is water vapour pressure (Pa).

The rate of water vapour transfer from the mashed potato surface to the headspace was modelled using a convective mass transfer expression, driven by the difference between vapour concentrations at the surface and in the headspace air (from Eq. 3.7):

$$\frac{dm_v}{dt} = k_m S_{mp}(C_v^{surf} - C_v^a) \quad 3.16$$

where, $m_v$ is mass of water vapour (kg), t is time (s), $k_m$ is the mass transfer coefficient (m/s), $C_v^{surf}$ and $C_v^a$ are the vapour concentration at the product surface and headspace air respectively (kg/m$^3$), and $S_{mp}$ is the surface area of mashed potato surface (m$^2$).

The initial vapour mass in the headspace was estimated from the relative humidity (RH = 0.6) taken from the meteorological data available for the city of Nantes, France and the saturation vapour pressure at the initial temperature, using the ideal gas relation:

$$m_{v,i} = RH \times \frac{P_{v,i}^{sat} M_v V_h}{RT_i} \quad 3.17$$

where, $m_{v,i}$ is initial mass of water vapour (kg), RH is the relative humidity at the headspace, $P_{v,i}^{sat}$ is initial saturation vapour pressure (Pa), $M_v$ is molar mass of water vapour (kg/mol), $V_h$ is headspace volume ($m^3$), R is universal gas constant (J/mol/K), and $T_i$ is initial headspace temperature (K).

The initial saturation vapour pressure was calculated as a function of temperature using an exponential correlation based on the modified Antoine-type equation (Nget et al., 2023):

$$P_{v,i}^{sat} = 1[Pa] \times \exp\left((A_f {T_i}^2) + (B_f T_i) + C_f + (D_f {T_i}^{-1})\right) \quad 3.18$$

where, $A_f = 1.2811805 \times 10^{-5} K^{-2}$, $B_f = -1.9509874 \times 10^{-2} K^{-1}$, $C_f = 34.04926034$, $D_f = -6.3536311 \times 10^3 K$

The vapour concentration at the mashed potato surface (in Eq. 3.16) was obtained from the ideal gas law, relating partial pressure to mass concentration:

$$C_v^{surf} = \frac{P_v^{mpsurf} M_v}{RT_{avg}^{mpsurf}} \quad 3.19$$

Where, $C_v^{surf}$ is the vapour concentration at the mashed potato surface ($kg/m^3$), $P_v^{mpsurf}$ is vapour pressure at the mashed potato surface (Pa), $M_v$ is molar mass of water vapour (kg/mol), R is universal gas constant (J/mol/K), and $T_{avg}^{mpsurf}$ is average temperature at mashed potato surface (K).

The vapour concentration in the headspace (in Eq. 3.16) was obtained from the ratio of vapour mass to the headspace volume:

$$C_v^a = \frac{m_v}{V_h} \quad 3.20$$

where, $C_v^a$ is the vapour concentration in the headspace air domain ($kg/m^3$), $m_v$ is the mass of water vapour (kg), and $V_h$ is the headspace volume ($m^3$).

The partial pressure of vapour at the food surface was expressed as the product of water activity ($a_w = 0.98$, which is a general value for high moisture food such as mashed potato) and the saturation vapour pressure corresponding to the surface temperature:

$$P_v^{mpsurf} = a_w P_{v_mpsurf}^{sat} \quad 3.21$$

where, $P_v^{mpsurf}$ is vapour pressure at the mashed potato surface (Pa), $a_w$ is the water activity, and $P_{v_mpsurf}^{sat}$ is the saturation vapour pressure (Pa).

The saturation vapour pressure at the mashed potato surface was calculated from temperature using the same exponential relation applied locally at the interface:

$$P_{v_mpsurf}^{sat} = 1[Pa] \times \exp\left((A_f T_{avg}^{mpsurf^2}\right) + (B_f T_{avg}^{mpsurf}) + C_f + (D_f T_{avg}^{mpsurf^{-1}})) \quad 3.22$$

where, $P_{v_mpsurf}^{sat}$ is the saturation vapour pressure (Pa), $T_{avg}^{mpsurf}$ is average temperature at mashed potato surface (K).

Finally, the water vapour pressure is calculated as:

$$P_v = \frac{m_v R_v T_{avg}^a}{V_h} \quad 3.23$$

where, $R_v$ is 461.5 J/(kg.K), $P_v$ is water vapour pressure (Pa), $m_v$ is the mass of water vapour (kg) calculated from the ordinary differential equation in Eq. 3.16 , $T_{avg}^a$ is average temperature of air in headspace (K), $V_h$ is the headspace volume ($m^3$).

### 3.3 Results and discussions

#### 3.3.1 Temperature distribution and model validation

##### 3.3.1.1 Experimental and simulated temperature distribution

Temperature profiles inside the cans were measured at four locations: top, center, bottom, and headspace. The heating behaviour was found to differ across these locations during the thermal sterilization cycle (Fig. 3.14). The headspace temperature increased rapidly during the initial stage. This is because air has a lower heat capacity compared to the solid food. Therefore, heat transfer quickly through the headspace (Mohamed, 2007). The top and bottom positions in the food also experienced a steady rise in temperature. These regions are in contact with the can walls, which receive heat directly from the external steam. Hence, conduction through the metal walls enables faster heating at these locations (Abdul Ghani et al., 2001). The center of the mashed potato showed the slowest temperature increase. This region is farthest from the heating boundary and relies entirely on conduction through the food matrix. Mashed potato is a semi-solid material with high water content and moderate thermal conductivity and heat capacity compared to low moisture and fatty foods. Therefore, the heat diffusion toward the center is slow, which is as expected. During the holding phase, all four locations approached the target temperature of 121°C. However, the center remained slightly lower, with a difference of about 4 °C and 5 °C from the top and bottom location respectively. This temperature lag indicates the need for sufficient holding time to ensure uniform sterilization (Bornhorst, Tang, et al., 2017). During the cooling phase, the headspace cooled the fastest. This occurred because air has lower thermal inertia than the food. The center region retained heat for a longer period because it is surrounded by food material on all sides and has a higher thermal inertia than the top and bottom regions, which are in direct contact with the can walls and therefore lose heat faster (Mohamed, 2016).

Simulations were conducted over the full sterilization cycle time of 7215 s. The comparison between experimental and simulated temperature data were carried out at each of the local temperature points (top, center, bottom, and headspace) (Fig. 3.15 -3.18) (Note: the different $h_{global}$ values presented in these figures correspond to the global convective heat transfer coefficients of the retort during the sterilization process. They are described in detail in the next section). The numerical results reproduced the general heating pattern observed experimentally. Comparison was also carried out with and without the usages of CFD (i.e only conduction phenomena within headspace air) during simulation for temperature prediction to study the

significance of CFD usages during simulation. In this case, the velocity field of the air phase was set to zero, which effectively removed the convective term from the energy equation. Here only $h_{global1}$ value (value is presented in the next section) was used. For the top, center, and bottom positions, the differences in between simulations with and without CFD were negligible. This indicates that, at these locations, heat transfer is governed only by conduction through the food, and the contribution of airflow is minimal, which is as expected. In contrast, at the headspace location, difference between CFD and non-CFD simulations was significant (Fig. 3.19) This shows that including CFD in the model significantly improves the prediction of headspace temperature, providing values much closer to the experimental results. The CFD module, by solving the Navier–Stokes equations, models natural convection phenomena within the headspace. These mechanisms are not represented in non-CFD simulations, which rely solely on conduction and therefore underestimate heat transfer in the gaseous zone. Hence, the use of CFD is essential for accurately describing heat transfer in the headspace, while its impact on the food domain (top, centre, and bottom) remains limited, as expected. Therefore, in the following study, results with CFD simulations are only reported.

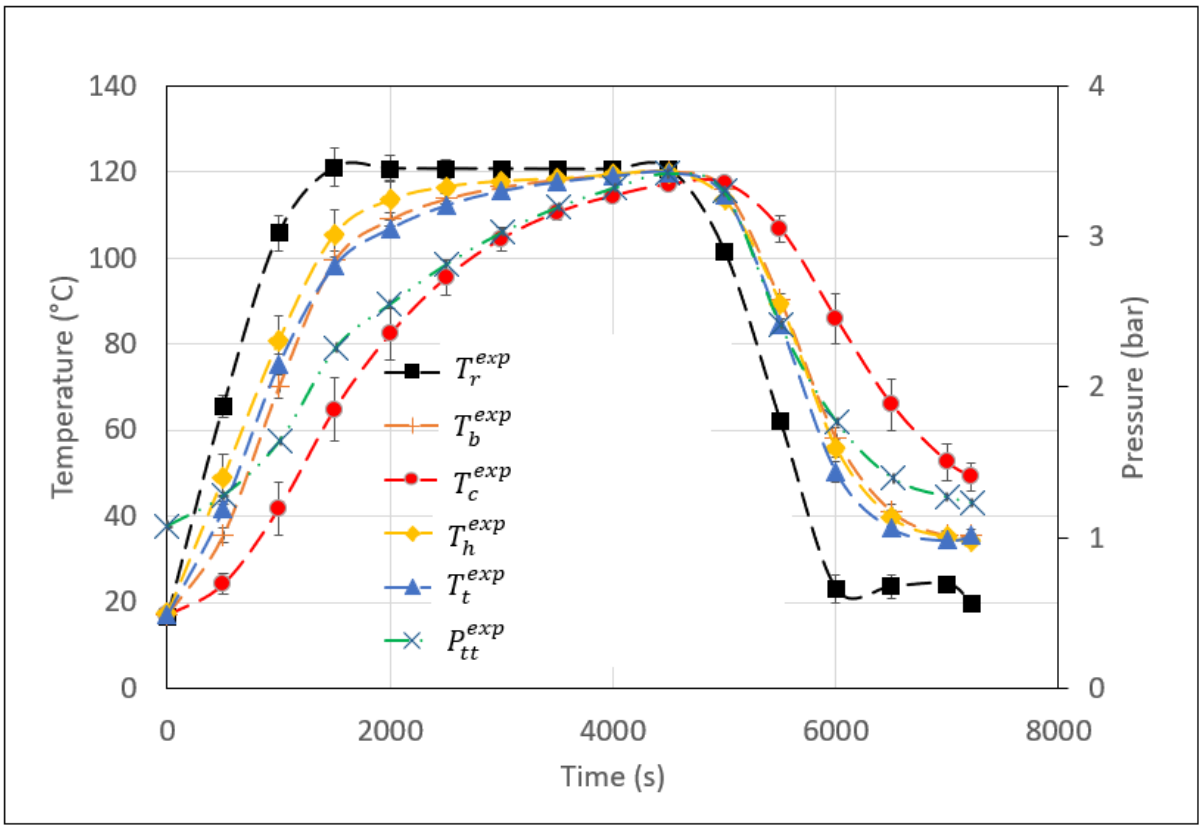



*Fig. 3. 14: Experimental temperature distribution at different locations and experimental total absolute pressure evolution inside the metal can. ($T_r^{exp}$: experimental temperature of retort; $T_b^{exp}$: experimental temperature of mashed potato at bottom location; $T_c^{exp}$: experimental temperature of mashed potato at center location; $T_h^{exp}$ experimental temperature of mashed potato at headspace location; $T_t^{exp}$: experimental temperature of mashed potato at top location; $P_{tt}^{exp}$: experimental total pressure inside can.).*

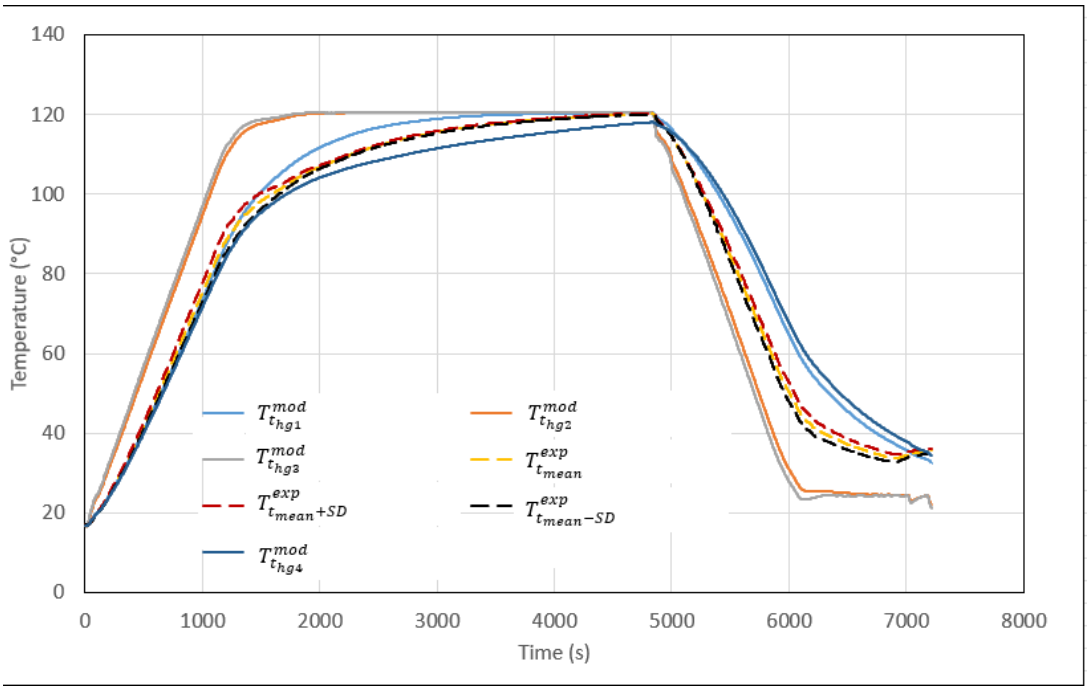



*Fig. 3. 15: Comparison between experimental and simulated temperature distribution in the mashed potato domain at top location. (T: temperature; mod: model; exp: experimental values; t: top location; hg1: global heat transfer coefficient 1; hg2: global heat transfer coefficient 2; hg3: global heat transfer coefficient 3; hg4: global heat transfer coefficient 4; mean : mean measurements of temperatures; SD: standard deviation of temperatures.)*

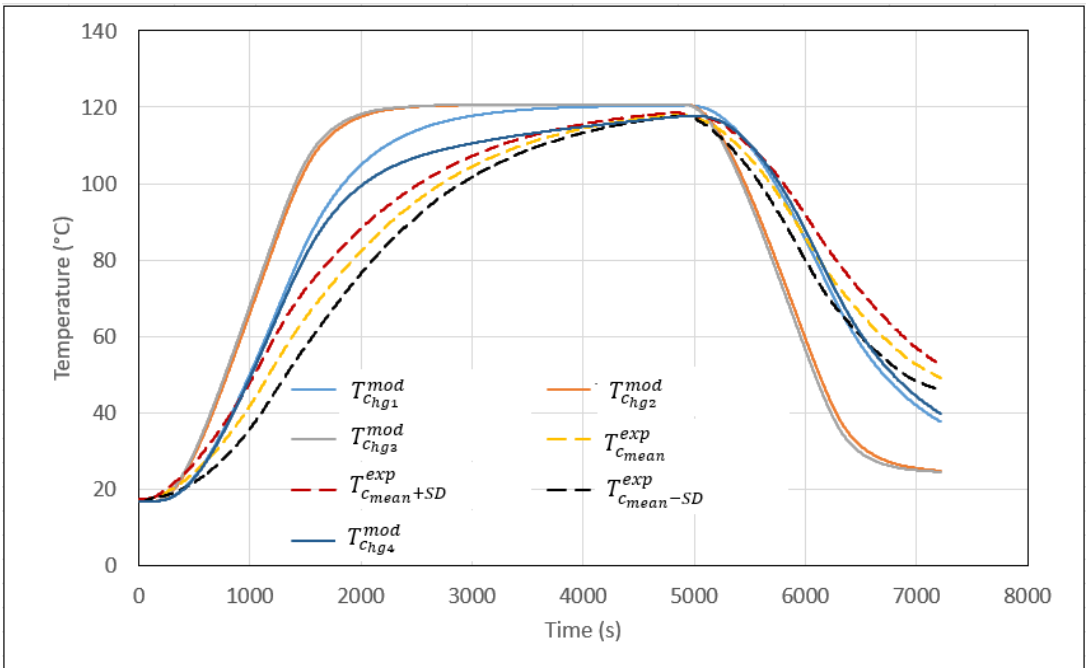



*Fig. 3. 16: Comparison between experimental and simulated temperature distribution in the mashed potato domain at center location. (T: temperature; mod: model values; exp: experimental values; c: center location; hg1: global heat transfer coefficient 1; hg2: global heat transfer coefficient 2; hg3: global heat transfer coefficient 3; hg4: global heat transfer coefficient 4; mean : mean measurements of temperatures; SD: standard deviation of temperatures.)*

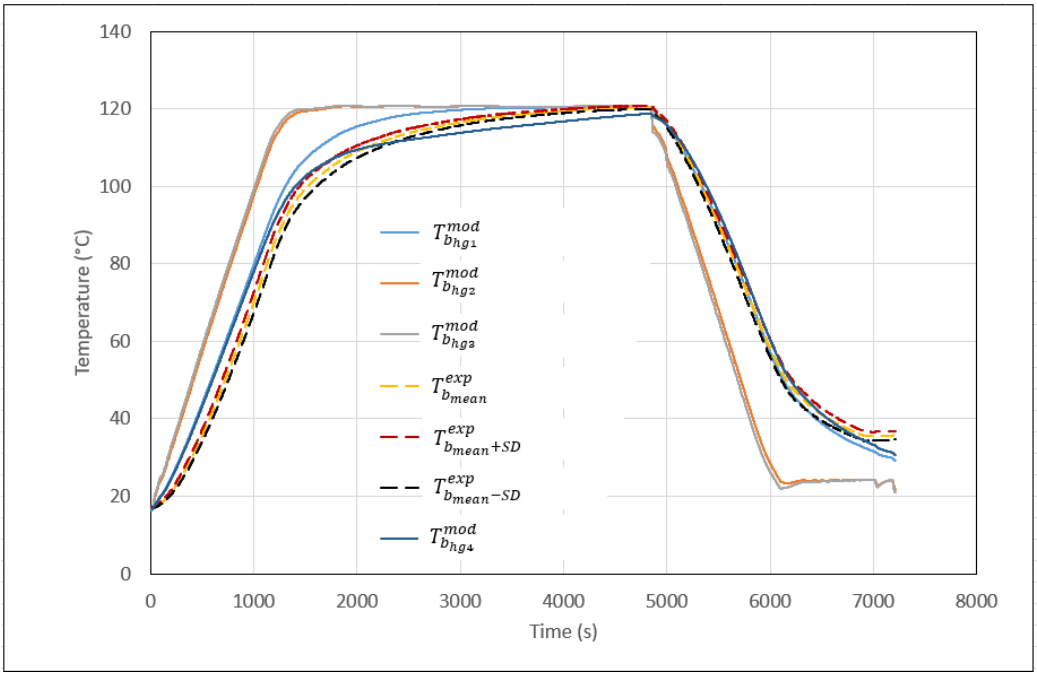



*Fig. 3. 17: Comparison between experimental and simulated temperature distribution in the mashed potato domain at bottom location.(T: temperature; mod: model; exp: experimental values; b: bottom location; hg1: global heat transfer coefficient 1; hg2: global heat transfer coefficient 2; hg3: global heat transfer coefficient 3; hg4: global heat transfer coefficient 4; mean : mean measurements of temperatures; SD: standard deviation of temperatures.)*

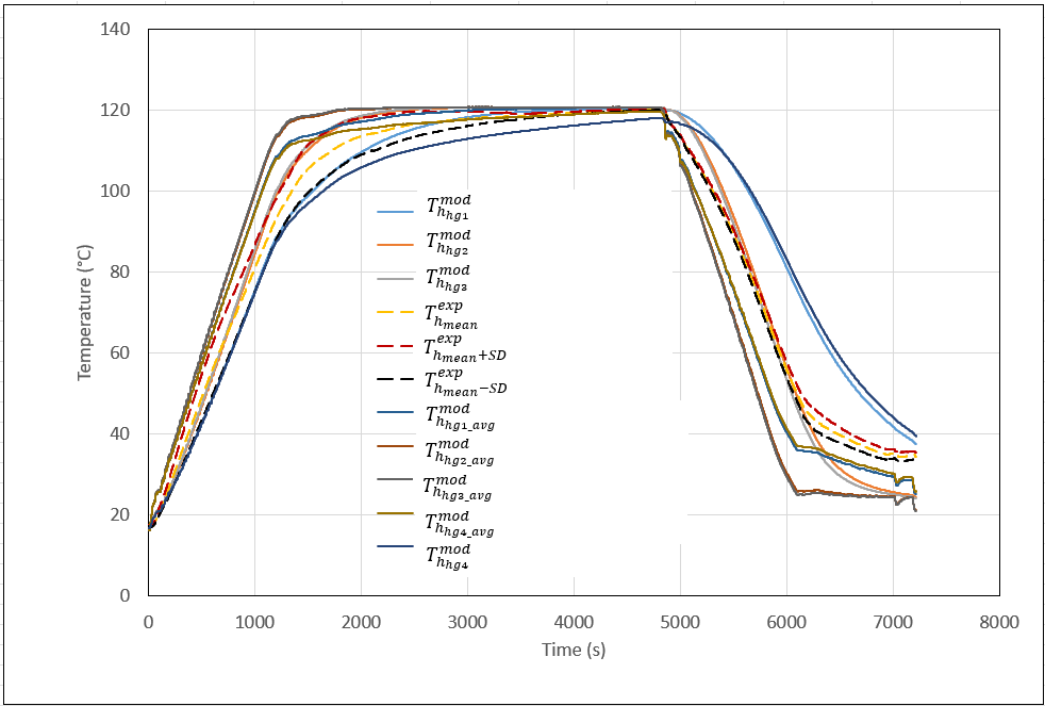



*Fig. 3. 18: Comparison between experimental and simulated temperature distribution in the headspace domain at headspace location. (T: temperature; mod: model; h: headspace location; exp: experimental values; hg1: global heat transfer coefficient 1; hg2: global heat transfer coefficient 2; hg3: global heat transfer coefficient 3; hg4: global heat transfer coefficient 4; mean : mean measurements of temperatures; SD: standard deviation of temperatures; avg: average measurement of headspace temperature within the sample)*

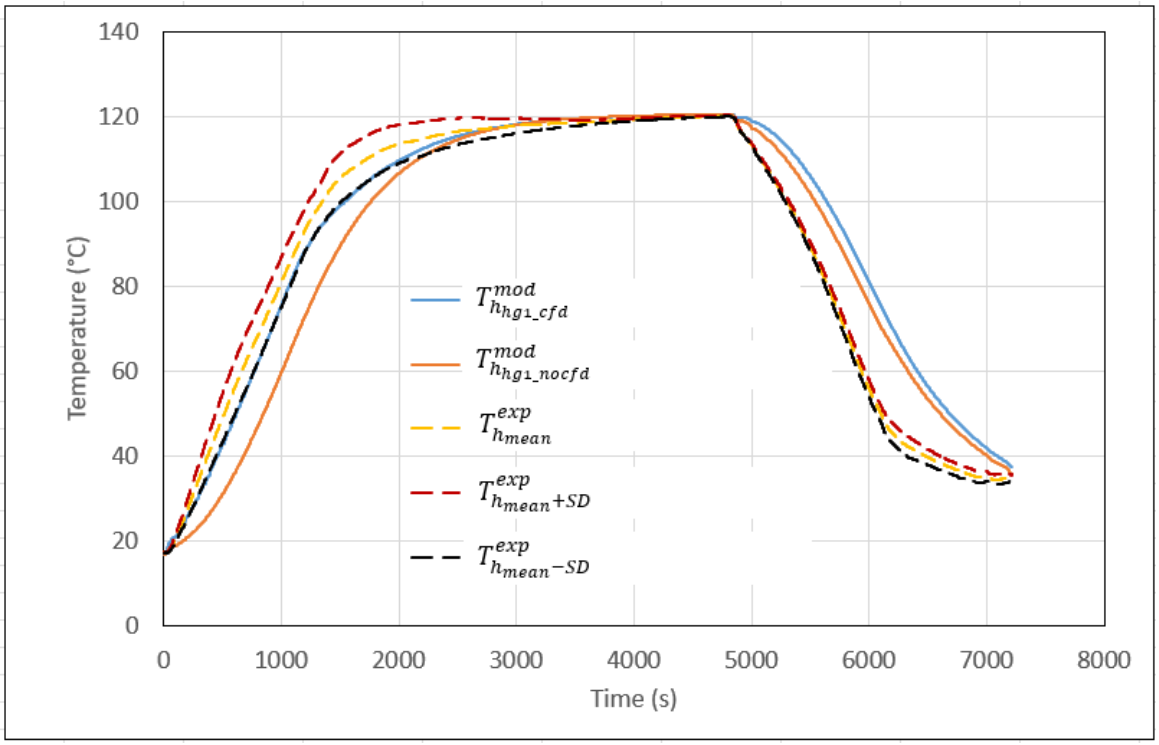



*Fig. 3. 19: Comparison between simulated temperature distribution in the headspace domain at headspace location with and without cfd. (T: temperature; mod: model; exp: experimental values; h: headspace location; hg1: global heat transfer coefficient 1; mean : mean measurements of temperatures; SD: standard deviation of temperatures; cfd: values when cfd is used is the model; nocfd: values when cfd is not used in the model.)*

### 3.3.1.2 Comparison of heat transfer coefficients

Building on these models for temperature predictions, this section examines the influence of different external convective heat transfer coefficients ($h_g$), on the overall heating behaviour within the can, in order to evaluate the influence of external heat transfer conditions on the temperature evolution at various locations during sterilization. Table 3.3 shows the various global heat transfer coefficient values used in the simulation study for heating, holding, and cooling phases during retort sterilization based on literature value ranges (Ağagündüz et al., 2025; Dwivedi & Ramaswamy, 2010; A. Singh et al., 2015; A. P. Singh & Ramaswamy, 2015; Vadivambal & Jayas, 2010; Varga & Oliveira, 2000). Among these, $h_{g2}$ and $h_{g3}$ were directly selected from the literature ranges, while $h_{g1}$ and $h_{g4}$, which are closer to each other, were manually adjusted to better align the simulated temperature profiles with the experimental results.

Fig. 3.20 shows the simulated results for the four sets of global heat-transfer coefficients at the end of the sterilization cycle (t = 7215 s) where temperature gradients are clearly visible. A very small difference was observed between $h_{g1}$ *and* $h_{g4}$ where values were in similar ranges. As expected, increasing the heat transfer coefficient produced faster cooling at the walls but also larger wall-to-center differences. For $h_{g1}$, the center cooled to about 39 °C while the regions near the walls dropped to 19 °C, giving a larger difference. For $h_{g2}$, the center reached 25 °C and the wall regions 19 °C, while for $h_{g3}$, the center was 24 °C and the wall regions 20 °C, and

for $h_{g4}$, the center was 41 °C and the wall regions 19 °C at the end of cooling. Therefore, lower coefficients slowed the cooling process across the can, so that heat loss was less intense near the boundaries, but the food center stayed warm for longer. The influence of the heat transfer coefficient, however, depends strongly on the location within the can. Near the walls, its effect is immediate due to direct contact with the external medium, while at the center, its influence is delayed and governed by conduction through the food matrix. These results indicate that the heat transfer coefficient has a strong influence on the prediction of temperature evolution during sterilization. The effect of the different $h_g$ values on temperature distribution at various location can also be seen in the figures presented above (Fig. 3.15 -3.18). Table 3.4 shows the comparison of the various heat transfer coefficients for prediction of temperatures at various location using $R^2$ value. Although $h_{g4}$ produced slightly higher $R^2$ values for the prediction of center temperature, the overall comparison across all measured points (top, bottom, center, and headspace) indicated that $h_{g1}$ provided a more balanced prediction accuracy. In the analysis, a trade-off was observed—$h_{g2}$ *and* $h_{g3,}$ gave better agreement for the headspace region, whereas $h_{g1}$ and $h_{g4}$ showed locally improved results either at the top, bottom, or center positions. Therefore, $h_{g1}$ was chosen as the representative case, as it offered the best compromise in reproducing the experimental temperature evolution across all positions within the tray, and hence $h_{g1}$ will be used for further studies from now on.

*Table 3. 3: Global heat transfer coefficient values used in the simulation study for heating, holding, and cooling phases during retort sterilization.*

| **Heat Transfer Coefficient** | $\boldsymbol{h_{heating}(W/(m^2.K)}$ | $\boldsymbol{h_{holding}(W/(m^2.K)}$ | $\boldsymbol{h_{cooling}(W/(m^2.K)}$ |
|---|---|---|---|
| $\boldsymbol{h_{g1}}$ | 150 | 180 | 100 |
| $\boldsymbol{h_{g2}}$ | 700 | 1500 | 1000 |
| $\boldsymbol{h_{g3}}$ | 1000 | 2500 | 3000 |
| $\boldsymbol{h_{g4}}$ | 140 | 40 | 90 |

*Table 3. 4: Comparison of various heat transfer coefficients for prediction of temperatures at various location using $R^2$ value.*

| | $\boldsymbol{h_{g1}}$ | $\boldsymbol{h_{g2}}$ | $\boldsymbol{h_{g3}}$ | $\boldsymbol{h_{g4}}$ |
|---|---|---|---|---|
| $\boldsymbol{T_t}$ | 0.97 | 0.88 | 0.85 | 0.96 |
| $\boldsymbol{T_b}$ | 0.98 | 0.78 | 0.75 | 0.99 |
| $\boldsymbol{T_c}$ | 0.87 | 0.50 | 0.45 | 0.94 |
| $\boldsymbol{T_h}$ | 0.91 | 0.98 | 0.98 | 0.89 |

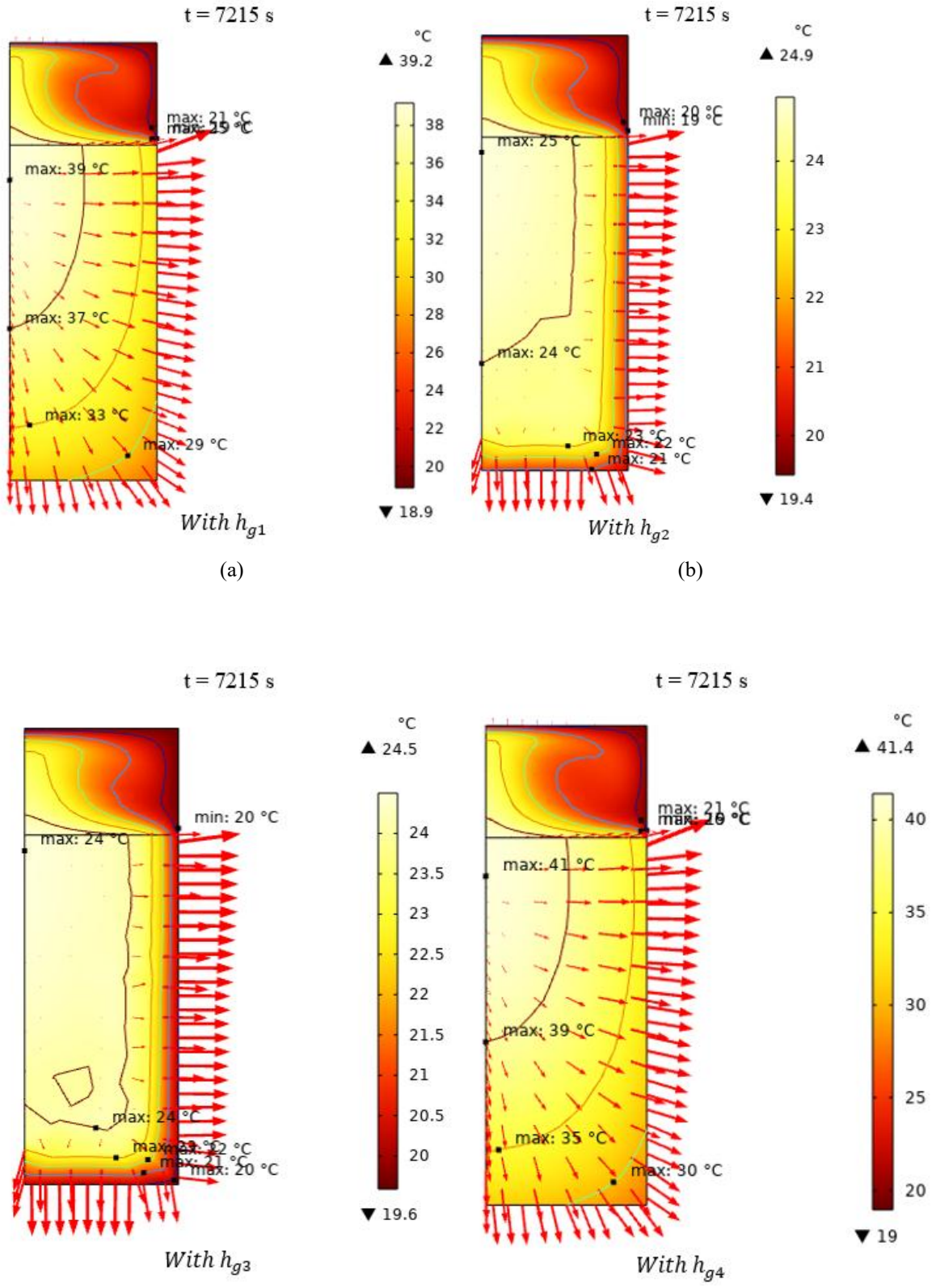



*Fig. 3. 20: Simulated temperature distribution using different heat transfer coefficients: $h_{g1}$, $h_{g2}$, $h_{g3}$, and, $h_{g4}$ at the end of sterilization process (t =7215 s). The arrows represent only the net heat flux (W/m$^2$) directions. Colour grades scales are different for each images.*

### 3.3.2 Pressure evolution

#### 3.3.2.1 Experimental and simulated pressure

The experimental pressure inside the container increased continuously from the start of the heating phase, reaching a maximum of 2.45 bar relative pressure at approximately 5000 s, marking the end of the holding phase (Fig. 3.21). This pressure rise corresponded with the temperature increase within the can and can be attributed to two simultaneous mechanisms: (i) the thermal expansion of dry air in the headspace, governed by the ideal gas law and (ii) the progressive generation of water vapour from the food matrix as the temperature increased. Simulation results showed that during the early heating phase, the pressure increase was mainly due to dry air expansion (Fig. 3.22), whereas at higher temperatures approaching sterilization conditions, evaporation from the mashed potato surface contributed additionally to the total pressure. The external pressure applied by the retort system (not shown) peaked at 2.30 bar relative pressure. The 0.15 bar difference between internal and external pressures indicates a net overpressure within the container. During the cooling phase, the pressure dropped rapidly, falling from its maximum to approximately 0.2 bar relative pressure within 2000 s. This sharp decline was caused by two combined effects. First, as the temperature of the dry air–water vapour mixture decreased, the partial pressure of dry air and vapour decreased as the total volume remained constant according to the ideal gas law. Second, the reduction in temperature caused the partial pressure of water vapour to fall below its saturation value, leading to condensation of vapour on the can walls and on the food surface. This phase change converted vapour back to liquid water, removing part of the gaseous content from the headspace and further reducing the total pressure in the system.

The simulated vapour pressure remained below 0.5 bar (relative) during most of the heating phase but rose sharply after the onset of holding, reaching about 2 bar before declining to ~0.2 bar during cooling. Notably, the increase in vapour pressure is not linear but accelerates once the food temperature rises, indicating thermally activated evaporation processes (Joseph et al., 1996). The total headspace pressure followed a similar trend to the simulated vapour pressure.

To assess the sensitivity of the model to interfacial mass transfer parameters, additional simulations were performed by varying the mass transfer coefficient and water activity within realistic physical ranges. It was found that variations in the mass transfer coefficient around the reference value of 0.008 $m \cdot s^{-1}$, between $10^{-2}$ and $10^{3}$ $m \cdot s^{-1}$, had negligible influence on the predicted pressure evolution. This behaviour can be explained by the formulation of the interfacial vapour mass balance (Eq. 3.16), in which the vapour generation rate is proportional to the product of the mass transfer coefficient and the concentration difference between the vapour on the food surface and the headspace air. With the headspace closed, the air quickly becomes saturated with moisture and consequently the vapour concentration difference between the food surface and the headspace air tends to zero. As a consequence, even large variations in the mass transfer coefficient do not significantly alter the vapour mass flux.Similar to the mass transfer coefficient, changes in water activity between 0.95 and 0.99 did not significantly affect the magnitude or temporal profile of vapour pressure. These observations suggest that, under the studied conditions, the overall pressure behaviour is primarily governed by temperature-dependent evaporation rather than by moderate variations in interfacial mass transfer or water activity parameters

Analysis of relative contributions shows that, up to around 1000 s (early heating), dry air dominated the headspace pressure because it expanded faster with temperature, while vapour

generation was still limited. At around 400 s, the dry air pressure was nearly 3x higher than the water vapour pressure, and by 1000 s, it was still about 1.5x greater, indicating that air expansion was the primary driver of pressurization during the initial phase of heating. Fig. 3.22 displays the zoomed pressure profiles for early stages ($t \leq 1000$ s) of heating during the sterilization cycle. This is consistent with the faster temperature rise in the headspace compared to the food domain, which accelerates the thermal expansion of the dry air. At later stages, particularly during holding, water vapour became the dominant contributor. This shift reflects the delayed but substantial evaporation of moisture from the food once its internal temperature rises. Consequently, while dry air drives the initial pressure build-up due to rapid headspace heating, water vapour governs the overall pressure profile during the majority of the sterilisation cycle. Fig. 3.23 shows the ratio of simulated pressure for dry air to simulated pressure for water vapour during the early stages ($t \leq 1000$ s) of heating in sterilization cycle. The diffusion of water vapour from the mashed potato to the headspace is confirmed from the moisture content analysis of the mashed potato at various locations (top, center, and bottom) immediately after the end of the sterilization cycle. As shown in Table 3.5, the moisture content is highest at the top layer and lowest at the bottom, indicating that water transfers upward from the bottom towards the top and subsequently into the headspace during sterilization. This observation is consistent with the model prediction shown in Fig. 3.24, where the total mass of water vapour in the headspace increases continuously during heating and reaches a maximum of approximately 110 mg near the end of the holding phase and less than 10 mg near the end of the sterilization cycle. The magnitude of this generated vapour aligns with the small but measurable moisture loss in the food, confirming that evaporation from the product contributes directly to the headspace vapour accumulation during the sterilization process as predicted by the model.

*Table 3. 5: Moisture content (wb) evolution at different location in mashed potato before and after sterilization.*

| **Moisture content (wb) at different locations** | **Before sterilization (g $H_2O$/100 g total mass)** | **After sterilization (g $H_2O$/100 g total mass)** |
|---|---|---|
| **Top** | 0.7670 ± 0.0035 | 0.7803 ± 0.0123 |
| **Center** | 0.7673 ± 0.0073 | 0.7698 ± 0.0177 |
| **Bottom** | 0.7660 ± 0.0087 | 0.7299 ± 0.0143 |

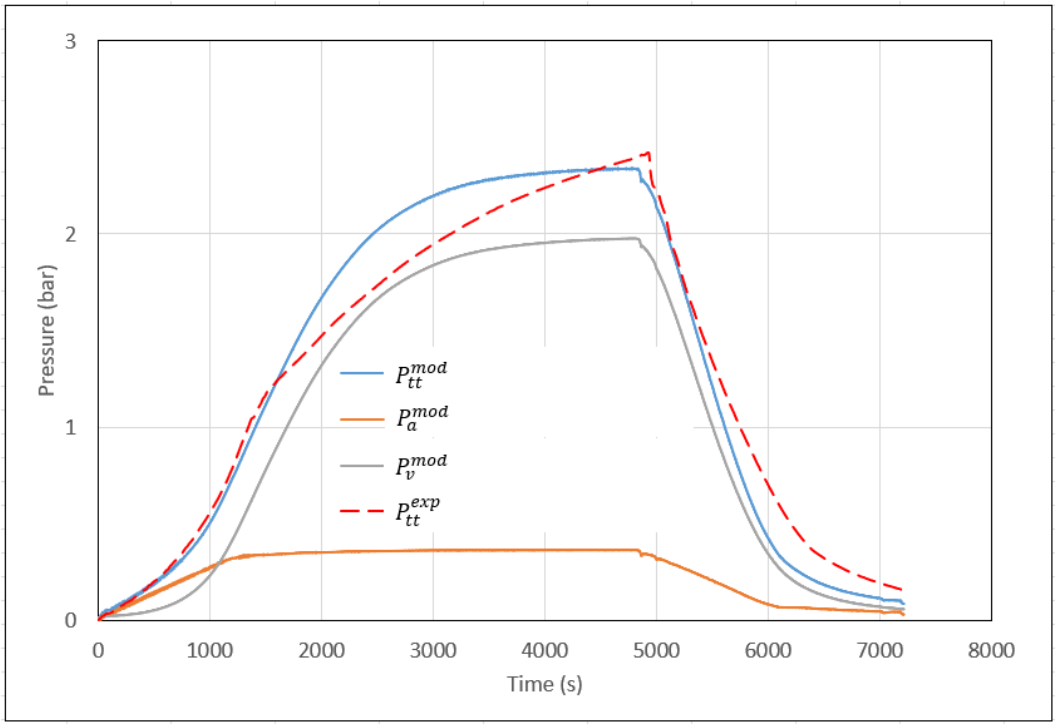



*Fig. 3. 21: Comparison between experimental and simulated total headspace pressure in the container. (P: pressure; mod: model values; exp: experimental values; a: dry air; v: water vapour; tt: total)*

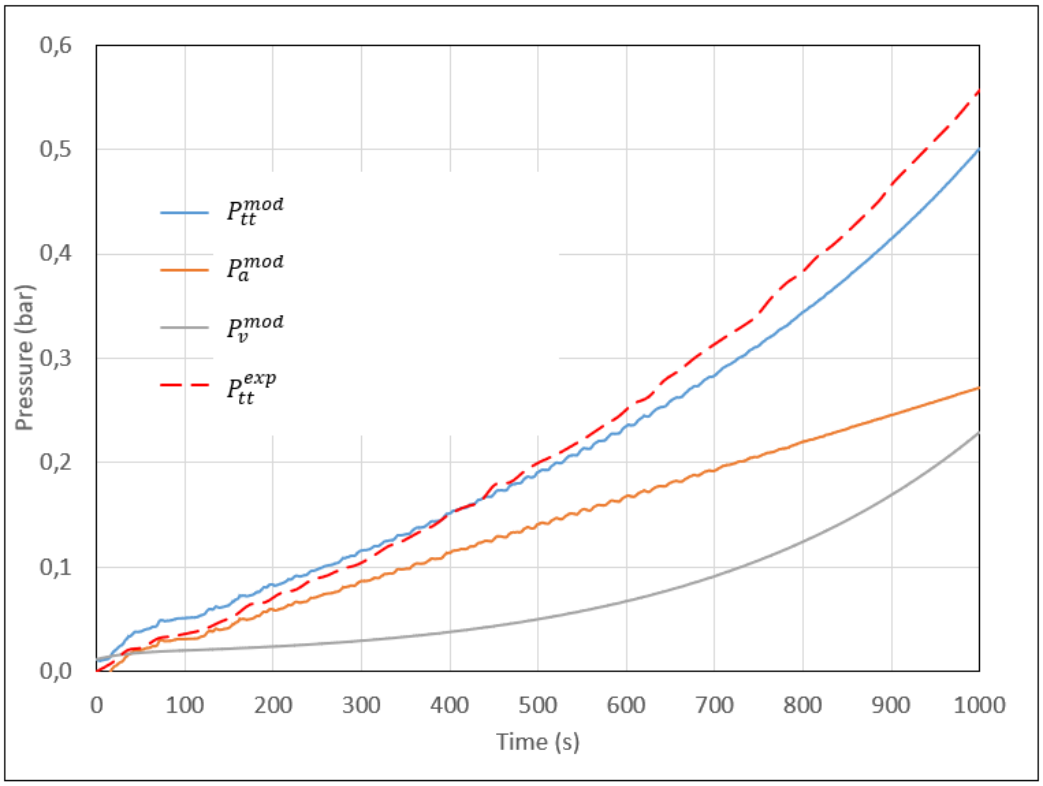



*Fig. 3. 22: Zoomed pressure profiles for early stages (t ≤ 1000 s) of heating during the sterilization cycle.(P: pressure; mod: model values; exp: experimental values; a: dry air; v: water vapour; tt: total)*

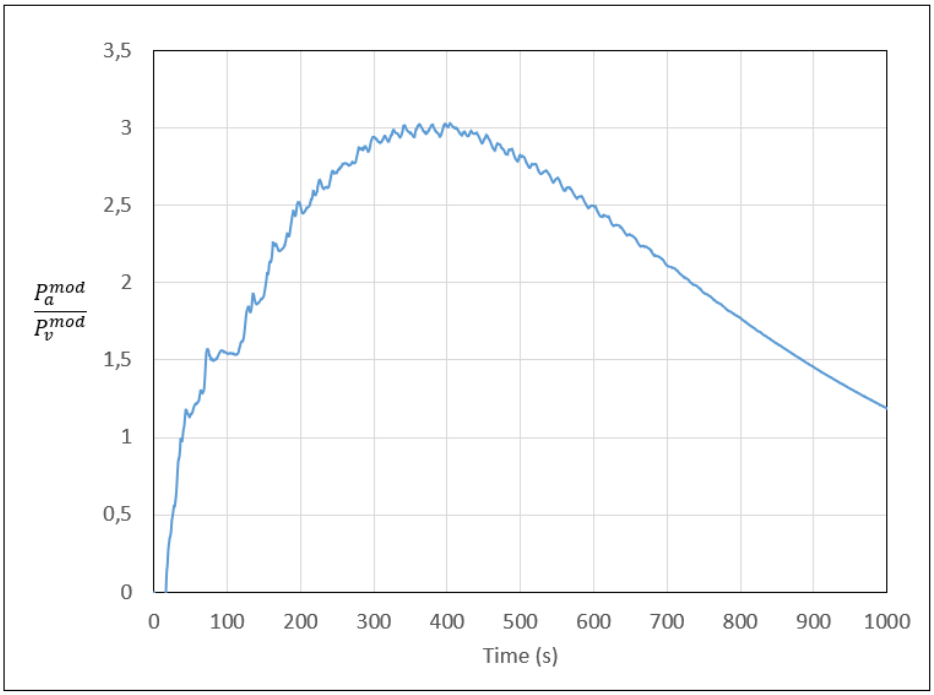



*Fig. 3. 23: Ratio of simulated pressure for dry air ($P_a^{mod}$) to simulated pressure for water vapour ($P_v^{mod}$) during the early stages ($t \leq 1000$ s) of heating in sterilization cycle.*

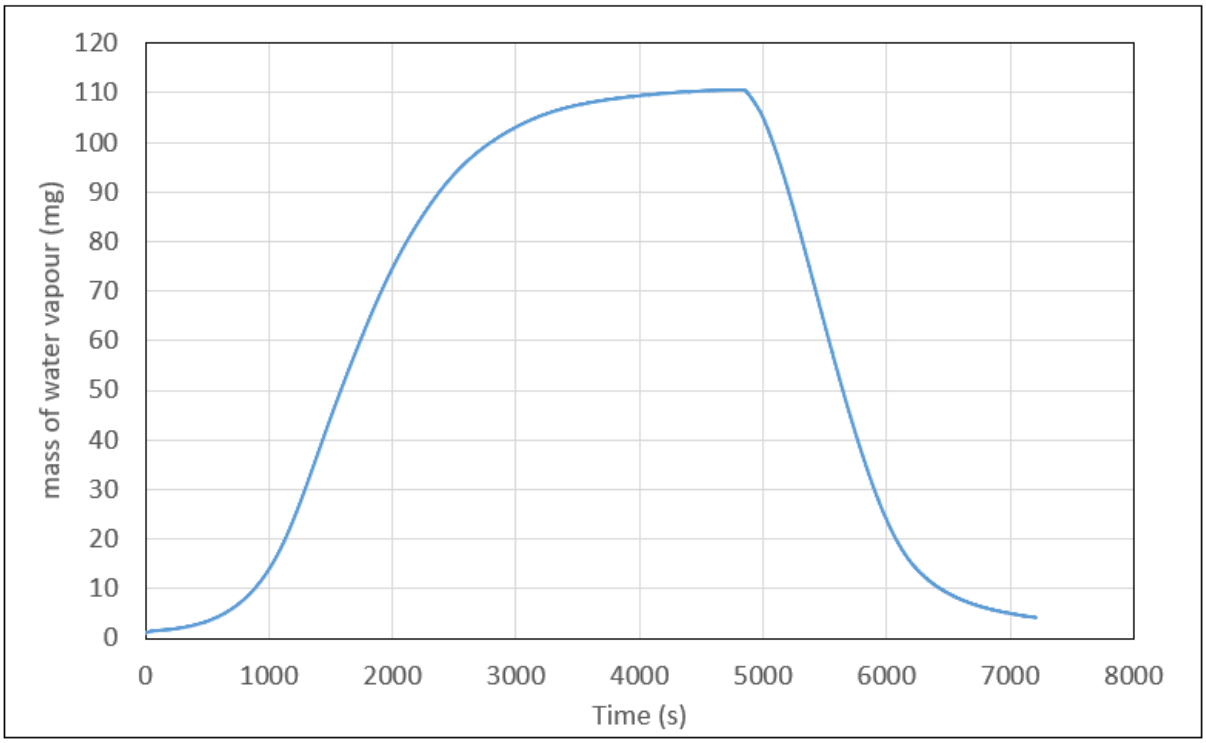



*Fig. 3. 24: Mass of water vapour generated during sterilization process predicted by model.*

### 3.3.3 Model limitations and improvement opportunities

The model analysis showed that predictions are highly sensitive to the choice of global heat transfer coefficient. It should also be noted that uncertainties in the positioning and sensitivity

of temperature probes during experiments, as well as the assumption of neglecting vapour generation inside the mashed potato, could further contribute to deviations between experimental and simulated results. This latter assumption was introduced deliberately, as the objective of the present model was to remain as simple as possible while still capturing the dominant trends in temperature and pressure evolution inside the container. Again, in the model, the mashed potato was also represented as a homogeneous solid, whereas in reality it is a porous medium containing entrapped air and water. Consequently, internal phase change phenomena within the porous structure of the mashed potato were not explicitly resolved, and evaporation was assumed to occur only at the food surface. The model also assumed the headspace volume as constant. However, the real system experiences a progressive decrease in headspace due to the slight expansion and upward shift of the mashed potato. This geometric change modifies both heat and mass transfer, particularly near the upper domain. Such effects have been highlighted in thermal studies of deformable foods, where ignoring shape changes reduces model fidelity (Fu et al., 2023). In the experiment, the mashed potato was observed to expand and shift upward, reducing the effective headspace volume. This geometric change was not accounted for in the model, and its omission contributes to underestimation of internal pressure buildup. Additionally, the model assumed perfect thermal contact between the food and can wall. In practice, imperfect filling or localized shrinkage during heating may result in the formation of air pockets, which create thermal resistance. Despite these limitations, the surface evaporation approach was sufficient for estimating the total water vapour transfer to the headspace, which directly governs the internal pressure as the combined contribution of dry air pressure and water vapour partial pressure. Even with these simplifying assumptions, the model provided a reasonable prediction of temperature and pressure distributions within the can, although further refinements could improve its accuracy.

### 3.4 Conclusions

This chapter presented a simple study of the conventional thermal sterilization process in rigid metal containers using a solid model food system. The objective was to study the coupled evolution of temperature and pressure inside the container under conventional retort conditions through experimental measurements and numerical simulation. The study also focused on understanding the influence of heat transfer coefficient in temperature prediction. A solid mashed potato formulation was selected as the model food due to its consistent physical structure and thermophysical properties. The food was characterized experimentally for moisture content, specific heat, thermal conductivity, and density. Thermal sterilization experiments were conducted in a pilot-scale retort system using metal cans. Temperature and pressure were monitored at multiple positions within the food and headspace. Internal pressure increased continuously during the heating and holding phases, reaching a peak of 2.45 bar relative pressure, and decreased rapidly during cooling.

A numerical model was developed in COMSOL® Multiphysics 6.3 using a 2D-axisymmetric geometry. The simulation accounted for heat conduction in the food, laminar flow in the headspace, and pressure evolution. Temperature predictions were found to be highly sensitive to heat transfer coefficients. This result highlights the strong role of boundary heat transfer conditions in controlling internal heating rates. For pressure evolution, the model simultaneously calculated the contributions of dry air and water vapour within the headspace using coupled heat and mass transfer equations. The dry air pressure was obtained directly from the ideal gas law based on its thermodynamic state, while the water vapour pressure evolved according to the interfacial mass flux between the mashed potato surface and the headspace. During the initial heating stage (up to around 1000 s), pressure rise was mainly governed by the

thermal expansion of dry air, which responded rapidly to temperature increase in the headspace. As heating progressed, evaporation from the food surface intensified and water vapour generation became the dominant factor, contributing significantly to the total headspace pressure. The model predicted that vapour pressure eventually exceeded the dry air component near the end of heating and during the holding period, indicating a transition from air-dominated to vapour-driven pressurization.

The framework developed in this chapter provided mechanistic insight into sterilization behaviour in rigid containers by distinguishing the contributions of dry air and water vapour to headspace pressure. These findings also define the scope for the next stage of this work. Since water vapour pressure only becomes significant at higher temperatures, while dry air pressure governs the initial heating period, subsequent modelling of packaging deformation during heating at lower temperatures will focus on dry air as the primary contributor. Furthermore, the selective importance of CFD in describing headspace behaviour supports its use in the next chapter, which addresses coupled CFD–FSI–thermal and structural mechanics analysis. This transition moves from rigid metal containers to flexible and semi-rigid polymeric packaging, where the response of the package itself becomes a critical factor. By integrating fluid–structure interactions with thermal modelling, the next chapter explores packaging materials deformation under the combined effects of internal pressure, and heat transfer.

# Chapter 4
# Coupled CFD–FSI–Thermal and Structural Mechanics Analysis of Deformation in Food Packaging under Air Injection and Heat Treatment

## 4.1 Introduction

The previous chapter provided a simple thermo–fluid framework for understanding internal pressure development during thermal sterilization in rigid containers, highlighting that pressure evolution arises primarily from dry air expansion at the initial stages of the sterilization process and pressure due to water vapour becomes dominant at the later stage and for majority of the sterilization process. Building on these findings, the present chapter extends the analysis to semi-rigid polymeric packaging, where the structural deformation of the container interacts dynamically with the internal air and temperature distribution.

In contrast to metallic cans, polypropylene (PP) trays possess a high degree of mechanical flexibility under internal pressurization, making them particularly sensitive to the combined thermal and mechanical effects during heating. These effects are especially relevant for flexible and semi-rigid systems, where the interactions between internal pressure, temperature, and material properties govern overall stability. Understanding these coupled thermo–fluid–mechanical interactions is therefore essential for predicting failure and improving process safety in heat-treated packaged foods. This investigation is also crucial for understanding the physical phenomena occurring inside polymer packaging during heat treatment, which will further support the design of mechanical constraints suited for processes such as microwave-based sterilization, where deformation control is critical.

To address this, the chapter integrates CFD–FSI–thermal and structural mechanics modelling with experimental investigations to study deformation of PP trays under two conditions:

(1) Air injection, simulating the early pressurization stage dominated by dry air without any heat treatment, and

(2) Heat treatment in oven, representing heat treatment conditions where temperature rise and dry air expansion occur.

This approach enables identification of maximum pressure holding capacity of the PP tray in different conditions, rupture-prone zones, quantification of stress concentration mechanisms, and analysis of airflow influence on internal pressure evolution. Additionally, the study also explores the role of mechanical constraints in the form of preloads on the packaging system.

## 4.2 Objectives and Research Questions

The objective of this chapter is to investigate the structural integrity of PP food trays with and without heat treatment by combining experimental analysis with numerical modelling. The study focuses on understanding how air flow, pressure buildup, deformation, and stress interact to cause rupture in food trays. Through numerical modelling, an additional objective is to identify the zones that are more prone to rupture based on stress concentration. The chapter also

aims to evaluate whether applying controlled preloads can alter rupture dynamics and provide greater stability to the packaging system.

It is important to note that water vapour generation and evaporation are not within the scope of this study. The heat treatment experiments are conducted for a shorter duration in an oven, representing only the initial stage of heating in a retort sterilization process, where dry air expansion dominates the internal pressure build-up at the early stages of heating. This approach allows the investigation to focus primarily on the mechanical effects acting on the packaging structure during the early phase of heating.

From this objective and scope, the following research questions are addressed, which have not been systematically studied so far:

1. How does the deformation of the lidding film evolve under internal pressure buildup, and where do stresses concentrate?
2. What are the rupture-prone regions of the tray–lid system as identified by von Mises stress analysis, and how do these compare with experimental rupture locations?
3. How does the application of mechanical constraints modify pressure evolution, and rupture?
4. Can mechanical preloads delay the onset of rupture, and how does this effect vary with the magnitude of applied force?

The detailed structure of the study, including the division into unconstrained (Part A) and constrained (Part B) configurations, is described in the following section on Experimental Protocols and Design. Hence, this chapter is structured into two parts. Part A addresses the rupture mechanisms of PP trays without mechanical constraint under pressure buildup, both without heat treatment (air injection) and with heat treatment conditions. It consists of experimental studies and numerical studies to investigate the physical phenomena of air flow and fluid–structure interactions using CFD, and structural mechanics. Part B experimentally addresses the influence of a mechanical constraint on pressure dynamics and rupture behavior of the food tray packaging.

## 4.3 Materials and Methods

### 4.3.1Experimental Study

#### 4.3.1.1 Tray Materials and Food Matrix

All experiments were conducted using commercially available ready-to-eat (RTE) PP food trays. The trays (Fig. 4.1) were sealed using a 65 µm PP film, with an industrial-grade Multivac system (Type Galaxy, Model TS 355, Multivac, France) at 160°C in 5s. The mashed potato formulation was similar to that prepared in Chapter 3.

Three types of tray configurations were used throughout the study:

(i) Empty trays with an air inlet, for air injection experiments.

(ii) Empty trays filled with air at atmospheric pressure, for thermal treatment experiments without mashed potato.

(iii) Trays filled with 300 g of mashed potato and with a headspace of 25 mm for food-loaded thermal experiments.

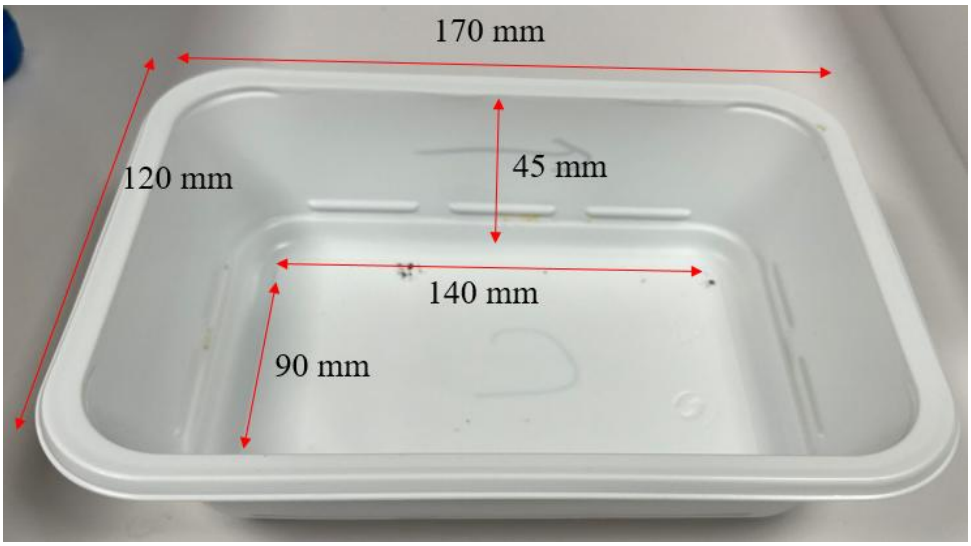



*Fig. 4. 1: PP ready-to-eat food tray dimensions.*

#### 4.3.1.2 Pressure and Temperature Measurement Devices

For thermal processing experiments, the ambient air temperature inside the oven (MIWE deck oven, CO 1.1208, Germany) was recorded using a SSR Type T thermocouples (Ellab SARL, France) placed at the side of the oven chamber. The thermocouple was connected to a data acquisition system (DATALOG, D9CO, AOIP, France) and provided real-time feedback on the oven's internal thermal profile.

To measure the internal conditions during all experiments, NanoVACQ PT sensors manufactured by TMI-Orion (Castelnau-le-Lez, France) were placed into the tray prior to sealing.

#### 4.3.1.3 Mechanical Constraint Device

For experiments involving fixed preloaded mechanical constraints, a custom mechanical fixture was designed to apply vertical loads to the upper surface of the PP sealing film (Fig. 4.2). The device included a rigid Polyether ether ketone (PEEK) plate to apply the force. The device also consisted of a manual force tuner which regulated the preloaded force.

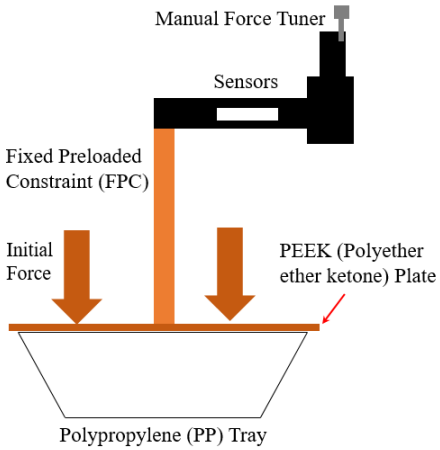



*Fig. 4. 2: Schematic of Fixed Preloaded Constraint (FPC).*

#### 4.3.1.4 Air injection system equipped with mechanical constraint

For experiments involving direct air pressurization, a custom-built air injection setup was designed to control and monitor the flow of air into the sealed trays (Fig. 4.3 and Fig. 4.4). The system consisted of a mass flow controller connected to a compressed air source, and a stainless-steel tube inserted into one edge of the tray. Three discrete air flow rates were selected to simulate low, intermediate, and high dynamic loading conditions: Q1= 0.1 L/min, Q2 = 0.15 L/min, and Q3= 0.6 L/min. Air injection was continued until rupture of the sealing film, at which point the tray was deemed to have failed.

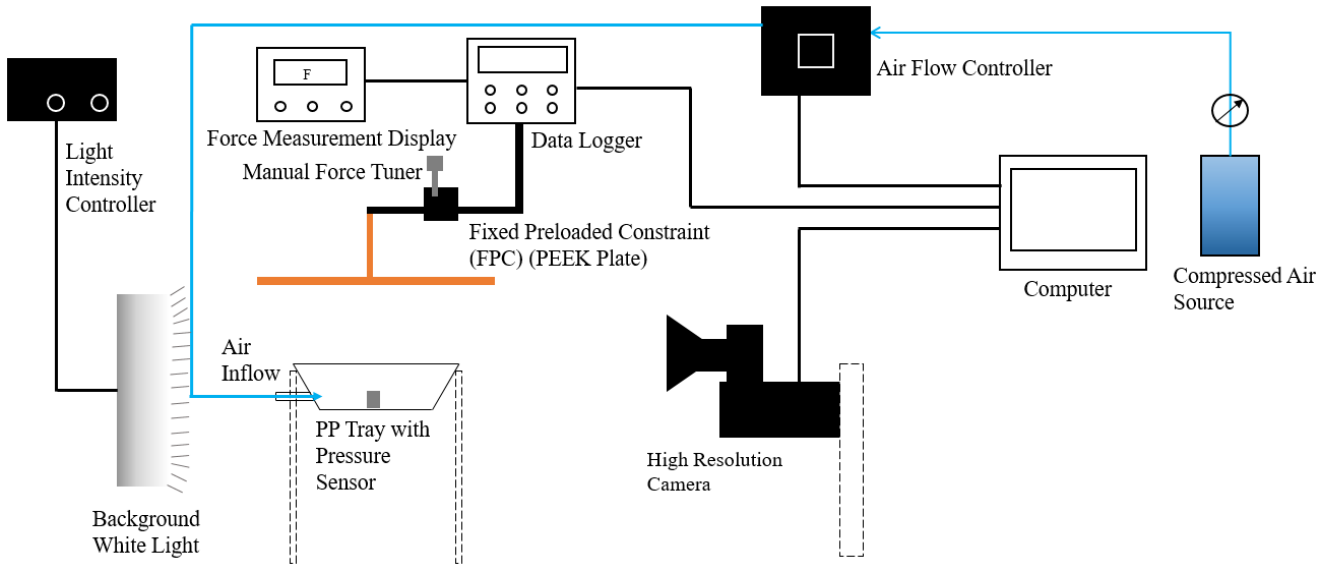



*Fig. 4. 3: Schematic representation of the various components in the air injection system with mechanical constraint.*

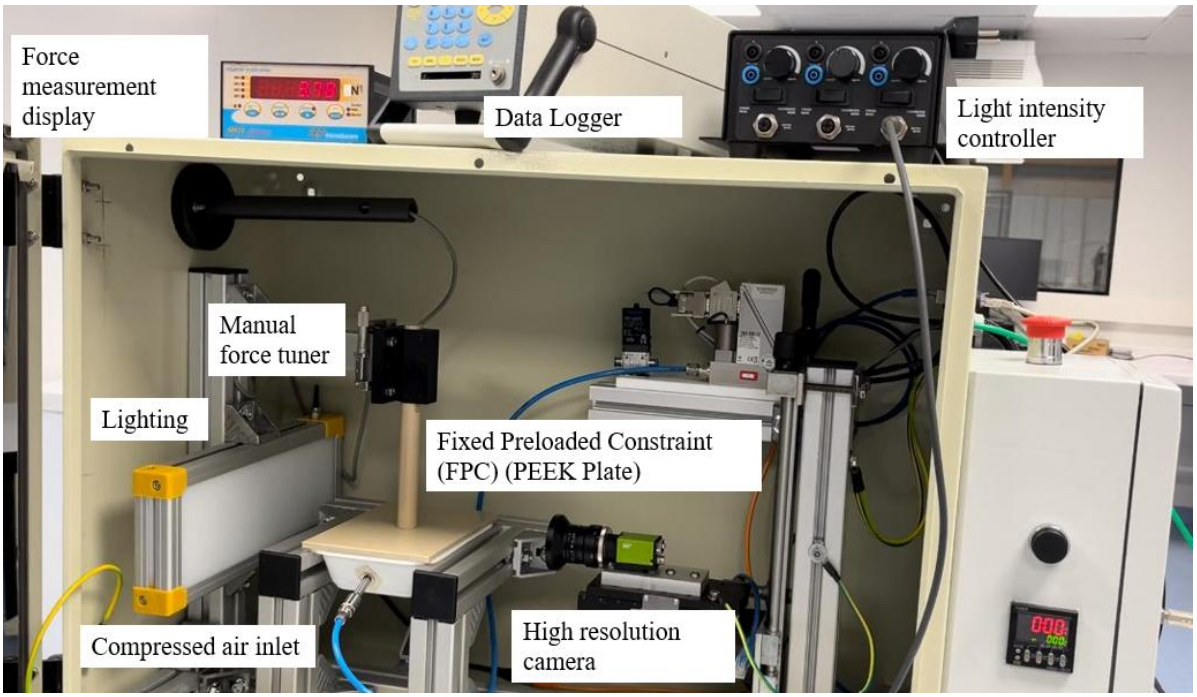



*Fig. 4. 4: Experimental setup of the air injection system equipped with mechanical constraint.*

#### 4.3.1.5 Imaging System for Deformation Monitoring

To observe deformation behavior and rupture during air injection experiments, a high resolution digital camera (Go, JAI Ltd., Japan) was positioned horizontally in front of the tray, at a fixed distance of approximately 20 cm. The camera captured images at a rate of 1 frame per second using an image acquisition software (HIRIS, R&D Vision, France). These images were later analyzed to track film displacement using ImageJ® software and identify rupture timing. Rupture was defined as the point of sudden pressure drop, accompanied by visible tearing of the sealing film on the camera feed.

#### 4.3.1.6 Thermal treatment equipped with mechanical constraint

All heat treatment experiments were conducted using a natural convection industrial oven (MIWE deck oven, CO 1.1208, Germany), which allows programmable temperature control (Fig. 4.5 and Fig. 4.6). The oven door was fitted with a glass window to visually monitor tray condition throughout the heating process. The SSR Type T thermocouple (Ellab SARL, France) placed in the side of the oven chamber continuously monitored oven temperature for consistency and process control.

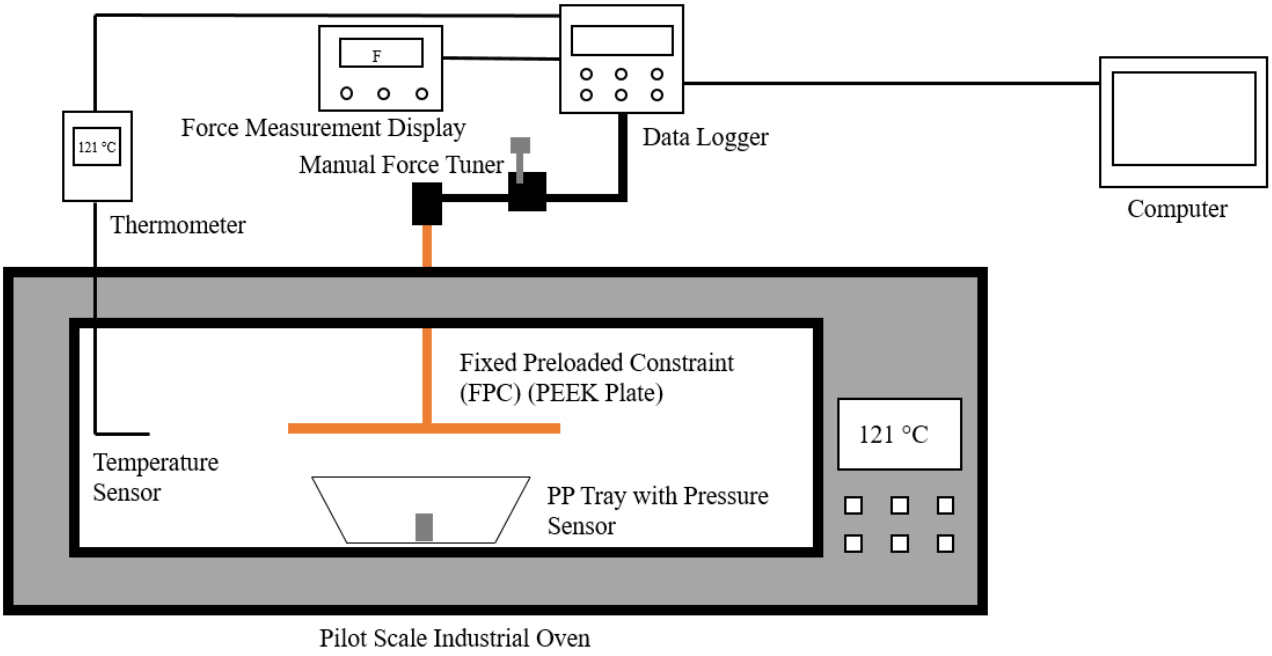



*Fig. 4. 5: Schematic representation of the various components in the thermal treatment of PP trays equipped with mechanical constraint.*

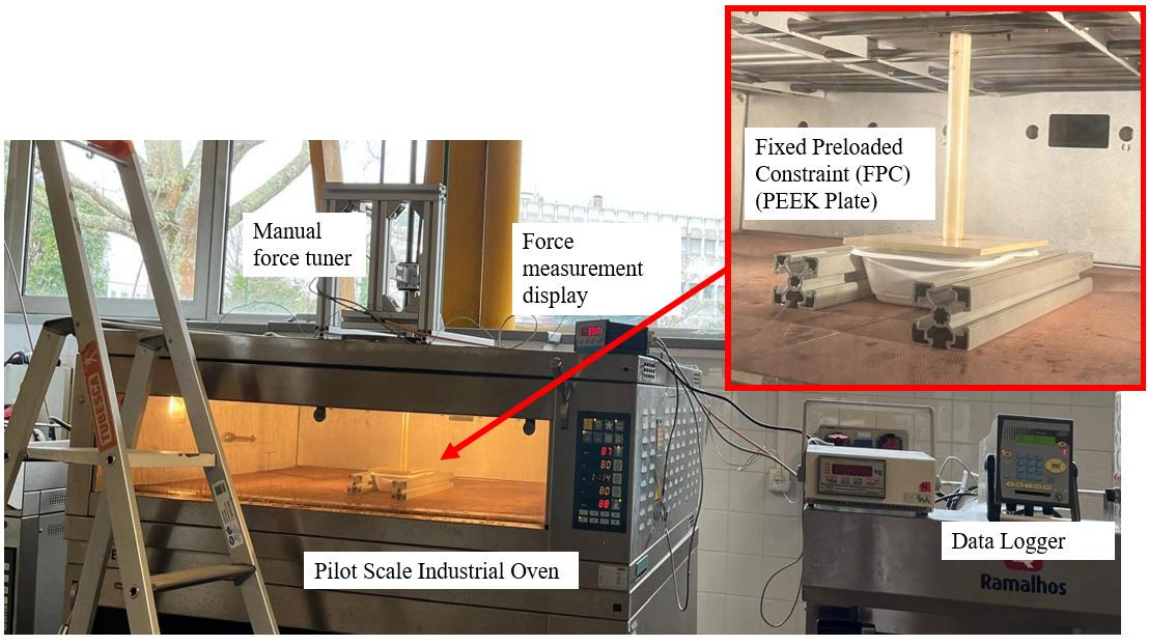



*Fig. 4. 6: Experimental setup of the thermal treatment of PP trays equipped with mechanical constraint.*

### 4.3.2 Experimental Protocols and Designs

The experimental study was structured in two main parts to investigate the structural response of ready-to-eat PP trays under different pressure and thermal conditions. In Part A, experiments were performed without applying any mechanical constraints to the upper sealing film. This condition is referred to as No Constraint (NC). In contrast, Part B involved the application of a fixed mechanical preload onto the film surface. This condition is referred to as the Fixed Preloaded Constraint (FPC). Each part was subdivided into three configurations: (1) air injection without heat (A1 and B1), (2) heat treatment in empty PP tray (A2 and B2), and (3) heat treatment in trays with food and headspace (A3 and B3). In total, six experimental configurations were explored. All experiments were conducted in triplicates except for the ones involving measurement of internal pressure due to the unavailability of enough pressure sensors during the experiments. The reuse of pressure sensors was also not possible within the timeframe of this study. In total, 80 trays were prepared and tested across all conditions for 80 experiments: 12 experiments corresponding to the A1 configuration, 4 experiments each corresponding A2 and A3 configurations, and total 60 experiments corresponding to the B1, B2, and B3 configurations. Table 4.1 summarizes the entire experimental protocols and designs used in this chapter.

In Part A1 (NC – air injection without heat), the goal was to investigate how the PP tray deforms and eventually ruptures under internal air pressure, without the involvement of heat or food moisture. The empty tray was sealed with a pressure sensor which also measures temperature, and air was injected through the tube using a mass flow controller. The injection was carried out at three distinct flow rates: Q1, Q2, and Q3. The key variables measured were internal pressure, rupture time, and film displacement.

In Part A2 (NC – heat treatment in empty PP tray), the objective was to understand pressure and temperature buildup inside sealed, empty air-filled trays during a heat treatment process.

Trays equipped with TMI-Orion sensors were placed inside the oven programmed to heat from 20°C to 121°C. The trays were placed when the oven air temperature was around 20°C and the air in the oven was heated to 121°C. The experiments were stopped whenever a rupture of the tray occurred which is usually before the oven air temperature arrived at 121°C. Fig. 4.7 shows the evolution of experimental oven air temperature. Internal headspace pressure and temperature were recorded, and rupture was identified by a sudden pressure drop. The measured outputs included internal pressure, headspace temperature, oven temperature, and rupture time.

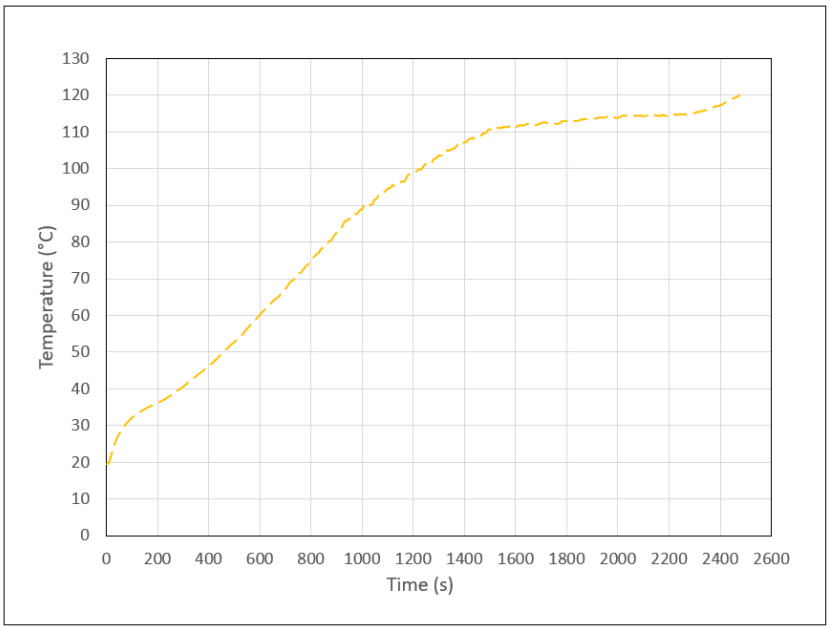



*Fig. 4. 7: Experimental measurement of temperature evolution of oven air.*

In Part A3 (NC – heat treatment in trays with food and headspace), the effect of moisture released from food during heating was studied. Each tray was filled with 300 g of mashed potato, and a sensor was inserted in the headspace before sealing. The trays were then subjected to the same heating profile used in Part A2. The aim was to record the internal pressure and temperature. Measured variables included headspace pressure, headspace temperature, oven air temperature, and rupture time.

In Part B1 (FPC – air injection without heat with mechanical constraint), the influence of external mechanical force on tray deformation during air injection was assessed. Sealed trays with a TMI sensor were placed into the custom-built then mounted in the mechanical fixture with one of the three preload levels (F1, F2, F3). Air injection was conducted at the same flow rates as in Part A1, and rupture was observed in terms of internal pressure buildup, visual deformation, and rupture time. The mechanical reaction force acting on the film was monitored using a data logger integrated into the fixture.

In Part B2 (FPC – heat treatment in empty PP tray with mechanical constraint), the trays were sealed with ambient air and a sensor, then mounted in the mechanical fixture with one of the three preload levels (F1, F2, F3). The air surrounding the tray in the oven was heated from 20°C to 121°C, and pressure, headspace temperature, and oven air temperature were recorded until rupture occurred. Additionally, the mechanical reaction force acting on the film was monitored using a data logger integrated into the fixture.

In Part B3 (FPC – heat treatment in trays with food and headspace and with mechanical constraint), each tray was loaded with 300 g of mashed potato, sealed with a TMI-Orion sensor, and fixed in the mechanical constraint fixture under one of the three preload conditions. The thermal profile and measurement approach remained the same as in Part B2. Variables measured included headspace pressure, headspace temperature, oven temperature, rupture time, and film reaction force.

*Table 4. 1: Summary of experimental protocols and designs.*

| Configuration | Configuration Meaning | Constraint Type | Tray Content | Air Flow (L/min) | Heating Profile | Preload (N) | Measured Variables |
|---|---|---|---|---|---|---|---|
| A1 | Air injection without heat | NC | Air only | Q1, Q2, Q3 | None | None | Pressure, rupture time, deformation (image-based) |
| A2 | Heat treatment in empty PP tray | NC | Air only | – | 20°C → 121°C | None | Pressure, headspace temperature, oven temperature, rupture time |
| A3 | Heat treatment with food and headspace | NC | Mashed potato (300 g) | – | 20°C → 121°C | None | Pressure, headspace temperature, oven temperature, rupture time |
| B1 | Air injection with mechanical constraint | FPC | Air only | Q1, Q2, Q3 | None | F1, F2, F3 | Pressure, rupture time, film reaction force |
| B2 | Heat treatment in empty PP tray with mechanical constraint | FPC | Air only | – | 20°C → 121°C | F1, F2, F3 | Pressure, headspace temperature, oven temperature, rupture time, film reaction force |
| B3 | Heat treatment in trays with food and headspace and with mechanical constraint | FPC | Mashed potato (300 g) | – | 20°C → 121°C | F1, F2, F3 | Pressure, headspace temperature, oven temperature, rupture time, film reaction force |

Notes:

- Q1 = 0.1 L/min, Q2 = 0.15 L/min, Q3 = 0.6 L/min
- F1 = 5 N, F2 = 20 N, F3 = 40 N
- NC = No Constraint; FPC = Fixed Preloaded Constraint

### 4.3.3 Numerical Modelling

Numerical modelling was performed for Part A of the study (NC). The objective was to simulate pressure build-up, airflow, heat transfer, and film deformation during air injection and heat treatment of PP trays. The modelling integrated Computational Fluid Dynamics (CFD), Heat Transfer, and Structural Mechanics within a Fluid–Structure Interaction (FSI) framework. Stress analysis was conducted using the von Mises criterion to locate rupture-prone regions. All simulations were carried out using COMSOL Multiphysics®6.3.

#### 4.3.3.1 Model Description

A simplified geometry without rounded tray corners was used in all models because it is assumed that the corners had a negligible effect on the global airflow and heat transfer behaviour. Three different models with the same tray geometry were constructed to represent the experimental configurations of Part A (Fig. 4.8). The geometries were built in COMSOL Multiphysics® based on the actual tray dimensions used in the experiments. Each model consisted of a fluid domain corresponding to the headspace, and in the case of food-loaded trays, an additional solid domain representing the food matrix. Model 1 represented the air injection experiments (A1). The geometry consisted of an empty PP tray with air. An inlet was included at one edge of the tray to allow air injection through the tube. Model 2 represented the empty tray subjected to heat treatment (A2). The geometry consisted of a sealed PP tray with air. Heat flux was applied through all six sides of the tray to simulate the heating profile of the oven. No inlets or outlets were defined, as the system was closed. Model 3 represented the food-loaded trays during heat treatment (A3). The geometry included a PP tray filled with 300 g of mashed potato, leaving a headspace of 25 mm above the food. The solid domain of mashed potato was modelled with its experimentally measured thermal properties (thermal conductivity, specific heat, and density) as described in Chapter 3. The headspace was defined as an air domain, with thermophysical properties imported directly from the COMSOL® material library as temperature-dependent functions. For all models, the PP tray and PP film were defined as solids. Their mechanical and thermal properties (Young's modulus, Poisson ratio, density, thermal conductivity, and specific heat) were taken from bibliographic sources. But only thermal properties were implemented for PP tray, as mechanical properties were only necessary for the PP film in this study. In Model 1, the air inlet was positioned at the center of one side of the tray. In Models 2 and 3, the complete geometry was simulated to provide a more realistic representation of the physical behaviour of the trays under heating conditions. Therefore, symmetry was not applied. Table 4. 2 lists the important parameters for numerical model.

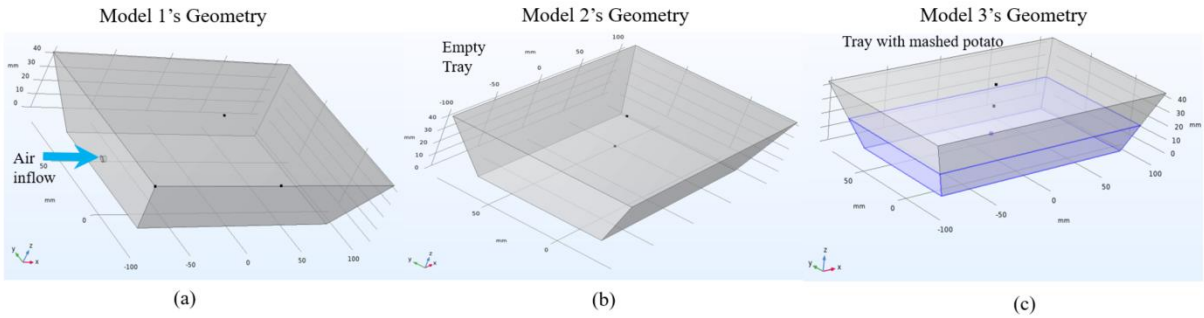



*Fig. 4. 8: Different model construction with same tray geometry for three different models with (a) Model 1: air injection in empty tray (b)Model 2: heat treatment in empty tray (c) Model 3: heat treatment in tray with mashed potato.*

*Table 4. 2: Important parameters for numerical model.*

| **Parameters** | **Value** | **References** |
|---|---|---|
| Density of PP | 930 kg/m$^3$ | Maddah, 2016 |
| Specific heat of PP | 1542.3 J/(kg.K) | Gaur & Wunderlich, 1981 |
| Thermal conductivity of PP | 0.22 W/(m.K) | Xu et al., 2020 |
| Thickness of PP film layer | $6.5 \times 10^{-5}$ m | measured |
| Thickness of PP tray layer | $3 \times 10^{-4}$ m | measured |
| Poisson ratio of PP | 0.42 | Kumar et al., 2015 |
| Young's modulus of PP | $1.847 \times 10^9$ Pa | Kumar et al., 2015 |
| Convective heat transfer coefficient | 40 W/(m$^2$.K) | Carson et al., 2006 |

For model 1, 2, and 3, the COMSOL® Laminar Flow interface solves the Navier-Stokes, and continuity equations within air domain. For model 2 and 3, the Navier–Stokes equations are coupled with heat transfer, which accounts for both fluid flow and temperature distribution. The momentum conservation equation and continuity equation are written as:

$$\frac{d(\rho_a \boldsymbol{u})}{dt} + \rho_a(\boldsymbol{u}.\nabla)\boldsymbol{u} = \rho_a \boldsymbol{g} - \nabla P + \mu_a \nabla^2 \boldsymbol{u} \quad 4.1$$

$$\frac{\partial \rho_a}{\partial t} + \nabla.(\rho \boldsymbol{u}) = 0 \quad 4.2$$

where $\rho_a$ is the density of air (kg/m$^3$), **u** is the velocity vector describing the air motion within the headspace domain (m/s), t is time (s), P is pressure (Pa), **g** is gravitational acceleration vector (m/s$^2$), $\mu_a$ is dynamic viscosity of air (Pa.s).

A no-slip boundary condition was applied to all the tray walls and film wall.

$$\boldsymbol{u} = 0 \quad 4.3$$

For model 2 and 3, the temperature distribution is computed using the general heat transfer equation for both the solids and fluid domain:

$$\rho_{mp} C_{p,mp} \frac{\partial T_{mp}}{\partial t} + \nabla.\boldsymbol{q} = 0 \quad 4.4$$

$$\boldsymbol{q} = -k_{mp}\nabla T_{mp} \tag{4.5}$$

$$\rho_a C_{p,a}\frac{\partial T_a}{\partial t} + \rho_a C_{p,a}\boldsymbol{u}\,.\nabla T_a + \nabla.\boldsymbol{q} = 0 \tag{4.6}$$

$$\boldsymbol{q} = -k_a\nabla T_a \tag{4.7}$$

where, $\rho_{mp}$ is the density of mashed potato (kg/m$^3$), $\rho_a$ is the density of air (kg/m$^3$), $C_{p,mp}$ is the specific heat of mashed potato (J/kg/K), $C_{p,a}$ is the specific heat of air (J/kg/K), $T_a$ is temperature of air (K), $T_{mp}$ is temperature of mashed potato (K), $k_{mp}$ is thermal conductivity of mashed potato (W/m/K), $k_a$ is thermal conductivity of air (W/m/K), $\boldsymbol{q}$ is heat flux vector (W/m$^2$), and $\boldsymbol{u}$ is velocity vector of air flow (m/s).

In all the three models (model 1, 2, and 3), structural mechanics and fluid-structure interactions were implemented only on the PP film and not on the PP tray. For the PP film, the conservation of momentum for a deformable solid was implemented as (Oden & Edition, 2008):

$$\rho_{pp}\frac{\partial^2 \boldsymbol{d_s}}{\partial t^2} = \nabla.S + \boldsymbol{F}_v \tag{4.8}$$

where $\rho_{pp}$ is the density of the PP film (kg/m$^3$), $\boldsymbol{d_s}$ is the displacement vector (m), $S$ the second Piola–Kirchhoff stress tensor (N/m$^3$), and $\boldsymbol{F}_v$ is the body force per unit volume (N/m$^3$).

To study the structural mechanics of the PP film, two important parameters were implemented in the models: the Young's modulus and Poisson ratio of PP. These two parameters were used to study the stiffness tensor ($\boldsymbol{C}$) which characterizes the material's elastic properties, determines the stress relation to strain in the elastic range. It is related to the material constants as (L. Zhang et al., 2014):

$$\boldsymbol{C} = \boldsymbol{C}(E, v) \tag{4.9}$$

where, E is the Young's modulus of PP, and $v$ is the Poisson ratio of PP.

A simplified mathematical relationship is used to express the stiffness tensor as (Quickfem, 2023):

$$\boldsymbol{C} = \frac{E}{1-v^2}\begin{bmatrix} 1 & v & 0 \\ v & 1 & 0 \\ 0 & 0 & \dfrac{1-v}{2} \end{bmatrix} \tag{4.10}$$

In all of the three models, the distortion energy theory, i.e., the von Mises Criterion (explained in 2.6.3 Chapter 2) was used in the identification of stress concentrations on the PP film. For this purpose, the von Mises equivalent stress ($\sigma_v$) was used and is expressed as (Semeliss et al., 1990):

$$\sigma_v = \sqrt{\frac{1}{2}[(\sigma_1 - \sigma_2)^2 + (\sigma_2 - \sigma_3)^2 + (\sigma_3 - \sigma_1)^2]} \quad 4.11$$

where, $\sigma_1, \sigma_2, and\ \sigma_3$ are the principal stresses, defined as the eigenvalues of the stress tensor (**T**) obtained by solving the characteristic equation (Semeliss et al., 1990):

$$|\sigma_{ij} - \sigma\delta_{ij}| = 0 \quad 4.12$$

where, $\sigma_{ij}$ represents the components of the stress tensor, $\sigma$ is the principal stress (scalar), $\delta_{ij}$ is the Kronecker delta.

According to the theory, yielding or rupture is expected when (Semeliss et al., 1990):

$$\sigma_v \geq \sigma_y \quad 4.13$$

where, $\sigma_y$ is the yield strength of the material.

#### 4.3.3.2 Initial and Boundary Conditions

*4.2.3.2.1 Initial conditions*

The initial temperature in all domains was set to

$$T_0 = 20°C \text{ [for model 1,2,3]} \quad 4.14$$

The initial air velocity field was defined as

$$u_0 = 0\ m/s \text{ [for model 1,2,3]} \quad 4.15$$

The initial relative pressure in the headspace was taken as

$$p_0 = 0\ Pa \text{ [for model 1,2,3]} \quad 4.16$$

The initial displacement of the PP film was set to

$$\boldsymbol{d_{PP}} = \begin{bmatrix} \mathbf{0} \\ \mathbf{0} \\ \mathbf{0} \end{bmatrix} m \text{ for all domains [for model 1,2,3]} \quad 4.17$$

The initial velocity of the PP film was specified as

$$\frac{\partial \boldsymbol{u_{PP}}}{\partial t} = \begin{bmatrix} \mathbf{0} \\ \mathbf{0} \\ \mathbf{0} \end{bmatrix} m/s \text{ for all domains [for model 1,2,3]} \quad 4.18$$

where is the $\boldsymbol{u_{PP}}$ velocity of the PP film.

*4.3.3.2.2 Boundary conditions*

**Model 1 (Air injection inside PP tray model):**

The inlet boundary condition was prescribed as a mass flow, ensuring that the injected air entered the tray at the defined flow rate:

$$\int \rho_a(\boldsymbol{u}.\boldsymbol{n})dS = \dot{m}_i \quad 4.19$$

$$\dot{m}_i = \rho_a Q_i \quad 4.20$$

where, $\dot{m}_i$ is the mass flowrate (kg/s), $\rho_a$ is the density of air (kg/m$^3$), and $Q_i$ is the inlet volumetric flow rates (L/min). i (i = 1,2,3) indicates the three cases of air flowrates i.e $Q_1 = 0.10\ L/min; Q_2 = 0.15\ L/min; Q_3 = 0.60\ L/min.$

On all tray walls, the no-slip condition was imposed to set the fluid velocity to zero:

$$\boldsymbol{u} = \begin{bmatrix}\mathbf{0}\\ \mathbf{0}\\ \mathbf{0}\end{bmatrix} m/s \text{ on tray walls} \quad 4.21$$

The tray body and film edges were fixed to prevent rigid-body motion:

$$\boldsymbol{d_{tray}} = \begin{bmatrix}\mathbf{0}\\ \mathbf{0}\\ \mathbf{0}\end{bmatrix} m \quad 4.22$$

where, $\boldsymbol{d_{tray}}$ is the displacement of the PP tray.

The fluid pressure field acted on the structural surface of the PP film as a traction load, expressed as a film load of pressure:

$$\delta W = \int [(-p\boldsymbol{n}) \cdot \delta \boldsymbol{d_{PP}}]dA \quad 4.23$$

where, A is surface area of the PP film over which the pressure acts in upward direction, p is the pressure obtained from CFD, $\boldsymbol{d_{PP}}$ is the displacement vector of the structural surface of PP film. This is used to couple fluid pressure to structural deformation. δW is the pressure-volume work associated with fluid motion that acts on the PP film.

**Model 2 (Heat treatment inside empty tray model):**

External heating from the oven was imposed as a convective heat-flux boundary condition on all outer tray and film surfaces:

$$q_0 = h_{oven}(T_{oven}(t) - T) \quad 4.24$$

where $h_{oven}$ is the heat transfer coefficient (W/m$^2$/K) and $T_{oven}$ is the experimental temperature evolution in the oven (T). For this study, a $h_{oven}$ of 40 W/m$^2$/K was chosen as presented by Carson et al., (2006) for industrial commercial ovens.

The headspace was sealed (no inlet/outlet), enforcing zero net mass flux across all boundaries:

$$\int \rho_a(\boldsymbol{u}.\boldsymbol{n})dS = 0 \quad 4.25$$

where, $\rho_a$ is the density of air (kg/m$^3$), $\boldsymbol{u}$ is the velocity vector (m/s), $\boldsymbol{n}$ is the outward unit normal vector to the boundary surface, $S$ is surface area of the boundary of PP film and PP tray (m$^2$).

The film was loaded by the internal pressure field in the same way as in Model 1 (Eq. 4.23).

**Model 3 (Heat treatment with mashed potato model):**

External heating from the oven was prescribed as a convective heat-flux boundary on all outer tray and film surfaces similar to model 2 (Eq. 4.24)

Evaporation at the mashed potato surface was not modelled, since it was shown in Chapter 3 that water vapour has a negligible effect on total pressure during the initial heating phase, where the total pressure is primarily governed by dry air expansion.

The headspace was sealed with no inlet or outlet, hence zero net mass flux across all boundaries of the fluid domain, similar to model 2 (Eq. 4.25)

The pressure distribution computed in the fluid domain was applied as a boundary load on the inner surface of the PP film, in the same way as described for Model 1 (Eq. 4.23).

#### 4.3.3.3 Mesh independence validation

A mesh independence study was performed to examine the influence of mesh density for accuracy and stability of the simulations for the three configurations: air injection, heat treatment in empty trays, and heat treatment in trays containing mashed potato. The mesh independence study was carried out while varying the number of tetrahedral elements. Four mesh levels (for air injection studies) and five mesh levels (for heat treatment studies), from extremely coarse to normal, were tested, and prediction error % (Eq.4.26) against experimental data were calculated.

$$\%\ Error = \frac{|y_{exp} - y_{mod}|}{y_{exp}} \times 100 \qquad 4.26$$

where, $y_{exp}$ is the experimental value, and $y_{mod}$ is the predicted value obtained from the numerical model.

Overall, the results indicated that in most mesh levels, the differences in error % were similar. Errors in pressure, displacement, and temperature at the time of rupture remained within similar ranges. For air injection, pressure prediction error % ranged from 1–17% (among Q1, Q2, Q3 flow rates) for all mesh sizes, and displacement error % varied between 1–19% (among Q1, Q2, Q3 flow rates). For the heat treatment cases, maximum pressure errors reached about 11% in the empty trays and about 28% in the trays with mashed potato, while temperature errors reached about 0.2% in the empty trays and about 6% in the trays with mashed potato. In general, meshing did not improve the absolute values during predictions and hence the model was independent of mesh sizes. Since finer meshing substantially increased computational cost without providing noticeable gains in accuracy, a coarse mesh with number of tetrahedral elements of 83378 for A1 (air injection configuration), 63649 for A2 (heat treatment in empty PP tray configuration), and 61970 for A2 (heat treatment in PP tray with mashed potato configuration) was chosen for all subsequent simulations.

## 4.4 Results and discussions

### 4.4.1 Deformation–pressure coupling and model validation during air injection

Experimental observations during air injection showed that the rise in internal headspace pressure was directly associated with the progressive bulging of the PP sealing film, with rupture occurring once the seal could no longer withstand the applied pressure. The deformation was predicted as maximum displacement of PP film which corresponds to the highest vertical deformation of the PP film observed just at the time of rupture. It was measured at the time of rupture, representing the peak dome height of the PP film reached during pressurization. Fig. 4.9 shows a schematic representation of the deformation sequence of the PP film during air injection. At Q1, experimentally, the film reached 10 mm displacement at 94 s before rupturing at 42 mbar; at Q2, rupture occurred at around 41 mbar after 83 s with around 10 mm displacement; and at Q3, rupture occurred much faster at 25 s with again around 10 mm displacement and a rupture pressure of around 45 mbar (Fig. 4.10 and Fig. 4.11). The numerical model simulated the dome-shaped displacement of the film observed experimentally (Fig. 4.12). It simulated this behavior with an error of 1.48-17.86% (among Q1, Q2, Q3 air flowrate models) for pressure prediction and 1-12.96% (among Q1, Q2, Q3 air flowrate models) for deformation prediction at the time of rupture. It should be noted that the numerical model predicts an approximately linear pressure increase with time, as it was designed to capture the dominant pressure–deformation coupling and provide a first-order representation of pressure evolution under controlled air injection conditions. The experimental pressure data, although showing slight non-linearities, were obtained from a single experimental run for each flow rate, which limits the ability to conclusively identify a systematic non-linear trend. With additional replicated experiments, the apparent non-linearity could be reduced or averaged out, and thereby might potentially reveal an overall linear behaviour consistent with the model predictions. Although there was the variation of injection rates, rupture pressures remained within the narrow range of 41–46 mbar. This is because the limiting factor is the ability of the heat seal to resist internal pressurization, which depends on seal strength and defect tolerance rather than pressurization rate. In normal conditions, seal performance has been shown to plateau once a threshold is reached. This behaviour occurs because, after a certain sealing temperature and pressure are achieved, the polymer interface reaches its maximum cohesive strength, and further increases in these parameters no longer contribute to improving seal performance (Bamps et al., 2023; Yamada et al., 2017). Furthermore, studies on seal integrity have shown that small imperfections such as wrinkles and pinholes strongly influence the point of failure, with defects below 10–25 μm often escaping detection and later serving as initiation sites for rupture (Ilhan et al., 2021).

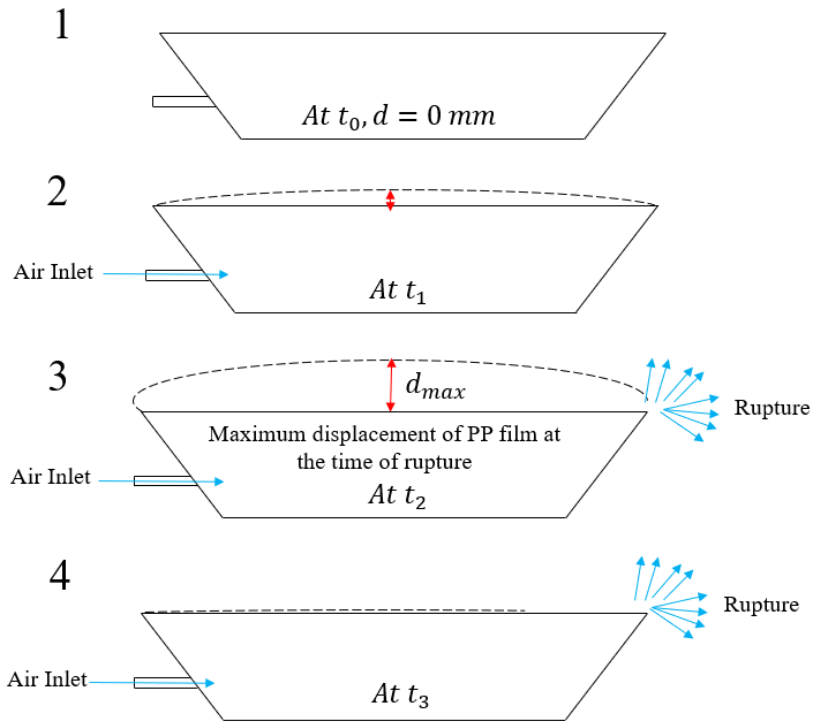



*Fig. 4. 9: Schematic representation of the deformation sequence of the PP film during air injection, showing the evolution of film displacement (d) with time (t) and the corresponding rupture of the seal at the tray edges. $d_2$ is the maximum displacement of PP film from its original position measured at the time of rupture ($t_2$).*

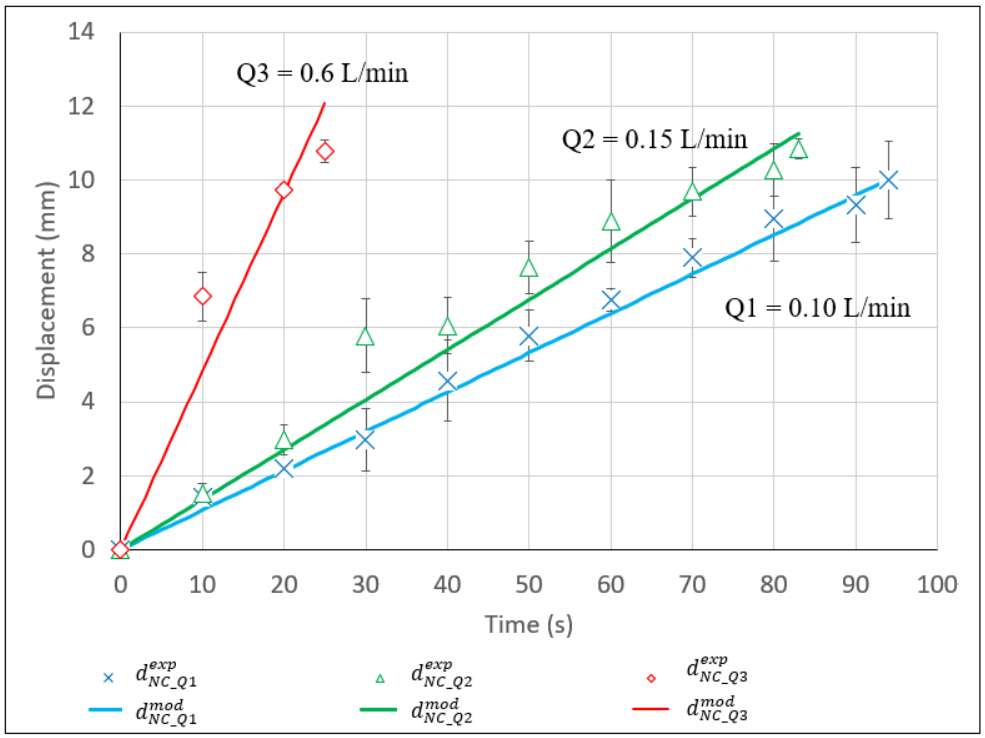



*Fig. 4. 10: Experimental and simulated displacement of PP film during air injection with no constraints (NC) at different air flowrates. (d: displacement of PP film in upward direction; exp: experimental values; mod: model values; Q1: air flowrate 1; Q2: air flowrate 2; Q3: air flowrate 3).*

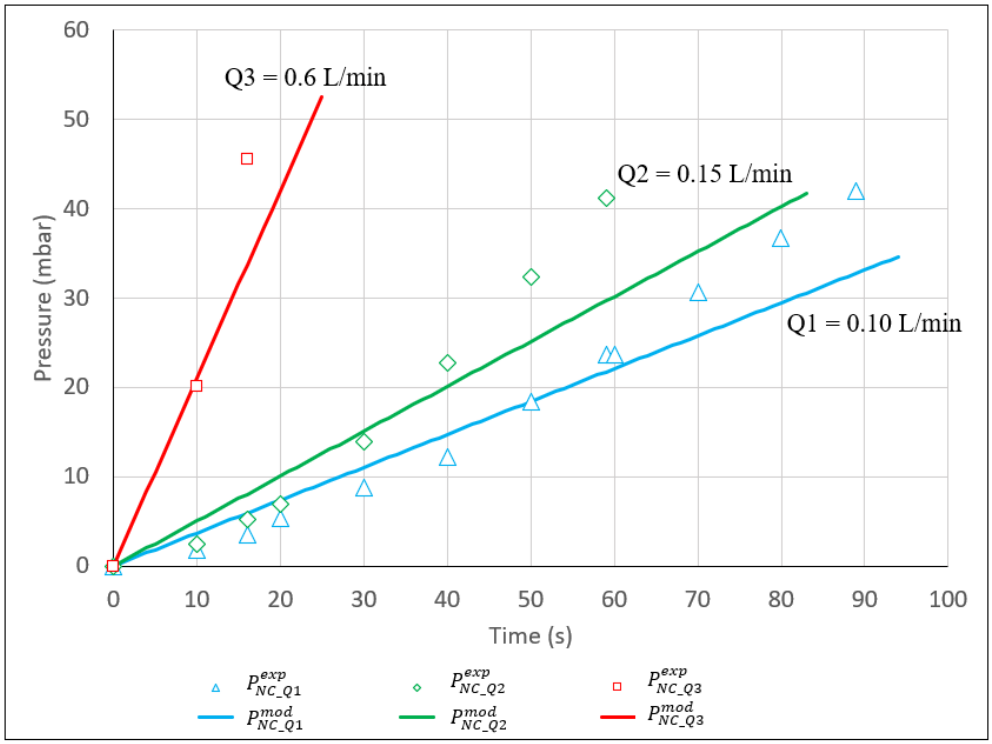
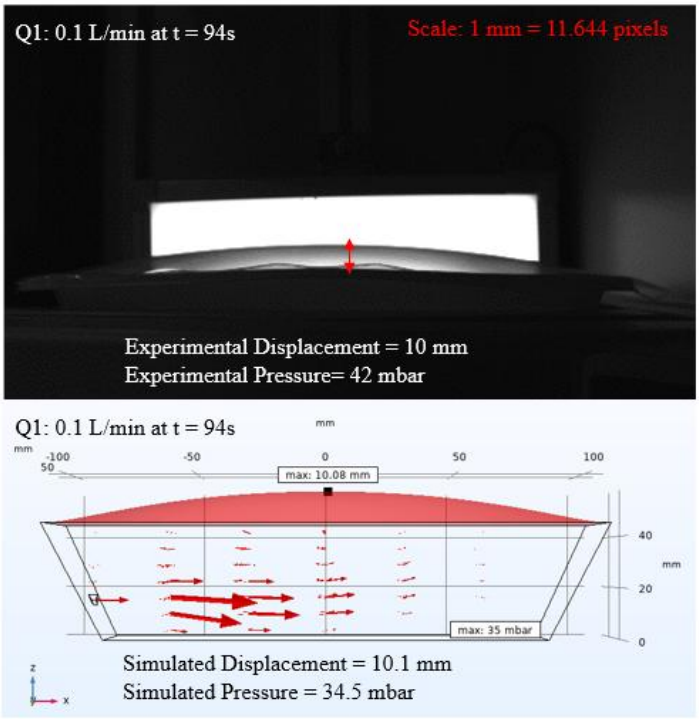
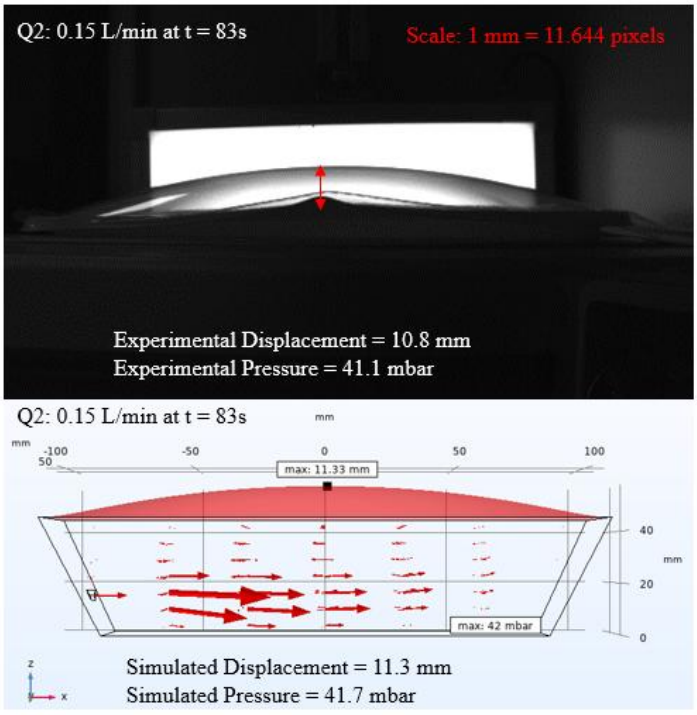



*Fig. 4. 11: Experimental and simulated relative pressure (P) inside PP tray during air injection with no constraints (NC) at different air flowrates. (P: pressure inside PP tray; exp: experimental values; mod: model values; Q1: air flowrate 1; Q2: air flowrate 2; Q3: air flowrate 3).*

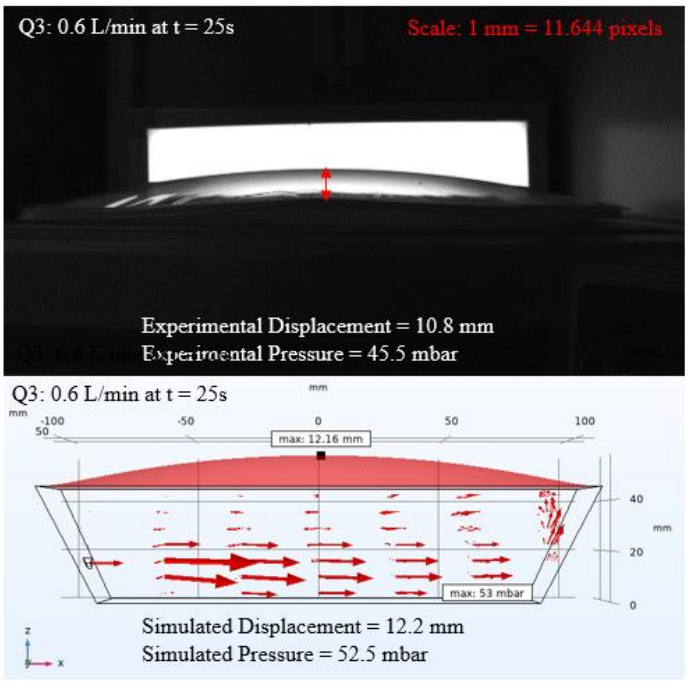
It should be noted that in the air injection experiments, deformation measurements (performed in triplicate) and pressure–temperature measurements (conducted once with sensors inside the tray) were carried out separately. As a result, the time of rupture obtained from these two sets of experiments were close but not identical. For the simulation studies, the time of rupture determined from the deformation experiments (Fig. 4.10) was considered as the reference time of rupture in this study.


Q1: 0.1 L/min at t = 94s
Scale: 1 mm = 11.644 pixels
Experimental Displacement = 10 mm
Experimental Pressure= 42 mbar
Q1: 0.1 L/min at t = 94s
mm
-100
-50
0
50
100
max: 10.08 mm
40
20
0
mm
max: 35 mbar
Simulated Displacement = 10.1 mm
Simulated Pressure = 34.5 mbar

(a)


Q2: 0.15 L/min at t = 83s
Scale: 1 mm = 11.644 pixels
Experimental Displacement = 10.8 mm
Experimental Pressure = 41.1 mbar
Q2: 0.15 L/min at t = 83s
mm
-100
-50
0
50
100
max: 11.33 mm
40
20
0
mm
max: 42 mbar
Simulated Displacement = 11.3 mm
Simulated Pressure = 41.7 mbar

(b)




(c)

*Fig. 4. 12: Experimental displacement images and 3D simulated displacement images of PP film along with relative pressure (P) values inside the PP tray with different air flow rates at respective time of rupture for (a) Q1: 0.1 L/min (b) Q2: 0.15 L/min (c) Q3: 0.6 L/min. The simulated figures are shown with scaled displacements for clarity; while the shapes appear similar, the actual magnitudes differ between each case. The arrows represent the direction of air flow.*

In the experiments, the pressure remained close to a linear relationship, and the model also predicted a linear trend. The simulated film displacement also evolved linearly with time because PP was considered a linear elastic material (Eq. 4.8).

After validating the model, a parametric sweep was conducted to examine the influence of the PP film's mechanical properties on deformation prediction. A parametric sweep was performed among various combinations of Young's modulus and Poisson ratio values to study the role of the influence of mechanical properties on the model. This was done to study the effect of mechanical properties, such as Young's modulus and Poisson's ratio, on the deformation behaviour of the PP film. Table 4.3 displays the different combinations of Young's modulus and Poisson ratio of PP film. The $R^2$ tool (Eq. 3.1) was used for analyzing the impact of these mechanical properties on deformation prediction. It was found that mechanical properties of the PP film have a significant role in deformation prediction. A slight change in these properties influences the deformation prediction. Several combinations such as O4, O5, O7 and O8 gave good agreement between experimental observations and model predictions. Therefore, out of these combinations, in this study, we have chosen to use the combination O7 from Table 4.3 for further studies where the Youngs modulus of $1.847 \times 10^9$ Pa and Poisson ratio of 0.42 from Kumar et al., (2015) was selected for subsequent analyses. Table 4. 4 lists the experimental and simulated values of pressure and displacement of PP film at the time of rupture for air injection studies with no constraints.

*Table 4. 3: Parametric sweep with different combinations of Young's Modulus and Poisson Ratio of PP film.*

| Combination | Young's Modulus (Pa) | Poisson Ratio | $R^2$ |
|---|---|---|---|
| O1 | $3.76 \times 10^8$ | 0.42 | 0.02 |
| O2 | $3.76 \times 10^8$ | 0.45 | 0.02 |
| O3 | $3.76 \times 10^8$ | 0.36 | 0.01 |
| O4 | $2 \times 10^9$ | 0.42 | 1 |
| O5 | $2 \times 10^9$ | 0.45 | 1 |
| O6 | $2 \times 10^9$ | 0.36 | 0.01 |
| O7 | $1.847 \times 10^9$ | 0.42 | 1 |
| O8 | $1.847 \times 10^9$ | 0.45 | 1 |
| O9 | $1.847 \times 10^9$ | 0.36 | 0.9 |

*Table 4. 4: Experimental and simulated values of pressure and displacement of PP film at the time of rupture for air injection studies with no constraints.*

| | Displacement of PP film at time of rupture | | | Pressure at time of rupture | | |
|---|---|---|---|---|---|---|
| **Air flow rate** | **Experimental (mbar)** | **Simulated (mbar)** | **Error %** | **Experimental (mm)** | **Simulated (mm)** | **Error %** |
| **Q1** | 10 | 10.1 | 1 | 42 | 34.5 | 17.86 |
| **Q2** | 10.8 | 11.3 | 4.63 | 41.1 | 41.7 | 1.46 |
| **Q3** | 10.8 | 12.2 | 12.96 | 45.5 | 52.5 | 15.38 |

### 4.4.2 Rupture of packaging deformation during heat treatments

Experimental observations during heat treatment showed that rupture of the PP trays occurred at much lower pressures than in the air injection tests. Fig. 4.13 shows the experimental and simulated relative pressure during heat treatment with A2 and A3 configuration and Fig. 4. 14 shows experimental and simulated headspace temperature during heat treatment with A2 and A3 configuration. In condition A2 (empty trays), rupture was observed at 540 s when the headspace temperature reached around 54 °C and the internal pressure was 8.5 mbar, while in condition A3 (trays with mashed potato), the rise in pressure and temperature was slower, with rupture occurring at 769 s when headspace temperature around 50 °C and an internal pressure of 8.8 mbar. Here, headspace means the region filled with air in both the cases. In both the cases, with or without mashed potato, rupture consistently occurred within the same narrow range of ~8–9 mbar once headspace temperatures reached between 50 and 54 °C. The numerical model simulated this pressure and headspace temperature profile and estimated these values with an error of 10.9% (for A2), 27.3%(for A3), and 0.16% (for A2), 4.3% (for A3) respectively at the time of rupture (Table 4.5). In comparison, rupture during air injection at room temperature required around 41–46 mbar, which means that the rupture pressure under heat treatment was reduced by about 80%. This large reduction is likely related to the temperature-dependent softening of PP at the heat seal zone during thermal treatment. In this study, although the temperature-dependent mechanical behaviour of the PP film was not explicitly modelled, the influence of its mechanical properties was nevertheless investigated through the parametric

sweep analysis presented in Table 4.3. Hence, based on this analysis of mechanical property variation (Section 4.4.1), it can be inferred that the mechanical properties, especially Young's modulus and Poisson ratio, strongly influence the deformation behaviour of PP film. The seal strength decreases sharply in the heat seal zone because molecular orientation relaxes and adhesion becomes weaker as temperature rises (Tetsuya et al., 2005). Hashimoto et al., 2006 reported that molecular orientation in the PP layer decreases significantly at higher temperatures, causing the seal zone to become mechanically weaker and more prone to failure. Hence, the rupture pressures of ~8–9 mbar correspond to the onset of seal failure when the softened PP film at the heat seal zone can no longer maintain adhesion with the tray, even under very low internal pressurization. This interpretation remains to be validated in future studies through dedicated experiments and simulations that incorporate the temperature-dependent mechanical properties of PP.

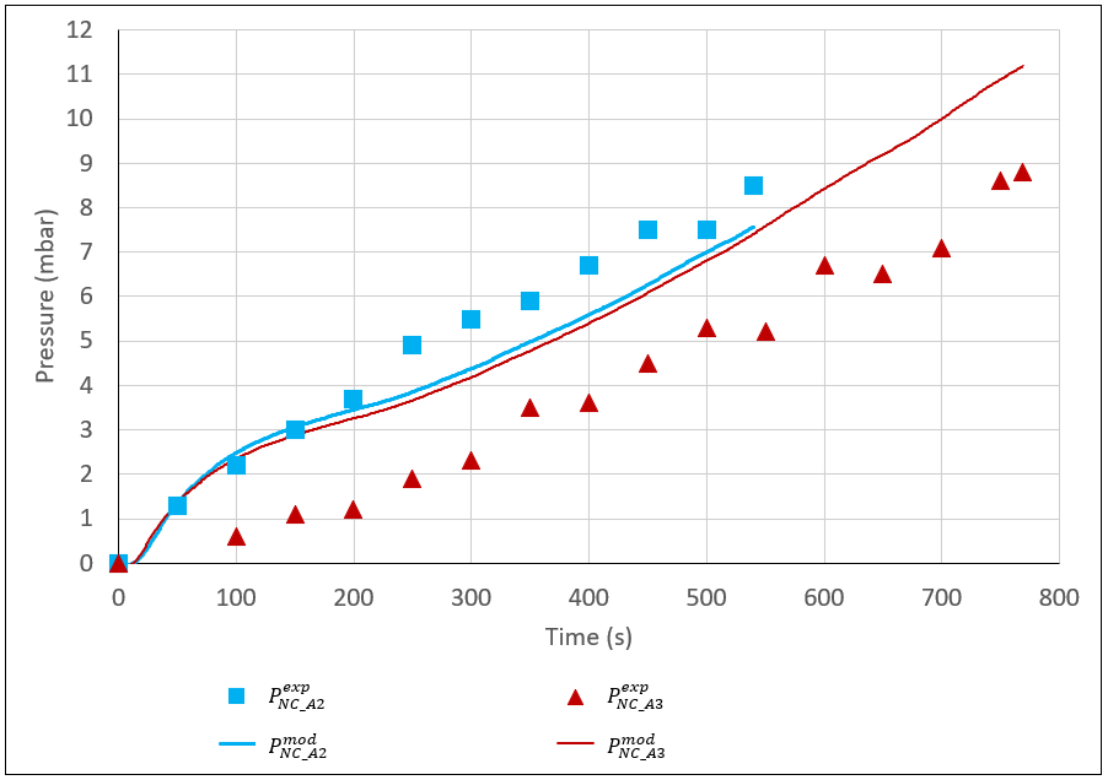



*Fig. 4. 13: Experimental and simulated relative pressure (P) during heat treatment with A2 and A3 configuration (NC: no constraint; A2: heat treatment on empty PP tray; A3: heat treatment on trays with mashed potato; P: pressure inside PP tray; exp: experimental values; mod: model values).*

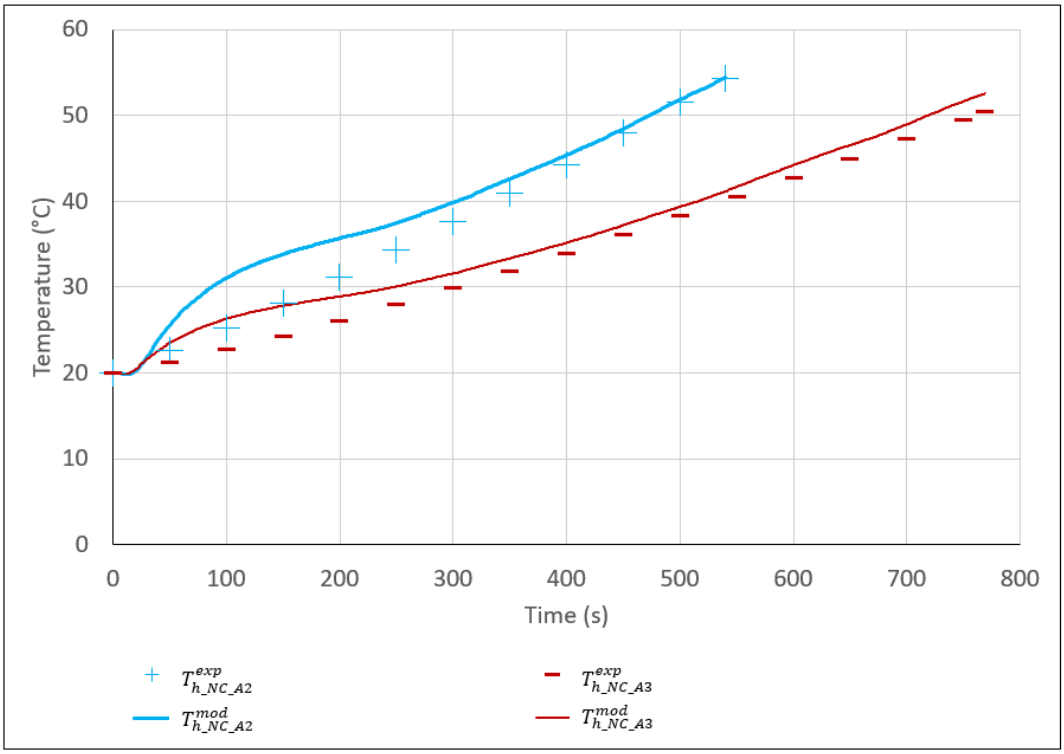



*Fig. 4. 14: Experimental and simulated headspace temperature during heat treatment with A2 and A3 configuration (NC: no constraint; A2: heat treatment on empty PP tray; A3: heat treatment on trays with mashed potato; T: temperature at headspace inside PP tray; exp: experimental values; mod: model values).*

*Table 4. 5: Experimental and simulated values of pressure and headspace temperature at the time of rupture for heat treatment studies with no constraints.*

| | **Pressure at time of rupture** | | | **Headspace temperature at time of rupture** | | |
|---|---|---|---|---|---|---|
| **Configuration** | **Experimental (mbar)** | **Simulated (mbar)** | **Error %** | **Experimental (°C)** | **Simulated (°C)** | **Error %** |
| **A2 (heat treatment in empty PP tray)** | 8.5 | 7.6 | 10.9 | 54.3 | 54.4 | 0.16 |
| **A3 (heat treatment with food and headspace)** | 8.8 | 11.2 | 27.3 | 50.4 | 52.5 | 4.3 |

### 4.4.3 Air Flow Patterns inside PP tray during Air Injection and Heat Treatment

Numerical simulations were performed to analyze the airflow and temperature fields inside the PP trays for the air injection (A1), heat treatment in empty trays (A2) configurations, and heat treatment in trays with mashed potato (A3). The analysis was performed along different cut planes depending on the configuration: for A1, airflow and temperature fields were examined along the center and lateral planes, while for A2 and A3, the analysis included the center, side,

and lateral planes (Fig. 4.15). All these analyses were performed at the time of rupture. In A1, airflow was dominated by the inlet jet. At Q1 = 0.1 L/min, the maximum velocity was concentrated near the inlet in the center plane. Increasing the flow rate to Q2 = 0.15 L/min caused the velocity peak to shift closer to the middle of the tray, while at Q3 = 0.6 L/min the airflow extended across the tray and concentrated near the opposite edge from the inlet (Fig. 4.16 – Fig. 4.20). In the lateral plane, flow was circular and centered at Q1, shifted at Q2, and became a distinct jet-like pattern at Q3 directed towards the opposite wall. Studies such as by Tutar et al., 2009 reported that at low inlet velocities airflow formed symmetric recirculating vortices, but as velocity increased these vortices shifted and were replaced by jet-dominated flow patterns. Even though that study employed a turbulence model to describe similar transitions, the present work used a laminar flow approach since the calculated Reynolds number for the highest inlet flow rate (0.6 L/min) was below 300.

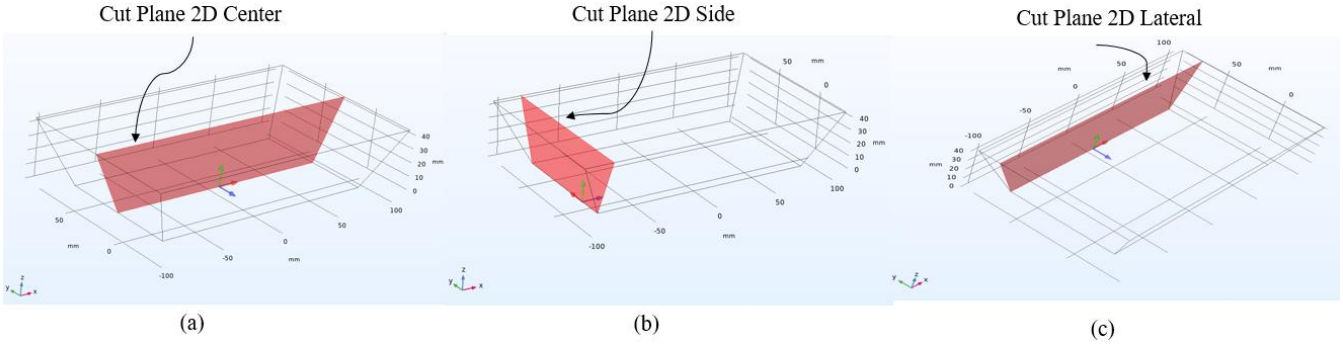
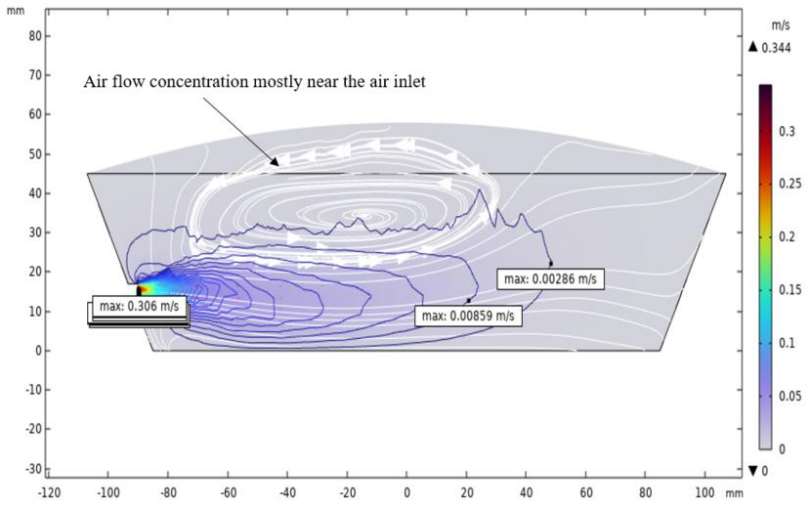
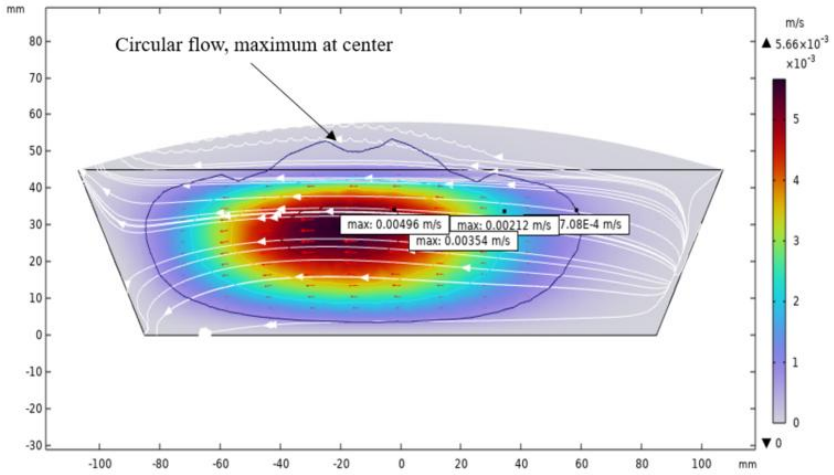



*Fig. 4. 15: Cut Plane 2D at three different locations (a) center (b) side and (c) lateral to study the air flow inside PP tray during air injection and heat treatment.*

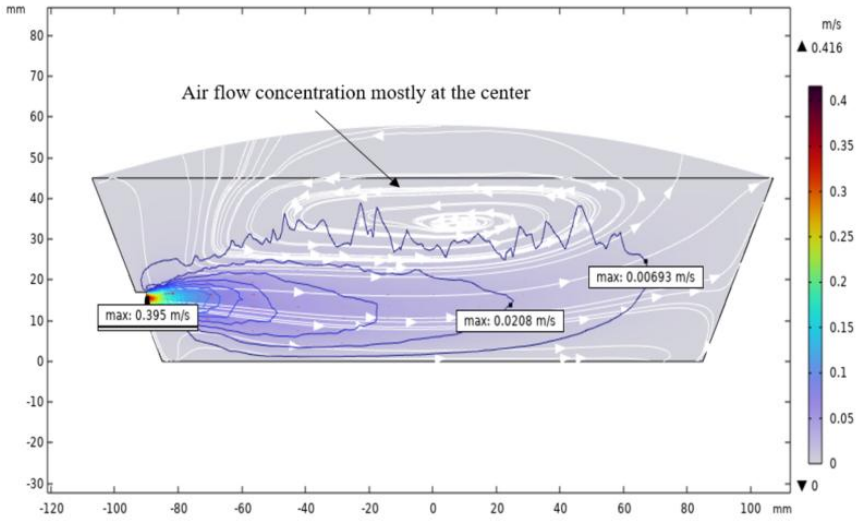



(a)

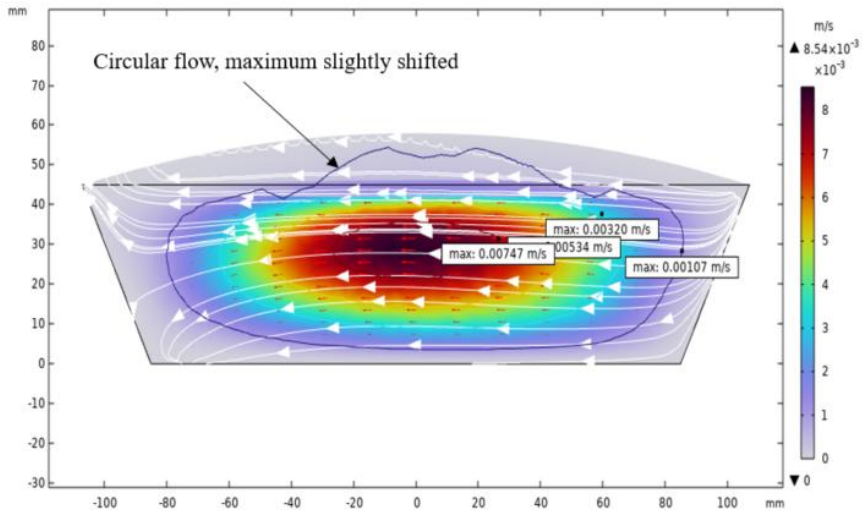



(b)

*Fig. 4. 16: Simulated air flow and velocity at Q1 = 0.1 L/min inside the tray at the time of rupture (t = 94s) along (a) Cut Plane Center (b) Cut Plane Lateral. The white streamlines represent the flow pattern of the air inside the tray.*

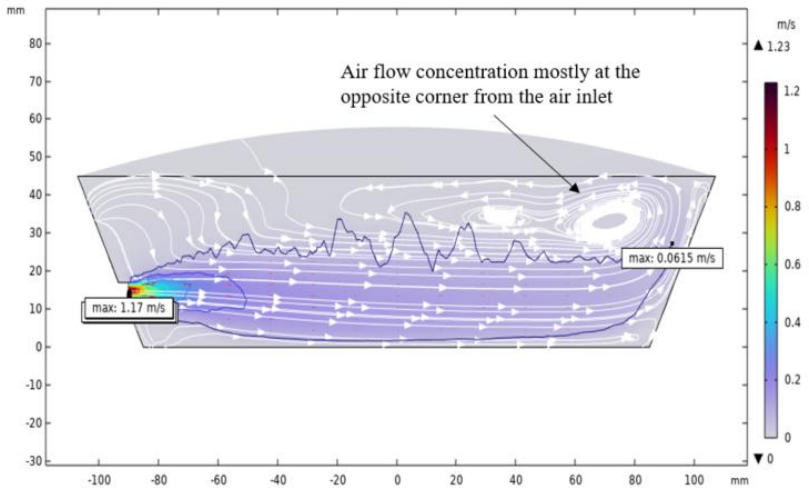



(a)

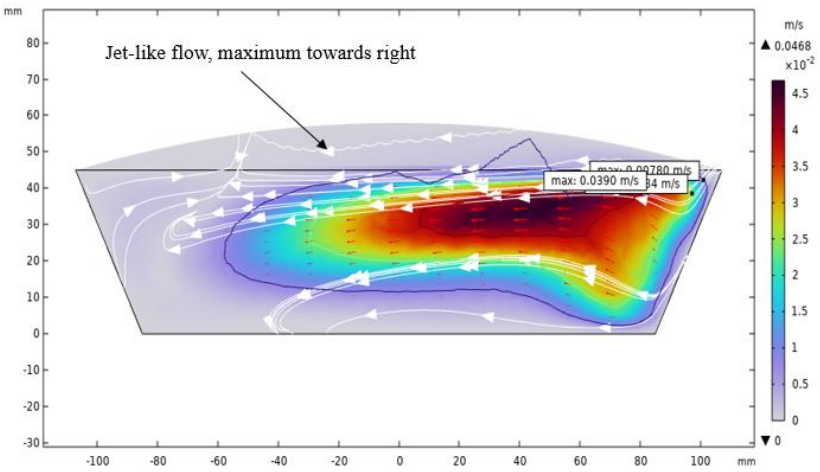



(b)

*Fig. 4. 17: Simulated air flow and velocity at Q2 = 0.15 L/min inside the tray at the time of rupture (t = 83s) along a) Cut Plane Center (b) Cut Plane Lateral. The white streamlines represent the flow pattern of the air inside the tray.*



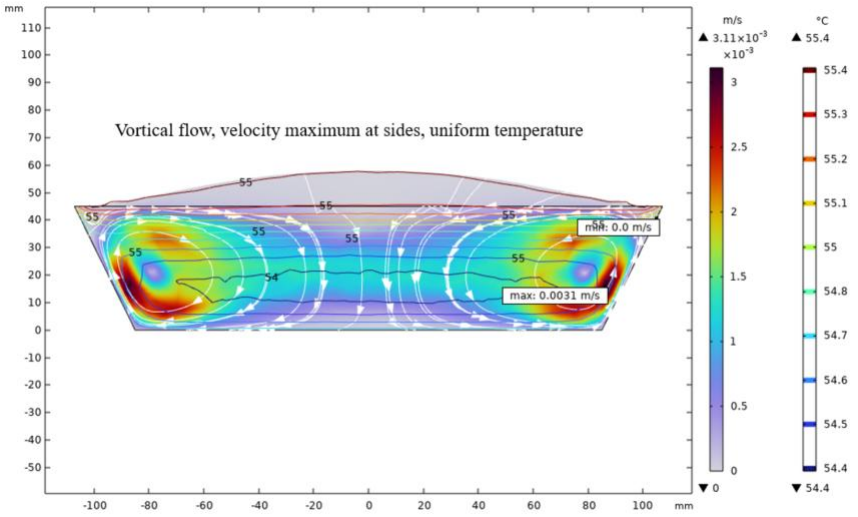

(a)



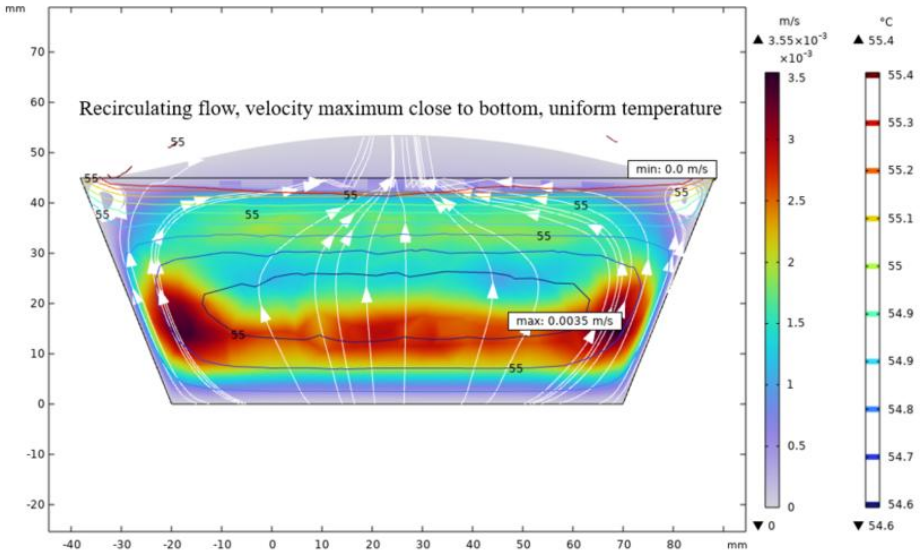

(b)

*Fig. 4. 18: Simulated air flow and velocity at Q3 = 0.6 L/min inside the tray at the time of rupture (t = 25s) along (a) Cut Plane Center (b) Cut Plane Lateral. The white streamlines represent the flow pattern of the air inside the tray.*

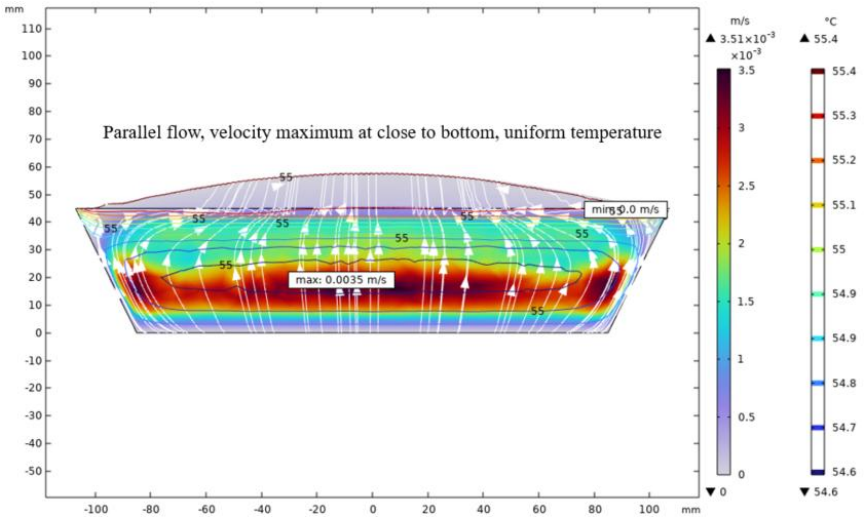
In A2 (heat treatment in empty trays), velocities were two to three orders of magnitude lower than in A1, generally below 0.003 m/s. This occurred because airflow arose solely from buoyancy-driven natural convection, and not by air injection within the tray. In the center plane, two large vortical regions formed at the opposite ends. In the side plane, a recirculating upward motion was concentrated close to the bottom wall. In the lateral plane, airflow moved upward in a near-parallel direction. The internal temperature distribution at rupture (~54 °C, t = 540 s) was nearly uniform, indicated by isothermal contours. Similar low-velocity buoyancy-driven flow in heated sealed cavities has been reported experimentally. Laguerre et al., 2008 carried out particle image velocimetry (PIV) measurements in an enclosure heated through its walls and observed that air velocities were "very weak (< 0.04 m/s) in the central zone" and that "circular airflow" and recirculation were present in the cavity.




(a)




(b)

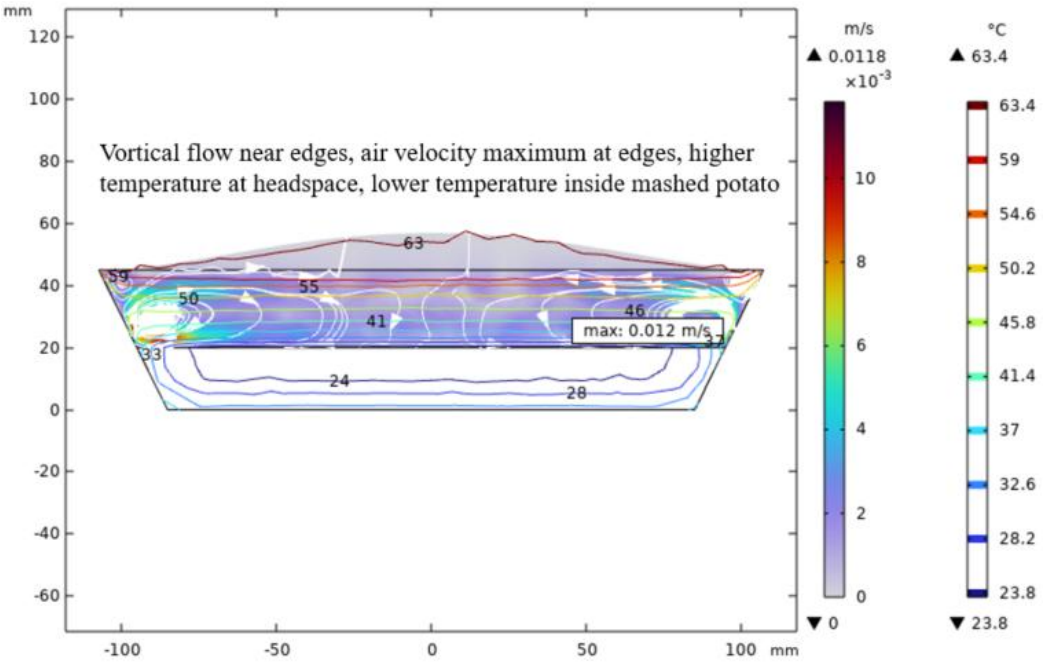



(c)

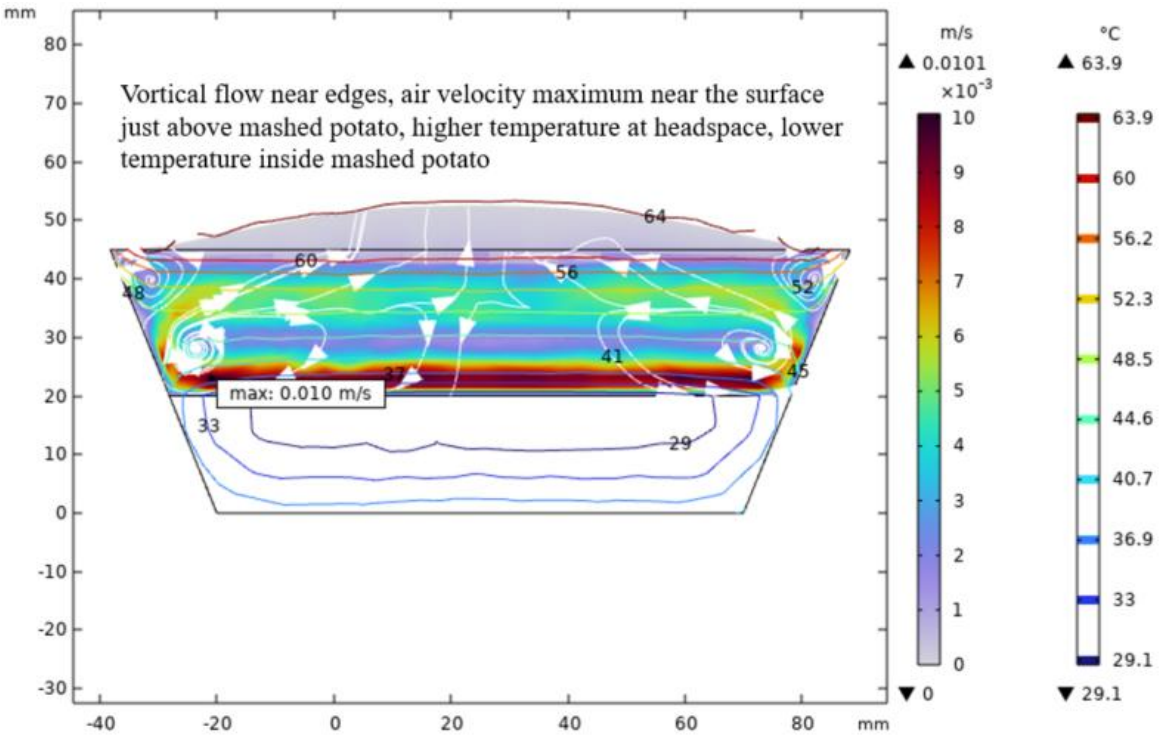
*Fig. 4. 19: Simulated air flow and temperature distribution during heat treatment inside empty PP tray at the time of rupture (t = 540s) along (a) Cut Plane Center (b) Cut Plane Side (c) Cut Plane Lateral. The white streamlines represent the flow pattern of the air inside the tray.*

In A3 (heat treatment with mashed potato), reduced headspace volume significantly altered airflow patterns (Fig. 4.20). Dry air velocities increased compared to A2 yet remained well below those of A1, typically around 0.01 m/s. In the center plane, vortical flow regions developed near the tray corners; in the side plane, circulation formed close to the food surface with maximum velocities above the mashed potato; and in the lateral plane, similar circulation localized near corners adjacent to the food surface. In addition, the temperature field exhibited notable heterogeneity. At rupture (t = 769 s), the headspace temperature reached ~50 °C, whereas the mashed potato remained relatively cool (~23–30 °C), creating thermal stratification. The resulting airflow behaviour showed similar convection features to those typically observed in humid heated cavities. However, since evaporation was not simulated in this study, this comparison is only indicative. The results suggest that it is not necessary to explicitly simulate evaporation to analyse the overall gas-flow pattern under the present conditions. This airflow pattern tends to intensify near warmer regions while the bulk region remains at lower temperature (Laguerre et al., 2008, 2009). For instance, Laguerre et al., 2009 observed that in natural convection cavities with humid conditions, thermal stratification and circular airflow in the cavity developed. Also humidification of the cavity contributes to increase air velocity near the humid zone (Laguerre et al., 2009). In the present work, although evaporation was not considered, the observed airflow patterns exhibited temperature-driven circulation features, indicating that buoyancy forces alone can generate comparable flow structures within the packaging headspace in conditions used in this present study. Therefore, the observed dry airflow patterns show comparable circulation behaviour, consistent with the general characteristics of buoyancy-driven flows in closed, thermally induced packaging systems. Overall, the three configurations demonstrated distinct airflow behaviours inside the trays. In air injection (A1), the airflow was dominated by vortical motion at low injection rates and transitioned into forced recirculating flow circulation at higher rates. In the empty trays during heating (A2), the absence of forced flow meant that only very weak buoyancy-driven convection developed, forming large but slow vortical circulations. In the food-loaded trays (A3), the presence of mashed potato reduced the available headspace. This created smaller

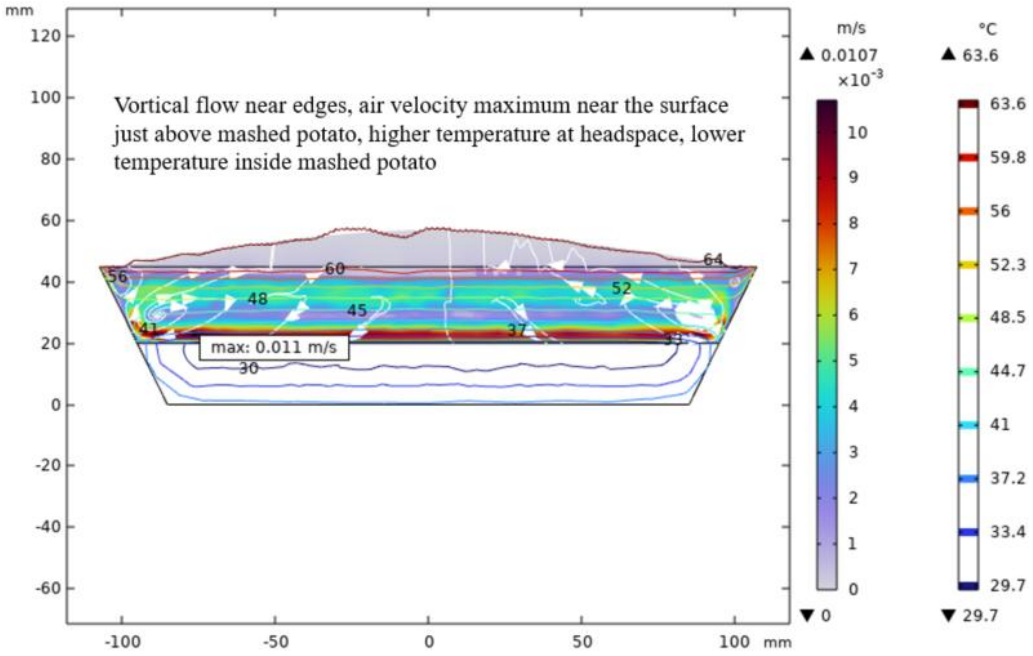
circulations localized near the product surface and resulted in non-uniform heating, with clear thermal stratification between the warmer headspace and the cooler bulk food. These airflow patterns are directly linked to the pressure build-up inside the trays and therefore to the reaction forces acting on the PP sealing film, which will be analyzed in the following section together with the distribution of von Mises stresses.




(a)




(b)




(c)

*Fig. 4. 20: Simulated air flow and temperature distribution during heat treatment inside PP tray containing mashed potato with a headspace at the time of rupture (t = 769s) along (a) Cut Plane Center (b) Cut Plane Side (c) Cut Plane Lateral. The white streamlines represent the flow pattern of the air inside the tray.*

### 4.4.4 Reaction force and von Mises stress analysis of PP film

The numerical model was used to calculate the reaction forces acting on the PP film as well as the von Mises stress distributions during the different configurations of air injection (A1) and heat treatment (A2, A3). A reaction force is the force required at a boundary to satisfy a prescribed constraint resulting in displacement. It comes from integrating the stress tensor over the constrained boundary. The simulated reaction force ($F_{RFz}$) (Fig. 4.21) is computed from the in-built COMSOL variable on normal stresses over the film surface area and interact with Eq. 4.24 to produce the pressure-volume work.

$$F_{RFz} = \int \sigma_{zj} n_j dA \qquad 4.27$$

where, $\sigma_{zj}$ is the stress tensor (Pa), $n_j$ is outward normal vector component, and $dA$ is area element of the boundary of the PP film.

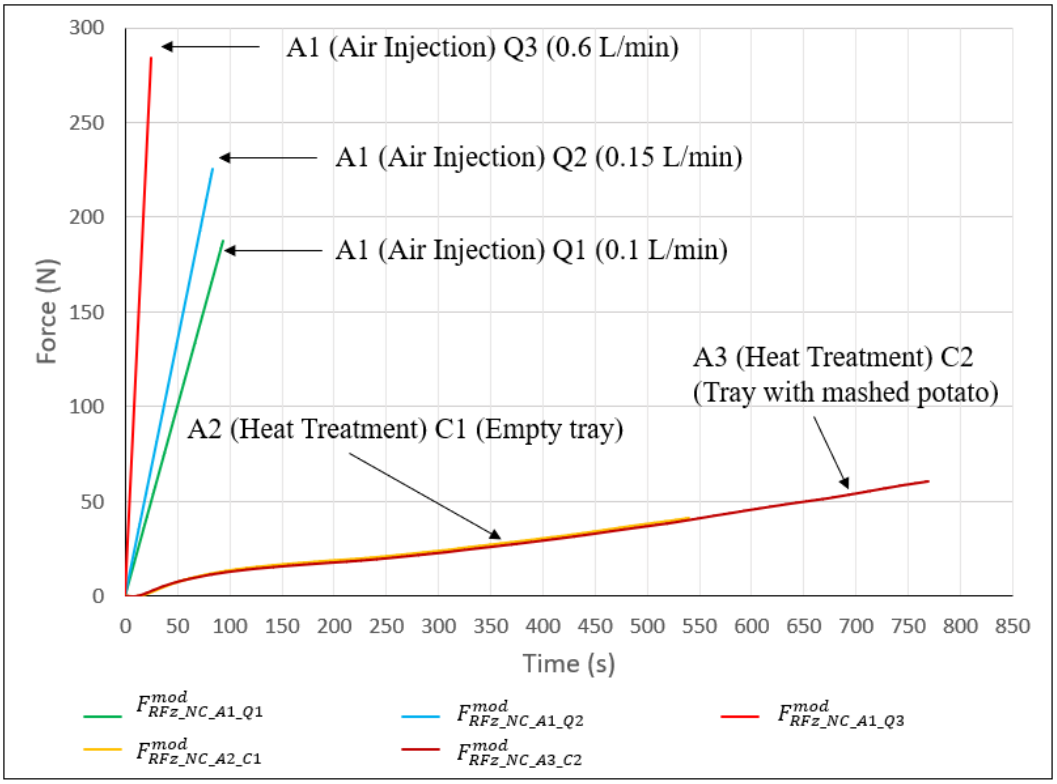


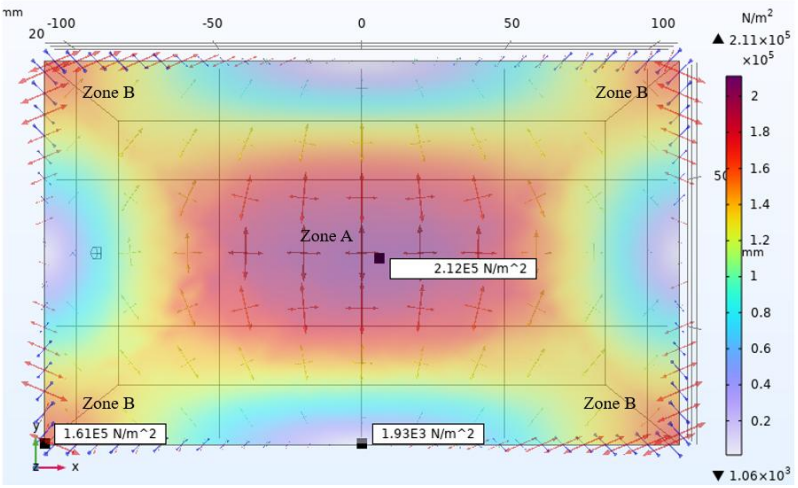

*Fig. 4. 21: Simulated reaction force ($F_{RFz}$) acting on the PP film as predicted by the model during no constraint (NC) configurations. (NC: no constraint; A1: air injection; A2: heat treatment on empty PP tray; A3: heat treatment on trays with mashed potato; exp: experimental values; mod: model values; Q1: air flowrate 1; Q2: air flowrate 2; Q3: air flowrate 3; C1: empty PP tray; C2: PP tray with mashed potato).*

The time evolution of the reaction force mirrored the internal pressure build-up but diverged across scenarios: in A1, the rapid pressure rise generated high peak forces at the experimental rupture time with simulated reaction forces of approximately 187 N (Q1), 226 N (Q2), and 284 N (Q3). Although the PP film material remained the same across all cases, the simulated reaction force depends on the stresses generated on the film, which are influenced by the airflow pattern varying with the different injection rates. This variation in airflow affects the resulting stress field acting on the film surface. Consequently, even small differences in pressure or deformation profiles leads to noticeably different simulated reaction forces. However, experimental analysis and further validations are necessary to confirm this relationship and its impact on the resulting stress distribution over the film surface. By contrast, A2 and A3 exhibited much lower simulated reaction forces at their corresponding experimental rupture times, around 41 N and 62 N respectively. This reduction in simulated reaction force compared to the air injection cases can be explained by the mechanism of pressure generation. In the air injection configuration, additional air mass is introduced into the closed cavity, which increases the total number of gas molecules and consequently raises the internal pressure. The injected airflow also creates a transient dynamic pressure component due to local velocity fields near the film surface. In contrast, in the heat-treatment configurations (A2 and A3), the pressure rise results primarily from air expansion caused by temperature increase, without additional air mass entering the cavity. As a result, the overall pressure increase is lower in these cases, leading to smaller reaction forces on the PP film. Simultaneously, the von Mises stress distribution consistently concentrated at specific zones on the film (Fig. 4.22 – 4.25). In A1, Zone A (the

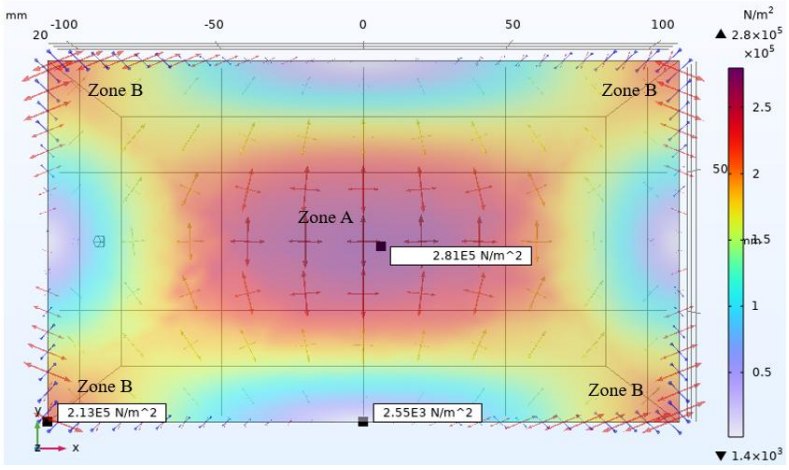
zone of maximum stress) was located at the film's center, where doming induced significant biaxial tension, with simulated von Mises stresses of $2.12 \times 10^5$, $2.81 \times 10^5$, and $3.38 \times 10^5$ N/m² for Q1, Q2, and Q3 respectively. Zone B, where simulated stress was slightly lower than in Zone A, was concentrated at the corners and showed values of $1.61 \times 10^5$, $2.13 \times 10^5$, and $2.57 \times 10^5$ N/m². The intra-film stresses remained below the typical yield strength of PP ($25–40 \times 10^6$ N/m²). Therefore, it can be stated that local zones with simulated stress concentrations correspond to the locations where rupture of the packaging was observed experimentally. Although the maximum simulated stress appeared at the center of the film (Zone A), the rupture occurred at the corners (Zone B) because the seal is the weakest part of the packaging. As a result, even if the center experiences higher simulated stresses, the film actually breaks at the corners. This is consistent with experimental results, where 100% (n = 54) of all the ruptures occurred at the corners during A1 experiments, aligning with Zone B simulated stress localization in the simulations. The airflow field provides a possible explanation for this observation, as the simulated air flow created a directional flow that recirculated near the tray corners, increasing mechanical loading on the film near the sealing edges. This correlation between airflow behaviour and stress localization suggests a coupled air–structure interaction but still needs to be experimentally verified to confirm its contribution to rupture. This suggests that local airflow–structure interactions may reinforce the concentration of stresses already present at the seal edges, making them more susceptible to rupture (Mezzacapo et al., 2025; Y. Sun et al., 2019). In contrast, during heat treatment, the simulated stress distribution pattern shifted compared with air injection. In A2 (empty trays), Zone A, was located along the longer edges of the PP film, with simulated von Mises stresses of $8.81 \times 10^4$ N/m², while Zone B appeared on the shorter edges and in the film center with lower stresses of $5.4 \times 10^4$ N/m². Because the longer edges concentrated more of the maximum stress, rupture was more likely to initiate there, which agreed with experiments where 78% (n = 24) of ruptures occurred along the long edges. In A3 (trays with mashed potato), Zone A was distributed around the corners and on the edges near the corners, with simulated stresses of $3.8 \times 10^5$ N/m², while Zone B was slightly further away from the corners along the edges with stresses of $1.5 \times 10^4$ N/m². These results suggest that rupture is more likely to initiate near the corners, although the exact locations cannot be precisely determined due to uncertainties in the simulated flow field. This general tendency is consistent with experimental observations, where 89% (n = 28) of ruptures occurred near the corners and the remainder directly at the corners. In both heat treatment cases (A2 and A3), the von Mises stress values were lower than those in air injection (A1), yet rupture still occurred, suggesting that the heat seal zone loses strength during heat treatments and fails at reduced internal loads. The airflow fields during heating may provide a partial explanation for the shift in rupture location. To evaluate the importance of these airflow fields on the simulated stress and also on the deformation of PP film, an additional simulation was performed by decoupling the CFD solution of A2 configuration and applying only the global pressure evolution from the previous coupled model to the film. The comparison between the CFD and non-CFD simulation can be visualized by comparing the simulated von Mises stress distributions from Fig. 4.23 (with CFD) vs Fig. 4.25 (with no CFD). In this case of non-usage of CFD, a perfectly mixed environment was assumed, i.e. that no local pressure or temperature gradients existed within the headspace. Without the CFD coupling, the heat distribution inside the tray became more uniform, eliminating the local hot and cold zones normally generated by convective air movement. Consequently, the resulting stress variations on the PP film were much lower. Significant differences were observed, with simulated stress concentrations on the film reduced by nearly one order of magnitude ($10^1$). Hence, the inclusion of CFD is essential

to capture the effect of airflow on the distribution and magnitude of stresses acting on the PP film during heating.

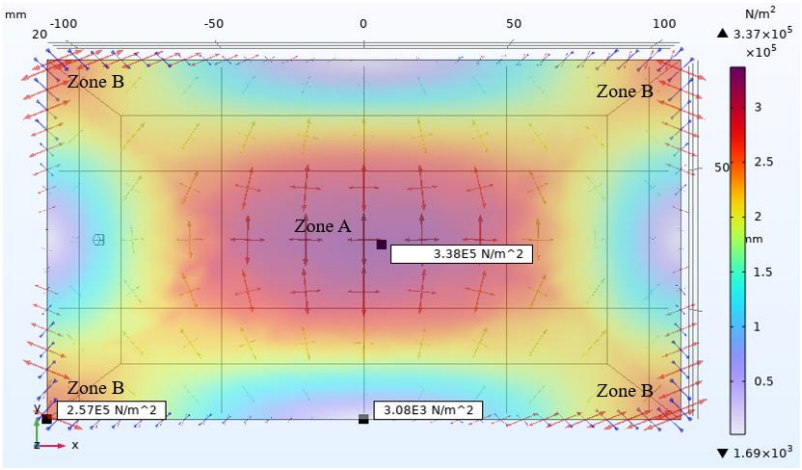
The simulated von Mises stress distribution revealed that stress concentration occurs mainly due to airflow-induced mechanical loading and internal pressure buildup. However, this explanation remains a working hypothesis, as the current model primarily accounted for pressure rise without considering temperature-dependent softening of the PP film. Both airflow pattern and film temperature play key roles in defining the stress magnitude, since airflow governs the spatial pressure distribution while temperature affects the mechanical strength of the polymer material. Therefore, experimental validation combining multipoint temperature measurements and airflow visualisation is needed to confirm this interpretation. In the next section, a mechanical constraint is therefore designed to provide a counter load opposite to the internal load on the PP film to investigate its impact on the rupture of food tray on the heat seal zone.




(a)




(b)




(c)

*Fig. 4. 22: Estimation of von-Mises stress on PP film in at the experimental time of rupture during (a) air injection in empty PP tray at Q1 = 0.1 L/min (t = 94 s) (b) air injection in empty PP tray at Q2 = 0.15 L/min (t = 83 s) (c) air injection in empty PP tray at Q3 = 0.6 L/min (t = 25 s).*Colour grades scales are different for each images.*

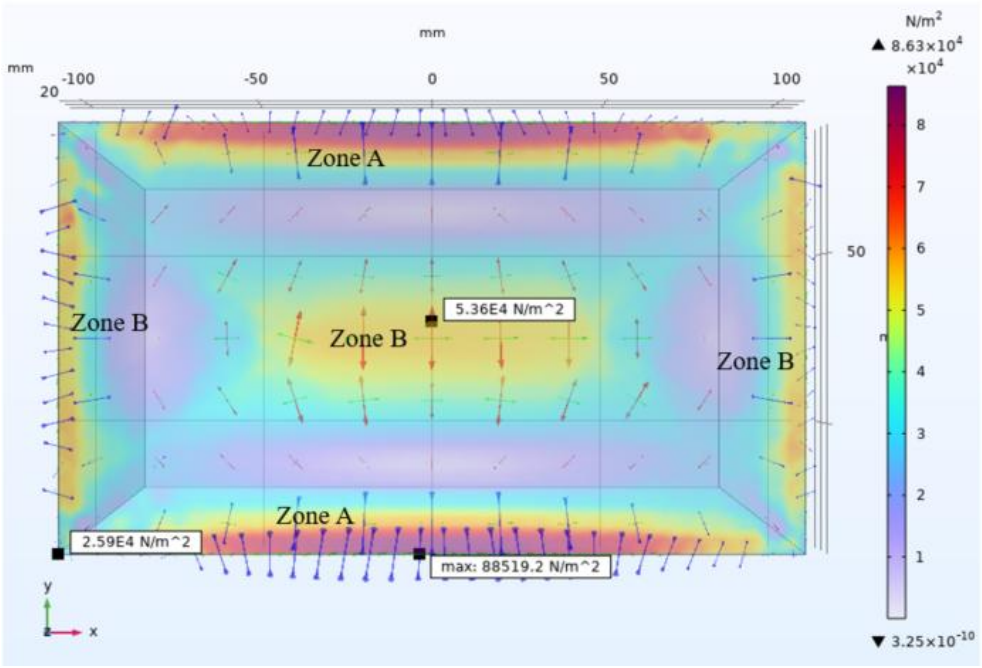



*Fig. 4. 23: Estimation of von-Mises stress on PP film in different simulated configuration at the experimental time of rupture during heat treatment on empty PP tray (A2) (t = 540 s). Zone A highlights the zone of maximum von-Mises stress on the PP film. Zone B highlights the zone where there is the presence of slightly lower von-Mises stress than the zone of maximum von-Mises stress on the PP film. The arrows represent the principal stresses acting on the PP film.*

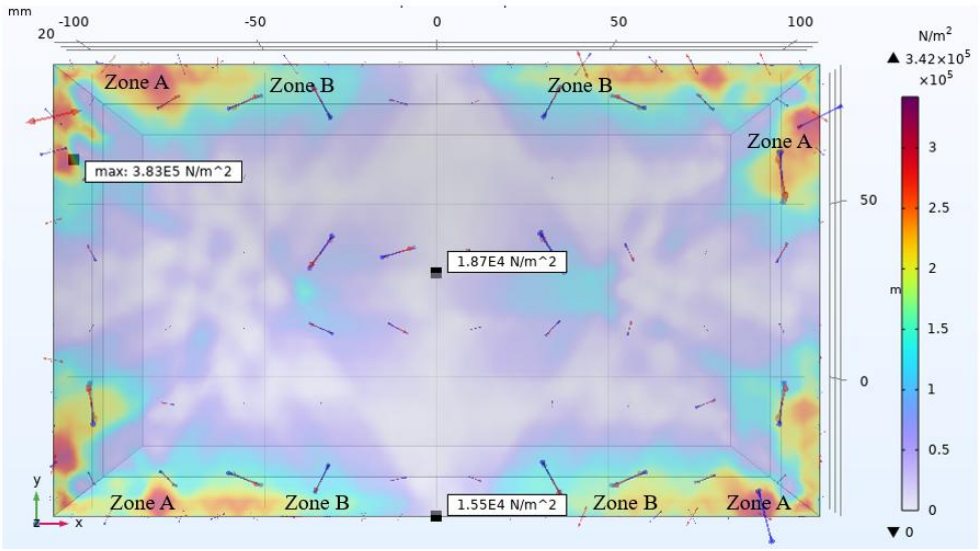



*Fig. 4. 24: Estimation of von-Mises stress on PP film at the experimental time of rupture during heat treatment on PP tray with mashed potato (A3) (t = 769 s). Zone A highlights the zone of maximum von-Mises stress on the PP film. Zone B highlights the zone where there is the presence of slightly lower von-Mises stress than the zone of maximum von-Mises stress on the PP film. The arrows represent the principal stresses acting on the PP film.*

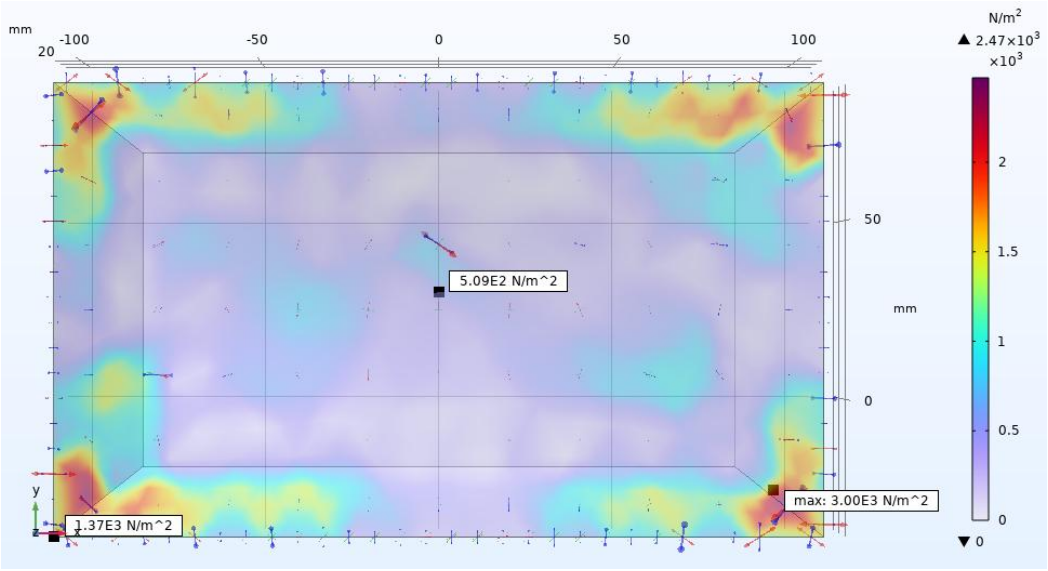



*Fig. 4. 25: Estimation of von-Mises stress on PP film at the experimental time of rupture during heat treatment on empty PP tray (A2) (t = 540 s) without the use of CFD. Zone A highlights the zone of maximum von-Mises stress on the PP film. Zone B highlights the zone where there is the presence of slightly lower von-Mises stress than the zone of maximum von-Mises stress on the PP film. The arrows represent the principal stresses acting on the PP film.*

### 4.4.5 Effect of Mechanical Constraint on Pressure Evolution and Rupture

In the air injection experiments with fixed preloaded constraint (B1), the application of preloads (F1 = 5 N, F2 = 20 N, F3 = 40 N) modified the rupture behaviour compared with the unconstrained trays (A1). Across all three flow rates (Q1, Q2, Q3), the trays with fixed preloaded constraint (FPC) sustained markedly higher rupture pressures, in the range of 100–129 mbar (Fig. 4.26), irrespective of preload level. A slight decrease in rupture pressure was

observed at the lowest flow rate (Q1) compared to the highest (Q3), consistent with the lower air injection rate and slower pressure buildup. During the application of lowest preload condition (F1), the PP film exhibited slightly greater deformation before rupture, whereas deformation was more limited with F2 and minimal with F3, where the applied force largely restricted upward motion of the film.

It can also be observed that for each air flow tested, the resulting reaction force acting on the PP film tends to decrease slightly as the applied preload increases, while the internal pressure shows the opposite trend, becoming higher at higher preloads. This apparent inverse relationship can be explained by the change in the effective contact surface area of the PP film during deformation. When larger preloads are applied, the upper surface of the film remains flatter and undergoes less dome expansion compared to F1, effectively reducing the surface area subjected to internal pressure. As a result, the total reaction force acting on the film decreases even though the internal pressure is higher. Therefore, surface evolution of the PP film plays an important role in the overall mechanical response under different preload conditions.

A minor upward displacement was still visible even with F3. The corresponding experimental reaction forces at the time of rupture were measured between 112 and 134 N (Fig. 4.27), with the applied preloads being zeroed at the beginning. This indicates that the FPC acted as a restraining support, spreading the applied load across the PP film, limiting excessive dome deformation. Similar effects have been described in standardized packaging burst tests, where the package is internally pressurized and enclosed within restraining plates and the plates serve to stabilize the product (Steris, 2020). Also as reported by the mechanical studies of Sheploak & Dugundji, 1998, introducing initial constraints modifies the stiffness and stress distribution of thin films under pressure. Consistent with these principles, the experimental results show that although rupture still occurred at times similar to the unconstrained case (94 s at Q1, 83 s at Q2, and 25 s at Q3), the trays were able to withstand much higher internal pressures before failure. This is due to the presence of the mechanical constraint, which increases the stiffness of the tray and limits film deformation, allowing it to resist higher internal pressure before rupture. However, since the air injection rate was unchanged, the overall pressure build-up followed a similar trend but with higher values of pressure resulting in comparable rupture times. Hence, experimentally it was seen that mechanical constraints enhance the load-bearing ability of the PP sealing film, but did not significantly improve the time of rupture.

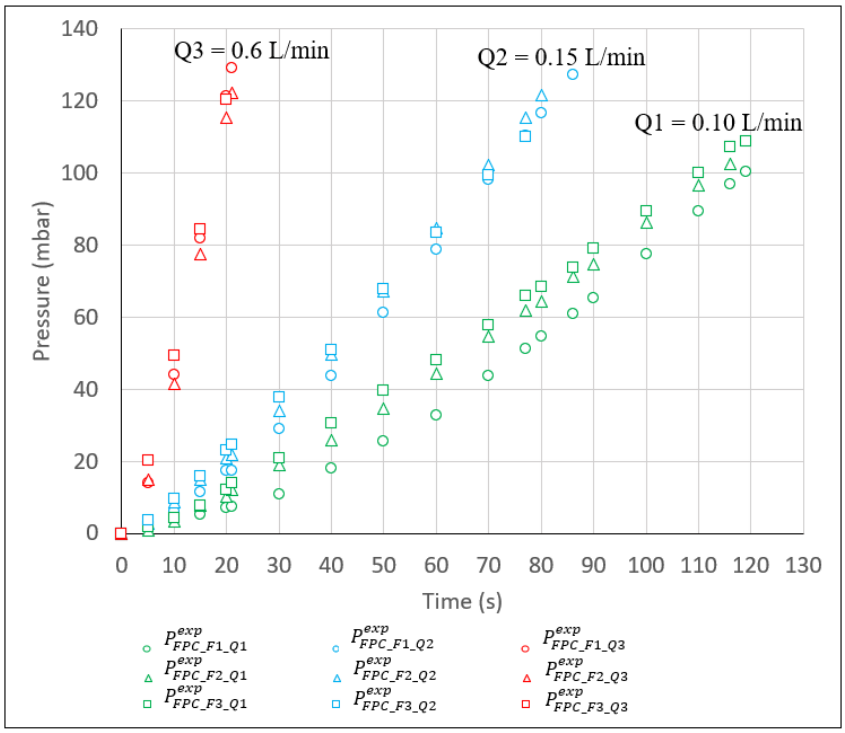



*Fig. 4. 26: Experimental relative pressure (P) inside PP tray during air injection with fixed preloaded constraint (FPC) of F1 = 5N, F2 = 20 N, and F3 = 40 N at different air flowrates. (exp: experimental values; Q1: air flowrate 1; Q2: air flowrate 2; Q3: air flowrate 3; F1: initial applied force 1 on PP film (5N); F2: initial applied force 2 on PP film (20N); F3: initial applied force 3 on PP film (40N)).*

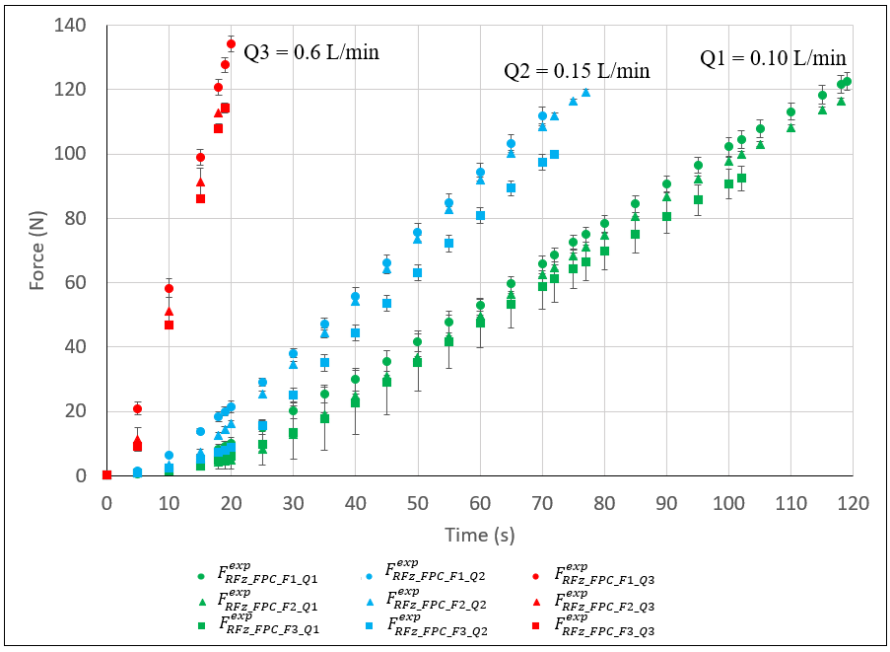



*Fig. 4. 27: Experimental reaction force ($F^{exp}_{RFz}$) on PP film during air injection with fixed preloaded constraint (FPC) at different air flowrates. (exp: experimental values; Q1: air flowrate 1; Q2: air flowrate 2; Q3: air flowrate 3; F1: initial applied force 1 on PP film (5N); F2: initial applied force 2 on PP film (20N); F3: initial applied force 3 on PP film (40N)).*

In the heat treatment experiments, the application of mechanical constraints also clearly influenced both the pressure and the force behaviour on the trays. For the empty trays (B2), the use of preloads enabled the trays to withstand higher internal pressures before rupture compared to the unconstrained trays (A2) just like B1. The rupture pressures for B2 were measured in the range of 27–49 mbar, while in the food-loaded trays (B3), rupture occurred at lower internal pressures between 12–29 mbar. The measured reaction forces acting on the PP film followed this same trend and were consistent with the recorded pressure values. In B2, reaction forces at rupture were between 15–24 N, whereas in B3, the values were lower, 8–14 N (Table 4.6). This is due to lower internal pressures leading to correspondingly lower reaction forces on the sealing film (Xiang et al., 2005). This suggests that the heat seal may become more prone to localised defects and premature failure. Nonetheless, this proposed mechanism requires further validation, as the current results only provide indirect evidence of this effect. Similar to the air injection experiments, the forces reported here represent delta forces, excluding the initial preloaded values (5 N, 20 N, or 40 N) and accounting only for the additional load caused by internal pressure buildup. Alongside these measurements, headspace temperatures at the time of rupture were also recorded. In B2, rupture occurred at headspace temperatures between 29–54 °C, and in B3, rupture occurred at headspace temperatures of around 26–34 °C. These results only give an initial indication that the presence of food may influence the thermal conditions in the headspace, independently of the applied mechanical constraint. In the food-loaded trays (B3), the headspace temperature was slightly lower than in the empty trays, suggesting that part of the absorbed heat was distributed within the food matrix, influencing the overall heat transfer pattern inside the tray. However, with limited number of experiments, these findings cannot yet be treated as statistically conclusive. Overall, the results suggest two main outcomes: first, that mechanical preloads increase the ability of trays to withstand higher pressures and reaction forces during pressurization and heating; and second, that the presence of food strongly affects both the thermal and pressurisation behaviour. To comprehensively understand the effect of mechanical constraints in more detail and to confirm their influence on heat and airflow distribution, more advanced numerical studies should also be performed alongside experiments.

*Table 4. 6: Experimental values of pressure, headspace temperature and force at the time of rupture for heat treatment studies with constraints.*

| | **B2 (heat treatment in empty PP tray with mechanical constraint)** | | | **B3 (heat treatment in trays with food and headspace and with mechanical constraint)** | | |
|---|---|---|---|---|---|---|
| | **F1** | **F2** | **F3** | **F1** | **F2** | **F3** |
| **Pressure (mbar) at time of rupture (n = 1)** | 28.5 | 27.4 | 48.9 | 12.3 | 24.1 | 29.3 |
| **Headspace temperature (°C) at time of rupture (n = 1)** | 54.32 | 29.08* | 43.83 | 34.46 | 26.91 | 27.93 |
| **Experimental reaction force (N) at time of rupture (n = 3)** | 15.1±3.8 | 18.1±5.3 | 23.6±9.7 | 14.1±7.2 | 12.9±1 | 8.8±1 |
| **Time of rupture (s) (n = 3)** | 729±52 | 359±48 | 710±62 | 733±56 | 488±60 | 488±82 |

* The headspace temperature value of 29.08 °C appears unusually low compared to the other measurements and is likely due to experimental variability or sensor placement deviation during data recording.

### 4.5 Conclusion

This chapter investigated the rupture behaviour of PP ready-to-eat food trays under air injection, heat treatment, and with mechanical constraints. The study combined experimental measurements of pressure, temperature, and displacement, and numerical studies for the analysis of airflow fields and stress distributions inside a PP food tray.

During air injection, rupture was governed by the pressurisation rate and the airflow loading on the PP film. The film displaced by approximately 10–11 mm before rupture, with pressures remaining within a narrow range of 41–46 mbar regardless of injection rate, indicating that pressurisation speed influenced rupture timing but not the rupture threshold. Simulations showed reaction forces at rupture between 187 and 284 N and revealed distinct airflow patterns, vortical recirculation at low injection rates and jet-driven flow at higher rates, both contributing to stress localisation. Maximum von Mises stresses appeared at the film centre, with secondary concentrations at the corners where rupture consistently initiated, confirming that airflow structure strongly influenced local stress development.

Heat treatment produced a markedly different rupture behaviour. Rupture occurred at very low pressures, around 8–9 mbar, once headspace temperatures reached 50–54 °C. This represents a reduction of nearly 80% compared with air injection. For empty trays, rupture occurred after 540 s at headspace temperature of around 50 °C and pressure of around 8 mbar. Also, in food-loaded trays rupture occurred at headspace temperature of around 50°C and pressure of around 9 mbar. Only the time of rupture was delayed to around 769 s. In this case, simulation showed that the simulated reaction forces at the time of rupture were correspondingly low, around 40 N. Also, failure occurred at the heat seal zones far below the bulk yield strength of PP (25–40 $\times 10^6$ N/m²). The air flow fields were simulated to analyze the flow patterns of air inside the packaging but not experimentally measured. Simulated airflow fields during heating were much much lower velocities than under injection, with natural convection velocities below 0.003 m/s.

Mechanical constraints using fixed preloaded constraints (FPC) changed rupture behaviour by redistributing stresses. In air injection with FPC, rupture pressures increased to 100–129 mbar, with experimental reaction forces of 112–134 N, but the time of rupture remained almost similar to unconstrained cases. The FPC limited dome deformation, spread the internal load, and reduced localised stress concentrations. This interpretation is based on the observed deformation behaviour and remains an assumption that should be further validated through detailed numerical simulations of stress distribution under constrained conditions in future work. In heat treatment with FPC (empty trays), rupture occurred around 27–49 mbar and experimental reaction forces of around 15–24 N, while in FPC (food-loaded trays), rupture occurred at lower pressures of around 12–29 mbar and experimental reaction forces of around 8–14 N. In both cases, headspace temperatures at the time of rupture ranged from around 25–50 °C. These results confirm two effects: first, that preloads increase rupture pressures during heating; and second, that the presence of food strongly modifies the thermal and pressurisation behaviour. However, further experimental and numerical validation is necessary to reinforce these findings.

Altogether, the results show that rupture of PP trays is governed by a chain of coupled phenomena: internal pressure produces reaction forces on the lidding film, airflow structures shape how loads are distributed, stresses concentrate at the seal edges, and rupture occurs once the seal interfacial strength is exceeded. Mechanical supports increase rupture pressures by redistributing stresses but cannot prevent failure.

This study contributes to addressing a knowledge gap in the field of process engineering and food packaging. Previous works on flexible and semi-rigid packaging have largely focused on seal strength testing or thermal performance in isolation, but no study has investigated how airflow, internal pressurisation, and structural deformation interact to cause rupture in ready-to-eat food trays. By combining experimental observations with numerical analysis using CFD, FSI, and structural mechanics, this study offers an integrated perspective on airflow patterns, pressure evolution, and von Mises stress localization to collectively govern rupture in packaging.

Building on these findings, the next chapter focuses on the influence of mechanical constraints on thermal and pressure behaviour during microwave heating of rigid and flexible food packaging systems. The study experimentally evaluates the effect of different constraint configurations on pressure buildup and thermal response under rapid unconventional microwave heating.

# Chapter 5
# Influence of Mechanical Constraints on Thermal and Pressure Behaviour During Microwave Heating of Rigid and Flexible Food Packaging Systems

## 5.1 Introduction

The previous chapter demonstrated that rupture of polypropylene (PP) trays during conventional treatments is governed by coupled phenomena such as internal pressurisation, and airflow-driven stress distribution. Mechanical constraints increased rupture pressures by redistributing stresses, yet failure still occurred once adhesion at the heat seal weakened under conventional thermal treatment. Building on this foundation, the present chapter shifts focus to microwave heating. Microwave heating differs from conventional heating by generating rapid volumetric heating at certain frequencies (915 MHz or 2450 MHz). Such conditions pose unique challenges for packaging stability, making the role of mechanical constraints even more important. While pressurized water systems like those used in MATS (Microwave-Assisted Thermal Sterilization) effectively prevent failure through external hydrostatic pressure, they require substantial water and energy inputs (Datta & Rakesh, 2013; Hong et al., 2021; Stanley & Petersen, 2017; Tang, 2015). In line with European sustainability targets for reducing water consumption in industrial processes (Water Europe, 2023), using mechanical constraint systems for counter-pressure offer a promising alternative. However, despite decades of research on microwave sterilization, little is known about the influence of mechanical constraints on pressure and temperature dynamics in food packaging during microwave heating.

Hence, this chapter investigates the influence of mechanical constraints on pressure and temperature evolution in food packaging during microwave heating at 915 MHz. Both flexible polypropylene (PP) trays and rigid Polyether ether ketone (PEEK) containers are examined. For flexible packagings, the study evaluates the effect of two different mechanical constraint configurations on internal pressure buildup, temperature rise, and the time to rupture. For rigid packaging, the goal is to determine whether sterilization-level temperatures can be reached, and to study pressure and temperature evolution throughout the microwave heating process. Therefore, there are two major objectives of this chapter. First, to assess the impact of different mechanical constraint configurations on the thermal and pressure performance of flexible packaging systems. Second, to evaluate the ability of a rigid pressurized constraint to achieve heating up to sterilization temperatures and to withstand internal pressure during microwave sterilization.

## 5.2 Materials and Methods

### 5.2.1 Materials

#### 5.2.1.1 Model Food

Mashed potato was used as the model food system for all experimental trials in this study. The formulation and preparation protocols were identical to those described in Chapter 3 (3.2.1.1).

#### 5.2.1.2 Packaging materials

Flexible packaging was used for Part A of the study. Polypropylene (PP) trays sealed with a heat-sealable PP film (65 µm thickness) were used as similar to typical ready-meal packaging. The film possesses a melting point around 160–165 °C. The PP tray (Fig. 5.1 (a)) was heat sealed using an industrial-grade Multivac system (Type Galaxy, Model TS 355, Multivac, France) at 160°C in 5s.

Rigid packaging was used for Part B of the study. Custom-fabricated cylindrical containers made of Polyether ether ketone (PEEK) (Fig. 5.1 (b)), a high-performance polymer with a high melting point (~343 °C) and mechanical rigidity was used.

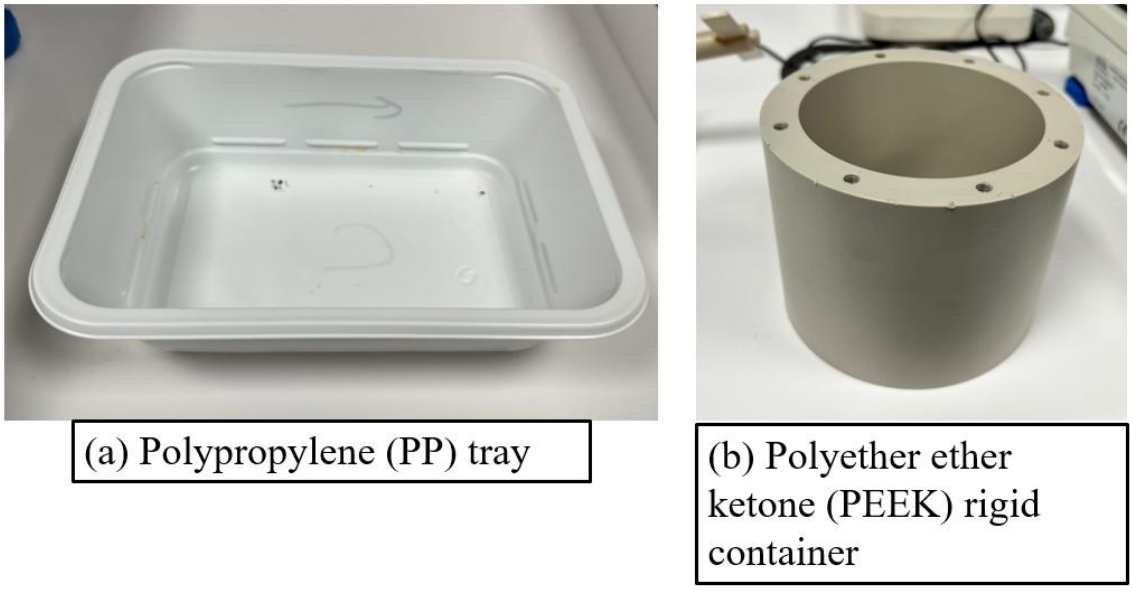



*Fig. 5. 1: Images of (a) Polypropylene (PP) trays (b) custom-made Polyether ether ketone (PEEK) rigid container.*

#### 5.2.1.3 Pressure and Temperature measurements

For Part A of the study, pressure and temperature were measured using NanoVACQ PT sensors sensors manufactured by TMI-Orion (Castelnau-le-Lez, France). These sensors used were specified for a measurement range of 30 mbar to 30 bar for pressure measurement and for a measurement range of 0°C to 140°C for temperature measurement. Special microwave shields (PicoVACQ microwave bullet, TMI-Orion, France) were used along with these sensors for microwave application. For Part B of the study, pressure and temperature were measured within the custom-built system designed. Temperature was measured using optical fibres with specific data logger (Rugged Monitoring H201, Quebec, Canada) and pressure was measured using a stainless steel pressure transmitter (IFM PT5400, Germany) and recorded with another data logger (AOIP, France). The system was designed in such a way that there is no pressure loss or water vapor leakage during the thermal treatment.

### 5.2.2 Experimental Setup

#### 5.2.2.1 915 MHz microwave system with pressure regulation system

A 915 MHz single-mode microwave device (SAIREM, France) (Fig. 5.2) was used for microwave heating. This was powered by a solid-state microwave generator (GLS1500 KSM 1500 W, SAIREM®, France) to produce a stable source of microwaves. The microwave power is transmitted to the antenna of a WR975 waveguide transition for microwave propagation. Its operating frequency is 902 MHz to 928 MHz with a maximum output power of 1500 W. The food container (PP tray or PEEK container) is placed within the single-mode microwave applicator. 2 iris rods and 1 sliding short circuit are used for impedance matching (maximizing microwave absorption and minimizing microwave reflection by the sample). A custom-built pressure regulation system using compressed air was added to the microwave system for Part B of the study. Compressed air was supplied from the source at 4 bar (relative) to the regulation unit. The initial starting pressure inside the PEEK container was set to 0.2 bar (relative) and was programmed to increase up to a maximum of approximately 1.5 bar (relative) during the microwave heating process, controlled by a pressure regulation unit. The upper measurement limit was fixed at 3 bar (relative), and a safety valve was installed in the system with the security pressure also set at 3 bar (relative) to prevent accidental overpressurization. The system maintained this preset internal pressure during the entire microwave heating phase. The pressure transmitter operates on the piezoresistive diaphragm principle where the internal pressure in the PEEK container is transmitted through airtight tubing to the transducer diaphragm, causing proportional deflection of a sensing element whose electrical resistance changes with applied pressure. This signal is converted into a voltage output and recorded in real time by the data logger. A detailed schematic diagram of the 915 MHz microwave system with the integration of pressure regulation system is presented in Fig. 5.3.

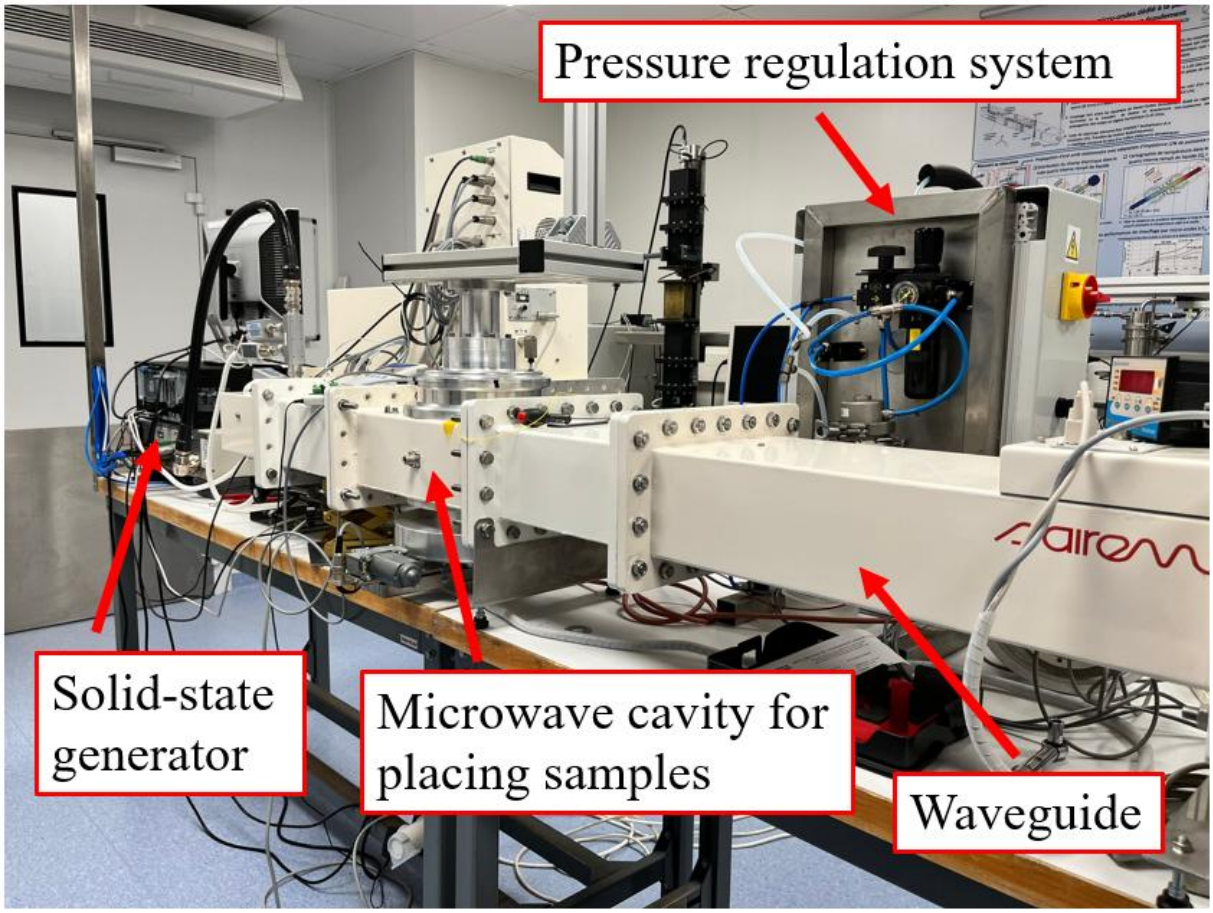



*Fig. 5. 2: Experimental setup of 915 MHz microwave system combined with custom-made pressure regulation system.*

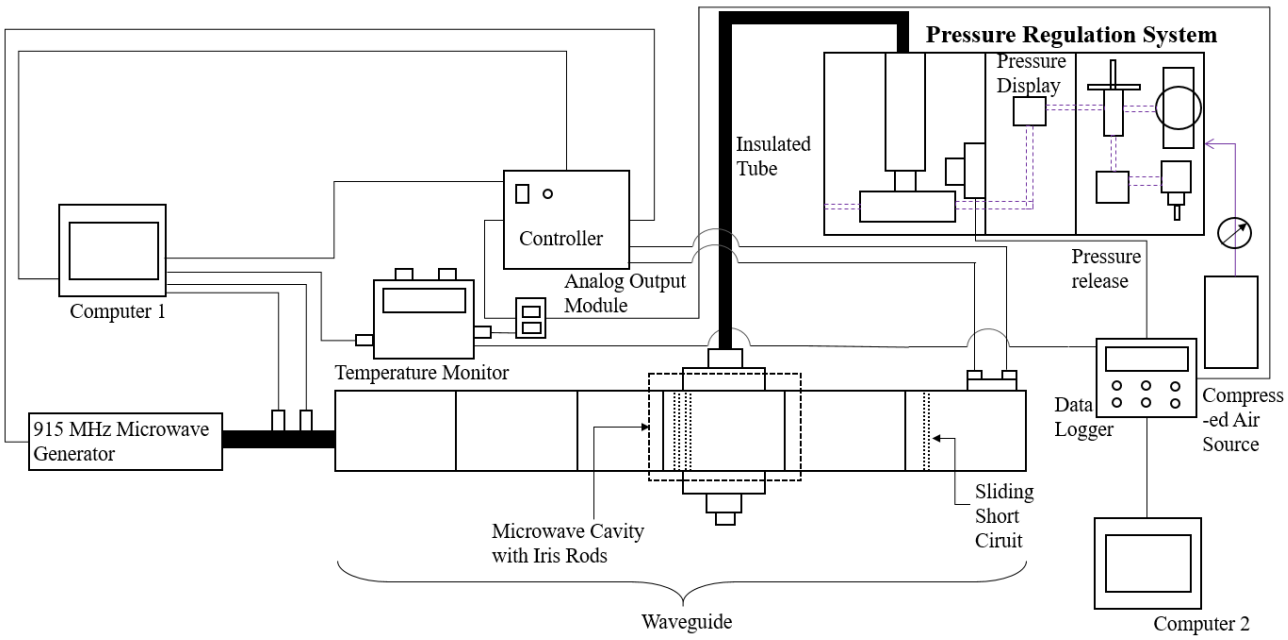



*Fig. 5. 3: Detailed schematic diagram of 915 MHz microwave system with the integration of pressure regulation system.*

### 5.2.3 Experimental Design

The experiments were designed to study the influence of mechanical constraints on pressure and temperature evolution during microwave heating of food packaging systems, with particular attention to the heating phase of the process. The focus was placed on achieving a controlled and reproducible thermal profile under microwave heating, rather than replicating the exact heating ramp of a conventional retort system. This approach was chosen because, with a fixed microwave power input, it was possible to monitor and adjust the temperature evolution to obtain a nearly linear heating ramp followed by a defined holding phase, representative of sterilization conditions. The study was divided into two main parts:

*Part A:* Investigation of flexible PP packaging under three mechanical configurations—no constraint (NC), free deformation with fixed preloaded constraint (FPC), and fixed mechanical constraint with no deformation (FMC).

*Part B:* Investigation of a rigid pressurized constraint (RPC) made of a PEEK container to assess its ability to withstand internal pressure while achieving temperatures representative of sterilization conditions. In the food industry, sterilization of low-acid foods is typically performed in the range of 115–125 °C, with 121.1 °C commonly used as the reference temperature for process validation. In this study, the target temperature was set at around 118 °C to remain within this industrial sterilization range while being achievable under the present experimental setup.

All tests were conducted under standardized microwave heating conditions (915 MHz) and terminated either at the point of rupture (Part A) or upon reaching the sterilization temperature above 100 °C (Part B).

#### 5.2.3.1 Part A – Flexible Polypropylene Packaging

Part A comprised three distinct experimental configurations that systematically varied the degree of mechanical constraint applied to the food packaging:

In Configuration A1 (no constraint (NC)), the packaging was unrestrained and allowed to deform freely under internal pressure.

In Configuration A2 (free deformation with fixed preloaded constraint (FPC)), was applied to the top sealing film using a vertically movable mechanical module. This enabled real-time measurement of the force applied to the top film during MW heating and its effect on package deformation and rupture behavior.

In Configuration A3 (Fixed Mechanical Constraint (FMC)), both the top and bottom surfaces of the packaging were rigidly immobilized using rigid Polyoxymethylene (POM) plates to eliminate all vertical deformation.

In all three configurations, experiments were conducted until the rupture of the PP sealing film. Time-to-rupture, pressure buildup, and temperature evolution at the center and headspace were analyzed to determine how the type and magnitude of mechanical constraint influence the ability to delay rupture and influence internal pressure and temperature. Special attention was given to comparing movable (A2) vs. fixed constraint conditions (A3), particularly in terms of their effect in premature rupture.

#### 5.2.3.2 Part B – Rigid Pressurized Constraint (RPC)

Part B of the study used a custom-made rigid container made from PEEK, a strong and heat-resistant polymer. This container was designed to prevent any deformation or rupture during microwave heating, providing a system with rigid mechanical constraints from all directions. The main goal was to test whether it is possible to safely reach the sterilization temperature above 100 °C at the center of the food without packaging failure or leakage of the model food. In addition, this setup was used to examine whether a rigidly confined system could achieve a uniform temperature distribution between the center and the side of the food. Table 5.1 summarizes the key features of each experimental condition.

*Table 5. 1: Summary of Experimental Design.*

| Part | Packaging Type | Constraint Type | Force Applied | Measured Variables | Termination Criterion | Objective |
|---|---|---|---|---|---|---|
| **A1 : NC** | Flexible (PP tray) | None | None | Temperature (center), Temperature (headspace), Pressure (headspace) | Rupture of sealing film | Establish baseline pressure and temperature evolution in an unconstrained system |
| **A2 : FPC** | Flexible (PP tray) | Movable top plate with initial preload | 80 N | Temperature (center), Temperature (headspace), Pressure (headspace), Applied Force (upper film) | Rupture of sealing film | Study the effect of initial preload on rupture delay and internal pressure buildup with the packaging |
| **A3 : FMC** | Flexible (PP tray) | Fixed constraints (top and bottom) | Not applicable | Temperature (center), Temperature (headspace), Pressure (headspace) | Rupture of sealing film | Evaluate if full mechanical immobilization can delay rupture and modify pressure–temperature evolution |
| **B : RPC** | Rigid (PEEK) | Fully rigid from all directions | Not applicable | Temperature (center), Temperature (side), Pressure (headspace) | Center temperature reaches above 100°C | Determine if completely rigid mechanical constraint can achieve sterilization temperature safely and ensure uniform heating |

### 5.2.4 Experimental Protocols

#### 5.2.4.1 Part A – Experiments with Flexible Packaging

Three configurations were tested to evaluate the influence of mechanical constraints on heating behavior and internal pressure development.

*A1: No Mechanical Constraint (NC)*

The PP tray was filled with 300 g of mashed potato and sealed. No additional constraint was applied. The sample was placed in the microwave cavity, and heating was continued until the PP film ruptured. Images of pressure and temperature sensors in PP trays are shown in Fig. 5.4. A schematic of the placement of temperature and pressure sensors is shown in Fig. 5.5.



*Fig. 5. 4: Images of pressure and temperature sensors in PP trays. Headspace temperature and pressure is measured by the larger sensor and is placed on the surface of the mashed potato. Mashed potato temperature is measured by the smaller sensor and is placed inside the mashed potato (approximately 10 mm above the bottom of the tray). *Placement of the sensors is not exactly depicted in the image.*

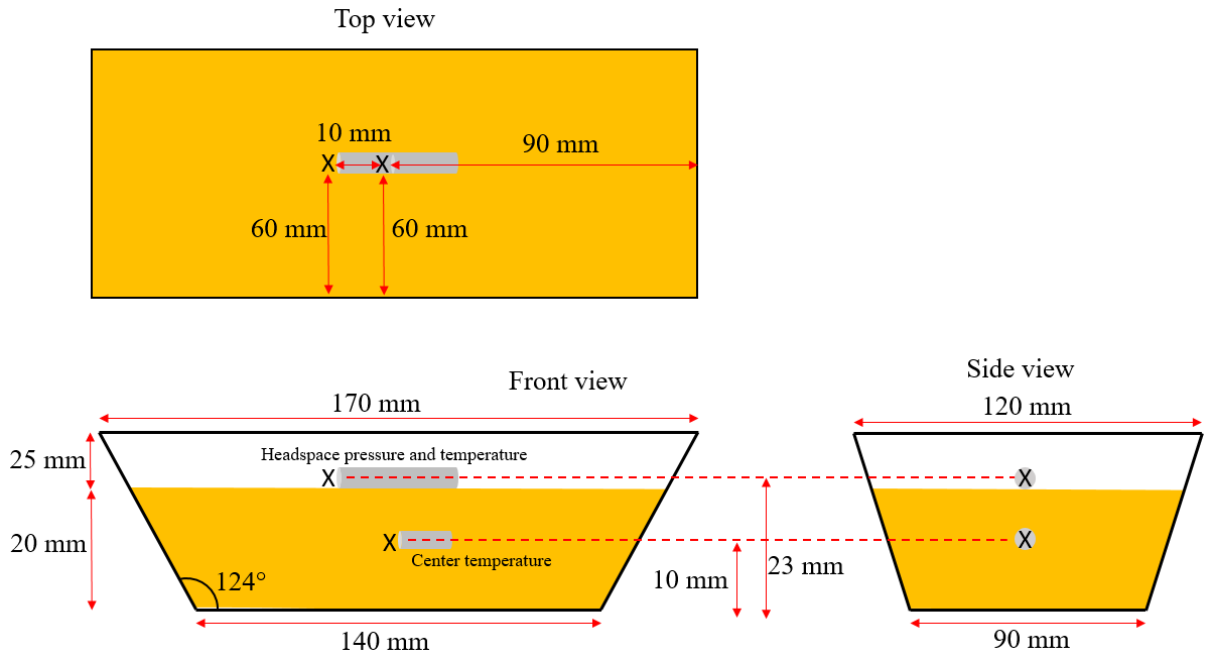



*Fig. 5. 5: Schematic of the placement of pressure and temperature sensors (center and headspace) from top, front, and side views.*

*A2: Free deformation with Fixed Preloaded Constraint (FPC)*

The same PP tray configuration (as in A1) was used. A vertical force of 80 N was initially applied (Fig. 5.6) on the upper surface of the PP film with a PEEK rectangular plate. The preload value of 80 N was selected based on preliminary compression tests conducted with a texture analyzer on identical PP trays. It was found that forces above 80 N caused structural failure of the PP tray. Therefore, 80 N was selected as the maximum preload that the tray could safely withstand without breaking down. The goal was to evaluate the influence of a compressive force on the rupture delay, pressure buildup, and temperature profiles during MW heating. Once the initial loading was applied, the pressure sensor was zeroed so that subsequent measurements reflected only the pressure generated during microwave heating. The sealed PP tray with mashed potato was placed inside the 915 MHz microwave cavity and the FPC was loaded into the cavity as shown in Fig. 5.7.

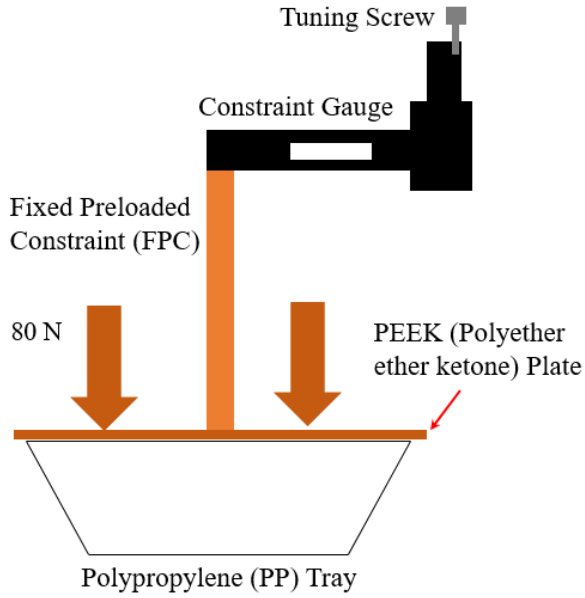



*Fig. 5. 6: Schematic of a vertical compression system exerting a force of 80 N on the upper surface of the PP film.*

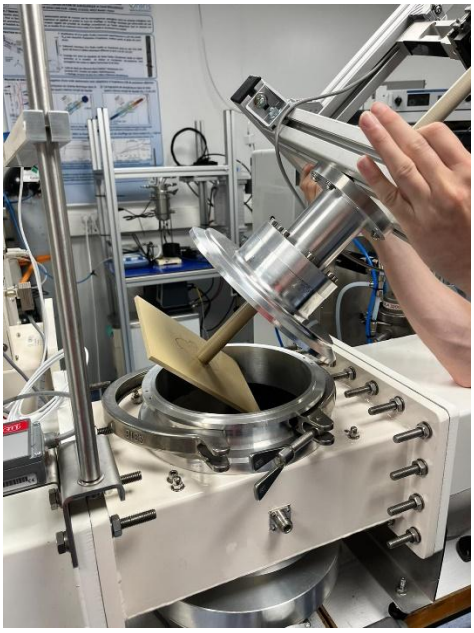


*Fig. 5. 7: Fixed Preloaded Constraint (FPC) placed inside the 915 MHz microwave cavity.*

*A3: Fixed Mechanical Constraint (Top and Bottom) (FMC)*

Again, the same PP tray configuration (as in A1) was used. The sealed PP tray sample was then positioned between two fixed Polyoxymethylene (POM) plates holding the top and bottom surfaces rigidly during heating. This setup constrained the packaging to have restricted movements on the top and bottom direction. Rupture behaviour, internal pressure evolution, and temperatures were recorded. Fig. 5.8 and Fig. 5.9 displays the images and schematic of the placement of FMC inside the 915 MHz microwave cavity.

All experiments were conducted starting from ambient temperature, and the microwave forward power was set at 200 W. The sliding short circuit was adjusted to 920 mm from the center of the sample to the metallic plate for minimum reflection power.

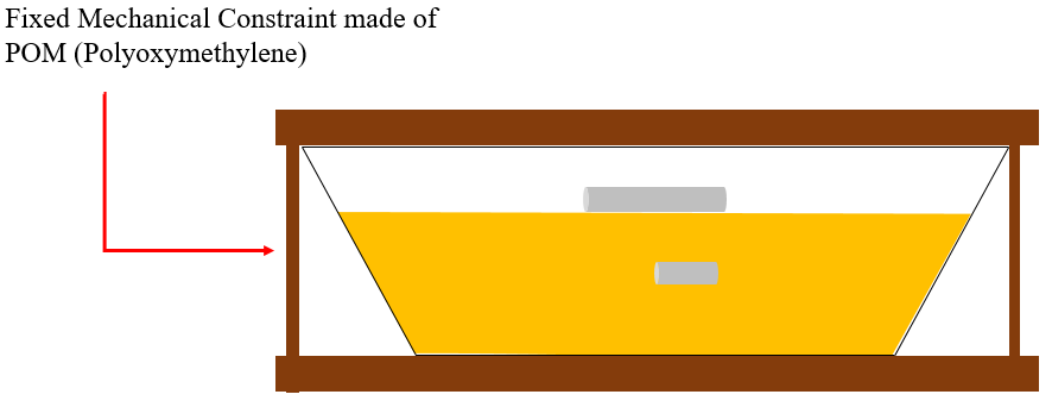



*Fig. 5. 8: Schematic of Fixed Mechanical Constraint (FMC) made of Polyoxymethylene (POM) containg heat sealed PP trays with pressure and temperature sensors.*



*Fig. 5. 9: Images of Fixed Mechanical Constraint (FMC) placed inside 915 MHz microwave cavity.*

### 5.2.4.2 Part B – Experiments with Rigid Pressurized Constraint (RPC)

A rigid container made of PEEK was used which acted as a solid cylindrical constraint from all direction. The PEEK container was connected to a pressure control apparatus that is used for measuring the internal pressure build-up within the headspace during MW heating. Two optical fibres were inserted into the container through two hermetic feedthroughs on top of the lid to measure the temperature at the center and the side location of mashed potato (Fig. 5.10). The system was initially pressurised with compressed air (0.2 bar above atmospheric pressure) in order to increase the boiling point of water and allow higher temperatures to be reached under saturated conditions. This overpressure ensured that sterilization-level temperatures could be achieved during microwave heating without premature boiling. In addition, maintaining internal pressure also prevented vapor or food material from escaping through the openings once temperatures exceeded 100 °C. The outer diameter of the container is 140 mm and the height of the container is 100 mm with a thickness of 10 mm. 388 g of mashed potatoes were filled into the container. The headspace height was maintained at 40 mm. The different components of the RPC system are shown in Fig. 5.11.

All experiments were conducted at ambient temperature, and the microwave forward power was set at 400 W continuously. This power level was selected to ensure a sufficient heating rate to reach sterilization temperatures within the experimental duration when using the rigid PEEK container. The mass of mashed potato filled into the container was increased from 300 g to 388 g because, with 300 g, the fixed optical fibre probes could not reach their dedicated measurement locations or make proper contact with the food. Increasing the filling mass to 388 g ensured that both optical fibre sensors accurately reached the target positions at the center and side of the mashed potato sample, The sliding short circuit was adjusted to 818 mm from the center of the samples to the metallic plate for minimum reflection power.

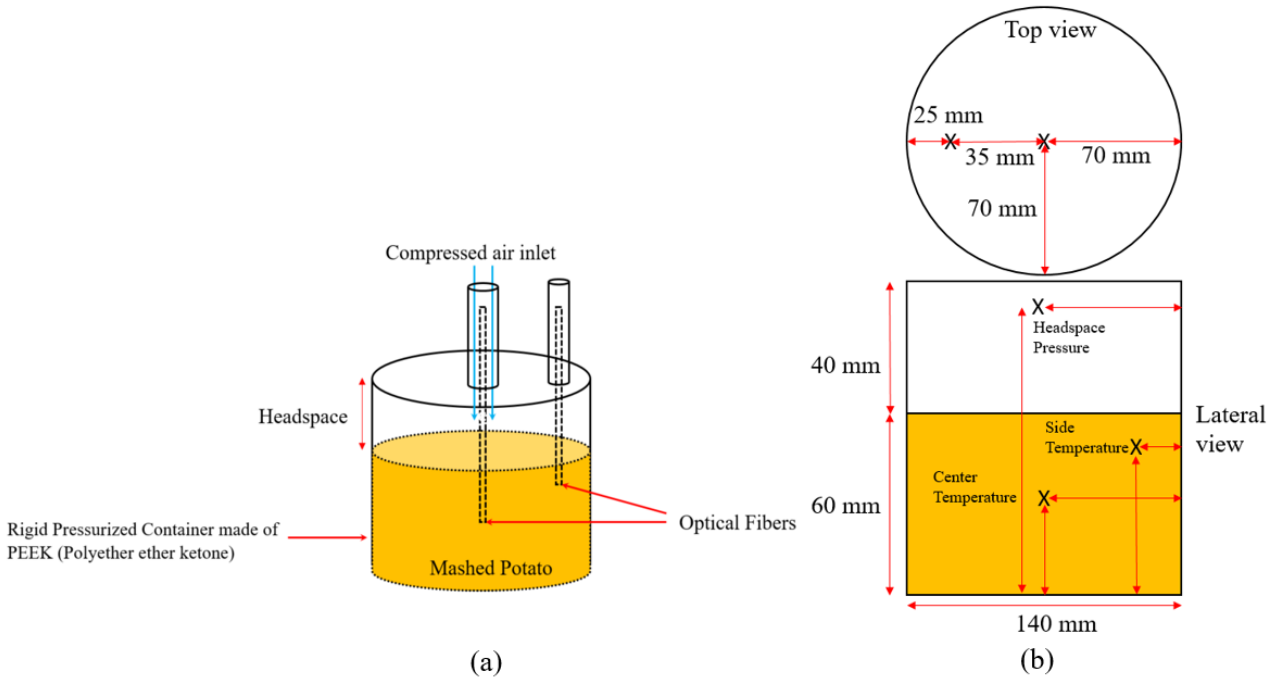



*Fig. 5. 10: (a) Rigid Pressurized Constraint (RPC) with a cylindrical PEEK container equipped with optical fibers and pressure measurements. (b) Locations of temperature and pressure measurements from top and lateral views.*

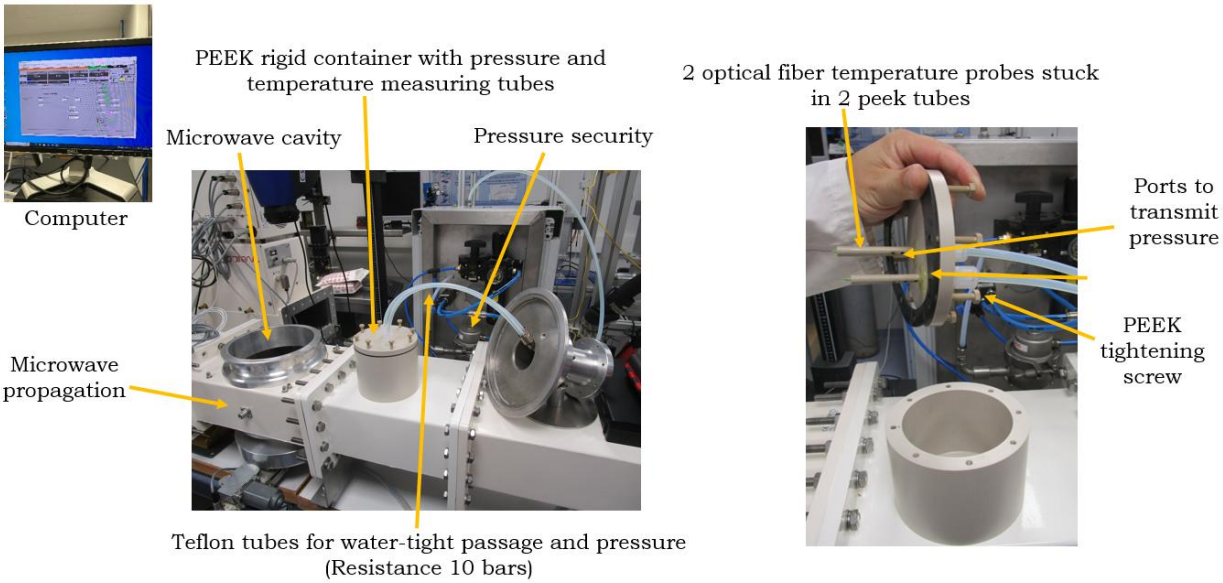



*Fig. 5. 11: Different components in Rigid Pressurized Constraint (RPC) system.*

## 5.3 Results and Discussions

### 5.3.1 Temperature and Pressure Evolution in Flexible Packaging (PP Tray)

#### 5.3.1.1 No Mechanical Constraint (NC)

In the no constraint (NC) configuration, the PP tray was heated in the microwave cavity without any external mechanical support. The headspace pressure remained low throughout the experiment and reached a maximum of around 7 mbar before the rupture occurred (Fig. 5.12). This was similar to the results of no constraint configuration during heating in the oven in Chapter 4 where rupture occurred around the same range of 8 mbar. The centre of the mashed potato heated more rapidly than the headspace air, producing a small but consistent difference of about 2–4 °C. This behaviour results from the dielectric heating mechanism of microwaves, in which the alternating electromagnetic field interacts with polar molecules, primarily water, causing their rapid rotation and frictional losses that generate heat within the food volume. As a result, the food matrix heats volumetrically, while the surrounding headspace air, which lacks significant polar content, warms mainly by convective heat transfer from the hot food.

Rupture was consistently at 265 ± 12 s where seal failure occurred once the headspace reached approximately 50–55 °C, as observed in Chapter 4 for heat treatment experiments,. At the time of rupture, the center temperature of the mashed potato reached 59.03 ± 6.22 °C (n = 3). The headspace temperature increased progressively during heating and reached 55.29 ± 5.31 °C (n = 3) (Fig 5.12) at the time of rupture. In both cases (heat treatment in oven and microwave treatment), rupture was not triggered by a significant increase in internal pressure (around 7 mbar in microwave treatment and around 8 mbar in oven heat treatment in Chapter 4) but by the observed (not measured) localization of failure at the seal interface. It is assumed that this failure may be linked to a loss of mechanical integrity at the heat-seal layer, possibly due to local temperature effects, although this hypothesis has not been experimentally verified in the present study. Therefore, the explanation of seal weakening or molecular relaxation at moderate temperatures remains a proposed mechanism requiring further experimental validation.

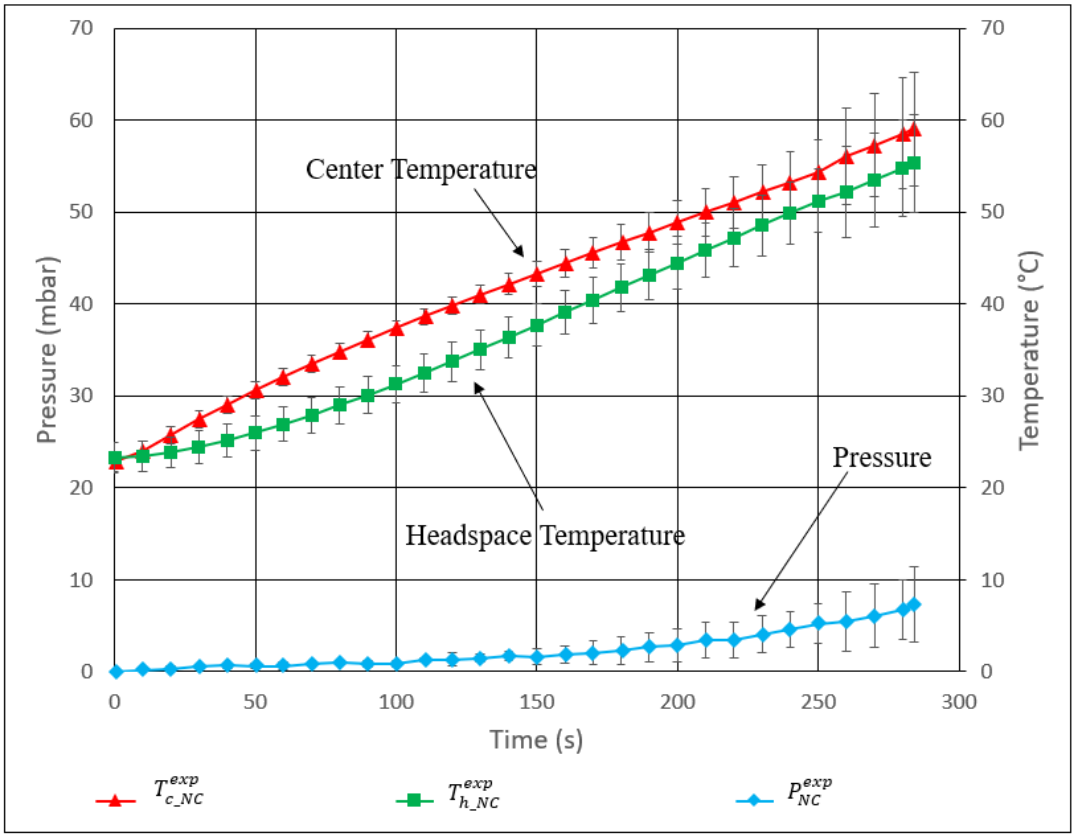



*Fig. 5. 12: Temperature (T) evolution at the center and headspace location of mashed potato and also relative pressure (P) evolution during microwave heating (915 MHz) with no constraint (NC) on PP tray.(c: center location; h: headspace location; exp: experimental values).*

### 5.3.1.2 Free deformation with Fixed Preloaded Constraint (FPC)

In the free deformation Fixed Preloaded Constraint (FPC) configuration with initial loading of 80 N at the top surface of the PP tray, the headspace pressure increased more significantly compared to the NC configuration, reaching 44.63 ± 4.57 mbar (n = 3) before rupture (Fig 5.13). The rupture occurred at 259 ± 9 s (n = 3) across all trials. The center temperature of the mashed potato increased gradually and reached 56.61 ± 1.53°C (n = 3) at the time of rupture (Fig 5.13). The headspace temperature also increased over time and reached 35.38 ± 0.84 °C (n = 3) (Fig 5.13). The force recorded on the top film increased steadily during heating. At the time of rupture the corresponding force acting on the upper surface of the PP film was 28.01 ± 2.78 N (n = 3) indicating the response of the system to internal pressure buildup (Fig 5.14).

Compared with the NC configuration (Section 5.3.1.1), the application of the preload led to a measurable increase in rupture pressure (from ~7 mbar, to ~47 mbar) at rupture. However, the rupture times were similar, occurring at ~260–277 s in both cases, and the centre rupture temperatures were nearly identical, around 57–58 °C. The main difference was that the headspace temperature was lower under FPC (36.6 °C) than in the NC case (54.7 °C). This lower headspace temperature can be explained by the change in thermodynamic conditions within the headspace due to the preload constraint. When the preload was applied, the reduction in air space caused the headspace air to remain compressed during heating. This compression increased the internal pressure more rapidly, even though the heating conditions were the same.

As a result, the available space for air expansion was limited, leading to faster pressure buildup but a lower headspace temperature. The same amount of thermal energy was therefore distributed within a smaller confined region.

Direct observation of the PP film movement was not possible during microwave heating because the experiments were performed in a closed cavity. However, from the deformation behaviour already demonstrated in Chapter 4, it can be inferred that upward displacement of the sealing film still occurred under microwave heating, as the applied preload was not sufficient to fully restrain doming of the lid (applied force at the top surface is higher than 30N at time of rupture). Although the vertical constraint reduced deformation at the top surface, the bottom and lateral sides of the tray remained unconstrained. This might have allowed radial expansion, which could have concentrated mechanical stresses at the sealing edges and eventually led to rupture. This hypothesis has not yet been verified and should be confirmed through future experimental and numerical investigations.

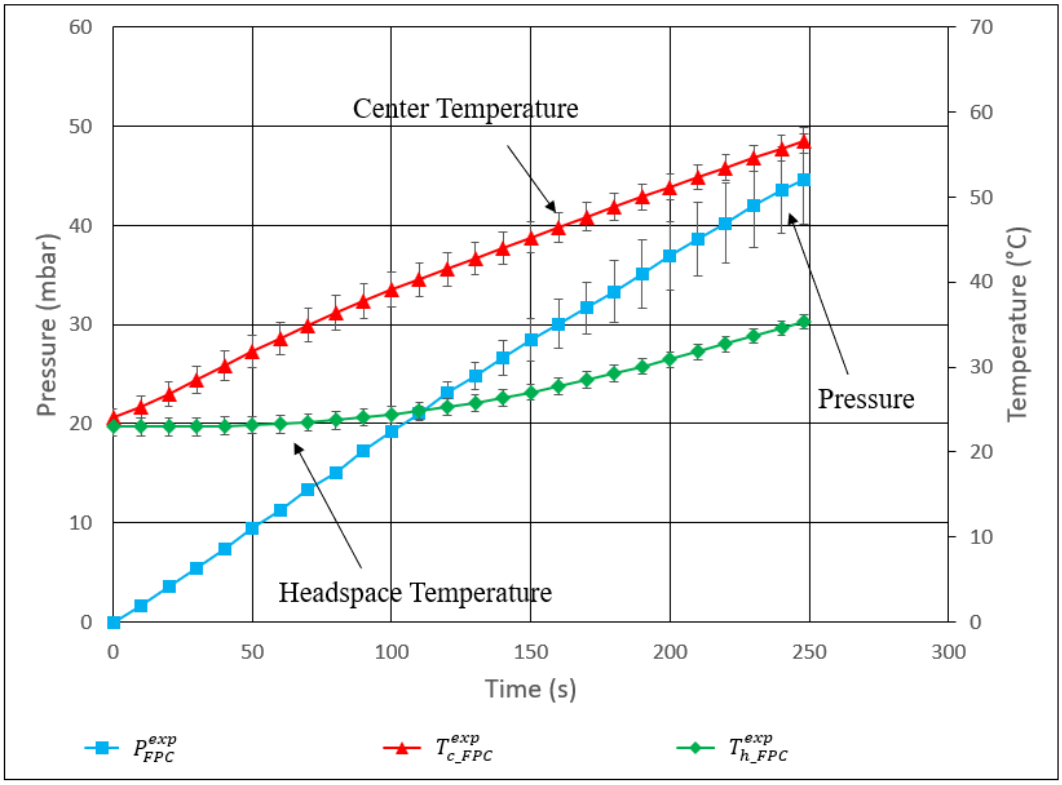



*Fig. 5. 13: Temperature (T) evolution at the center and headspace location of mashed potato and also relative pressure (P) evolution during microwave heating (915 MHz) with fixed preloaded constraint (FPC) on PP tray. Initial force on PP film was 80 N (c: center location; h: headspace location; exp: experimental values).*

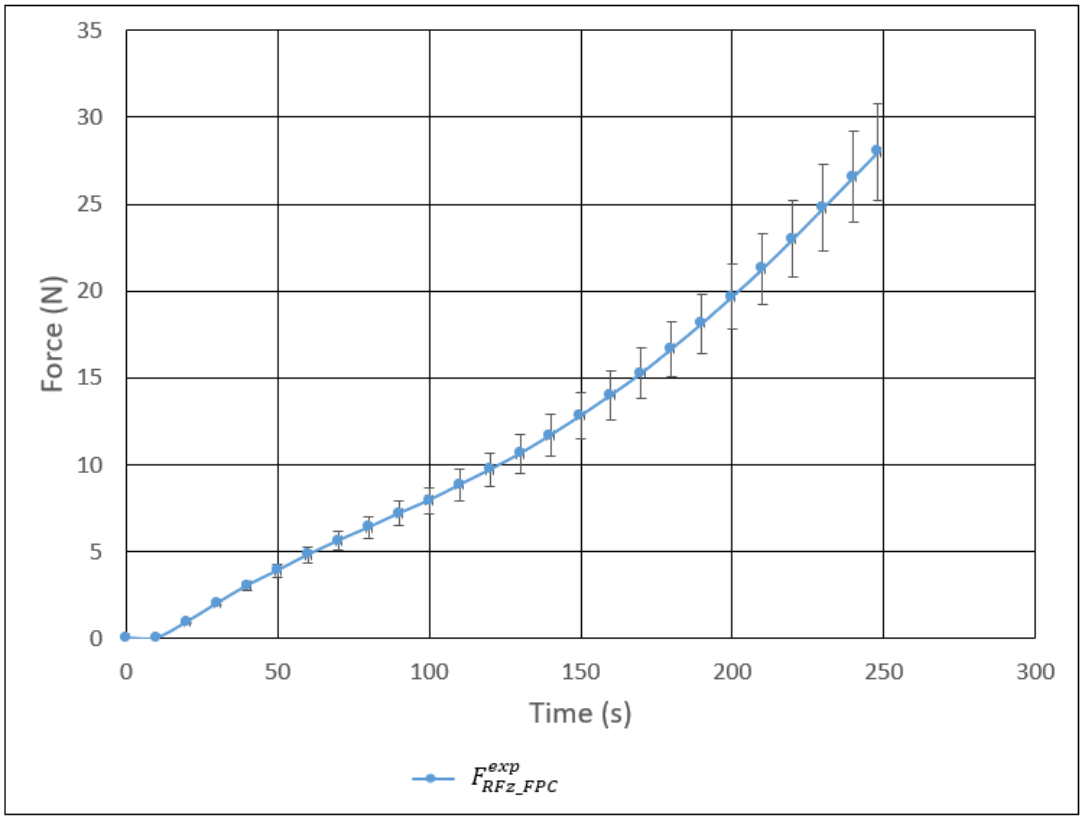



*Fig. 5. 14: Evolution of experimental reaction force ($F^{exp}_{RFz}$) exerted on the upper PP film surface due to pressure build-up inside PP tray in different trials with fixed preloaded constraint (FPC). Initial force on PP film was 80 N.*

#### 5.3.1.3 Fixed Mechanical Constraint (FMC)

In the fixed mechanical constraint (FMC) configuration, the PP tray was clamped between two rigid POM plates to prevent vertical displacement from both the top and bottom. The internal headspace pressure increased progressively and reached 41.63 ± 0.04 mbar before the sealing film ruptured (Fig 5.15). The rupture occurred at 256 ± 15 s (n = 3), which is within the uncertainty range of the rupture times measured in the NC (265 ± 12 s) (n = 3) and FPC (259 ± 9 s) (n = 3) configurations. Therefore, there is no significant difference in rupture time between FMC and the other configurations. The center temperature of the mashed potato reached 50.59 ± 1.51 °C at the time of rupture (Fig 5.15). The headspace temperature followed a similar trend as in other configurations and reached 38.69 ± 1.53 °C at the time of rupture (Fig 5.15). The center temperature here is similar to those of NC (59.03 ± 6.22°C) and FPC (56.61±1.53°C). On the other hand the headspace temperature here is similar to FPC configuration (35.38±0.84°C) but lower than NC configuration (55.29±5.31°C). This behaviour can be attributed to the reduced and fixed air space inside the tray caused by the mechanical constraint. The confined air was compressed during heating, which led to a faster rise in internal pressure despite identical heating conditions. Because the available space for expansion was limited, the same amount of thermal energy was distributed in a smaller confined region, resulting in a lower headspace temperature.

In this FMC configuration, the lateral sides of the tray remained unconstrained, allowing radial expansion that might have imposed tangential stresses on the sealing edges. The combination

of restricted dome formation thereby reducing headspace volume, and tangential loading at the seal interface lead to the rupture of the PP tray despite the fixed vertical support. This behaviour is consistent with the mechanisms discussed in Chapter 4, where rupture was attributed primarily to the combined effects of internal pressure and stress concentration at the sealing zone, rather than to bulk polymer yielding. In the present case, the increased absolute pressure inside the tray appears to have been the dominant factor initiating failure at the seal interface. Nevertheless, further experiments and numerical simulations are needed to confirm these interpretations and to directly establish the link between packaging deformation, headspace fluid flow, and stress concentration during microwave heating.

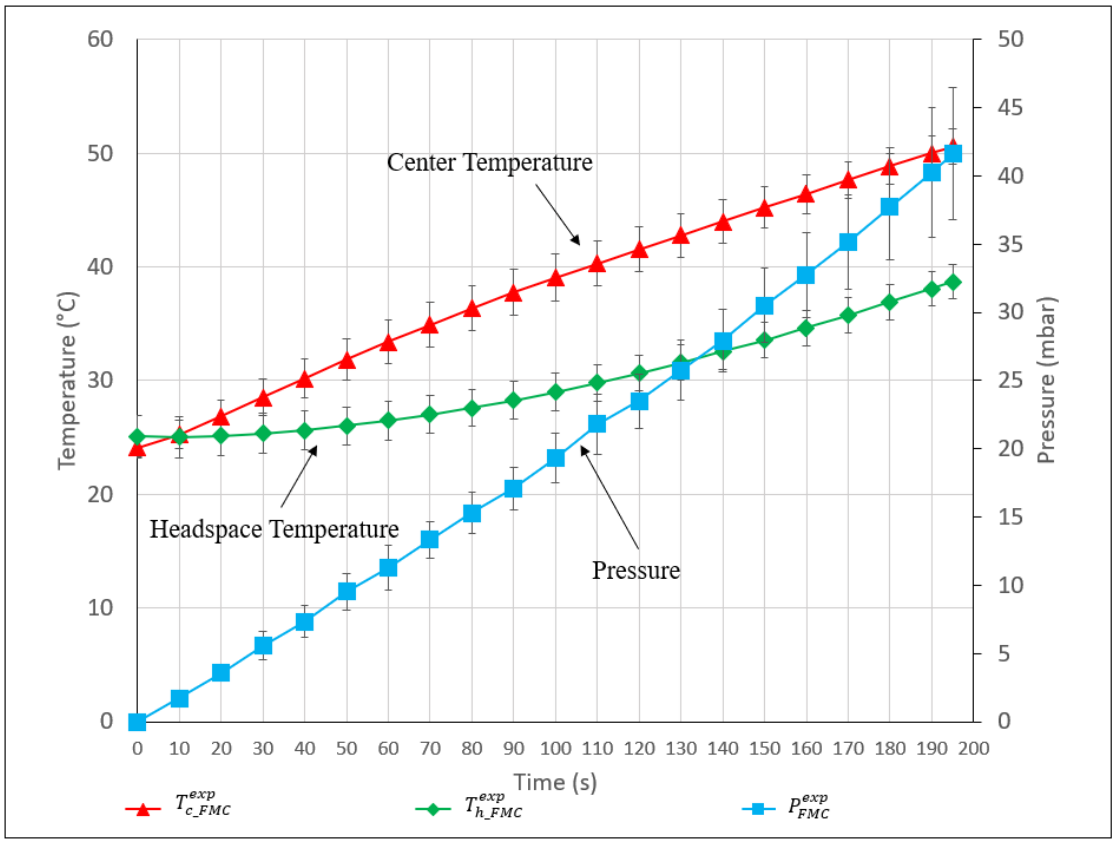



*Fig. 5. 15: Temperature (T) evolution at the center and headspace location of mashed potato and also relative pressure (P) evolution during microwave heating (915 MHz) with fixed mechanical constraint (FMC) on PP tray. (c: center location; h: headspace location; exp: experimental values).*

### 5.3.2 Comparative Analysis of Mechanical Constraints in Flexible Packaging (PP trays)

When no mechanical constraint (NC) was applied, the packaging ruptured at a relatively low internal pressure of around 7 mbar. In contrast, the application of FPC and FMC increased the rupture pressure significantly to 44.63 ± 4.57 mbar and 41.63 ± 0.04 mbar respectively which are similar. This represents an increase in rupture pressure of around 6 to 7 times higher for FPC and FMC cases relative to the unconstrained NC case. A summary of pressure, center temperature, headspace temperature, and time of rupture for NC, FPC, and FMC configuration at the time of rupture during microwave heating can be found in Table 5.2. When the volume

expansion of the headspace is restricted by mechanical constraint, the same amount of gas at a given temperature results in a higher pressure. Thus, even when the constraint is applied only in the vertical direction or vertical movement of the PP film is restricted, it limits volume expansion and consequently allows greater pressure retention inside the packaging before mechanical failure occurs. In contrast, in the unconstrained NC case, the film dome expands quickly, which increases headspace volume and limits pressure buildup. Similar observations were made in retort studies on semi-rigid containers, where increased constraint or structural rigidity led to higher pressure tolerance during thermal processing (P. N. Patel et al., 1991).

The rupture times were 265 ± 12 s for the unconstrained case (NC), 259 ± 9 s for FPC, and 256 ± 12 s for FMC. Given the overlap in uncertainties, these values are not significantly different. The similar rupture times observed across all configurations suggest that failure occurred once comparable internal conditions were reached, regardless of the applied constraint.

The center temperature at rupture was comparable across all three configurations. It was measured as 59.03 ± 6.22 °C for NC, 56.61 ± 1.53 °C for FPC, and 50.59 ± 1.51 °C for FMC. These results indicate that the temperature evolution during microwave heating followed a similar trend in all cases. Additionally, none of the configurations reached sterilization temperature targets, confirming that rupture remains the dominant limiting factor.

Although vertical deformation was reduced in the FPC configuration and further restricted in FMC, the lateral sides of the tray remained unconstrained in both cases. This condition may have allowed radial expansion during internal pressurisation, which could have generated additional stresses at the heat-seal zone leading to its rupture (Fig. 5.16). However, since the microwave cavity was non-transparent, deformation could not be directly observed, and this explanation must therefore be regarded as a hypothesis. The interpretation is consistent with the rupture patterns observed in this study and with the deformation behaviour described in Chapter 4, but further experimental validation and numerical modelling will be required to confirm whether radial expansion and associated tangential forces play a dominant role in the rupture mechanism during microwave heating. These suggest that while vertical constraints improve pressure resistance, a multidirectional constraint may be required to significantly enhance the mechanical stability of flexible packaging under microwave.

*Table 5. 2: Summary of pressure, center temperature, headspace temperature, and time of rupture for NC, FPC, and FMC configuration at the time of rupture during microwave heating.*

| | | |
|---|---|---|
| **Pressure (mbar)** | NC | 7±4.10 |
| | FPC | 44.63±4.57 |
| | FMC | 41.63±0.04 |
| **Center Temperature (°C)** | NC | 59.03±6.22 |
| | FPC | 56.61±1.53 |
| | FMC | 50.59±1.51 |
| **Headspace Temperature (°C)** | NC | 55.29±5.31 |
| | FPC | 35.38±0.84 |
| | FMC | 38.69±1.53 |
| **Time of Rupture (s)** | NC | 265±12 |
| | FPC | 259±9 |
| | FMC | 256±12 |



*Fig. 5. 16: Failure at heat seal zone with and without mechanical constraint.*

### 5.3.3 Temperature and Pressure Evolution of Rigid Pressurized Constraint (RPC)

In the RPC configuration, the center of the mashed potato exhibited a two-phase heating profile (Fig. 5.17). The center temperature increased rapidly from ambient to 100 °C within approximately 266 seconds, corresponding to a heating rate of about 16 °C/min under a microwave power of 400 W. It should be noted that the reported 400 W corresponds to the generator set-point (forward power), whereas the effective absorbed power within the load can differ due to impedance mismatch and time-varying coupling conditions, leading to a non-zero reflected power during heating. The forward microwave power is nearly double the rate observed in the NC, FPC, and FMC configurations (~8 °C/min at 200 W). Beyond 100 °C, the heating rate decreased to around 2 °C/min as water evaporation began within the food matrix, consuming part of the absorbed energy as latent heat of vaporization and slowing further temperature rise. Water vapour is generated inside the mashed potato as the internal moisture undergoes phase change, and the produced vapour gradually diffuses into the headspace. During this evaporation phase, a significant portion of the absorbed microwave energy is consumed as latent heat of vaporization rather than contributing to further temperature increase. This evaporation process under sealed conditions contributes not only to thermal stabilization but also to a steady increase in internal pressure. The internal pressure increased continuously as heating progressed. Initially stable, the pressure began to rise notably after 150 seconds and continued in a nearly linear trend. At 829 seconds, which was the termination of the microwave heating process, the pressure reached approximately 0.89 bar (relative) (Fig 5.17). This steady pressure rise is due to the continuous steam generation from water evaporation within the sealed container from the mashed potato domain. The measured pressure rise is consistent with the thermodynamic relationship between saturated temperature and saturated pressure. In general, at ~119 °C, the corresponding saturation pressure is about ~1.2 bar relative according to standard steam tables. The slightly lower value observed in this study (~0.89 bar relative) may be explained by local non-equilibrium conditions, including temperature gradients inside the food matrix, incomplete equilibration between liquid and vapour phases in the headspace, and minor heat losses to the container walls. These factors can lead to a lower measured pressure because some regions inside the mashed potato might remain at relatively lower temperatures and hence might not generate as much vapour as expected under uniform heating. At the same

time, a part of the vapour may condense on the cooler container walls, reducing the amount of vapour present in the headspace. As a result, the total vapour mass contributing to pressure is smaller, leading to a measured pressure slightly below the theoretical saturated value.

At the side of the container, the temperature rise was delayed. It took 578 seconds to reach 100 °C and an additional 251 seconds to reach 118 °C (Fig. 5.17). During the early stage of heating, a large temperature difference developed between the center and side. The maximum difference of approximately 40 °C occurred around 190 seconds, when the center reached approximately 80 °C while the side remained near 40 °C. This difference began to decrease once the side temperature rose beyond 40 °C. The initial formation of this temperature difference is mainly due to the non-uniform distribution of the electromagnetic field inside the microwave cavity, which causes some regions, such as the center, to absorb more microwave energy than others at the beginning of the process. In addition, under a constant forward power setting (400 W), the spatially non-uniform field distribution implies that the local volumetric power density is higher near the center at early times. Concurrently, the microwave absorbed power can evolve because the reflected power depends on the instantaneous effective permittivity of the load, which changes with temperature and moisture redistribution. As heating continues, this difference is further reinforced by the temperature-dependent dielectric properties of the mashed potato, since the dielectric loss factor ($\epsilon''$) increases with temperature, enhancing energy absorption in the already warmer regions (Fig. 5.18). $\epsilon''$ rises markedly with temperature (from 10 °C to 90 °C), so once the centre becomes slightly warmer, it dissipates microwave energy more efficiently due to higher dielectric loss factor. Specifically, the dielectric loss factor, which determines how effectively microwave energy is converted into heat, is relatively low at lower temperatures and increases as the temperature rises. Therefore, at the beginning of the process, the center, which heats faster, absorbs more energy. The electromagnetic field distribution inside the container created localised regions of higher energy density near the centre, favouring early microwave absorption. At the same time, the dielectric constant ($\epsilon'$) also varies moderately with temperature (Fig. 5.18), which can affect wave penetration and local field patterns. Thus, temperature-induced changes in $\epsilon'$ and $\epsilon''$ can modify the reflected power, altering the net absorbed power even when the forward power is held constant. Liu et al., (2023) also reported that regions located near the center of the load tend to absorb more microwave energy due to stronger field intensity in a cylindrical geometry container. A secondary contributing factor could be a slight cooling effect near the wall, since the sensor located closer to the container wall may be influenced by minor external heat losses. However, this effect is likely limited given the distance between the wall and the probe. As the process continued and the side temperature rose from around 20 °C to above ~40 °C, its ability to absorb microwave energy improves. Meanwhile, the center region, which remained at higher temperatures, continued to absorb more energy but also experienced the onset of evaporation. This phase change process consumed part of the absorbed energy as latent heat of vaporisation, thereby limiting further temperature increase at the center. As a result, the temperature difference between the center and the side gradually decreased. This behaviour is consistent with the findings presented in Chapter 3, where significant evaporation effects were observed at similar high temperatures.

The experiments were terminated when the temperature difference between the center and side fell below 2 °C. At the final moment, a temperature differences of only 1.2 °C were recorded between the centre and side. This narrow difference suggests that the system approached more

uniform heating conditions. However, because measurements were taken at only two locations, it cannot be concluded with certainty that the entire food domain was heated homogeneously. Additional temperature mapping with more measurement points would be required to fully validate heating uniformity.

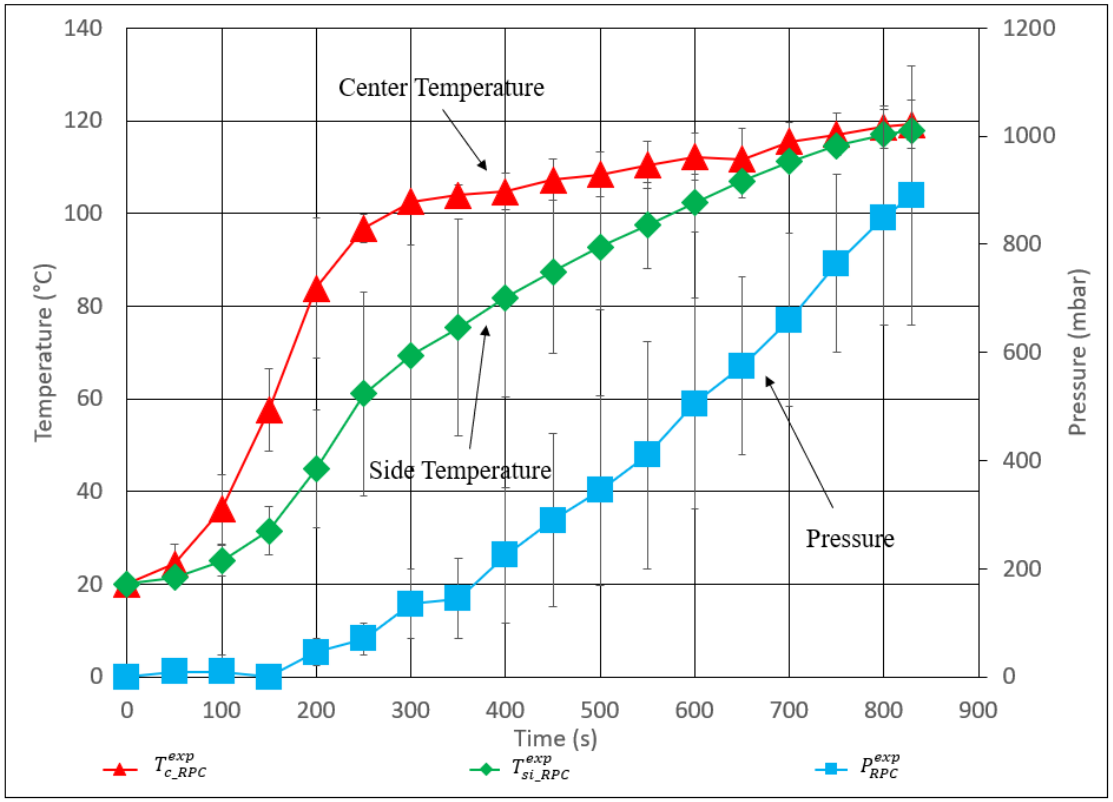



*Fig. 5. 17: Temperature (T) evolution at the center and side location of mashed potato and also relative pressure (P) evolution during microwave sterilization process (915 MHz) with pressurized PEEK rigid container (rigid pressurized constraint).(c: center location; si: side location; exp: experimental values).*

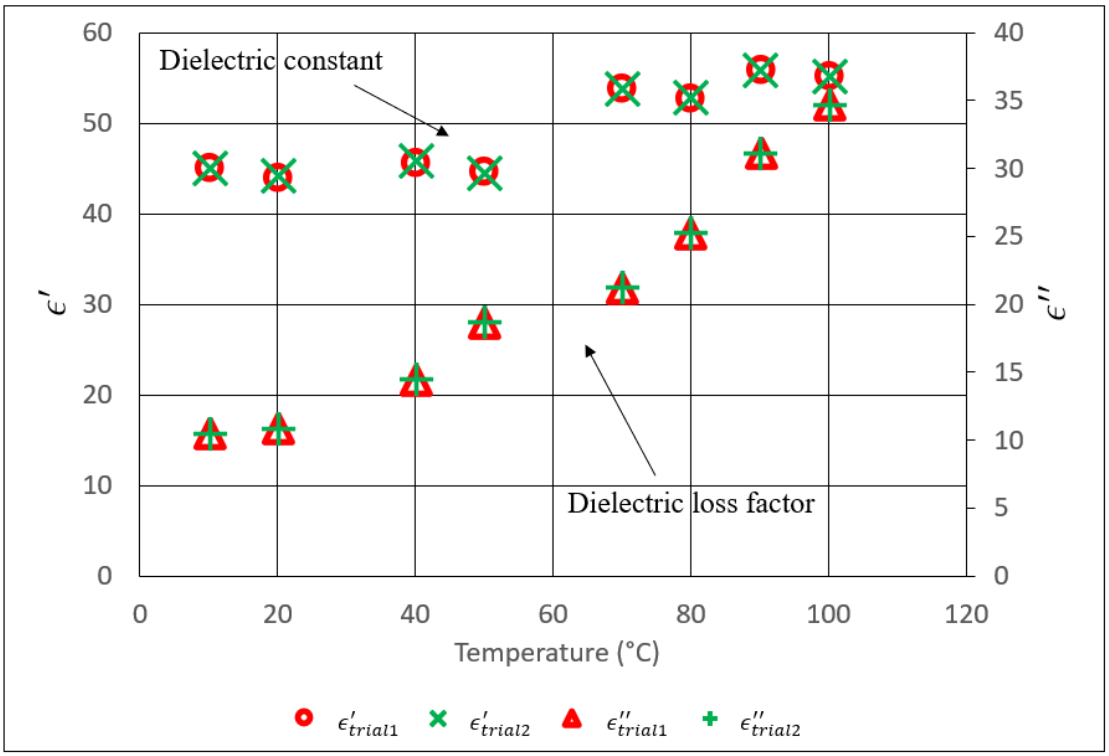



*Fig. 5. 18: Dielectric constant ($\epsilon'$) and dielectric loss factor ($\epsilon''$) in mashed potato as a function of temperature. Trial: two dielectric measurements were performed within the same sample.*

### 5.4 Conclusions

This study experimentally investigated the influence of mechanical constraints on the thermal and pressure behaviour of flexible and rigid food packaging systems during microwave heating at 915 MHz. The findings concluded differences in heating performance, structural response, and internal pressure buildup between flexible polypropylene (PP) trays and rigid PEEK containers under varying constraint conditions.

Both constraint methods (FPC and FMC) led to earlier rupture than the NC configuration, indicating that pressure accumulation reached the mechanical limit of the heat-seal interface. Although the heating rates among NC, FPC, and FMC remained nearly identical under 200 W microwave power, the RPC configuration operated at 400 W exhibited a distinctly faster initial heating, followed by a slower phase once evaporation began. Overall, while heating dynamics varied with power level, rupture behaviour was predominantly influenced by mechanical factors, particularly as failure consistently initiated at the heat-seal zone, which remains the weakest region of the packaging system under microwave treatment for polymer packaging such as PP trays.

This study indicated that although vertical constraints minimize vertical deformation and improve pressure retention, they do not eliminate rupture. In contrast, the RPC configuration using a sealed PEEK container demonstrated the ability to safely achieve sterilization temperatures without structural failure or food leakage. The center temperature reached 119 °C in 829 seconds, while the side temperature reached 118 °C. It should be noted that this heating duration is specific to the applied microwave power (400 W) and experimental conditions of this study. Internal pressure increased steadily to 0.89 bar (relative), driven by continuous water

evaporation under sealed conditions. A significant temperature difference at the early stage of the process between the center and side (maximum $\Delta T = around$ 40 °C at nearly 200 s) decreased as heating progressed. The final temperature difference was only 1.2 °C in this study, indicating that the temperature field became more even toward the end of heating. However, since measurements were recorded at only two points, this result cannot be generalised to the entire food volume. A true demonstration of three-dimensional heating uniformity would require either multiple temperature probes or validated electromagnetic–thermal modelling to capture the full spatial distribution.

This chapter examined a first study on the influence of mechanical constraints on the interaction between pressure build-up, temperature rise, and packaging deformation during microwave heating. The results lay the groundwork for future studies by showing that flexible trays are fundamentally limited by the weakness of the heat-seal zone, while rigid pressurised containers have the potential to withstand internal pressure long enough to reach sterilisation conditions. These findings provide a basis for developing multidirectional mechanical constraints for flexible packaging and for applying coupled three-dimensional electromagnetic–thermal–mechanical modelling to better understand deformation, and stress localisation during microwave sterilisation.

Future studies should first focus on investigating the role of radial constraint in flexible systems, since lateral expansion is hypothesized to contribute to rupture; multi-axial constraint configurations could help clarify this behaviour. A second priority should be the optimisation of packaging materials by developing flexible films with improved sealing strength and thermal resistance, for example through modified polypropylene grades, adhesive tie layers, or functional coatings, while also exploring alternatives such as PET, PA, or multilayer laminates. Finally, future work should focus on developing industrially adaptable rigid packaging systems and also glass containers that can tolerate internal pressurisation while maintaining thermal sealing integrity under microwave exposure.

# Chapter 6
# Conclusions and prospects

## 6.1 General conclusion

This thesis investigated the coupled thermo–fluid–mechanical behaviour of food packaging systems during thermal and microwave sterilization, with the long-term goal of supporting the development of water-free and energy-efficient counter-pressure processes. The central scientific problem addressed concerned the evolution of internal pressure, deformation, and rupture in flexible and semi-rigid polymeric containers, particularly polypropylene (PP) trays sealed with thin films. By combining experimental measurements and multiphysics numerical modelling, this research provides a mechanistic framework describing the interactions among heat transfer, CFD and structural mechanics that determine packaging stability during heat treatment.

The first study examined conventional retort sterilization of rigid metallic containers filled with a high-moisture model food (mashed potato). Experimental measurements of temperature and pressure, together with numerical simulations, demonstrated that pressure evolution results from the coupled contribution of dry-air expansion and water-vapour generation. The numerical model, developed and validated using experimental data, predicted temperature evolution at various locations inside the food container as well as the total headspace pressure arising from the combined effects of dry air expansion and water-vapour evaporation. The simulations also revealed that the applied heat transfer coefficient at the wall has a strong influence on heating kinetics. A key outcome of this work was the identification of the relative contribution of the gaseous phases to the total pressure, where dry air acts as the primary contributor only during the very early stage of heating, while water vapour dominates the majority of the sterilization cycle. This distinction defines the thermodynamic basis of pressure build-up in conventional retort systems and provides the reference for the subsequent analysis of packaging deformation in flexible polymer trays.

Building upon the understanding of pressure evolution established in the first study, the second study extended the investigation to semi-rigid polypropylene (PP) trays to analyse deformation under controlled air injection and heat treatment, both with and without pre-loaded mechanical constraints. This transition from rigid to flexible systems allowed the assessment of pressure-induced structural response in deformable packaging. Experimental results showed that rupture was governed by the effects of pressure development. Under air injection, the PP film displaced by approximately 10–11 mm before failure, with rupture consistently occurring between 41 and 46 mbar, regardless of the airflow rate. Failure initiated at the seal corners, confirming that stress localisation at these regions determines rupture onset. During heat treatment, rupture occurred at substantially lower pressures (8–9 mbar) and headspace temperatures near 50 °C. CFD–FSI simulations revealed airflow-driven stress concentration patterns, where the distribution of von Mises stress changed depending on the treatment mode: during air injection, the stress zones concentrated at the corners, whereas during heat treatment, the concentration shifted toward the seal edges. These stress zones corresponded closely with experimental

rupture sites. Introducing fixed pre-loaded mechanical constraints (FPC) increased the ability of the trays to withstand higher internal pressures, reaching values up to four times greater than those observed in unconstrained conditions. However, the time of rupture remained nearly unchanged, indicating that the FPC configuration allowed the tray to sustain higher pressures without significantly delaying failure. Variations in the applied pre-loads (5 N, 20 N, and 40 N) produced no marked difference in the maximum pressure attained, although rupture occurred at slightly different times. These findings suggest that pre-loading does not fundamentally alter the limiting pressure capacity of the packaging. Further experimental and numerical studies are required to confirm these observations and to fully validate the influence of mechanical constraints on the pressure–time behaviour of flexible trays. The results established that the structural integrity of flexible packaging is primarily governed by the thermo-mechanical behaviour and the internal flow-induced stress distribution.

Following the investigation of deformation and rupture behaviour under conventional heating, the third study extended the analysis to microwave heating at 915 MHz to evaluate the combined thermal and mechanical response of flexible and rigid packaging systems. Flexible polypropylene (PP) trays without constraint (NC) ruptured at internal pressures of approximately 7-8 mbar and headspace temperatures around 50°C, which was similar to heat treatment in the second study. The application of fixed (FPC with 80 N preload) and movable (FMC) mechanical constraints increased the maximum internal pressure to around 40 mbar, consistent with the values observed under conventional heating in the second study. A separate investigation was conducted using a rigid pressurised configuration (RPC) based on a sealed PEEK container to study microwave heating under confined pressure conditions. The system maintained structural integrity throughout heating, reaching centre and side temperatures of approximately 119 °C under a peak internal pressure of 0.89 bar (relative). The rigid containment provided stable pressurisation and allowed the food to reach sterilisation conditions without structural rupture or leakage, demonstrating the suitability of this configuration for high-temperature microwave processing. Further experimental and numerical studies are required to characterise spatial temperature distribution using multiple probes and to examine foods with different compositions, in order to validate these findings across a broader range of dielectric and moisture conditions.

### 6.2 Contributions to knowledge

This thesis represents a multidisciplinary contribution to the understanding of thermo–fluid–mechanical phenomena in food packaging during conventional and microwave sterilisation. It combines concepts from food engineering, materials science, computational modelling, and structural mechanics to describe the physical interactions that occur inside sealed containers during heat treatment. The work provides a scientific basis that was necessary before developing water-free and energy-efficient counterpressure processes to ensure both packaging integrity and process reliability.

A major contribution lies in the development of a multi-physics framework that couples heat transfer, internal pressurisation, and mechanical deformation through computational fluid

dynamics (CFD), structural mechanics, and fluid–structure interaction (FSI) modelling. This was supported by an extensive series of experiments conducted under different process configurations, including conventional retort sterilisation, tray systems with air injection, tray systems placed inside ovens, and microwave treatments, which together constitute an important contribution to understanding the coupled thermal and mechanical behaviour of food packaging. This approach also extends beyond conventional heat-transfer analysis by incorporating the mechanical response of the packaging.

The thesis also introduces a preliminary systematic experimental methodology combining controlled pressurisation, heat treatment, and mechanical constraints. This design made it possible to quantify the effects of internal pressure, airflow, and reinforcement on deformation and rupture behaviour in semi-rigid polymer trays. The use of preloaded fixtures provided a practical means of assessing the limits of vertical reinforcement and of identifying parameters for future multidirectional constraint systems.

From an applied perspective, the research establishes the operational boundaries of flexible and rigid packaging under coupled pressure and temperature conditions. It identifies the seal region as the critical zone governing overall structural reliability and highlights the potential of rigid confinement as a viable route for high-temperature microwave sterilisation without hydrostatic counterpressure.

Finally, the thesis advances the field through its cross-disciplinary methodology. By integrating CFD, FSI, structural mechanics, and material sciences for packaging applications, it proposes a step towards a more comprehensive framework for analysing packaging dynamics. This methodological contribution provides a useful basis for improving the understanding of structural, thermal, and mechanical interactions during high-temperature sterilisation and represents a foundation for future efforts aimed at developing more robust and sustainable packaging systems.

### 6.3 Recommendations for future work

Several important directions emerge from this research that should be pursued in future studies. One priority is the mechanics of the seal interface, since seal failure was consistently identified as the limiting factor in packaging integrity. Future work should characterise the temperature-dependent behaviour of PP films in detail. The modelling of temperature-dependent mechanical properties of PP is also mandatory, as it plays a critical role in accurately predicting deformation under thermal and mechanical loads. Study should also focus on the role of polymer relaxation, adhesion, and moisture exposure. In addition, the development of microwave heating models dedicated to sterilisation conditions is recommended to better predict the local temperature distribution within the food, instead of relying solely on assumed dielectric property variations. Numerical models should also be extended with cohesive-zone modelling (CZM) to explicitly simulate seal rupture within FSI frameworks, rather than inferring it indirectly from stress localisation.

Another direction concerns the development of multidirectional mechanical constraints. The findings of this thesis demonstrated that vertical constraints alone significantly increase rupture pressures, yet failure still occurred due to lateral expansion. Future designs should therefore incorporate reinforcement in both vertical and lateral planes, potentially using modular or adjustable preload systems. These should be evaluated systematically to identify optimal combinations of load capacity, pressure retention, and practical feasibility for industrial deployment. The exploration of materials such as multilayer films, reinforced polymers, and high-performance thermoplastics with enhanced sealing strength and thermal resistance also represents a critical research avenue. In addition, the long-term durability of these materials under repeated sterilisation cycles, varying heating rates, and fluctuating moisture conditions should be assessed to ensure reliable performance.

The results obtained with PEEK containers in this work highlight the need for further validation of rigid packaging systems and also the need to investigate the cooling stage during microwave sterilization for such rigid containers. Future studies should adapt such containers for manufacturability, automated filling and sealing, and integration into continuous microwave sterilisation lines. Equally important will be the evaluation of economic feasibility, sustainability advantages, and regulatory compliance, to determine whether rigid polymer containers can realistically be scaled into commercial production.

Finally, future work should extend beyond model foods such as mashed potato to realistic, heterogeneous food systems, since compositional variability and structural complexity can significantly influence pressure generation and heating uniformity. Moreover, the entire sterilisation cycle, including cooling, should be studied. Experimental validation of airflow fields, for example using particle image velocimetry (PIV), is also necessary to confirm the role of localised vortices in stress development and rupture initiation.

# References


AOAC, A. of O. A. C. (2000). AOAC Method 925.10 (air oven method) for moisture in flour. *Official Methods of Analysis*.

Abdul Ghani, A. G., Farid, M. M., Chen, X. D., & Richards, P. (1999). Numerical simulation of natural convection heating of canned food by computational fluid dynamics. *Journal of Food Engineering*, *41*(1), 55–64. https://doi.org/10.1016/S0260-8774(99)00073-4

Abdul Ghani, A. G., Farid, M. M., Chen, X. D., & Richards, P. (2001). Thermal sterilization of canned food in a 3-D pouch using computational fluid dynamics. *Journal of Food Engineering*, *48*(2), 147–156. https://doi.org/10.1016/S0260-8774(00)00150-3

Ağagündüz, D., Ayakdaş, G., Katırcıoğlu, B., & Ozogul, F. (2025). Advances in non-thermal food processing: a comprehensive approach to nutrient retention, food quality, and safety. *Sustainable Food Technology*.

Aiyengar, R., & Divecha, J. (2012). Experimental and statistical analysis of the effects of the processing parameters on the seal strength of heat sealed, biaxially oriented polypropylene film for flexible food packaging applications. *Journal of Plastic Film & Sheeting*, *28*(3), 244–256.

Al-Ghamdi, S. M. (2020). *Flexible and semirigid packaging for high pressure and microwave-based pasteurization and sterilization processes* (S. S. Sablani, J. Tang, & B. Rasco (Eds.)).

Al-Sharify, Z. T., Al-Najjar, S. Z., Naser, Z. A., Alsherfy, Z. A. I., & Onyeaka, H. (2025). The Impact of Fluid Flow on Microbial Growth and Distribution in Food Processing Systems. *Foods*, *14*(3), 401.

Allué Hoyos, C. (2014). *Applicability of COMSOL Multiphysics to combined heat, air and moisture transfer modelling in building envelopes*.

Annor-Nyarko, M., Xia, H., & Ayodeji, A. (2022). Thermomechanical analysis of a reactor pressure vessel under pressurized thermal shock caused by inadvertent actuation of the safety injection system. *Science and Technology of Nuclear Installations*, *2022*(1), 5886583.

Atuonwu, J. C., & Tassou, S. A. (2018). Quality assurance in microwave food processing and the enabling potentials of solid-state power generators: A review. *Journal of Food Engineering*, *234*, 1–15. https://doi.org/10.1016/j.jfoodeng.2018.04.009

Auksornsri, T., Bornhorst, E. R., Tang, J., Tang, Z., & Songsermpong, S. (2018). Developing model food systems with rice based products for microwave assisted thermal sterilization. *Lwt - Food Science and Technology*. https://doi.org/10.1016/J.LWT.2018.05.054

Auksornsri, T., Tang, J., Tang, Z., Lin, H., & Songsermpong, S. (2018). Dielectric properties of rice model food systems relevant to microwave sterilization process. *Innovative Food Science and Emerging Technologies*. https://doi.org/10.1016/J.IFSET.2017.09.002

Awuah, G. B. (2003). Dimensionless correlation for estimating internal pressure in thin-walled aluminum containers during thermal processing. *Journal of Food Process Engineering*, *26*(2), 223–236. https://doi.org/10.1111/j.1745-4530.2003.tb00598.x

Ayoub, J., Berkowitz, D., Kenyon, E., & Wadsworth, C. (1974). Continuous microwave sterilization of meat in flexible pouches. *Journal of Food Science*, *39*, 309–313. https://doi.org/10.1111/j.1365-2621.1974.tb02882.x

Ayvaz, H., Schirmer, S., Parulekar, Y., Balasubramaniam, V. M., Somerville, J. A., & Daryaei,

H. (2012). Influence of selected packaging materials on some quality aspects of pressure-assisted thermally processed carrots during storage. *LWT - Food Science and Technology*, *46*(2), 437–447. https://doi.org/https://doi.org/10.1016/j.lwt.2011.12.004

Bamps, B., Buntinx, M., & Peeters, R. (2023). Seal materials in flexible plastic food packaging: A review. *Packaging Technology and Science*, *36*(7), 507–532.

Barbosa-Cánovas, G. V, Medina-Meza, I., Candoğan, K., & Bermúdez-Aguirre, D. (2014). Advanced retorting, microwave assisted thermal sterilization (MATS), and pressure assisted thermal sterilization (PATS) to process meat products. *Meat Science*. https://doi.org/10.1016/J.MEATSCI.2014.06.027

Basar, Y., Weichert, D., & Petrolito, J. (2001). Nonlinear continuum mechanics of solids: fundamental mathematical and physical concepts. *Applied Mechanics Reviews*, *54*(6), B98–B99.

Bazilevs, Y., Hsu, M.-C., & Scott, M. A. (2012). Isogeometric fluid–structure interaction analysis with emphasis on non-matching discretizations, and with application to wind turbines. *Computer Methods in Applied Mechanics and Engineering*, *249–252*, 28–41. https://doi.org/https://doi.org/10.1016/j.cma.2012.03.028

Bhunia, K., Zhang, H., Liu, F., Rasco, B., Tang, J., & Sablani, S. S. (2016). Morphological changes in multilayer polymeric films induced after microwave-assisted pasteurization. *Innovative Food Science & Emerging Technologies*, *38*, 124–130. https://doi.org/https://doi.org/10.1016/j.ifset.2016.09.024

Bhuwan Pandit, R., Tang, J., Liu, F., & Mikhaylenko, G. (2007). A computer vision method to locate cold spots in foods in microwave sterilization processes. *Pattern Recognition*, *40*(12), 3667–3676. https://doi.org/10.1016/j.patcog.2007.03.021

Bornhorst, E. R., Liu, F., Tang, J., Sablani, S. S., & Barbosa-Cánovas, G. V. (2017). Food Quality Evaluation using Model Foods: a Comparison Study between Microwave-Assisted and Conventional Thermal Pasteurization Processes. *Food and Bioprocess Technology*. https://doi.org/10.1007/S11947-017-1900-9

Bornhorst, E. R., Tang, J., Sablani, S. S., & Barbosa-Cánovas, G. V. (2017). Thermal pasteurization process evaluation using mashed potato model food with Maillard reaction products. *LWT - Food Science and Technology*, *82*, 454–463. https://doi.org/10.1016/j.lwt.2017.04.019

Burfoot, D., & Self, K. P. (1988). Prediction of heating times for cubes of beef during water cooking. In *International Journal of Food Science and Technology* (Vol. 23, Issue 3, pp. 247–257). Oxford University Press.

Carson, J. K., Willix, J., & North, M. F. (2006). Measurements of heat transfer coefficients within convection ovens. *Journal of Food Engineering*, *72*(3), 293–301.

Celuch, M., Kopyt, P., & Olszewska-Placha, M. (2020). Modeling of cavities and loads with FDTD and FEM methods. In *Development of packaging and products for use in microwave ovens* (pp. 459–511). Elsevier.

Chandrasekaran, S., Ramanathan, S., & Basak, T. (2013). Microwave food processing—A review. *Food Research International*, *52*(1), 243–261. https://doi.org/10.1016/j.foodres.2013.02.033

Chen, H., Tang, J., & Liu, F. (2006). Coupled Simulation of an Electromagnetic Heating Process Using the Finite Difference Time Domain Method. *Journal of Microwave Power and Electromagnetic Energy*, *41*(3), 50–68. https://doi.org/10.1080/08327823.2006.11688563

Chen, H., Tang, J., & Liu, F. (2008). Simulation model for moving food packages in microwave heating processes using conformal FDTD method. *Journal of Food Engineering*. https://doi.org/10.1016/J.JFOODENG.2008.02.020

Chen, M., Siochi, E. J., Ward, T. C., & McGrath, J. E. (1993). Basic ideas of microwave processing of polymers. *Polymer Engineering & Science*, *33*(17), 1092–1109. https://doi.org/10.1002/pen.760331703

Cherbański, R., & Rudniak, L. (2013). Modelling of microwave heating of water in a monomode applicator – Influence of operating conditions. *International Journal of Thermal Sciences*. https://doi.org/10.1016/J.IJTHERMALSCI.2013.07.001

Ciancio, V., Dolfin, M., Francaviglia, M., & Preston, S. (2008). *Uniform materials and the multiplicative decomposition of the deformation gradient in finite elasto-plasticity*.

Curet, S., Rouaud, O., & Boillereaux, L. (2008). Microwave tempering and heating in a single-mode cavity: Numerical and experimental investigations. *Chemical Engineering and Processing: Process Intensification*, *47*(9), 1656–1665. https://doi.org/10.1016/j.cep.2007.09.011

Datta, A. K., & Rakesh, V. (2013). Principles of Microwave Combination Heating. *Comprehensive Reviews in Food Science and Food Safety*, *12*(1), 24–39. https://doi.org/https://doi.org/10.1111/j.1541-4337.2012.00211.x

De Albuquerque, C. D., Curet, S., & Boillereaux, L. (2021). Influence of heating rate during microwave pasteurization of ground beef products: Experimental and numerical study. *Journal of Food Process Engineering*, *44*(7), e13722. https://doi.org/10.1111/jfpe.13722

Decareau, R. V. (1968). *Sterilization* (E. C. B. T.-M. P. E. OKRESS (Ed.); pp. 98–100). Academic Press. https://doi.org/10.1016/B978-1-4831-9679-4.50016-1

Decareau, R. V. (1985). Microwaves in the food processing industry. In *Food science and technology (USA)*.

Dhawan, S., Varney, C., Barbosa-Cánovas, G. V, Tang, J., Selim, F., & Sablani, S. S. (2014). The impact of microwave-assisted thermal sterilization on the morphology, free volume, and gas barrier properties of multilayer polymeric films. *Journal of Applied Polymer Science*. https://doi.org/10.1002/APP.40376

Dowell, E. H., & Hall, K. C. (2001). Modeling of fluid-structure interaction. *Annual Review of Fluid Mechanics*, *33*(1), 445–490.

Dutta, S. J., Rouaud, O., Dole, P., Thillier, A., Belaubre, N., & Curet, S. (2024a). CFD-based Approach For Prediction Of Headspace Pressure In Can During Thermal Sterilization Of Foods. *COMSOL Conference 2024*. https://www.comsol.com/paper/cfd-based-approach-for-prediction-of-headspace-pressure-in-can-during-thermal-sterilization-of-foods-135292

Dutta, S. J., Rouaud, O., Dole, P., Thillier, A., Belaubre, N., & Curet, S. (2024b). Microwave Sterilization: Interlinking Numerical Modelling, Food Packaging, and Engineering Solutions. *Food Engineering Reviews*, *16*(2), 192–224. https://doi.org/10.1007/s12393-024-09370-w

Dwivedi, M., & Ramaswamy, H. S. (2010). An empirical methodology for evaluating the fluid to particle heat transfer coefficient in bi-axially rotating cans using liquid temperature data. *Food and Bioprocess Technology*, *3*(5), 716–731.

El Ouafa, S., Vincent, S., Le Chenadec, V., Trouette, B., Fereka, S., & Chadil, A. (2024). A Compressible Formulation of the One-Fluid Model for Two-Phase Flows. *Fluids*, *9*(4), 90.

Farah, S., Anderson, D. G., & Langer, R. (2016). Physical and mechanical properties of PLA, and their functions in widespread applications — A comprehensive review. *Advanced Drug Delivery Reviews*, *107*, 367–392. https://doi.org/10.1016/j.addr.2016.06.012

Fleckenstein, B. S., Sterr, J., & Langowski, H.-C. (2016). The Influence of High Pressure Treatment and Thermal Pasteurization on the Surface of Polymeric Packaging Films. *Packaging Technology and Science*, *29*(6), 323–336. https://doi.org/10.1002/pts.2213

Fragassa, C., Topalovic, M., Pavlovic, A., & Vulovic, S. (2019). Dealing with the Effect of Air in Fluid Structure Interaction by Coupled SPH-FEM Methods. *Materials*, *12*(7), 1162.

Fu, Z., Liu, H., Duan, L., Huang, L., Wang, Y., Sun, X., & Zhou, C. (2023). *Numerical simulation of thermal sterilization heating process of canned fruits with different shapes based on UDM and RDM*. *19*(5), 159–175. https://doi.org/10.1515/ijfe-2022-0181

Garrell, M. G., Shih, A. J., Lara-Curzio, E., & Scattergood, R. O. (2003). Finite-element analysis of stress concentration in ASTM D 638 tension specimens. *Journal of Testing and Evaluation*, *31*(1), 52–57.

Gaur, U., & Wunderlich, B. (1981). Heat capacity and other thermodynamic properties of linear macromolecules. IV. Polypropylene. *Journal of Physical and Chemical Reference Data*, *10*(4), 1051–1064.

Geedipalli, S. S. R., Rakesh, V., & Datta, A. K. (2007). Modeling the heating uniformity contributed by a rotating turntable in microwave ovens. *Journal of Food Engineering*, *82*(3), 359–368. https://doi.org/10.1016/j.jfoodeng.2007.02.050

Gezahegn, Y. A., Tang, J., Sablani, S. S., Pedrow, P. D., Hong, Y.-K., Lin, H., & Tang, Z. (2021). Dielectric properties of water relevant to microwave assisted thermal pasteurization and sterilization of packaged foods. *Innovative Food Science & Emerging Technologies*, *74*, 102837. https://doi.org/10.1016/j.ifset.2021.102837

Ghai, G., Teixeira, A. A., Welt, B. A., Goodrich-Schneider, R., Yang, W., & Almonacid, S. (2011). Measuring and Predicting Head Space Pressure during Retorting of Thermally Processed Foods. *Journal of Food Science*, *76*(3), E298–E308. https://doi.org/10.1111/j.1750-3841.2011.02075.x

Goldblith, S. A. (1966). Basic Principles of Microwaves and Recent Developments. In C. O. Chichester, E. M. Mrak, & G. F. B. T.-A. in F. R. Stewart (Eds.), *Advances in Food Research* (Vol. 15, pp. 277–301). Academic Press. https://doi.org/10.1016/S0065-2628(08)60082-8

Gulati, T., Zhu, H., & Datta, A. K. (2016). Coupled electromagnetics, multiphase transport and large deformation model for microwave drying. *Chemical Engineering Science*, *156*, 206–228.

Halim, L., Pascall, M. A., Lee, J., & Finnigan, B. (2009). Effect of pasteurization, high-pressure processing, and retorting on the barrier properties of nylon 6, nylon 6/ethylene vinyl alcohol, and nylon 6/nanocomposites films. *Journal of Food Science*, *74*(1), N9–N15. https://doi.org/10.1111/j.1750-3841.2008.00990.x

Han, J.-W., Zhao, C.-J., Yang, X.-T., Qian, J.-P., & Fan, B.-L. (2015). Computational modeling of airflow and heat transfer in a vented box during cooling: Optimal package design. *Applied Thermal Engineering*, *91*, 883–893.

Hashimoto, Y., Ishiaku, U. S., Leong, Y. W., Hamada, H., & Tsujii, T. (2006). Effect of heat-sealing temperature on the failure criteria of oriented polypropylene/cast polypropylene heat seal. *Polymer Engineering & Science*, *46*(2), 205–214.

Hirschey, J. A., Reeve, M. L., Cassel, J. M., Brejcha, L. J., Legan, J. D., & Mohr, L. M. (2017). *A Microwave Retort System, A Process For Heating Food Products Using A Microwave Retort System, And Food Products Formulated For Microwave Retort* (International Application No. PCT/US2015/050650). https://patentscope.wipo.int/search/en/detail.jsf?docId=WO2016044571

Hong, Y.-K., Roger, S., Tang, J., Bui, L., & Ghandi, A. (2021). Effect of Electric Field Distribution on the Heating Uniformity of a Model Ready-to-Eat Meal in Microwave-Assisted Thermal Sterilization Using the FDTD Method. *Foods*, *10*(2), 311. https://doi.org/https://doi.org/10.3390/foods10020311

Ilhan, I., Turan, D., Gibson, I., & ten Klooster, R. (2021). Understanding the factors affecting the seal integrity in heat sealed flexible food packages: A review. *Packaging Technology and Science*, *34*(6), 321–337.

Jain, D. (2017). *Electromagnetic and Thermal Analysis of Microwave Heating in 915 MHz Single Mode Cavity Systems: Microwave Assisted Thermal Sterilization and Pasteurization* [ProQuest Dissertations Publishing]. https://www.proquest.com/openview/6891a0c85973e63a9b718a38aa2aa0ed/1?pq-origsite=gscholar&cbl=18750

Jain, D., Tang, J., Liu, F., Tang, Z., & Pedrow, P. D. (2018). Computational evaluation of food carrier designs to improve heating uniformity in microwave assisted thermal pasteurization. *Innovative Food Science and Emerging Technologies*. https://doi.org/10.1016/J.IFSET.2018.06.015

Jeppson, M. R. (1964). Techniques of continuous microwave food processing. *Cornell Hotel and Restaurant Administration Quarterly*, *5*(1), 60–64.

Jeppson, M. R., & Harper, J. C. (1967). *Microwave heating of substances under hydrostatic pressure* (3,335,253). Washington, DC: U.S. Patent and Trademark Office.

Jimenez, P. S., Bangar, S. P., Suffern, M., & Whiteside, W. S. (2024). Understanding retort processing: A review. *Food Science & Nutrition*, *12*(3), 1545–1563. https://doi.org/doi.org/10.1002/fsn3.3912

Joseph, S. J., Speers, R. A., & Pillay, V. (1996). Effect of head space variation and heat treatment on the thermal and rheological properties of nonagitated, conduction-heated materials. *LWT-Food Science and Technology*, *29*(5–6), 556–560.

Kenyon, E. M., Westcott, D. E., La Casse, P., & Gould, J. W. (1971). A System For Continuous Thermal Processing Of Food Pouches Using Microwave Energy. *Journal of Food Science*, *36*(2), 289–293. https://doi.org/10.1111/j.1365-2621.1971.tb04045.x

Komarov, V., & Yakovlev, V. (2001). Simulations of components of microwave heating applicators by FEMLAB, MicroWaveLab and QuickWave-3D. *36th Annual Microwave Symposium, Proceedings, San Francisco, CA, USA*.

Kumar, M., Gaur, K. K., & Shakher, C. (2015). Measurement of material constants (Young's modulus and Poisson's ratio) of polypropylene using digital speckle pattern interferometry (DSPI). *Journal of the Japanese Society for Experimental Mechanics*, *15*(Special_Issue), s87–s91.

Laguerre, O., Amara, S. Ben, Charrier-Mojtabi, M.-C., Lartigue, B., & Flick, D. (2008). Experimental study of air flow by natural convection in a closed cavity: Application in a domestic refrigerator. *Journal of Food Engineering*, *85*(4), 547–560.

Laguerre, O., Benamara, S., Remy, D., & Flick, D. (2009). Experimental and numerical study of heat and moisture transfers by natural convection in a cavity filled with solid obstacles.

*International Journal of Heat and Mass Transfer*, *52*(25–26), 5691–5700.

Landy, J. J. (1965). *Method of sterilizing food in sealed containers* (3,215,539). Washington, DC: U.S. Patent and Trademark Office.

Lau, M. H., Tang, J., Taub, I. A., Yang, T. C. S., Edwards, C. G., & Mao, R. (2003). Kinetics of chemical marker formation in whey protein gels for studying microwave sterilization. *Journal of Food Engineering*, *60*(4), 397–405. https://doi.org/10.1016/S0260-8774(03)00063-3

Lau, W. (2015). *Numerical modelling of heat and mass transfer in a steam-air sterilisation process inside an industrial autoclave*. UNSW Sydney.

Lespinard, A. R., Arballo, J. R., Badin, E. E., & Mascheroni, R. H. (2019). Comparative study between conventional and microwave-assisted pasteurization of packaged milk by finite element modeling. *Journal of Food Processing and Preservation*, *43*(11), e14207. https://doi.org/10.1111/jfpp.14207

Li, H., Shi, S., Lin, B., Lu, J., Lu, Y., Ye, Q., Wang, Z., Hong, Y., & Zhu, X. (2019). A fully coupled electromagnetic, heat transfer and multiphase porous media model for microwave heating of coal. *Fuel Processing Technology*, *189*, 49–61.

Li, P., Guo, W., Fan, J., Su, C., Zhao, X., & Xu, X. (2023). Fluid-structure interaction analysis of airflow, structural mechanics and aerosol dynamics in a four-generation acinar model. *Journal of Aerosol Science*, *171*, 106166.

Li, X., & Farid, M. (2016). A review on recent development in non-conventional food sterilization technologies. *Journal of Food Engineering*, *182*, 33–45. https://doi.org/doi.org/10.1016/j.jfoodeng.2016.02.026

Lin, C. C., & Li, C. F. (1971). Microwave sterilization of oranges in glass-pack. *Journal of Microwave Power*, *6*(1), 45–47.

Liu, C., Shen, L., Liu, H., Gong, X., Liu, C., Zheng, X., Zhang, S., & Yang, C. (2023). Improvement of Temperature Distribution Uniformity of Ready-to-Eat Rice during Microwave Reheating via Optimizing Packaging Structure. In *Foods* (Vol. 12, Issue 15). https://doi.org/10.3390/foods12152938

Loh, J., & Breene, W. M. (1983). A laboratory microwave sterilizer and its possible application toward improving texture of sterilized vegetables. *Journal of Food Processing and Preservation*, *7*(2), 77–92.

Long, F. E., Shaw, F. B., & Lisle, H. C. (1966). *Microwave sterilization and vacuumizing of products in flexible packages and apparatus therefor* (3,261,140.). Washington, DC: U.S. Patent and Trademark Office. https://patents.google.com/patent/US3261140A/en

Luan, D., Tang, J., Pedrow, P. D., Liu, F., & Tang, Z. (2016). Analysis of electric field distribution within a microwave assisted thermal sterilization (MATS) system by computer simulation. *Journal of Food Engineering*. https://doi.org/10.1016/J.JFOODENG.2016.05.009

Lubarda, V. A., & Krajcinovic, D. (1995). Some fundamental issues in rate theory of damage-elastoplasticity. *International Journal of Plasticity*, *11*(7), 763–797.

Maddah, H. A. (2016). Polypropylene as a promising plastic: A review. *Am. J. Polym. Sci*, *6*(1), 1–11.

Mcavoy, B. R. (1971). *Solid state microwave oven* (U.S. Patent No. 3,557,333). U.S. Patent and Trademark Office.

McGinnis, D. S. (1986). Surface heat transfer distribution in a weir type pressurized water retort for processing foods in flexible retort pouches. *Canadian Institute of Food Science and Technology Journal*, *19*(2), 45–52.

Mesías, M., Wagner, M., George, S., & Morales, F. J. (2016). Impact of conventional sterilization and ohmic heating on the amino acid profile in vegetable baby foods. *Innovative Food Science & Emerging Technologies*, *34*, 24–28. https://doi.org/doi.org/10.1016/j.ifset.2015.12.031

Mezzacapo, A., D'Addio, R., & De Stefano, G. (2025). A Computational Thermo-Fluid Dynamics Simulation of Slot Jet Impingement Using a Generalized Two-Equation Turbulence Model. *Energies*, *18*(14), 3862.

Mohamed, I. O. (2007). Determination of an effective heat transfer coefficients for can headspace during thermal sterilization process. *Journal of Food Engineering*, *79*(4), 1166–1171.

Mohamed, I. O. (2016). Modeling and simulation of thermal sterilization of conduction heat canned foods using heat transfer coefficients boundary conditions. *International Journal*, *3*(2), 49.

Mokwena, K. K., Tang, J., Dunne, C. P., Yang, T. C. S., & Chow, E. (2009). Oxygen transmission of multilayer EVOH films after microwave sterilization. *Journal of Food Engineering*, *92*(3), 291–296. https://doi.org/10.1016/j.jfoodeng.2008.11.011

Nget, S., Mith, H., Boué, G., Curet, S., & Boillereaux, L. (2023). The Development of a Digital Twin to Improve the Quality and Safety Issues of Cambodian Pâté: The Application of 915 MHz Microwave Cooking. *Foods*, *12*(6), 1187. https://doi.org/10.3390/foods12061187

Oden, J. T., & Edition, T. (2008). Non-linear continuum mechanics. *Introduction to Mathematical Modelling, September*, 69.

Pandit, R. B., Tang, J., Mikhaylenko, G., & Liu, F. (2006). Kinetics of chemical marker M-2 formation in mashed potato—a tool to locate cold spots under microwave sterilization. *Journal of Food Engineering*, *76*(3), 353–361. https://doi.org/10.1016/j.jfoodeng.2005.05.032

Parhi, A., Bhunia, K., Rasco, B., Tang, J., & Sablani, S. S. (2019). Development of an Oxygen Sensitive Model Gel System to Detect Defects in Metal Oxide Coated Multilayer Polymeric Films. *Journal of Food Science*, *84*(9), 2507–2519. https://doi.org/10.1111/1750-3841.14755

Patel, J., Sonar, C. R., Al-Ghamdi, S., Tang, Z., Yang, T., Tang, J., & Sablani, S. S. (2021). Influence of ultra-high barrier packaging on the shelf-life of microwave-assisted thermally sterilized chicken pasta. *LWT*, *136*, 110287. https://doi.org/10.1016/j.lwt.2020.110287

Patel, P. N., Chanoarana, D. I., & III, A. G. (1991). Internal Pressure Profile in Semi-Rigid Food Packages During Thermal Processing in Steam/Air. *Journal of Food Science*, *56*(3), 831–834. https://doi.org/10.1111/j.1365-2621.1991.tb05393.x

Pathak, S. K., Liu, F., & Tang, J. (2003). Finite Difference Time Domain (FDTD) Characterization of a Single Mode Applicator. *Journal of Microwave Power and Electromagnetic Energy*, *38*(1), 37–48. https://doi.org/10.1080/08327823.2003.11688486

Pitchai, K. (2011). *Electromagnetic and heat transfer modeling of microwave heating in domestic ovens*. University of Nebraska.

Prakash, A., Kim, H. J., & Taub, I. A. (1997). Assessment of microwave sterilization of foods

using intrinsic chemical markers. *Journal of Microwave Power and Electromagnetic Energy*, *32*(1), 50–57. https://doi.org/10.1080/08327823.1997.11688323

Quickfem. (2023). *Chapter 14: The plane stress problem*. Quickfem.

Ramalingam, R., VA, S., George, J., & SN, S. (2015). Effect of pasteurization and retort processing on spectral characteristics, morphological, thermal, Physico-Mechanical, barrier and optical properties of Nylon-Based food packaging materials. *Packaging Technology and Science*, *28*(5), 425–436.

Reddy, J. N. (2015). *An Introduction to Nonlinear Finite Element Analysis: with applications to heat transfer, fluid mechanics, and solid mechanics*. Oxford university press.

Resurreccion, F. P., Tang, J., Pedrow, P., Cavalieri, R., Liu, F., & Tang, Z. (2013). Development of a computer simulation model for processing food in a microwave assisted thermal sterilization (MATS) system. *Journal of Food Engineering*, *118*(4), 406–416. https://doi.org/10.1016/j.jfoodeng.2013.04.021

Segui, J. (2013). *Equation-Based Modeling, a Custom Model of a Beating Heart*. https://www.comsol.fr/blogs/equation-based-modeling-a-custom-model-of-a-beating-heart/

Semeliss, M., Wong, G., & Turtle, M. (1990). *The yield and post-yield behavior high-density polyethylene*. NAG-I-974.

Sheng, Q. (2013). *Tribological and mechanical characterization of thin polymer films*. Northeastern University.

Sheploak, M., & Dugundji, J. (1998). *Large deflections of clamped circular plates under initial tension and transitions to membrane behavior*.

Singh, A. P., & Ramaswamy, H. S. (2015). Effect of can orientation on heat transfer coefficients associated with liquid particulate mixtures during reciprocation agitation thermal processing. *Food and Bioprocess Technology*, *8*(7), 1405–1418.

Singh, A., Singh, A. P., & Ramaswamy, H. S. (2015). A refined methodology for evaluation of heat transfer coefficients in canned particulate fluids under rapid heating conditions. *Food and Bioproducts Processing*, *94*, 169–179.

Spencer, P. L. (1950). *Method of treating food stuff* (2495429A). Washington, DC: U.S. Patent and Trademark Office.

Stanley, R. A., & Petersen, K. (2017). Microwave-assisted pasteurization and sterilization—commercial perspective. In *The Microwave Processing of Foods (Second Edition)*. https://doi.org/10.1016/B978-0-08-100528-6.00010-3

Steris. (2020). *Sterile Barrier Integrity and Seal Strength*. https://www.steris-ast.com/solutions/testing-and-validation/packaging-testing/sterile-barrier-integrity-and-seal-strength

Su, T., Zhang, W., Zhang, Z., Wang, X., & Zhang, S. (2021). Numerical investigation of the deformable porous media treated by the intermittent microwave. *Processes*, *9*(5). https://doi.org/10.3390/pr9050757

Sun, X., Yu, C., Wang, Y., & Liu, Y. (2007). Numerical simulation of soft palate movement and airflow in human upper airway by fluid-structure interaction method. *Acta Mechanica Sinica*, *23*(4), 359–367.

Sun, Y., Liu, Q., Cattafesta III, L. N., Ukeiley, L. S., & Taira, K. (2019). Effects of sidewalls and leading-edge blowing on flows over long rectangular cavities. *AIAA Journal*, *57*(1),

106–119.

Szpicer, A., Bińkowska, W., Stelmasiak, A., Zalewska, M., Wojtasik-Kalinowska, I., Piwowarski, K., Piepiórka-Stepuk, J., & Półtorak, A. (2025). Computational fluid dynamics simulation of thermal processes in food technology and their applications in the food industry. *Applied Sciences*, *15*(1), 424.

Taghian Dinani, S., Hasić, M., Auer, M., & Kulozik, U. (2020). Assessment of uniformity of microwave-based heating profiles generated by solid-state and magnetron systems using various shapes of test samples. *Food and Bioproducts Processing*, *124*, 121–130. https://doi.org/10.1016/j.fbp.2020.08.013

Taghian Dinani, S., Kubbutat, P., & Kulozik, U. (2020). Assessment of heating profiles in model food systems heated by different microwave generators: Solid-state (semiconductor) versus traditional magnetron technology. *Innovative Food Science & Emerging Technologies*, *63*, 102376. https://doi.org/10.1016/j.ifset.2020.102376

Tang, J. (2015). Unlocking Potentials of Microwaves for Food Safety and Quality. *Journal of Food Science*, *80*(8), E1776–E1793. https://doi.org/10.1111/1750-3841.12959

Tang, J., Hao, F., & Lau, M. (2002). *Microwave heating in food processing*. https://doi.org/10.1142/9789812706584_0001

Tang, J., Hong, Y.-K., Inanoglu, S., & Liu, F. (2018). Microwave pasteurization for ready-to-eat meals. *Current Opinion in Food Science*. https://doi.org/10.1016/J.COFS.2018.10.004

Tang, J., & Liu, F. (2020). *Microwave sterilization or pasteurization transport carriers*. Google Patents.

Tang, J., Liu, F., Pathak, S. K., & Eves, I. I. E. E. (2006). *Apparatus and method for heating objects with microwaves* (7,119,313.). Washington, DC: U.S. Patent and Trademark Office.

Teleken, J. T., Dutra, A. C., Laurindo, J. B., & Carciofi, B. A. M. (2023). Numerical modeling of heating tomato pulp in continuous flow microwave-assisted thermal processing: Estimation of quality parameters. *Journal of Food Process Engineering*, *46*(2), e14216. https://doi.org/10.1111/jfpe.14216

Tetsuya, T., Ishiaku, U. S., Mizoguchi, M., & Hamada, H. (2005). The effect of heat sealing temperature on the properties of OPP/CPP heat seal. I. Mechanical properties. *Journal of Applied Polymer Science*, *97*(3), 753–760.

Thorborg, J., Klinkhammer, J., & Heitzer, M. (2012). Transient and residual stresses in large castings, taking time effects into account. *IOP Conference Series: Materials Science and Engineering*, *33*(1), 12050.

Tolve, R., Galgano, F., Caruso, M. C., Tchuenbou-Magaia, F. L., Condelli, N., Favati, F., & Zhang, Z. (2016). Encapsulation of health-promoting ingredients: applications in foodstuffs. *International Journal of Food Sciences and Nutrition*, *67*(8), 888–918.

Tutar, M., Erdogdu, F., & Toka, B. (2009). Computational modeling of airflow patterns and heat transfer prediction through stacked layers' products in a vented box during cooling. *International Journal of Refrigeration*, *32*(2), 295–306.

Vadivambal, R., & Jayas, D. S. (2010). Non-uniform temperature distribution during microwave heating of food materials—A review. *Food and Bioprocess Technology*, *3*(2), 161–171.

Varga, S., & Oliveira, J. C. (2000). Determination of the heat transfer coefficient between bulk medium and packed containers in a batch retort. *Journal of Food Engineering*, *44*(4), 191–

198.

Wang, Y., Wig, T. D., Tang, J., & Hallberg, L. M. (2003a). Dielectric properties of foods relevant to RF and microwave pasteurization and sterilization. *Journal of Food Engineering*, *57*(3), 257-268. https://doi.org/10.1016/S0260-8774(02)00306-0

Wang, Y., Wig, T. D., Tang, J., & Hallberg, L. M. (2003b). Sterilization of foodstuffs using radio frequency heating. *Journal of Food Science*, *68*(2), 539–544.

Water Europe. (2023). *The value of water: Towards a water-smart society*. https://watereurope.eu/

Williams, A. (1993). New Technologies in Food Preservation and Processing: Part I. *Nutrition & Food Science*, *93*(6), 16–19. https://doi.org/10.1108/EUM0000000001007

Xiang, Y., Chen, X., & Vlassak, J. J. (2005). Plane-strain bulge test for thin films. *Journal of Materials Research*, *20*(9), 2360–2370.

Xu, S., Liu, J., & Wang, X. (2020). Thermal conductivity enhancement of polymers via structure tailoring. *Journal of Enhanced Heat Transfer*, *27*(5).

Yamada, K., Miyata, K., & Kumaresan, R. (2017). A novel methodology for peel strength enhancement of heat-sealed oriented polypropylene/cast polypropylene film by tensile cyclic loading. *Materials Chemistry and Physics*, *187*, 112–118.

Yang, H. Y., Yan, B. W., Meng, L. L., Jiao, X. D., Huang, J. L., Gao, W. H., Zhao, J. X., Zhang, H., Chen, W., & Fan, D. M. (2022). Mathematical modeling of continuous microwave heating of surimi paste. *Journal of Food Engineering*, *315*. https://doi.org/10.1016/j.jfoodeng.2021.110797

Yang, H., Yan, B., Chen, W., & Fan, D. (2023). Prediction and innovation of sustainable continuous flow microwave processing based on numerical simulations: A systematic review. *Renewable and Sustainable Energy Reviews*, *175*, 113–183. https://doi.org/10.1016/j.rser.2023.113183

Ye, J., Hong, T., Wu, Y., Wu, L., Liao, Y., Zhu, H., Yang, Y., & Huang, K. (2017). Model Stirrer Based on a Multi-Material Turntable for Microwave Processing Materials. *Materials*, *10*(2). https://doi.org/10.3390/ma10020095

Yoon, C. S., Hong, S. I., Cho, A. R., Lee, H. S., Park, H. W., & Lee, K. T. (2015). Analysis of the causes of deformation of packaging materials used for ready-to-eat foods after microwave heating. *Korean Journal of Food Science and Technology*, *47*(1), 63–69.

Zhang, H., Datta, A. K., Taub, I. A., & Doona, C. (2001). Electromagnetics, heat transfer, and thermokinetics in microwave sterilization. *AIChE Journal*, *47*(9), 1957–1968. https://doi.org/10.1002/aic.690470907

Zhang, H., Tang, Z., Rasco, B., Tang, J., & Sablani, S. S. (2016). Shelf-life modeling of microwave-assisted thermal sterilized mashed potato in polymeric pouches of different gas barrier properties. *Journal of Food Engineering*, *183*, 65–73. https://doi.org/10.1016/J.JFOODENG.2016.03.021

Zhang, J., Mannheim, C. H., Gilbert, S. G., & Zheng, C. (1992). Prediction of overpressure required for seal integrity during sterilization of semirigid food and drug packages. *Packaging Technology and Science*, *5*(5), 271–280. https://doi.org/10.1002/pts.2770050508

Zhang, L., Barrett, R., Cloetens, P., Detlefs, C., & Sanchez del Rio, M. (2014). Anisotropic elasticity of silicon and its application to the modelling of X-ray optics. *Synchrotron Radiation*, *21*(3), 507–517.

Zhang, W., Tang, J., Liu, F., Bohnet, S., & Tang, Z. (2014). Chemical marker M2 (4-hydroxy-5-methyl-3(2H)-furanone) formation in egg white gel model for heating pattern determination of microwave-assisted pasteurization processing. *Journal of Food Engineering*, *125*, 69–76. https://doi.org/10.1016/j.jfoodeng.2013.10.020

Zhou, X., Gezahegn, Y., Zhang, S., Tang, Z., Takhar, P. S., Pedrow, P. D., Sablani, S. S., & Tang, J. (2023). Theoretical reasons for rapid heating of vegetable oils by microwaves. *Current Research in Food Science*, *7*, 100641. https://doi.org/10.1016/j.crfs.2023.100641

Zhou, X., Pedrow, P. D., Tang, Z., Bohnet, S., Sablani, S. S., & Tang, J. (2023). Heating performance of microwave ovens powered by magnetron and solid-state generators. *Innovative Food Science & Emerging Technologies*, *83*, 103240. https://doi.org/10.1016/j.ifset.2022.103240

Zhou, X., Tang, Z., Pedrow, P. D., Sablani, S. S., & Tang, J. (2023). Microwave heating based on solid-state generators: New insights into heating pattern, uniformity, and energy absorption in foods. *Journal of Food Engineering*, *357*, 111650. https://doi.org/10.1016/j.jfoodeng.2023.111650

Zhu, H., Sun, Q., Liu, X., Liu, J., Sun, H., Wu, W., Tan, P., & Chen, Z. (2021). Fluid–structure interaction-based aerodynamic modeling for flight dynamics simulation of parafoil system. *Nonlinear Dynamics*, *104*(4), 3445–3466.

Zhu, J., Kuznetsov, A. V, & Sandeep, K. P. (2007). Mathematical modeling of continuous flow microwave heating of liquids (effects of dielectric properties and design parameters). *International Journal of Thermal Sciences*, *46*(4), 328–341. https://doi.org/10.1016/j.ijthermalsci.2006.06.005

# Publications and Communications

**Peer Reviewed Publications (Published (*))**

1) *Dutta, S. J., Rouaud, O., Dole, P., Thillier, A., Belaubre, N., & Curet, S. (2024a). CFD-based Approach For Prediction Of Headspace Pressure In Can During Thermal Sterilization Of Foods. COMSOL Conference 2024. https://www.comsol.com/paper/cfd-based-approach-for-prediction-of-headspace-pressure-in-can-during-thermal-sterilization-of-foods-135292

2) *Dutta, S. J., Rouaud, O., Dole, P., Thillier, A., Belaubre, N., & Curet, S. (2024b). Microwave Sterilization: Interlinking Numerical Modelling, Food Packaging, and Engineering Solutions. Food Engineering Reviews, 16(2), 192–224. https://doi.org/10.1007/s12393-024-09370-w

3) *Dutta, S. J., Rouaud, O., Dole, P., Thillier, A., Belaubre, N., & Curet, S. (2025). Coupled CFD-Structural Mechanics Simulation Of Deformation In Non-Rigid Polypropylene Food Packaging, COMSOL Conference 2025.

4) *Curet, S., Dutta, S. J., & Rouaud, O. (2025). Effect of a wireless temperature/ pressure sensor location during in-packaged food microwave heating, COMSOL Conference 2025.

**Titre :** Développement d'un traitement de chauffage par micro-ondes comme substitut au procédé classique de stérilisation en autoclave

**Mots clés :** Traitement thermique ; Mécanique des structures ; Emballage alimentaire ; Modélisation numérique ; Simulation ; Micro-ondes

**Résumé :** Cette recherche porte sur le développement d'un procédé de traitement thermique par micro-ondes comme alternative durable à la stérilisation conventionnelle, en mettant l'accent sur le comportement thermo-mécanique des emballages alimentaires soumis à des températures élevées. Les études de stérilisation conventionnelle réalisées sur des récipients métalliques rigides ont combiné des expériences et des modélisations numériques sous COMSOL Multiphysics® afin d'analyser l'évolution de la température et de la pression. Les résultats ont montré que l'air sec contribue principalement à la pression interne totale au début du chauffage, tandis que la pression de vapeur devient dominante pendant le reste du processus. Des barquettes flexibles en polypropylène (PP) ont ensuite été étudiées sous différentes contraintes mécaniques afin d'évaluer leur réponse structurelle lors d'injections d'air, de traitements thermiques et de chauffages par micro-ondes. Bien que l'application de contraintes ait augmenté la tolérance à la pression interne, la rupture s'est produite de manière récurrente au niveau de la zone de scellage. L'étude finale a été réalisée avec un récipient rigide en polyétheréthercétone (PEEK) conçu pour résister à la pression interne lors du chauffage par micro-ondes, atteignant des températures supérieures à 118 °C. Dans l'ensemble, ce travail pose les bases du développement des procédés de stérilisation par micro-ondes en établissant, dans un premier temps, une compréhension scientifique des dynamiques thermo-mécaniques des emballages alimentaires lors du traitement thermique, ouvrant la voie à la conception de systèmes de transformation des aliments plus sûrs et plus économes en énergie. mécaniquement confinés constituent une voie prometteuse vers un traitement thermique sûr, sans eau et économe en énergie.

**Title :** Development of a microwave heating treatment as a substitute for the classical retort sterilization process

**Keywords :** Thermal processing ; Structural mechanics ; Food packaging ; Numerical modelling; Simulation; Microwaves

**Abstract :** This research investigates the development of a microwave-based heat treatment process as a sustainable alternative to conventional sterilization, focusing on the thermo–mechanical behavior of food packaging during high-temperature processing of a model food product (mashed potato). Conventional sterilization studies on rigid metal containers combined experiments and numerical modelling using COMSOL Multiphysics® to analyze temperatures within the food product and pressure evolution within the head space, showing that dry air contributes to total internal pressure mainly during the early heating stage, while vapour pressure becomes dominant during the rest of the process. Flexible polypropylene (PP) trays (empty and filled with mashed potato) were then examined under different mechanical constraints to evaluate their structural response under air injection, convective heating treatment, and microwave heating. Although the application of mechanical constraints increased internal pressure tolerance of the packaging, rupture consistently occurred at the heat-seal interface. The final study was conducted with a rigid Polyether ether ketone (PEEK) container designed to withstand internal pressure during microwave heating, achieving internal temperatures above 118 °C. Overall, this work lays the groundwork for understanding the thermo–mechanical dynamics of food packaging during heat treatment, providing a foundation for designing safer and more energy-efficient food processing systems.